Plasma Diagnostics

H. Ji, Y. Raitses and L. Berzak Hopkins

Department of Astrophysical Sciences, Princeton University, 4 Ivy Lane, Princeton, 08544, New Jersey, U.S.A.

*E-mail: hji@princeton.edu

Abstract

This is a series of lecture notes from Plasma Diagnostics (course code AST555) taught by Professor Hantao Ji in spring 2013 and 2014, and then with Professors Yevgeny Raitses and Laura Berzak Hopkins in spring 2025 and 2026 at Princeton University. These notes have been compiled by Adam Robbins – please contact him with questions or typos.

Diagnostics (*May 2, 2026*)

1 Introduction to Plasma Diagnostics

Measurement science is a fundamental and important part of all fields of science and engineering, as well as almost all everyday activities. It involves theoretical, numerical, and experimental methods to determine the outcome of a measurement at any level of uncertainty. There is even a specific field called metrology designated to study the science of measurement. The capability of measurement, alongside of theoretical and numerical predictability, often defines the frontier or maturity of a particular field. In fact, there have been numerous Nobel prizes awarded based on the success of a particular measurement technique or its outcome. Table 1 provides an non-exhaustive list of Nobel Prizes falling in this category of achievements. Plasma physics is no exception - plasma measurement methods or diagnostics are an integral part of the field. The purpose of this course is to provide an overview and introduction to plasma diagnostics across nearly all sub-fields of plasma physics.

1.1 Diversity of Plasmas

Plasmas are extremely diverse. One important category is low-temperature plasmas which include capacitively coupled plasmas (CCP), inductively coupled plasmas (ICP), helicon plasmas, arc discharges, glow discharges, flames,

Table 1: A non-exhaustive list of Nobel prizes awarded to measurement achievements or experimental techniques relevant to plasma.

Name(s)	Year	Discipline	Citation
Victor Hess	1936	Physics	"for his discovery of cosmic radiation"
Martin Ryle	1974	Physics	"for their pioneering research in radio astrophysics: Ryle for his observations and inventions, in particular of the aperture synthesis technique"
Arno Penzias, Robert Wilson	1978	Physics	"for their discovery of cosmic microwave background radiation"
Frederick Reines	1995	Physics	"for the detection of the neutrino"
Raymond Davis, Masatoshi Koshiba	2002	Physics	"for pioneering contributions to astrophysics, in particular for the detection of cosmic neutrinos"
Riccardo Giacconi	2002	Physics	"for pioneering contributions to astrophysics, which have led to the discovery of cosmic X-ray sources"
John C. Mather, George F. Smoot	2006	Physics	"for their discovery of the blackbody form and anisotropy of the cosmic microwave background radiation"
Eric Betzia	2014	Chemistry	"for the development of super-resolved fluorescence microscopy"
Takaaki Kajita, Arthur McDonald	2015	Physics	"for the discovery of neutrino oscillations, which shows that neutrinos have mass"
Rainer Weiss, Barry Barish, Kip Thorne	2017	Physics	"for decisive contributions to the LIGO detector and the observation of gravitational waves"
Gérard Mourou, Donna Strickland	2018	Physics	"for their method of generating high-intensity, ultra-short optical pulses"

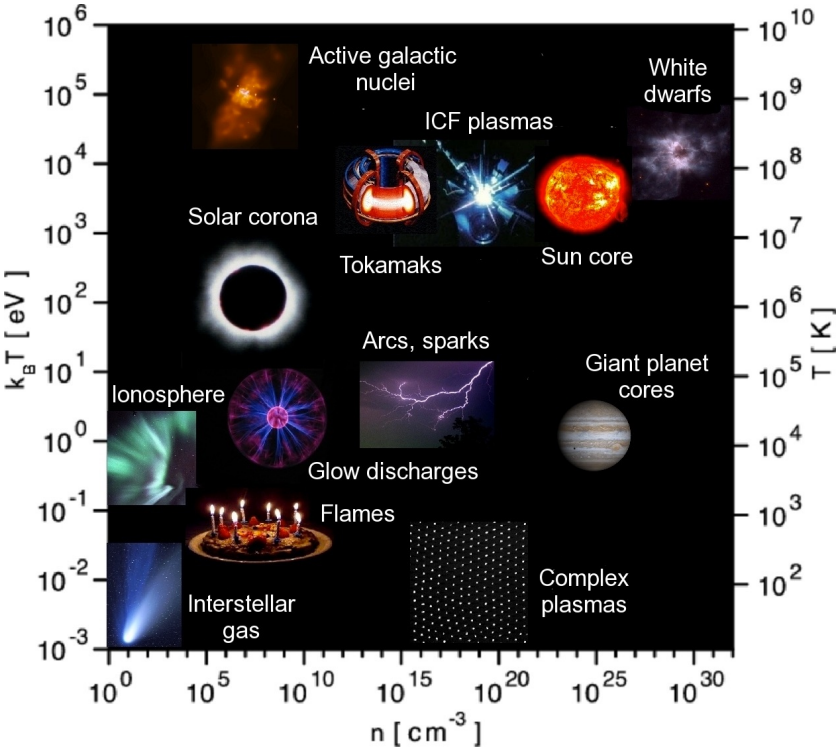

Fig. 1: Various plasmas across the universe and in the laboratory in the parameter space of density and temperature.

hot cathode discharges, plasma gun discharges, and dusty (complex) plasmas. Another category is non-neutral plasmas, either pure electron or pure ion plasmas, some of which are being developed as qubits for quantum computing. Furthermore we have those plasma used in magnetic confinement fusion made by ohmic discharges or heated by RF power or neutral beam injection (NBI). Inertial confinement fusion uses plasmas made by high-power lasers, pulsed power, or heavy ion beams. Natural plasmas include those in Earth's ionosphere, near-Earth space, heliosphere, and on the Sun, collectively called heliophysical plasmas. Giant planet cores and the solar interior are also in the plasma state but with much higher densities and pressures. Plasmas beyond our solar system are astrophysical plasmas, which are extremely diverse themselves, from intestellar medium or galactic plasma, to much more tenuous intergalactic plasmas, to much denser and exotic plasmas in white dwarfs and neutron stars, to those surrounding black holes. Their measurements and study are an integral part of astronomy. Figure 1 illustrates plasmas' extreme diversity in the parameter space of number density over 30 decades and temperature over 9 decades.

Not shown in Fig. 1 are other properties which encompass a wide diversity. For example, the magnetic field can be extremely weak ($< \mu$Gauss or 10^{-10} Tesla) in intergalactic plasmas or extremely strong (10^{9-11} Tesla) in magnetized neutron stars or magnetars. Plasmas can be extremely poorly ionized (ionization fraction $< 10^{-12}$) in protoplanetary disks, or can be fully ionized, even with all electrons fully stripped from their heavy metal ions at relativistic energies above GeV. Plasmas can be nearly collisionless with very long Coulomb collision mean free paths or strongly coupled where Coulomb coupling dominates inter-particle interactions, and can even be degenerated at high density as in the neutron star interior. Plasmas can be an active ingredient of a complex system involving chemical radicals as in plasma chemistry, or an active agent interacting with other forms of matter as in micro-electronic processing or even with biological systems in plasma medicine. The definition of plasma can be further extended to intermediate areas between different states of matter, such as warm dense matter which is too dense to be described by weakly coupled plasma physics yet too hot to be described by condensed matter physics.

1.2 Components of a Plasma

Given the extreme diversity of plasmas, we take a broader definition of what constitutes a plasma:

- **Charged particles** consist of: free electrons; ions with various degrees of ionization until all of their bounded electrons are fully stripped or with extra electrons attached so that ions are negatively charged; and positively or negatively charged molecules. These particles can be in the form of matter or anti-matter. Charged ions with at least one bound electron, as well as charged molecules, can have their electron(s) in an excited state ready to fall to a lower energy state by emitting an electromagnetic wave (line radiation), or to jump to a higher energy state by absorbing an incoming electromagnetic wave (line absorption). Charged particles can emit electromagnetic waves when they experience acceleration or de-acceleration (Bremsstrahlung radiation due to electric field and cyclotron or synchrotron due to magnetic field).
- **Electromagnetic fields** at all frequencies and wavelengths can influence the motion of charged particles by exerting forces on them. The charge density and the motion of charged particles (thus electric current) are linked to electromagnetic fields via Maxwell equations. In extremely dense plasmas such as in the solar interior where electromagnetic waves are constantly absorbed and emitted, **photons can be treated as another particle species** carrying momentum and energy but no mass. In these case, plasmas often become opaque or the *opacity* becomes larger than unity.
- **Neutral particles**, such as charge-neutral atoms or molecules, do not normally interact with electromagnetic fields and instead influence charged particles through collisions. In addition, when a plasma is sufficiently

opaque, electromagnetic waves or photons can directly interact with neutral particles by exchanging energy and momentum with them.
- **Neutrino and gravitational waves**, emerged in recent years as new information carriers from the plasma where they originate in some extreme astrophysical events such as supernovae and compact object mergers.

Since the discovery of gravitational waves, combining information from multiple carriers like light waves (photons), neutrinos, cosmic rays (charged particles), and gravitational waves to study extreme astrophysical events is often called multi-messenger astronomy.

1.3 Plasma Properties

Of the above plasma constituents, charge and neutral particles are usually treated statistically due to their sheer numbers. Below are plasma models following the hierarchy of plasma models in order of increasing simplicity and more assumptions.

1. Exact microscopic descriptions of each particles (Chap.7 in Krall and Trivelpiece, 1973).
2. Boltzman/Vlasov Equations: the Boltzmann equation describes evolution of particle distribution $f(\boldsymbol{x}, \boldsymbol{v}, t)$ with binary interactions (collisions):

$$\frac{df}{dt} = \frac{\partial f}{\partial t} + \boldsymbol{v} \cdot \frac{\partial f}{\partial \boldsymbol{x}} + \frac{q}{m}\left(\boldsymbol{E} + \boldsymbol{v} \times \boldsymbol{B}\right) \cdot \frac{\partial f}{\partial \boldsymbol{v}} = \left(\frac{\delta f}{\delta t}\right)_{\text{coll}}, \tag{1}$$

   where $\boldsymbol{x}$ and $\boldsymbol{v}$ are the particle location and velocity vectors, respectively. $\boldsymbol{E}$ and $\boldsymbol{B}$ are the electric and magnetic field vectors, respectively. The Vlasov equation is the Boltzmann equation *without* collisions, i.e. where $(\delta f/\delta t)_{\text{coll}} = 0$.
3. Drift-kinetic/Gyro-kinetic Models: approximation based on guiding center motion or charge ring motion.
4. Multi-fluid Models: approximation based on fluid descriptions for each species.
5. Single fluid (MHD) Models: approximation based on a combined one-fluid description.
6. Mean-field Theory/Models: approximation based on *averaged* fluid quantities over a certain spatial or temporal scale.

The macroscopic fluid quantities are obtained by *taking moments* of the Boltzmann equation, Eq. (1), to remove the dependence on particle velocity $\boldsymbol{v}$,

$$\langle g(\boldsymbol{x}, t)\rangle \equiv \int g(\boldsymbol{x}, \boldsymbol{v}, t) f(\boldsymbol{x}, \boldsymbol{v}, t) d\boldsymbol{v}, \tag{2}$$

which calculates any quantity (can be a vector or a general tensor), g, with *weighted* contributions based on the distribution f at each location and time.

Taking $g = 1$ yields the macroscopic particle density,

$$n(\boldsymbol{x}, t) = \int f(\boldsymbol{x}, \boldsymbol{v}, t) d\boldsymbol{v}, \tag{3}$$

while taking $g = m\boldsymbol{v}$ yields the momentum density,

$$m \langle \boldsymbol{v}(\boldsymbol{x}, t) \rangle) = m \int \boldsymbol{v} f(\boldsymbol{x}, \boldsymbol{v}, t) d\boldsymbol{v}, \tag{4}$$

leading to the macroscopic fluid velocity $\boldsymbol{V}(\boldsymbol{x}, t) = \langle \boldsymbol{v}(\boldsymbol{x}, t) \rangle / n(\boldsymbol{x}, t)$.

When $g = \frac{1}{2} m (\boldsymbol{v} - \boldsymbol{V})(\boldsymbol{v} - \boldsymbol{V})$, *i.e.* the velocity spread after the frame shift to $\boldsymbol{V}$, the corresponding moment of g becomes the pressure tensor,

$$\frac{1}{2} m \langle (\boldsymbol{v} - \boldsymbol{V})(\boldsymbol{v} - \boldsymbol{V}) \rangle = p\boldsymbol{I} + \boldsymbol{\Pi}, \tag{5}$$

where p is the *isotropic* macroscopic pressure, $\boldsymbol{I}$ is a unit tensor, and $\boldsymbol{\Pi}$ is the off-diagonal pressure tensor. Thus, the macroscopic temperature in *units of energy* can be defined as $T(\boldsymbol{x}, t) = p(\boldsymbol{x}, t)/n(\boldsymbol{x}, t)$. Note that the diagonal components of the pressure here can be *anisotropic* with respect to the magnetic field, *i.e.* pressure in the parallel direction of the field lines can be different from pressure in other directions, $p_\parallel \neq p_\perp$. For simplicity, we take the pressure to be isotropic here.

The next and final moment we consider is the heat flux

$$\boldsymbol{q} = \frac{1}{2} m \left\langle (\boldsymbol{v} - \boldsymbol{V})^2 (\boldsymbol{v} - \boldsymbol{V}) \right\rangle. \tag{6}$$

The terms due to Coulomb collisions include the plasma source via *e.g.* ionization or recombination $S = \int \left(\frac{\delta f}{\delta t}\right)_{\text{coll}} d\boldsymbol{v}$, the frictional force $\boldsymbol{R} = \int m (\boldsymbol{v} - \boldsymbol{V}) \left(\frac{\delta f}{\delta t}\right)_{\text{coll}} d\boldsymbol{v}$, and the heating $Q = \int \frac{1}{2} m (\boldsymbol{v} - \boldsymbol{V})^2 \left(\frac{\delta f}{\delta t}\right)_{\text{coll}} d\boldsymbol{v}$.

The above fluid moment can be constructed for each species in a plasma, and then combined for a single fluid MHD model. We define macroscopic quantities of a single fluid MHD model by combining electron and ion fluids as

$$\rho = m_i n_i + m_e n_e \approx m_i n_i, \tag{7}$$

$$\boldsymbol{V} = \frac{m_i n_i \boldsymbol{V}_i + m_e n_e \boldsymbol{V}_e}{\rho} \approx \boldsymbol{V}_i, \tag{8}$$

$$\boldsymbol{j} = e (Z n_i \boldsymbol{V}_i - n_e \boldsymbol{V}_e) \approx e n_e (\boldsymbol{V}_i - \boldsymbol{V}_e), \tag{9}$$

where Z is the ion charge and $n_e \approx Z n_i$. These fluid quantifies are related via Maxwell's equations. For example, together $\boldsymbol{B}$, n_e, $\boldsymbol{V}_e$, and $\boldsymbol{V}_i$ need to satisfy Ampére's law in the non-relativistic limit where the displacement current is negligible,

$$\boldsymbol{\nabla} \times \boldsymbol{B} = \mu_0 \boldsymbol{j} \approx e \mu_0 n_e (\boldsymbol{V}_i - \boldsymbol{V}_e). \tag{10}$$

See GPPII lecture notes (Ji, 2024) for more detailed derivations and discussion of fluid models including the standard magnetohydrodynamic or MHD model.

1.4 Diversity of Plasma Diagnostics

Unsurprisingly, extremely diverse plasmas are matched by extremely diverse measurement methods or diagnostics, which can be categorized in several different ways. One traditional way is by plasma categories:

- Laboratory plasmas which can be further subdivided into:
  - Low-temperature plasmas
  - High-temperature plasmas

  which can be measured by both *in-situ* and *ex-situ* (or remote sensing) techniques. Each of these techniques can be further subdivided into passive ones (such as emission measurements) and active ones (such as techniques using lasers).
- Space plasmas which include the Earth's ionosphere and magnetosphere, the magnetospheres of other planets in the solar system, the solar wind or interplanetary plasmas, as well as the near-solar interstellar medium. These plasmas can be primarily measured *in-situ* by spacecraft launched from Earth, and are collectively covered by heliophysical plasmas.
- Solar and astrophysical plasmas, which are primarily measured by *ex-situ* (or remote-sensing) techniques, such as cosmic ray measurements. They are basically all natural plasmas beyond heliophysical plasmas, except solar plasmas.

Typical courses based on this categorization are offered by each subfield of plasma physics: laboratory plasma physics, heliophysics (space and solar physics), and astrophysics (astronomy).

Plasma diagnostics can also be categorized in several other ways, each with its own advantages. They include

- Measurement techniques, such as *in-situ* and *ex-situ* (or remote sensing). Each of these techniques can be based on the detection of particles (neutral, charged, photon, neutrino) or waves (wavelengths from gamma-rays to radio-frequency light waves, and gravitational waves). A complementary way to categorize plasma diagnostics based on measurement techniques is by whether they are active or passive diagnostics:
  - Passive versus active techniques. The latter include measurements of particles, fields, and waves with external interference by injecting particles (such as charged or neutral particle probe beams) or waves (microwaves or laser as light waves) while the former does not involve external interference. Active diagnostics sometimes can achieve localized measurements at a remote distance via proper arrangement of injection and detection angles.

Table 2: A list of plasma diagnostics and the quantities they measure. V_{sp} is the plasma potential relative to a reference ground.

diagnostics	quantities	categories	subfields
Energy analyzer / particle flux measurements	f_e, f_i, f_0	*in-situ*, *ex-situ*	lab, space, astro
Magnetic probes/loops	$\boldsymbol{B}$	*in-situ*, global	lab, space
Electric probes	$f_e, n_e, T_e, V_{sp}, \boldsymbol{V}_i, \boldsymbol{E}$	*in-situ*	lab, space
Refraction index	n_e, B_{path}	*ex-situ*	lab, astro
EM radiation by free electrons	f_e, n_e, T_e, Z, B	*ex-situ*	lab, astro
Line radiation by bounded electrons	n_e, n_i, n_0, T_e, T_i, $V_{i,\text{path}}$, B	*ex-situ*, *in-situ*	lab, astro
EM wave scattering	$n_e, T_e, V_e, Z, n_i, T_i, V_i$	passive, active	lab, astro
Diagnostics using neutral beam injection (NBI)	$n_e, n_i, T_i, \boldsymbol{V}_i, B$	active	lab
Laser-induced-fluorescence (LIF)	f_i, f_0	active	lab
Neutron measurements	fusion reaction rates	*ex-situ*	lab
Neutrino and gravitational waves measurements	indirect information on plasmas	*ex-situ*	astro

This categorization is sometimes used in programs emphasizing engineering aspects of plasma diagnostics focusing on implementation, including detector and sensing technology.

- Measurement principles. This categorization emphasizes the physical principles of diagnostics and is suitable for the study or development of measurement techniques sometimes called metrology. This categorization is often used by programs emphasizing the physics behind measurement methods, especially laboratory plasma physics.
- Measurement quantities, such as electron density, magnetic field etc. Each of these quantities can be measured by multiple techniques, and each can serve as a benchmark or for the calibration of others. This categorization is often used in programs emphasizing the usage of various data sources for their synthesis to develop new physics insights.

In AST555, we use several of these categorizations: primarily based on laboratory plasma physics (including both high-temperature and low-temperature plasmas), but supplemented by providing overviews in space, solar and astrophysical plasma measurements to provide a broader understanding of each diagnostic. We also emphasize the physical principles of each diagnostic, which are universal regardless of their specific applications, supplemented by specific measurement techniques to provide some practical knowledge on how they are implemented in real world. However, the purpose of this course is *not* to train students to be experts on any specific diagnostic but rather to provide a basic foundation in the field.

1.5 Summary

- Measurement science (metrology) is a fundamental and important part of all fields of science and engineering, including plasma physics.
- Plasma is extremely diverse across laboratory, space, solar physics and astrophysics.
- Plasma consists of particles (charged, neutral, and neutrino), fields (electric, magnetic, their combination as light waves). Gravitational waves also carry information about the plasmas from which they originate.
- Plasma diagnostics are also extremely diverse across each subfield of plasma physics. They can be categorized in several different ways, each with its own advantages.
- A list of plasma diagnostics is summarized in Table 2.

1.6 Further Reading

- Hutchinson (2002)
- Pfaff et al (1998a,b)
- Wüest et al (2007)
- Rieke (2012)

2 Magnetized Plasma Experiments

Magnetized laboratory plasma experiments can be divided into two broad categories: magnetic confinement experiments of high-temperature ($\gtrsim 1$ keV) plasmas to achieve and control the conditions for nuclear fusion reactors and magnetized experiments of low-temperature ($\lesssim 10$ eV) plasmas to provide a platform for the study of basic plasma processes and phenomena. There are many plasma diagnostics common to both categories but there are also significant differences. In this lecture, a brief introduction is given for both categories to provide context for the diagnostics that will be discussed in the following Lectures.

2.1 Magnetic Confinement Experiments

We begin with a primer for magnetically confined plasmas. As shown by the *Virial Theorem* (see Sec 2.2, Ji, 2024), a plasma cannot be confined in steady state by the magnetic field it generates. In order to confine a plasma magnetically, it is thus necessary to supply current to external coils. The coil design, therefore, dictates the confinement magnetic configuration, and there are literally infinite degrees of freedom in coil design.

The simplest magnetic geometry is linear geometries which include the magnetic cusp, magnetic mirror, theta pinch, Z pinch, and screw pinch (or stabilized pinch). They have many favorable characteristics for confining plasmas, in addition to being simple, but they all suffer end losses that cannot be avoided. This naturally leads to the solutions based on toroidal configurations, which are classified into six categories briefly described below. We begin by following **Chap. 2 of Ji (2024) on magnetostatic equilibrium**. Then we describe the six categories in turn by using the toroidal coordinates shown in Fig. 2 where various definitions are given.

2.1.1 Toroidal Configurations

In all toroidal configurations, a finite *poloidal magnetic field* B_θ is required since the plasma cannot be confined by a pure vacuum toroidal magnetic field, $B_{\phi,v}$. This is because $B_{\phi,v} \propto R^{-1}$, causing particles drift vertically due to the ∇B drift, but its direction depends on the charge. This charge separation results in a vertical electric field, E_Z, which drives plasma out of the confinement region radially by the $E_Z \times B_{\phi,v}$ drift. To suppress E_Z, a finite poloidal magnetic field can short out the charge separation by connecting areas with opposite charges via helical field lines.

The poloidal field B_θ can be provided by current flowing either in the coils or in the plasma. The dimensionless parameters to quantify B_θ are

$$q(r) \equiv \frac{2\pi}{\iota(r)} \equiv \frac{\#\text{ of toroidal turn}}{\#\text{ of poloidal turn}} \approx \frac{rB_\phi}{R_0 B_\theta}, \tag{11}$$

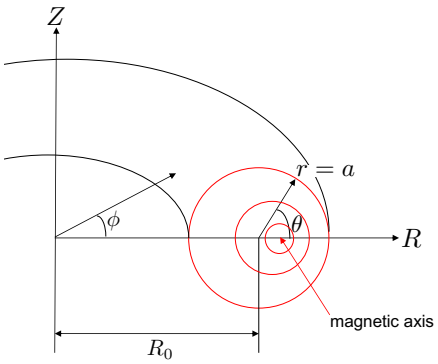

Fig. 2: Magnetic configuration of a toroidal confinement system. The cylindrical coordinate system is defined as (R, ϕ, Z) while the toroidal coordinate system is defined as (r, θ, ϕ). Here the toroidal angle is ϕ and the poloidal angle is θ. Other definitions: the major radius is R_0 and the minor radius is a. The magnetic axis is also shown in the figure. Surfaces shown in red represent magnetic flux surfaces, on which the magnetic field and current density vectors lie and the plasma density and temperature are constant (when in magnetostatic equilibrium) (see Sec 2.3, Ji, 2024).

when integrating along the field line at large aspect ratio $R_0/r \gg 1$. Here $\iota(r)$ is the rotational transform used in stellarators while $q(r)$ is the *safety factor* used elsewhere.

The $q(r)$ profile determines MHD stability against *current-driven instabilities* which appear in discrete pairs of mode numbers (m, n), where m (n) is the poloidal (toroidal) mode number. The locations where $q = m/n$ are called rational surfaces where $\boldsymbol{k} \cdot \boldsymbol{B} = (B_\theta/r)(m - nq) = 0$ so that perturbations have constant phases along the field lines, meaning instabilities grow easily without bending them. Usually, the higher the q, the more stable the plasma is against current-driven instabilities.

In contrast, profiles of plasma kinetic parameters (n_e, T_e, and T_i), together with $q(r)$, determine MHD stability against *pressure-driven instabilities*, such as interchange instabilities or ballooning mode instabilities, which also appear in (m, n). Interchange instabilities are sensitive to the balance between the good curvature of field lines on the inboard side and the bad curvature on the outboard side, while ballooning mode instabilities are localized on the bad curvature side. Pressure-driven instabilities can be stabilized by finite magnetic shear $q' \equiv \partial q/\partial r$ so that bending field lines, which is stabilizing, becomes unavoidable even slightly away from the rational surfaces. A finite toroidal flow V_ϕ can also contribute to plasma stability, especially when coupled with the nearby electrically conducting wall. More detailed descriptions of toroidal confinement configurations and their MHD stability are given by **the GPP II lecture notes (Chap.5-8, Ji, 2024)**.

Collisional transport in toroidal plasmas is dominated by *neoclassical transport* mediated by the trapped particles along field lines on the outer-board side where the magnetic field is relatively weak. However, the overall transport is dominated by *anomalous transport*, especially for electrons, due to drift-wave turbulence driven by radial temperature gradients.

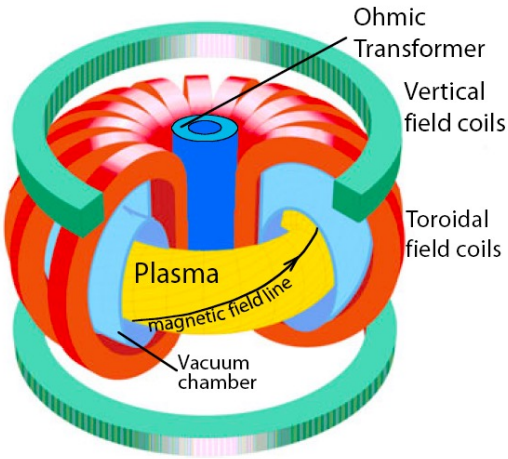

Fig. 3: Tokamak configuration.

2.1.2 Tokamaks

The tokamak, illustrated in Fig. 3, is the most advanced and mature fusion configuration, the one ITER will use. It generates a poloidal magnetic field by its toroidal current or simply plasma current. Typically, its toroidal cross-section takes an *elongated shape* which not only increases the plasma volume, but also increases q for improved MHD stability as it takes more toroidal turns for field lines to complete a poloidal turn. More recently, further fine-tuning of the plasma shape for negative *triangularity* (reversed D-shaped plasmas) seems to show better confinement than the usual positive triangularity (D-shaped plasmas) shown in Fig. 3.

In order to illustrate how tokamaks, or magnetically confined fusion plasmas in general, work in the laboratory, a typical sequence of events are listed below for an Ohmically heated plasma:

1. Vacuum vessel is evacuated to a sufficiently low residual pressure $< 10^{-7}$ Torr.
2. Toroidal field coils are energized to provide B_ϕ in vacuum.
3. The Ohmic transformer is "pre-charged", i.e., its primary current is flat-topped at a full value for a short time, when possible.

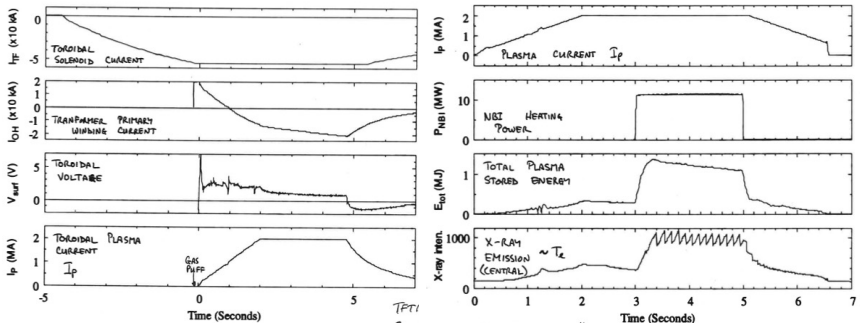

Fig. 4: Discharge waveforms of TFTR Tokamak: Ohmic plasma and NBI-heated plasma.

4. The vacuum vessel is filled with the gas of choice (H, D, or D-T), up to a pressure of a few 10^{-4} Torr.
5. The primary Ohmic transformer current is decreased so that the loop voltage $V_{\rm loop}$ (measured by a flux loop, Lecture 3) increases leading to a finite $E_\parallel$. When $E_\parallel$ is sufficiently large, the gas breaks down to generate plasma, and the plasma current I_p increases while it drops.
6. The vertical field is increased as the plasma current is increased to keep the plasma centered radially.
7. The plasma is heated and fueled (by gas puffing etc.) while the discharge is sustained.
8. The primary transformer current reaches its negative maximum and decays, leading to $V_{loop} \propto E_\parallel < 0$. I_p decreases with narrowing current channel and eventually the discharge terminates or disrupts.

An example discharge from TFTR (Tokamak Fusion Test Reactor) is shown in Fig. 4. TFTR was a large tokamak with a circular cross-section. Its major radius was $R_0 = 2.45$ m and minor radius $a = 0.8$ m. $E_\parallel$ can be calculated by $V_{\rm loop}/2\pi R_0 \approx 0.39$ V/m in peak and 0.06 V/m in steady state. The latter translates to an averaged resistivity of $E_\parallel/(I_p/\pi a^2) \approx 6.5 \times 10^{-8}\Omega$ m which is only a factor of four larger than that of copper of $1.7 \times 10^{-8}\Omega$ m. Also shown in Fig. 4 is a Neutral Beam Injection (NBI) heated discharge which is much hotter with sawtooth oscillations in X-ray emission, indicating central electron temperature T_e drops during repeated reconnection events.

To develop some physical intuition, some key dimensionless parameters are listed in Table 3 for a typical L-mode discharge in TFTR with corresponding comments.

One particular dimensionless figure of merit for tokamak confinement efficiency is the *beta normal*, $\beta_{\rm N}$, defined as the beta limit,

$$\beta < \beta_{\rm N} \frac{I({\rm MA})}{a({\rm m})B({\rm T})} = \beta_{\rm N} \left(\frac{I}{1\ {\rm MAmp}}\right)\left(\frac{a}{1\ {\rm meter}}\right)^{-1}\left(\frac{B}{1\ {\rm Tesla}}\right)^{-1}, \qquad (12)$$

Table 3: A list of dimensionless parameters for a typical L-mode discharge in TFTR: line-averaged density $\bar{n}_e \sim 5\times10^{19}$ m^{-3}, $T_i \sim T_e \sim 9$ keV, $B_{\phi,V} = 5$ T, $I_p \sim 2$ MA, $\tau_E \sim 0.1$ s, $R_0 \sim 2.6$ m, $a \sim 1.0$ m.

parameter	value	comment
$(4\pi/3)\lambda_D^3 n$	$\sim 10^8$	plasma approximation valid
$\lambda_{\rm mfp}/2\pi R_0$	$\sim 10^2$	plasma is quite kinetic along the field line; uniformity on flux surfaces
$v_\parallel/v_{th,e}$, $v_\parallel \equiv \frac{I_p}{\pi a^2}/en_e$	$\sim 2.5\times10^{-3}$	electron drift speed $\ll$ thermal speed: f_e, f_i nearly Maxwellian despite long $\lambda_{\rm mfp}$
$\rho^* \equiv \rho_i/a$	2×10^{-3}	MHD description valid despite long $\lambda_{\rm mfp}$ [see Chap 1 of Ji (2024)]
τ_E/τ_A	$\sim 3\times10^7$	transport much slower than ideal MHD time, justifying MHD equilibrium and stability analysis
β_p (see Lecture 3)	~ 1	plasma energy comparable to B_θ energy

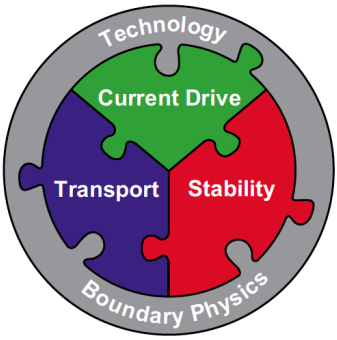

Fig. 5: Three major interconnected pillars of tokamak research and their couplings to boundary physics as well as technology such as controls from Luce (2011).

where $\beta_{\rm N} = 4.4$ for the Sykes limit (1974, 1983) and $\beta_{\rm N} = 2.8$ for the Troyon limit (1984) due to ballooning mode instabilities. A nominal $\beta_{\rm N} = 2.1$ has been chosen for ITER.

Tokamaks typically start with Ohmically heated plasma by inductively driving plasma current through a transformer, but its heating becomes inefficient when T_e reaches about 1 keV due to reduced plasma resistance. Thus, *auxiliary heating* by Neutral Beam Injection (NBI), Ion Cyclotron Range of Frequency (ICRF or ICRH), and Electron Cyclotron Resonance Heating (ECRH) are needed for the plasma to reach the fusion temperatures $\gtrsim 10$ keV. Tokamaks also require a continuous supply of plasma current beyond the initial Ohmic induction for steady-state operation. *Current drive* techniques such as those via Electron Cyclotron Current Drive (ECCD) and NBI have been used with some success but there is more work to be done.

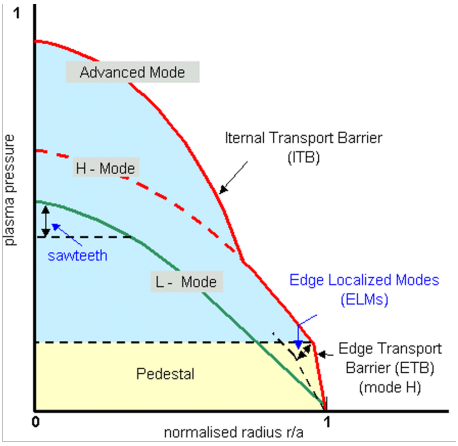

Fig. 6: Tokamak pressure profile for L-mode and advanced modes including H-mode with an Edge Transport Barrier (ETB) and an Internal Transport Barrier (ITB).

Figure 5 illustrates relationships between the three major pillars of tokamak research: global stability, transport, and current drive. Their solutions must be compatible with each other to be viable for a tokamak fusion reactor. In addition, they must also be compatible also with boundary conditions (such as plasma-material interactions or PMI) and available technologies (such as controls to avoid disruptions). More details of the integrated tokamak research can be found in Luce (2011).

2.1.3 Advanced Tokamaks and Spherical Torus (ST)

Compared to the relatively conservative ITER design based on the so-called *L-mode* (L stands for low) operation, there are several more "advanced" features that can be used to improve efficiency and thus reduce the size and cost of a tokamak fusion reactor. Sometimes they are called "advanced tokamaks" although there is no formal definition. The advanced modes include the *H-mode* (H stands for high) with an ETB (Edge Transport Barrier) and an ITB (Internal Transport Barrier) mode. Figure 6 illustrates their differences in pressure profile. As a result, β_N can be substantially larger, as shown in Fig. 7.

A larger pressure gradient can also benefit current drive by inducing *bootstrap current* through neoclassical effects. Trapped particles do not carry net current themselves, but their gradient can yield a current just like diamagnetic current but with a finite parallel component to the local magnetic field. Passing and trapped particles are illustrated in Fig. 8. A gradient in the trapped particles (either in their density or temperature) can result in a net current in the green box in Fig. 8. The bootstrap current helps sustain the toroidal plasma current as long as the pressure gradient is maintained. Collisions can spread bootstrap current to passing particles leading to a net flowing current,

which can be a significant fraction of the required current in advanced tokamak scenarios. See more details in Luce (2011).

The Spherical Torus (ST) can be regarded as an advanced tokamak with a lower aspect ratio (see Fig. 9). Many advanced features depend on the aspect ratio and become more pronounced at lower aspect ratios. For example, at lower aspect ratios the fraction of bootstrap current is larger while the beta normal increases substantially (see Fig. 7) due to better confinement efficiency. These can make fusion reactors based on ST more compact and thus more economical. However, STs are less developed in general compared to tokamaks and they are also more restrictive in the available space for the reactor.

Finally, high confinement efficiency in advanced tokamaks and STs inherently carries higher risks in terms of global stability, requiring advanced control technologies such as robust disruption avoidance. The recent interest in data science in Artificial Intelligence and Machine Learning techniques is timely to address this issue.

2.1.4 Stellarators

In contract to tokamaks and STs where the poloidal magnetic field is generated by current flowing in the plasma, the poloidal field can be generated by specially designed coils in stellarators. The stellerator was originally invented by Spitzer (1958) and has been intensively researched in Princeton (Fig. 10) before the switch to tokamaks in the 1970s. Tokamaks are axisymmetric while stellarators are necessarily non-axisymmetric in configuration. Three dimensional shapes have much more freedom, but stellarators have two major types: in one type helical coils are used inside otherwise axisymmmetric coils, and the other type uses modular coils all together as shown in Fig. 11. The former type is represented by the Large Helical Device (LHD) in Japan while an example of the latter is the Wendelstein 7-X device in Germany.

The main advantage of stellarators over tokamaks is that they do not require plasma current. This not only removes the need for current drive but also eliminates a source of free energy which can lead to disruptions. The main disadvantage is that stellarators lack symmetry and so are also necessarily

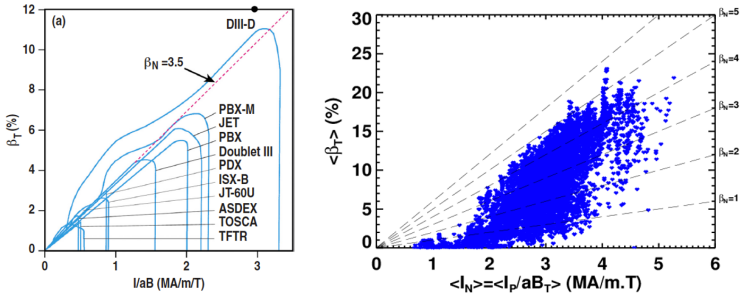

Fig. 7: Achieved beta values in various tokamaks (left from Luce (2011)) and NSTX (right).

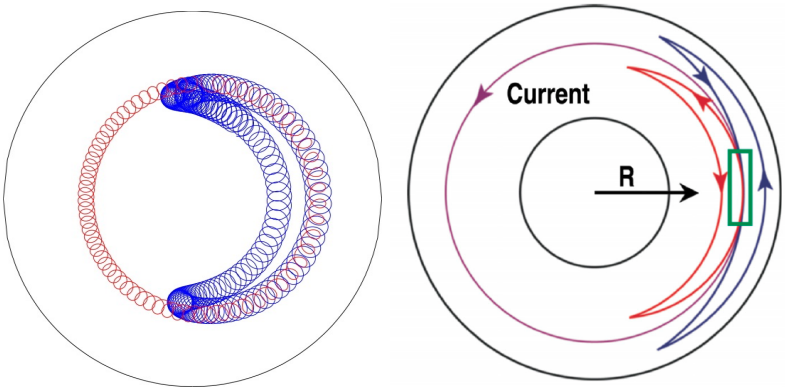

Fig. 8: Left: Passing (red) and trapped (blue) particle trajectories projected to a toroidal cross section. Right: Schematic illustration of trapped particle orbits in a tokamak as viewed from above. The plasma current is taken to be in the counterclockwise direction as shown (from Luce (2011)).

complex and large (and thus expensive) due to the specially designed coils. The 3D shapes also lead to complex plasma edge geometry for divertors to remove intense heat.

Neoclassical transport, which is important especially for alpha particles, is largely due to the so-called field ripples which are much larger in the 3D geometry of stellarators. An outstanding, yet untested, idea is to use the vast coil design freedom to achieve *quasi-symmetry* to lower field ripples or

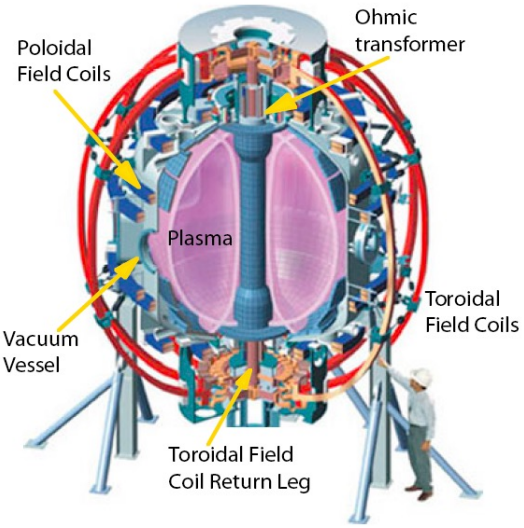

Fig. 9: Spherical Torus (ST) configuration.

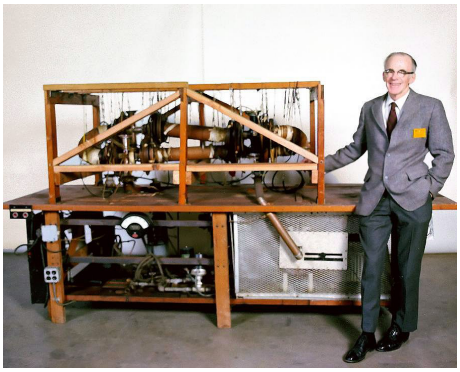

Fig. 10: Lyman Spitzer and his Model A Stellarator.

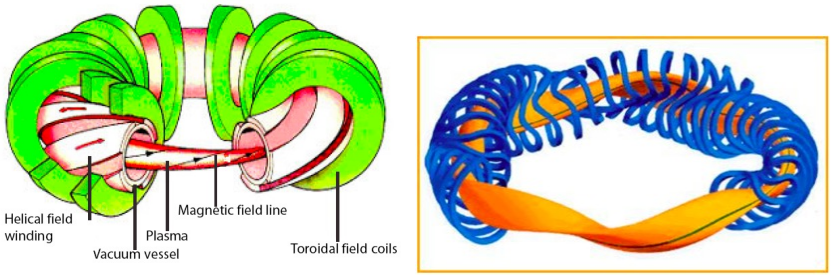

Fig. 11: Two main types of stellarators.

magnetic field strength variations along field lines to levels comparable in tokamaks (Boozer, 1983). On the other hand, the existing confinement scaling from stellarators is nearly identical to those from tokamaks, suggesting that both configurations suffer from the same anomalous transport rather than neoclassical transport.

2.1.5 Low-Field Configurations

Quite opposite to the direction that stellarators are aiming for, the last three categories of magnetic confinement configurations, shown in Fig. 12, use low external magnetic field but a much larger current in the plasma to generate the poloidal magnetic field. The safety factor, q, is therefore smaller than that in tokamaks. Thus these low-field configurations are much more prone to current-driven MHD instabilities. Due to their large currents, these low-field configurations can lead to much more compact fusion reactors if their disadvantages can be overcome.

The *Reversed Field Pinch (RFP)* (Marrelli et al, 2021) can be regarded as a tokamak at a much larger (by an order of magnitude) plasma current or low q. It requires much weaker external toroidal fields, a significant advantage, but has many MHD instabilities to avoid. Due to its unstable nature, RFP

plasmas are said to experience magnetic self-organization or relaxation (see Lecture 12, Ji, 2024) resulting in a toroidal field profile with its edge values having opposite sign relative to those in the core. The reversal of toroidal field can be explained by Taylor's relaxation theory (Taylor, 1974) where magnetic energy is minimized while magnetic helicity is conserved. In addition to the MHD instabilities, RFPs have difficulty sustaining their large plasma current for fusion applications.

The *Spheromak* (Jarboe, 1994) can be regarded as an RFP at unity aspect ratio. Its main advantage is that it does not require a center stack. Toroidally confined plasmas without a center stack are sometimes called a compact toroid. Spheromaks fall into the same category of magnetic self-organization, which is also associated with MHD instabilities. Spheromaks can be made by flux cores (see below) or by coaxial guns. Current drive is also a challenging issue.

The *Field Reversed Configuration (FRC)* (Steinhauer, 2011) is another type of compact toroid and can be regarded as a spheromak without a toroidal field. It has the highest plasma beta, closer to unity, but also more free plasma energy for instabilities. Classical FRCs do not have flux surfaces due to their field lines forming loops within their poloidal planes. There are three methods to generate FRCs: the theta-pinch followed by reconnection at each end – the merging of two counter-helicity spheromaks – and a rapidly rotating magnetic field. The first two methods can only be used to form the FRCs but the last one can also be used to sustain the configuration. Neutral beam injection can be used to sustain FRCs with the additional benefit of stabilizing MHD instabilities via kinetic finite ion Larmor radius effects.

Magnetic mirror confinement is not a toroidal confinement configuration but is closely related to FRCs which often are embedded within to enhance confinement, as done recently. Magnetic mirrors originated back in early days of fusion research in the 1950s but their research was discontinued due to severe loss cones at each end. The concept has recently been revisited due to renewed interest in its simplicity.

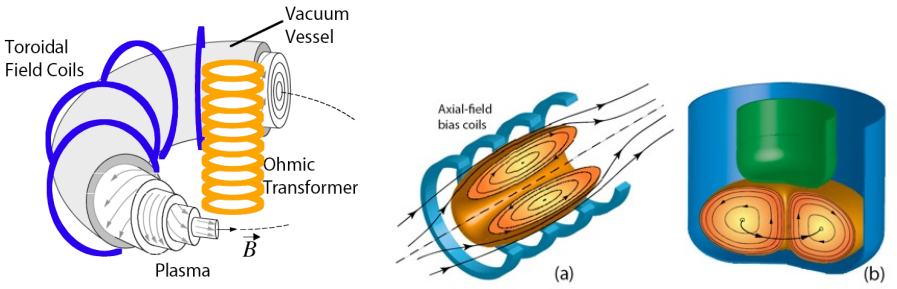

Fig. 12: Three configurations using low field and high currents: Reversed Field Pinch (RFP), Field Reversed Configuration (FRC), and spheromak.

2.2 Magnetized Low-temperature Plasma Experiments

There have been many magnetized plasma experiments using various techniques and diagnostics. In this Lecture, we discuss briefly only three representative ones:

- The Large Plasma Device (LAPD) which is a linear device at University of California, Los Angeles:
- The Magnegtic Reconnection Experiment (MRX) and Facility for Laboratory Reconnection Experiments (FLARE) which are toroidal devices at Princeton Plasma Physics Laboratory (PPPL): and
- The Big Red Ball (BRB), which is a spherical device at the University of Wisconsin - Madison.

2.2.1 LAPD

The latest LAPD device, shown in Fig. 13, is a linear device described in Gekelman et al (2016). The 20-meter-long cylindrical plasma with a 1 m diameter is made by hot BaO and LaB_6 cathodes. Typical plasma parameters are: $n_e = (1\text{–}4) \times 10^{18}\text{m}^{-3}$, $T_e = 6$ eV, $T_i = 1$ eV, and $B_Z = 400\text{–}2500$ Gauss. Typically plasma is made from Helium, Nitrogen, Neon, or Argon gases. A plasma discharge is made every second and each discharge lasts 6-20 ms. The main diagnostics are various types of probes and the strategy taken to collect data is to repeat nearly identical discharges while scanning a small number of probes over space by automated probe drives.

2.2.2 MRX and FLARE

The Magnetic Reconnection Experiment (MRX) (Yamada et al, 1997) and its successor, the Facility for Laboratory Reconnection Experiments (FLARE)

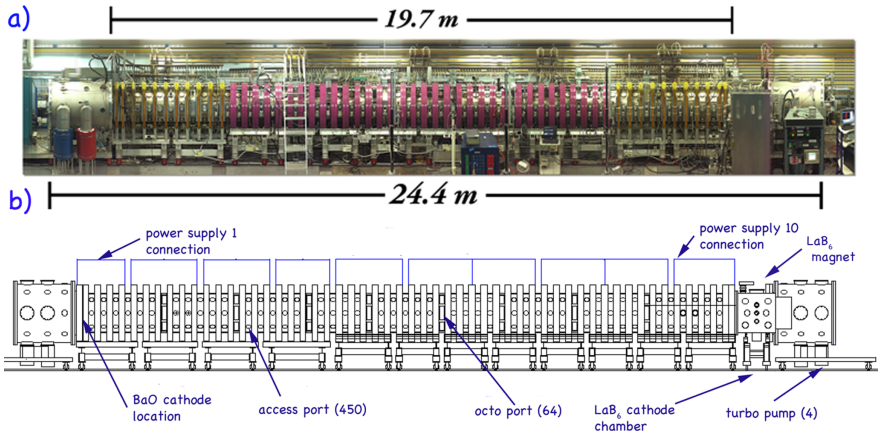

Fig. 13: The LAPD device from Gekelman et al (2016).

(http://flare.pppl.gov), are toroidal devices designed to study magnetic reconnection in a well-controlled environment.

Figure 14 shows a device photo and illustrations on how magnetic reconnection is driven in MRX. The vacuum chamber has a 1.5 meter diameter and is 2 meters long. The main internal coils are a pair of flux cores in a donut shape with a major radius of 0.75 meter and a minor radius of 0.094 meter. Each flux core consists of a set of toroidal field (TF) coils and poloidal field (PF) coils. The PF coil currents are raised first to generate the poloidal field, and when they are in the same direction between two flux cores, an X-line magnetic configuration is generated, see the middle panel of Fig. 14. Then the TF coil currents are increased as shown in the left panel of Fig. 15, to induce a parallel electric field in the poloidal direction along field lines to break down the gas to form plasma. When the PF coil currents are driven lower, a reconnecting current sheet is generated leading to the so-called "pull" reconnection, as shown in the right panel of Fig. 14, with measured magnetic flux evolution shown in the right panel of Fig. 15. See Lecture 3 for measurement details. A guide field can additionally be imposed along the toroidal field coils. The typical reconnecting field strength is up to 300 Gauss and guide field is up to 500 Gauss. Typical plasma parameters are $n_e = (1 - 100) \times 10^{20}$ m^{-3}, and $T_e \sim T_i = 5 - 20$ eV. Plasmas can be made of Hydrogen, Deuterium, Helium, and Argon gases. The main diagnostics are an extensive set of magnetic probes to measure time evolution of 2D and sometimes 3D magnetic field profiles for a single discharge. Electric probes and optical diagnostics are used to collect data over space using repeated discharges.

A similar approach has been taken for FLARE, though it is a larger device at much higher energy levels in order to provide experimental access to different regimes of magnetic reconnection. The vacuum chamber has a 3 meter diameter and 3.6 meter length. The flux cores have a major radius of 0.75 meter and a minor radius of 0.15 meter. Compared to about 30 kJ of magnetic energy in MRX, FLARE uses a much larger energy of 6.5 MJ. Figure 16 shows the FLARE device and its internal structure.

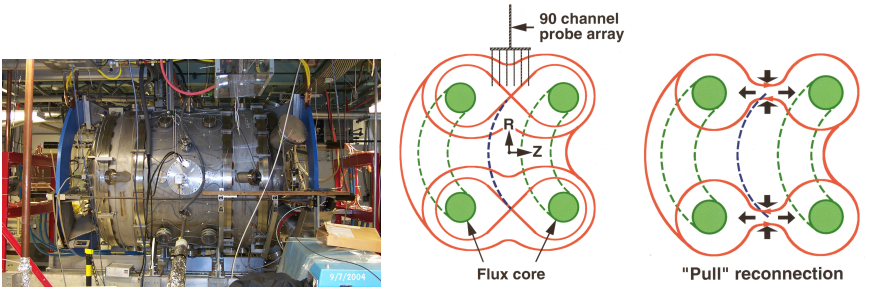

Fig. 14: The MRX and illustrations on how does it drive magnetic reconnection.

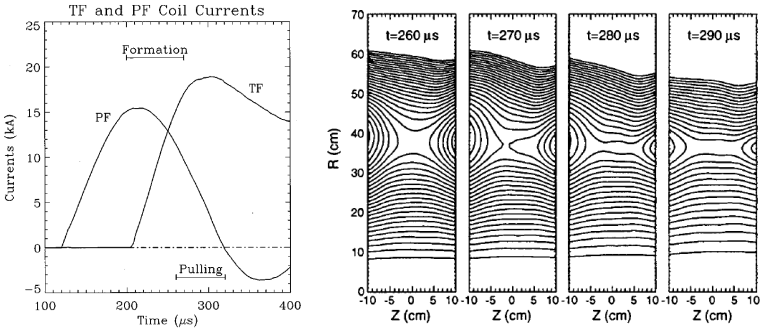

Fig. 15: Sequence of PF and TF coil currents and the time evolution of the poloidal magnetic flux during magnetic reconnection on MRX. From Yamada et al (1997).

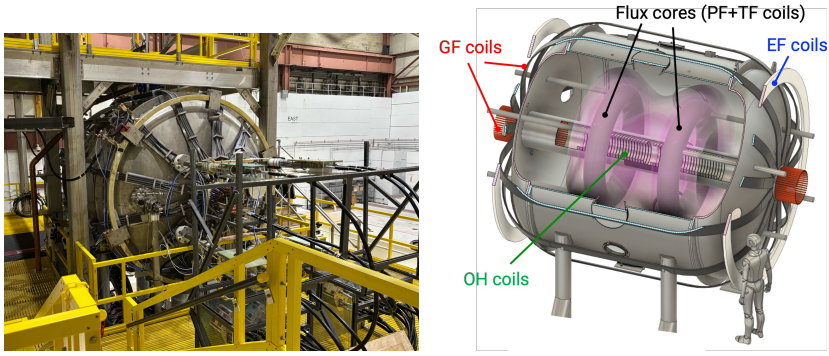

Fig. 16: The FLARE device and an illustration of internal structures.

2.2.3 BRB

The Big Red Ball (BRB) is a spherical device with a 3 meter diameter, described in Cooper et al (2014). It can be split into two halves for easy access to switch experimental configuration and conduct maintenance. The plasma is made by hot LaB_6 cathodes and is confined by a multipolar cusp magnetic field configuration from about 3000 Samarium Cobalt (SmCo) permanent magnets distributed on the spherical surface. Typical plasma parameters are: $n_e = 10^{17} - 10^{18}\mathrm{m}^{-3}$, $T_e = 5 - 20$ eV, $T_i = 1$ eV, and gases include Helium and Argon. A hallmark of BRB is that the plasma away from the edge is essentially unmagnetized with plasma $\beta \gg 1$, a condition not easily achievable in other magnetized plasma experiments. The unmagnetized plasma is useful for modelling many space and astrophysical plasmas.

The Terrestrial Reconnection Experiment (TREX) is a configuration on the BRB which utilizes a pair of internal coils to drive magnetic reconnection with an opposing background field (Olson et al, 2021). In this configuration,

Table 4: A list of plasma diagnostics in the lab and the quantities they measure. V_p is plasma potential relative to a reference ground.

diagnostics	quantities	Magnetized high- or low-temp
Energy analyzer / particle flux measurements	f_e, f_i, f_0	low-temp, edge of high-temp
Magnetic probes/loops	$\boldsymbol{B}$	low-temp, edge of high-temp
Electric probes	$f_e, n_e, T_e, V_p, \boldsymbol{V}_i, \boldsymbol{E}$	low-temp, edge of high-temp
Refraction index	n_e, B_{path}	high-temp, low-temp
EM radiation by free electrons	f_e, n_e, T_e, Z, B	high-temp
Line radiation by bounded electrons	n_e, n_i, n_0, T_e, T_i, $V_{i,\text{path}}$, B	high-temp, low-temp
EM wave scattering	$n_e, T_e, V_e, Z, n_i, T_i, V_i$	high-temp, low-temp
Diagnostics using neutral beam injection (NBI)	$n_e, n_i, T_i, \boldsymbol{V}_i, B$	high-temp
Laser-induced-fluorescence (LIF)	f_i, f_0	low-temp
Neutron measurements	fusion reaction rates	high-temp

the field strength is on the order of 100 Gauss which magnetizes electrons and also ions at low ion temperature.

2.3 Summary

- Toroidal magnetic confinement experiments on high-temperature plasma include strong field configurations (tokamaks and their advanced versions, spherical tori, and stellarators) and low-field configurations (Reversed Field Pinch, spheromaks, and Field Reversed Configuration).
- Magnetized low-temperature plasma experiments include linear devices, toroidal devices and spherical devices.

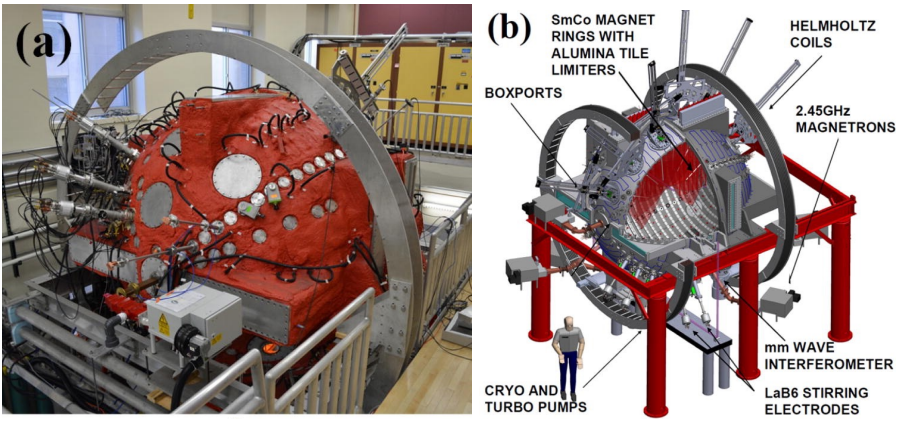

Fig. 17: The Big Red Bowl (BRB) and a illustration of internal structures.

- Table 4, as a subset of Table 2, lists the laboratory diagnostics which apply to the above two categories.

2.4 Further Reading

- Freidberg (2014)
- Chap. 2, 5-8 of Ji (2024)

2.5 Homework Problem Set 1

Due February 6, 2026

1. Each diagnostic provides limited information about plasma under a specific set of assumptions. Combining multiple diagnostics can greatly reduce uncertainties and one particular statistical method is called Bayesian inference. Explain its principle, and provide one particular example of its application to plasma diagnostics in any subareas of plasma physics covered by this class.

2. Virial theorem with self-gravity
   (a) When gravity is important such as in the sun, we need to add the gravitational force density $\rho \boldsymbol{g}$ to the equation of motion. In the presence of a nearby massive body, $\boldsymbol{g}$ is a constant vector. When the system is influenced by its gravity (also known as a self-gravitating system), $\boldsymbol{g}$ will vary according to
   $$\boldsymbol{g} = -\boldsymbol{\nabla}\phi, \tag{13}$$
   where gravitational potential ϕ satisfies
   $$\nabla^2\phi = 4\pi G\rho. \tag{14}$$
   Here G is the gravitational constant. Prove the corresponding stress tensor is given by
   $$\boldsymbol{T}_g = \frac{\boldsymbol{\nabla}\phi\boldsymbol{\nabla}\phi}{4\pi G} - \frac{(\boldsymbol{\nabla}\phi)^2}{8\pi G}\boldsymbol{I}. \tag{15}$$
   (b) Generalize the Virial Theorem to include self-gravity and show that gravity can confine plasma (and magnetic field!).

3. List as many magnetic confinement systems for both high-temperature and low-temperature plasmas as you can, with their advantages and disadvantages. How about confinement systems using electric field?

3 Magnetic Diagnostics

Of course, in magnetized plasma experiments we need to be able to measure the magnetic field strength itself. In this Lecture, the principle and applications of magnetic coils will be discussed along with other magnetic-field measurement techniques.

3.1 Magnetic Coils

This measurement principle is based on the integrated form of Faraday's law so that the output voltage V shown in Fig. 18 is proportional to the rate of change of the magnetic flux threading the coil,

$$V = n \oint \boldsymbol{E} \cdot d\boldsymbol{l} = -n \int_S \frac{\partial \boldsymbol{B}}{\partial t} \cdot d\boldsymbol{s} = -nA \frac{\partial B_n}{\partial t}, \tag{16}$$

where n is the number of turns, A is the coil area, and B_n is the normal component of $\boldsymbol{B}$ to the surface S. Thus, the spatial resolution is limited by A. The signal V can be integrated to obtain B_n,

$$B_n = -\frac{V}{nARC}, \tag{17}$$

where RC is the integration time constant. The example shown in Fig. 18 is an *active integrator* which provides large signals but can suffer from drifting issues especially during long time integration. In contrast, simple RC *passive integrators* do not suffer from this drifting issue but have low signal levels.

Magnetic coils are sensitive to time-varying magnetic fields (i.e., waves), so there are cases where non-integrated signals V are directly recorded. In these cases the frequency response of magnetic coils is limited by $L_{\rm coil}/R_{\rm coil}$,

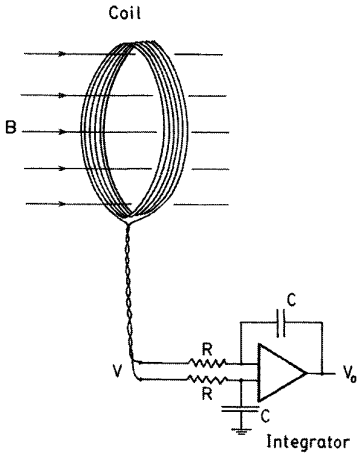

Fig. 18: Magnetic coil and integrating circuit. From Hutchinson (2002).

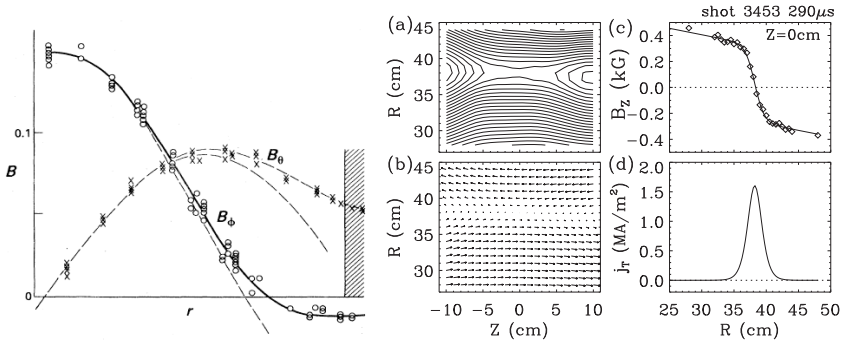

Fig. 19: (left panel) Experimentally measured and theoretically predicted profiles ofthe magnetic field from the HBTX-1A RFP device from (Chap. 12, Ji, 2024). (right panel) Example measurements from MRX: (a) contour plots of poloidal flux, (b) 2D magnetic field in vectors, (c) 1D magnetic field profile, and (d) 1D toroidal current density from Ji et al (1999).

the coil's time constant. If a magnetic probe is designed to measure DC or the low-frequency part of a magnetic field, typically it should have a large number of turns such that the signals are large with a long $L_{\rm coil}/R_{\rm coil}$ time constant suitable for time integration. In contrast, if a magnetic probe is designed to measure magnetic fluctuations, it should have fewer turns with a short $L_{\rm coil}/R_{\rm coil}$ time constant in order to have a good frequency response.

The lead wires of magnetic coils need special care as they can pick up additional signals (called pickups) along a typically long path before digitizers. A usual practice is to twist them abound each other as twist-pairs to preserve symmetry between two leads. Using co-axial cables or even tri-axis cables (with the outmost sheath grounded) have better shielding capability against pick-ups but without symmetry between two leads. On the other hand, symmetry usually has high common mode rejection capabilities.

3.1.1 Magnetic Probes

Magnetic coils can be applied for both local measurements of the magnetic field and global measurements of the total magnetic flux threading the plasma. For the local measurements, magnetic coils can be miniature probes inserted in (relatively) low-temperature laboratory plasmas (called *internal magnetic probes*) or can be *external probes* located outside but in close proximity to the plasma boundary.

For internal probe measurements, the magnetic field can be measured in multiple locations, either by array(s) of probes in a single discharge or by scanning a small number of probes in multiple *reproducible* discharges over one, two, or three dimensions. The left panel of Fig. 19 shows example 1D measurements of internal toroidal and poloidal magnetic field components of an RFP plasma. The toroidal field reverses its direction at the edge compared

to its core values. The sub-panel (b) from the right panel of Fig. 19 shows an example of 2D measurements of poloidal field components in R and Z in MRX.

Knowing the magnetic field at multiple locations enables the determination of other important quantities. The current density $\boldsymbol{j}$ can be determined by differentiating $\boldsymbol{B}$ in space via Ampere's law, $\mu_0 \boldsymbol{j} = \boldsymbol{\nabla} \times \boldsymbol{B}$. In the example shown in the right panel of Fig. 19, the toroidal current density can be determined by

$$j_\phi = \frac{1}{\mu_0}\left(\frac{\partial B_Z}{\partial R} - \frac{\partial B_R}{\partial Z}\right), \tag{18}$$

where the first term dominates in the thin current sheet as shown in the sub-panels (c) and (d). On the other hand, the sub-panel (a) shows contours of poloidal flux which can be determined under axisymmetry by radial integration,

$$\psi(R, Z, t) = 2\pi \int_{R_0}^{R} B_Z(R', Z, t) R' dR', \tag{19}$$

where R_0 can be cylindrical axis, $R = 0$, or the inner radius of conducting wall. Furthermore, the toroidal *inductive* electric field (or reconnection electric field) can be determined via Faraday's law by the time derivative of ψ,

$$E_\phi(R, Z, t) = -\frac{1}{2\pi R}\frac{\partial \psi(R, Z, t)}{\partial t}. \tag{20}$$

These examples demonstrate the power of multi-dimensional internal measurements of important quantities, such as magnetic field, in characterizing the plasma processes under investigation.

For external probe measurements, the right panel of Fig. 20 shows a typical setup in tokamaks. In such situations these probes are typically referred to as Mirnov coils. The position of a plasma column can be determined by magnetic probe measurements along the measurement circle of a radius of a. For the case of a straight plasma with cylindrical symmetry about an axis

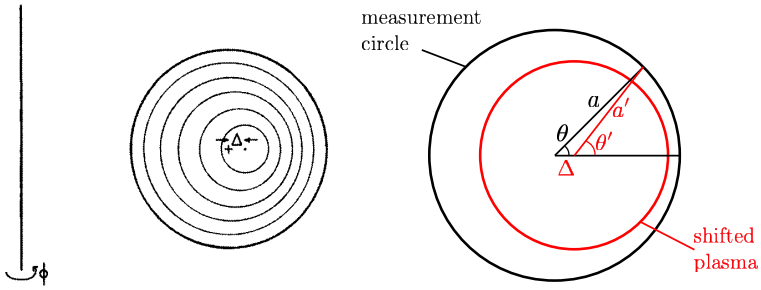

Fig. 20: (left panel) The Shafranov shift of magnetic axis relative to the last flux surface. From Hutchinson (2002). (right panel) Shift of the last flux surface position relative to the measurement circle.

which is shifted horizontally by $\Delta(\ll a)$ in the x direction, the azimuthal magnetic field measured by external probes is given by

$$B_\theta(\theta) = \frac{\mu_0 I_p}{2\pi a'}\cos(\theta'-\theta) \approx \frac{\mu_0 I_p}{2\pi a'} = \frac{\mu_0 I_p}{2\pi}\frac{1}{\sqrt{a^2\sin^2\theta + (a\cos\theta-\Delta)^2}}$$
$$\approx \frac{\mu_0 I_p}{2\pi a}\frac{1}{\sqrt{1-2\frac{\Delta}{a}\cos\theta}} \approx \frac{\mu_0 I_p}{2\pi a}\left(1+\frac{\Delta}{a}\cos\theta\right), \tag{21}$$

where I_p is the plasma current. Therefore, Δ can be determined by the $B_\theta(\theta)$ values measured by external magnetic probes. The vertical shift can be determined similarly.

In a toroidal plasma, however, measuring $B_\theta(\theta)$ alone is insufficient to determine the horizontal plasma position due to the Shafranov shift (Chap.4 Freidberg, 2014) of magnetic axis relative to the last flux surface as shown in the left panel of Fig. 20. This effect can be quantified by solving the Grad-Shafranov equation in vacuum (Ji et al, 1990): the magnetic field on *the plasma surface* can be approximated as by Hutchinson (2002)

$$B_\theta(\theta) \approx \frac{\mu_0 I_p}{2\pi a}\left(1+\frac{a}{R}\Lambda\cos\theta\right) \tag{22}$$
$$B_r(\theta) \approx 0 \tag{23}$$

where R is the major radius and the asymmetry factor is given by $\Lambda = \beta_p + l_i/2 - 1$. β_p is poloidal beta and l_i is plasma internal inductance. They are defined as

$$\beta_p = \frac{\langle p\rangle}{B_\theta^2(a)/2\mu_0}$$
$$l_i = \frac{\langle B_\theta^2\rangle}{B_\theta^2(a)},$$

where $\langle ...\rangle$ represents volume average. Larger β_p means more plasma pressure, leading to more Shafranov shift while larger l_i means more peaked current density profile with larger poloidal magnetic energy, also leading to more Shafranov shift. See Hutchinson (2002) and p.28 of Chap. 2 of Ji (2024) for more detailed discussion. Therefore, the knowledge of $B_\theta(\theta)$ alone cannot distinguish the effects due to Δ according to Eq. (21) or due to Λ according to Eq. (22).

In this case, in addition to $B_\theta(\theta)$, measuring $B_r(\theta)$ can uniquely determine Δ. According to the right panel of Fig. 20, we have

$$B_r(\theta) = \frac{\mu_0 I}{2\pi a'}\sin(\theta'-\theta) \approx \frac{\mu_0 I}{2\pi a}\frac{\Delta}{a}\sin\theta, \tag{24}$$

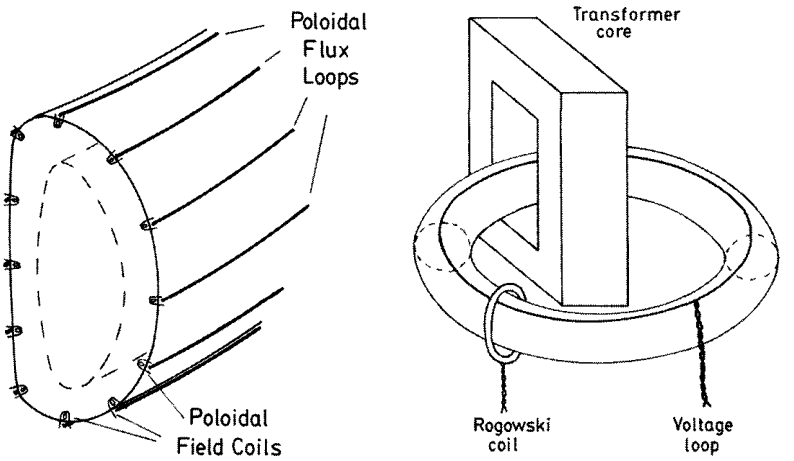

Fig. 21: Illustrations of external magnetic probes and flux loops for equilibrium reconstruction (left panel), and a Rogowski coil and a voltage loop to measure the total current and loop voltage of a toroidal plasma (right panel). From Hutchinson (2002).

where the law of sines, $\sin(\theta' - \theta)/\Delta = \sin\theta/a'$, is used. Since Δ can be determined by $B_r(\theta)$ alone, the variation of $B_\theta(\theta)$ due to Δ can be removed according to Eq. (21), the remaining variation based on Eq. (22) can be used to determine Λ which contains valuable information about the plasma pressure and the toroidal current density distribution. Λ can be also determined by the required vertical magnetic field to achieve the force balance in the major radius direction, see Chap. 8 of Ji (2024). This simple example illustrates the how external magnetic probe measurements can elucidate the inner properties of a plasma. This forms the basis for equilibrium reconstruction using the Grad-Shafranov equation for axisymmetric toroidal systems as will be discussed more below.

3.1.2 Flux Loops and Rogowski Coils

When magnetic coils are used for global measurements of the total magnetic flux, they are typically called *flux loops* or *voltage loops* as shown in Fig 21. Measuring the poloidal flux directly via flux loops is advantageous as the Grad-Shafranov equation for axisymmetric systems is constructed to solve for *poloidal flux*, ψ, or *flux per radian*, $\psi/2\pi$, which is being used here. The Grad-Shafranov equation is given by (Hutchinson, 2002),

$$\Delta^*\psi = R\frac{\partial}{\partial R}\left(\frac{1}{R}\frac{\partial\psi}{\partial R}\right) + \frac{\partial^2\psi}{\partial Z^2} = -R\mu_0 j_\phi = -F\frac{dF}{d\psi} - \mu_0 R^2\frac{dp}{d\psi} \qquad (25)$$

where $F(\psi) \equiv RB_\phi$ is the total *poloidal* current contained within the volume defined by ψ (see p.25 in Chap. 2, Ji, 2024). This equation can be solved

once two functions, $F(\psi)$ and $p(\psi)$, are given with two proper boundary conditions since the equation is second order. β_p and l_i mentioned above are two important parameters quantifying the effects of $F(\psi)$ and $p(\psi)$ in determining magnetic equilibrium. Poloidal flux measurements, such as shown in the left panel of Fig. 21, can provide one of two boundary conditions. The other boundary condition can be provided by external probe measurements often at the same locations of flux loops to provide derivatives of the poloidal flux at the boundary. This is because axismmetric magnetic field is given by $\boldsymbol{B} = B_\phi\hat{\boldsymbol{\phi}} + \hat{\boldsymbol{\phi}} \times \boldsymbol{\nabla}\psi$ where $\hat{\boldsymbol{\phi}}$ is the toroidal unit vector and poloidal field components are expressed in gradients of ψ.

While flux loops measure the total magnetic flux that they enclose, Rogowski coils measure the total current that they enclose. Rogowski coils are another application of magnetic coils by which magnetic flux generated by a current is measured along a loop that encloses the current. The concept is shown in Fig. 22. The output voltage from the Rogowski coil is proportional to time-change rate of the magnetic flux generated by the current at the small loop paths enclosing an area of A,

$$V = -n \oint_l \int_A dA \frac{\partial \boldsymbol{B}}{\partial t} \cdot d\boldsymbol{l}, \tag{26}$$

where n is the number of turns. Note further that there is a return loop in the middle of helical coil to remove the unwanted pick up from the large loop path, l, and $d\boldsymbol{l}$ is its line element vector. Assuming uniform $\boldsymbol{B}$ in the small loops, the area integration simply results in A. According to Ampere's law, therefore,

$$V = -nA\frac{\partial}{\partial t}\int \boldsymbol{B} \cdot d\boldsymbol{l} = -\mu_0 nA\frac{dI}{dt}. \tag{27}$$

Thus, similar to the flux loop measurement, integrating V gives a measurement of the total current, I, enclosed by the large loop path. As a practical matter, the helical loops should be wound uniformly to help justify the approximations made above.

In additional to the total current, the total *toroidal flux* is needed to reconstruct equilibrium. Often a flux loop is added to Rogowski coils enclosing toroidal plasmas to provide such a measurement. How different the toroidal flux is from its vacuum value depends on poloidal beta, β_p: the toroidal flux increases when $\beta_p < 1$ and the plasma is said to be *paramagnetic* while the toroidal flux decreases when $\beta_p > 1$ and the plasma is said to be *diamagnetic*. See p.27 in Chap. 2, of Ji (2024) for details. Tokamaks can be either paramagnetic or diamagnetic while configurations with large plasma currents (and therefore strong poloidal field), such as RFP or spheromak, the plasma is paramagnetic. The information for both β_p and Λ can provide a valuable constraint on the plasma internal inductance, l_i. The loop measuring toroidal flux is called a diamagnetic loop.

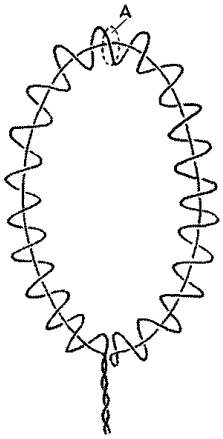

Fig. 22: Concept of a Rogowski coil. From Hutchinson (2002).

Using the measured total plasma current and toroidal flux, the boundary conditions based on poloidal flux and the external magnetic probe measurements, the Grad-Shafranov equation can be solved to provide global equilibrium solutions of the poloidal flux function ψ. Additional information, such as the internal plasma pressure measurements, can be added to further constrain the equilibrium solutions. This equilibrium reconstruction process becomes routine in modern tokamaks, forming a solid foundation to further analysis and even real-time control, see Hutchinson (2002) for more details.

3.1.3 Ohmic Power Balance

Magnetic measurements discussed above are powerful, allowing additional physics analysis of toroidally confined plasmas, especially via equilibrium reconstructions. Since the electric field energy is negligible in plasmas, the electromagnetic energy conservation law reads

$$\int_V \boldsymbol{E}\cdot\boldsymbol{j}dV + \frac{1}{2\mu_0}\int_V \frac{\partial B^2}{\partial t}dV = -\frac{1}{\mu_0}\int_S (\boldsymbol{E}\times\boldsymbol{B})\cdot d\boldsymbol{s}, \tag{28}$$

where the LHS represents dissipation and magnetic energy changes in volume V while the RHS represents the Poynting flux of electromagnetic energy through surface S to the volume. In the axisymmetric systems discussed here, the RHS reduces to $I_\phi V_\phi + I_\theta V_\theta$ where I_ϕ is usually called the plasma current, I_p, while V_ϕ is usually referred as loop voltage, $V_{\rm loop}$. The second term is typically negligible as toroidal flux remains constant in typical takamak operation though it could be important in RFPs or spheromaks. The second term of the LHS can be expressed in the form of inductance energy during the transient

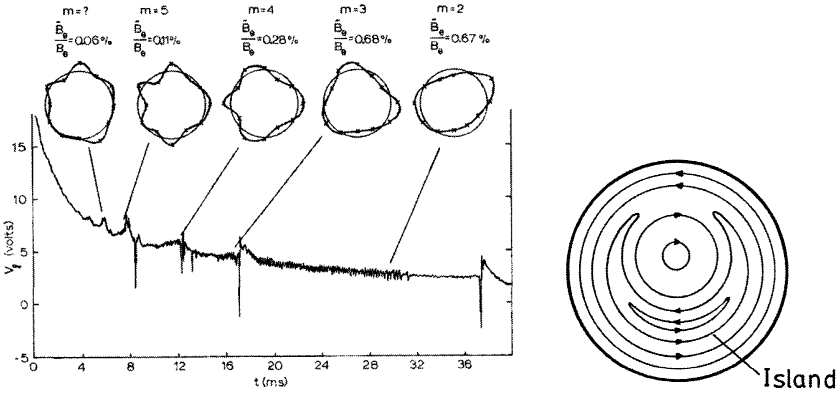

Fig. 23: Example of Mirnov coil measurements and illustration of a $m = 1$ magnetic island. From Hutchinson (2002).

phase,

$$\frac{\partial}{\partial t}\left(\frac{1}{2}L_p I_p^2\right); \quad L_p = \mu_0 R\left(\ln\frac{8R}{a} - 2 + \frac{l_i}{2}\right); \quad l_i = \frac{\langle B_\theta^2\rangle}{B_\theta^2(a)}, \tag{29}$$

where the plasma inductance, L_p, is given in p.28 of Chap. 2 of Ji (2024). With the knowledge of these terms, the dissipation term within the plasma, $\int_V \boldsymbol{E}\cdot\boldsymbol{j}dV$, is largely constrained, and thus can be quantitatively compared with various models. For example, in the simplest form of resisitive MHD Ohm's law, $\boldsymbol{E} + \boldsymbol{V}\times\boldsymbol{B} = \eta\boldsymbol{j}$, by assuming $I_p = \pi a^2 j$ a volume-averaged effective resistivity η_{eff} can be defined,

$$\int_V \boldsymbol{E}\cdot\boldsymbol{j}dV = \int_V \eta j^2 dV = \eta_{\text{eff}} I_p^2 \frac{2R}{a^2}, \tag{30}$$

and can be calculated using Ohmic input power in steady state,

$$\eta_{\text{eff}} = \frac{2RV_{\text{loop}}}{a^2 I_p}. \tag{31}$$

This effective resistivity can be compared with Spitzer's value to determine an effective electron temperature, $T_{e,\text{eff}}$, which was shown to be ~ 1 keV in the first tokamaks built in USSR, much higher than those from other experiments around the world during that time.

3.1.4 Magnetic Fluctuation Measurements

Magnetic probes are often used to measure magnetic fluctuations in the laboratory. In these cases, integrators are not typically used and the probes are designed to have short L/R time constants so that their frequency responses

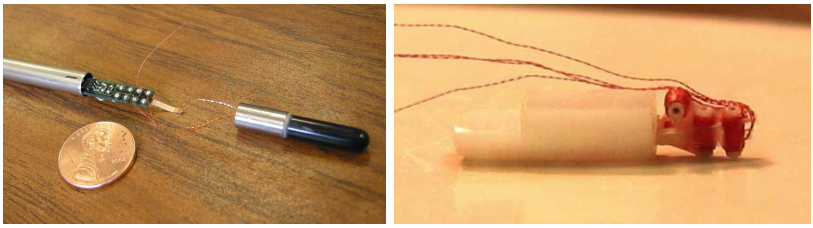

Fig. 24: (left panel) Four in-shaft pre-amplifiers with a combined frequency response up to 30 MHz; (right panel) three-component, four channel coils with 1.25 mm diameter used on MRX.

are high. For external magnetic coils, often called Mirnov coils in tokamak research, they can measure multiple modes around the torus resonating at different flux surfaces where $q = m/n$; m being the poloidal mode number and n being the toroidal mode number. An example measurement shown in Fig. 23 where magnetic fluctuations with different mode numbers appear during the course of a tokamak discharge at different times when the loop voltage exhibits spikes indicting MHD instabilities. An example $m = 1$ magnetic island is shown as a consequence of such MHD instabilities. Magnetic islands are undesirable as they do not contribute to confinement; the electron temperature is typically flat within islands. Magnetic islands are often precursors to disruptive activities including major disruptions which can terminate the discharges.

Internal magnetic coils are also used to measure magnetic fluctuations, often at higher frequencies. Sometimes in order to boost signal levels against ambient noise, pre-amplifiers are used right next to the coil in the probe shaft (Ji et al, 2004) (see Fig. 24), to measure Lower-Hybrid Drift Waves (LHDW) during magnetic reconnection.

3.2 Other Methods to Measure Magnetic Field

As discussed above, magnetic coils are powerful tools to measure magnetic fields or fluxes. However, the requirement for time integration to obtain magnetic field strength and its *in-situ* nature can have major drawbacks depending on specific situations. In this subsection, we briefly discuss alternative ways to measure the magnetic field *in-situ* or *ex-situ* which do not require time integration.

3.2.1 Hall Probes

The principle of a Hall probe is shown in Fig. 25. When a current flows across magnetic field, electrostatic charges appear between the two sides along the $\boldsymbol{j} \times \boldsymbol{B}$ direction, which becomes the signal proportional to $\boldsymbol{B}$. Hall probes used to be difficult to implement due to their complexity, low saturation level or dynamic range, and temperature dependence, but modern Hall sensors have become more sophisticated with automatic temperature compensation

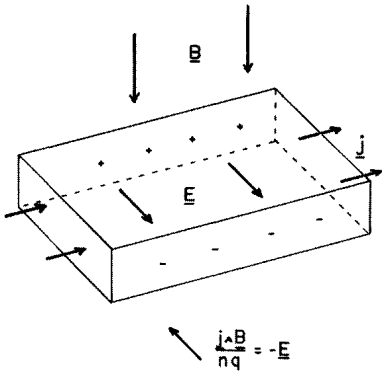

Fig. 25: Illustration of Hall probe operation. From Hutchinson (2002).

included. The recent successful detection of the MagnetoRotational Instability (MRI) in the liquid metal experiment (Wang et al, 2022) was based on the measurements using Hall probes. It is expected to see expanding use of Hall probes in the future.

3.2.2 Faraday Rotation

A finite magnetic field component along the propagation direction can change polarization direction of the light, and this change in angle is called Faraday rotation. The effect is proportional to $\int n_e \boldsymbol{B} \cdot d\boldsymbol{l}$ where n_e is electron density and integration is along line of the sight. If the Faraday rotation angle is measured together with interferometer measurements of line-integrated electron density, $\int n_e dl$, valuable information on magnetic field can be obtained. This will be discussed in Lecture 13.

3.2.3 Optical Spectroscopy

When the magnetic field is strong enough, certain strong lines can be split into measurable multiple lines. This is called Zeeman splitting and can be used to measure magnetic field strength, and will be discussed in Lecture 19.

The magnetic field can be also measured by Stark splitting of certain lines due to the motional electric field, $\boldsymbol{v} \times \boldsymbol{B}$ (called "Motional Stark Effect" or MSE), where $\boldsymbol{v}$ is the velocity of injected neutral particles with known velocity. This technique will be discussed in Lecture 19.

3.3 Summary

- Magnetic coils can be used as internal or external magnetic probes to measure the local magnetic field. Global measurements include flux loops to measure magnetic flux and Rogowski coils to measurement electric current.

- The internal measurement of magnetic field profiles can be used to determine current density, magnetic flux, and inductive electric field under the axisymmetric assumption.
- External magnetic probes (Mirnov coils) can be used to directly determine the plasma position as well as to indirectly determine internal information on the plasma pressure and internal inductance.
- Combined information from external magnetic probes, flux loops (both poloidal flux loops and toroidal diamagnetic loops) and Rogowski coils can be used to construct the magnetic equilibrium of toroidal plasmas. These magnetic measurements alone can provide an estimated averaged plasma resisitity during the ohmic phase of tokamak operation in quasi steady state.
- Both internal and external magnetic probes can be used to measure magnetic fluctuations.

3.4 Further Readings

- Chap. 2 of Hutchinson (2002)
- Chap. 2 and 8 of Ji (2024)

4 Space, Solar and Astrophysical Plasmas

As described in Lecture 1, diagnostics of space, solar, and astrophysical plasmas can be categorized based on whether they rely upon *in-situ* or *ex-situ* techniques. In this Lecture, we provide an overview of these techniques focusing on their working principles rather than the implementation details. Refer to the references listed in Further Reading for more detailed descriptions.

It is probably not an oversimplification to say that space plasmas are defined as plasmas which spacecraft can directly enter, i.e. such that *in-situ* diagnostics are possible. The plasmas covered by this definition are expanding rapidly: the closest distance from the sun reached by Parker Solar Probe is just about 10 solar radii during the 2024 Christmas Eve's flyby, while both Voyager I and II spacecraft have left the solar system plasma and entered the local galactic plasma of the Milky Way at a distance of more than 169 AU as of early 2026 from the sun (1 Astronomical Unit = distance of Earth from the sun = 215 solar radii which is about 700,000 km). Space plasmas include planetary plasmas (the ionospheres and magnetospheres of Earth and other planets, as well as their satellites) and interplanetary plasmas or solar wind plasmas in the solar system. Figure 26 shows an illustration of the current spacecraft fleet measuring space plasmas via *in-situ* techniques.

By contrast, solar and astrophysical plasmas are measured by *ex-situ* diagnostics. The measurements are performed over the full wavelength range of electromagnetic waves or photons from radio frequency to gamma rays. Particles arriving at detectors on Earth or onboard spacecraft are measured *ex-situ*, and they include charged particles as well as neutrinos. Since 2015 when the first gravitational wave detection was confirmed, astrophysical plasma

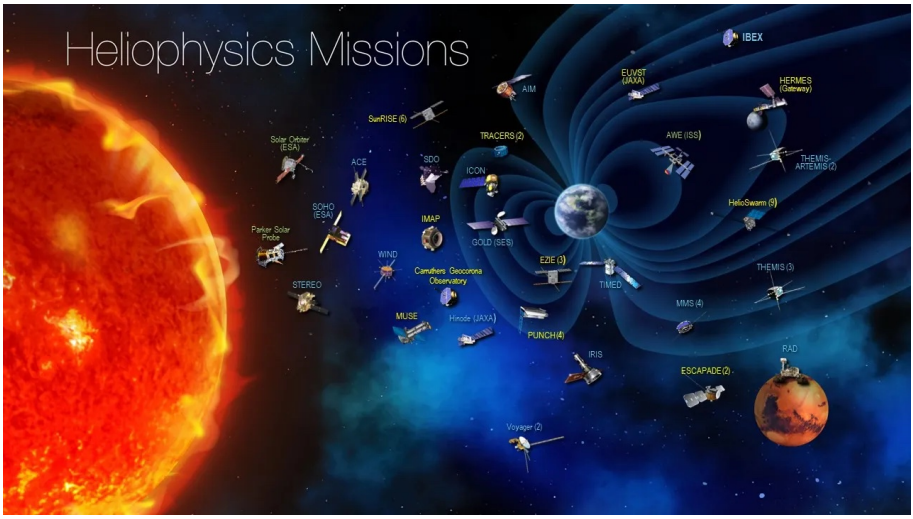

Fig. 26: Spacecraft in orbit measuring plasmas in the solar system as of January 2024 from https://science.nasa.gov/heliophysics/.

measurements, or more commonly referred to as "astronomy", have formally entered a multi-messenger era wherein astronomical plasmas may be observed simultaneously by multiple "messengers", including photons, particles, and gravitational waves. By combining data from multiple sources, a clearer understanding can be attained.

4.1 Space Plasma Measurements

In-situ diagnostics include those measuring fields and those measuring particles. The field here refers to either the electric field or the magnetic field, not in the sense of electromagnetic waves or photons. In the following, we discuss each in turn.

4.1.1 Field Measurements

Measuring fields in tenuous space plasmas is challenging because of their small amplitude, typically on the order of mV/m and nT, respectively, for electric

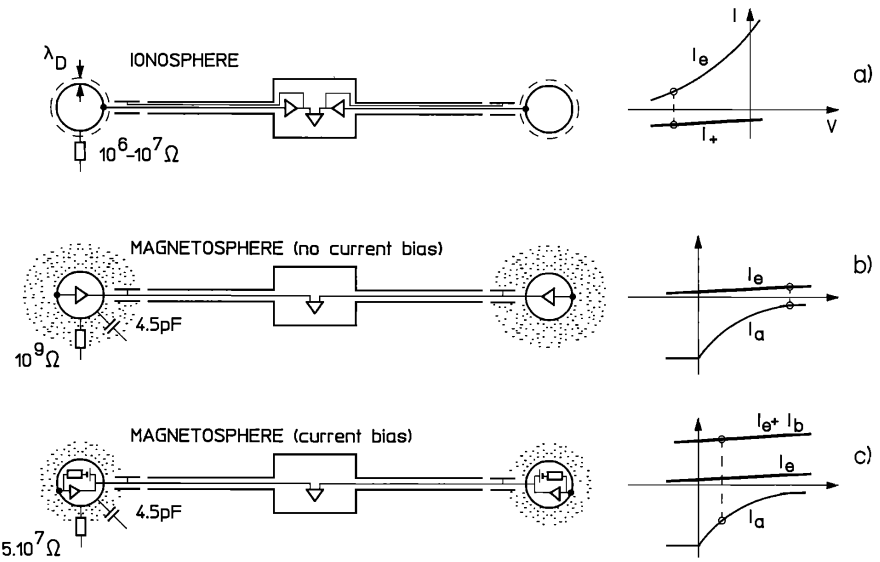

Fig. 27: (a) A double probe in the ionosphere operates in a similar regime as in the laboratory where electron current dominates, resulting in a negative floating potential. Debye length is much smaller than probe size leading to a low sheath impedance. (b) A floating probe in the magnetosphere where plasma is much more tenuous so that escaping photoelectrons dominate, resulting a positive floating potential. A thick sheath due to orbiting photoelectrons leads to a high sheath impedance demanding pre-amplifiers. (c) A negative bias current cancels a large portion of photoelectron current, leading to a thinner sheath and lower impedance. From Pfaff et al (1998a).

and magnetic fields. In order to have meaningful signals for electric field measurements, a pair of long booms (which can be as long as $\sim$ 100 m) are used to extend the probes away from the spacecraft in the opposite direction. The electric field components in the spacecraft spin plane are easier to measure as the modulation due to spin effectively serves as a calibration even for the DC component. The electric field component along the spin axis is more difficult, requiring careful DC offset calibrations.

Since the Earth's ionosphere has a much larger electron density $\sim 10^{12}\mathrm{m}^{-3}$, the situation is similar to the laboratory. The probe is well coupled to the local plasma at a low impedance ($\sim$ MΩ) with a thin sheath so pre-amplifiers are not needed until the signal transmits to the spacecraft. The probe is at a floating potential negative to plasma potential so that the electron current is largely suppressed to balance the ion current, see Fig. 27(a). In the more tenuous plasma of magnetosphere where electron densities drop as low as $\sim 10^{4-5}\mathrm{m}^{-3}$ in the magnetotail, the situation becomes much more complicated. Photoelectrons dominate when probes are exposed to sunlight, leading to a *positive* floating potential relative to the plasma potential while the ion current is negligible. The probes are not well coupled to the local plasma at a high impedance ($\sim$ GΩ) due to a thick sheath made of orbiting photoelectrons, see Fig. 27(b). Local pre-amplifiers to each probe become necessary to have a meaningful signal but any asymmetry in the thick photoelectron sheath can break the delicate charge balance jeopardizing DC electric field measurements. The solution is to provide a bias negative current to cancel the photoelectron current, reduce the sheath thickness, and thereby improve the probe-plasma coupling at a lower impedance of ($\sim$ 10MΩ), see Fig. 27(c). This technique has been widely used in spacecraft measurements.

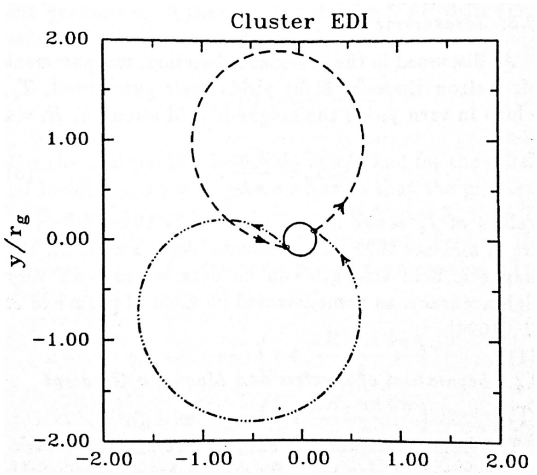

Fig. 28: Illustrative two electron beam trajectories starting from one side of spacecraft and arriving the opposite side. From Pfaff et al (1998a).

The double-probe technique is supplemented by the electron drift technique for *in-situ* electric field measurements. The measurement principle is simple: the electric field can cause electrons to drift across the magnetic field even when they are not completely magnetized. However, since the magnetic field is also unknown, at least two electron beams are needed to simultaneously determine the responsible electric and magnetic fields. Figure 28 provides an illustrative example for two electron beams injected from one side of the spacecraft and arriving on the opposite side. By detecting returning beams on the opposite side, both the electric field and magnetic field can be simultaneously determined.

There are also two primary magnetic field diagnostics for *in-situ* measurements. The vector fluxgate magnetometers provide accurate measurements of magnetic field at the level of nT from DC to a low frequency while the search coil magnetometers (in a way similar to magnetic pickup coils in the laboratory, see Lecture 3) provide AC measurements of waves at higher frequencies.

The development of the vector fluxgate magnetometer has had a long history, and the current widely used version is the version based on a ring core of a highly magnetically permeable (high-μ) alloy. Figure 29 illustrates its working principle. Without an external magnetic field, the magnetic flux from two halves of a ring core (blue and green waveforms in the second panel on the right) induced by the driving winding (black winding) cancels exactly and any finite external field will lead to a residual field (the black waveform in the third panel on the right) which is detected by sensing winding (red winding). Sensitivity of the measurement comes from the high-μ nature of the ring core which amplifies the response. A more sophisticated version of the fluxgate magnetometer uses feedback from the residual field measurements to form a closed loop by adjusting the balance of two halves until no residual field is detected. The feedback signal is proportional to the external field and thus provides the magnetic field measurement.

The search coil magnetometers also use ferromagnetic cores but in the shape of a thin rod in order to have a good frequency response. Feedback is also used here but for a constant response over a large frequency range, see Pfaff et al (1998a) for more details.

4.1.2 Particle Measurements

Langmuir probes used to determine electron density and temperature in the ionosphere are based on the ordinary lab-based ones with which we are familiar. Retarding potential analyzers (RPA) are widely used to measure particle energy distribution, known as either electron energy analyzers (EEAs) for electrons or ion energy analyzers (IEAs) for ions. As a special type of IEA, Faraday Cups are also used to collect ion current with an electron suppression lid. These diagnostics are routinely used in low-temperature plasmas and will be discussed in Lecture 11.

Unlike electrons, ion energy distribution measurements present the additional challenge of distinguishing their mass which is critically important. The

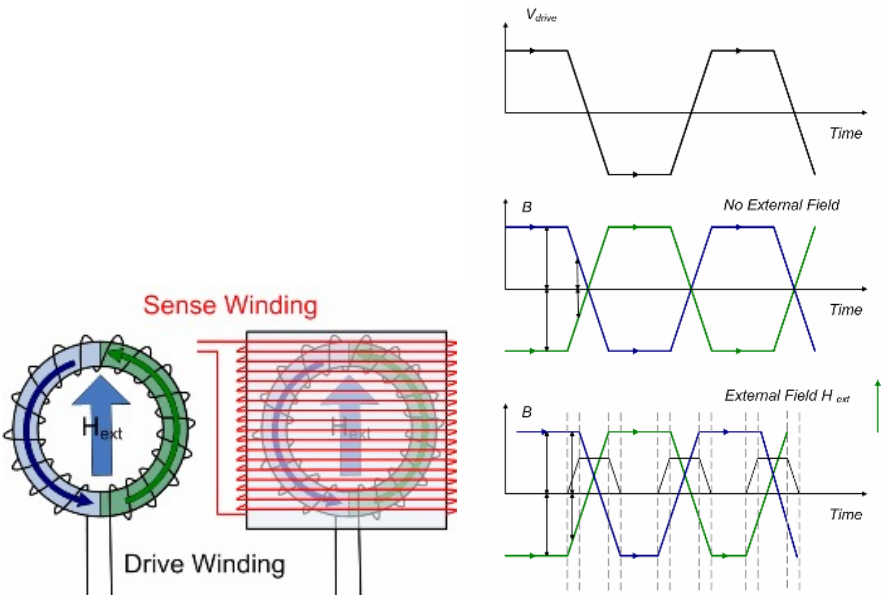

Fig. 29: Illustration on how a fluxgate magnetometer works. (left panel) Driving and sensing windings wrapped around a ring core. (right panel) Various waveforms of driving signals and response signals without and with external magnetic field. From https://bit.ly/2OqyQ3n.

RPA method selects the incoming ions' energy but not their mass. There are three methods to provide mass selection: radio frequency (RF), magnetic deflection, and time-of-flight (TOF), see Pfaff et al (1998b).

The RF method is based on the phase resonance between ion motion and the oscillatory electric field at a known frequency. Ions that achieve phase resonance with the electric field must have a specific velocity, which uniquely depends on the ion mass for a given energy. This technique has been implemented in several different schemes such as the Bennett spectrometer and its improved versions as well as the quadrupole spectrometer. The main limitation of the RF-based spectrometer is its low time resolutions since it measures a single ion species at a time.

The magnetic deflection method is based on an ion's deflection angular dependence on its mass for a given energy in a known magnetic field. It works for electrons as well. Combined with an electric field as in the RPA, a widely used method utilizes a double-focusing mass spectrometer to simultaneously select the ion's speed, V, and mass-per-charge, m/q. If only an electric field, E, is applied, ions are selected based on $qE = mV^2/2$. In other words, for a given E, ions satisfying

$$\frac{m}{q}V^2 = 2E \tag{32}$$

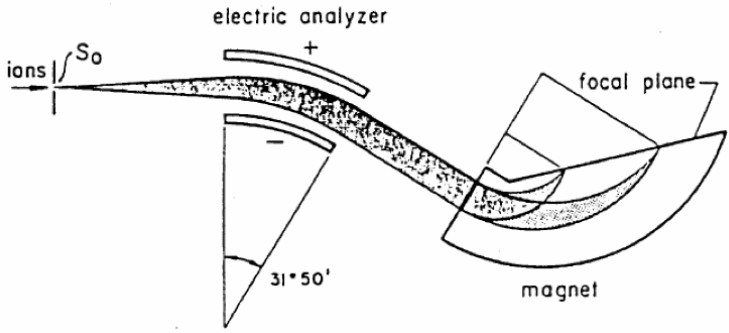

Fig. 30: Principle of an energy-mass spectrometer for ion measurements. From Nier and Schlutter (1985).

are selected. When only a magnetic field B is applied, ions are selected based on the radial force balance $qVB = mV^2/R$ where R is the deflection radius. For a given B and R, therefore, ions satisfying

$$\frac{m}{q}V = BR \tag{33}$$

are selected. Solving Eqs.(32) and (33) together yields

$$V = \frac{2E}{BR} \tag{34}$$

$$\frac{m}{q} = \frac{(BR)^2}{2E}. \tag{35}$$

Figure 30 shows an example of such an implementation. E is varied by changing the bias voltage of the electric analyzer and the detecting location on the focal plane, providing a range of R for a fixed B. As a result, the ion velocity distribution $f_i(V)$ for each m/q can be obtained by measuring the peak value of the corresponding spikes appearing on the focal plane when E is scanned.

The time-of-flight (TOF) method applies to ions or atoms which have sufficiently large energy to generate secondary electrons twice when they pass through thin foils. Secondary electrons are detected by microchannel plates (MCP) or other detectors with sufficient sensitivity and time response. For particles with lower energy, they need to be pre-accelerated. More details are provided in Pfaff et al (1998b).

4.2 Solar and Astrophysical Plasma Measurements

Any plasmas beyond the reach of *in-situ* diagnostics must be measured *ex-situ*. This applies to all solar and astrophysical plasmas, but a subset of space plasmas, such as those emitting aurora lights, can also be measured *ex-situ* via imaging and sometimes spectroscopy techniques. The latter however still

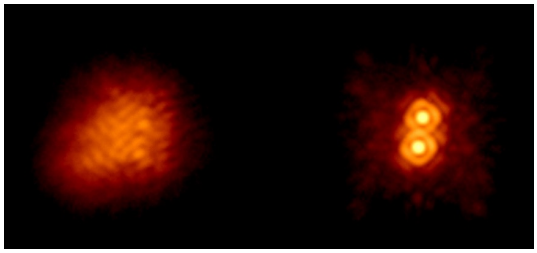

Fig. 31: Before (left) and after (right) AO is applied to a 5-m telescope when viewing a binary star system (IW TAU). From http://www.astro.iag.usp.br/~jorge/aga5802/12_otica_adaptativa.pdf.

belongs to a general description of remote sensing technology and will not be discussed separately in this class.

This part of plasma diagnostics is commonly referred as "astronomy" which is ususally discussed in its own courses. Here we choose to focus on several topics beyond traditional optical instrumentation described in typical astronomy textbooks. They include adaptive optics (AO) for ground-based optical astronomy: aperture synthesis for radio astronomy and later for optical/infrared astronomy: and X-ray/gamma-ray astronomy. Multi-messengers by neutrinos and gravitational waves are also not covered here as they belong more to high-energy physics and cosmology than plasma diagnostics.

4.2.1 Adaptive Optics (AO)

Ground-based observations suffer from the effects of atmospheric distortion due to turbulence. An adaptive optics system dynamically adjusts every small part of a mirror system to remove the distortion and achieve the expected resolution. An example is shown in Fig. 31 wherein a binary star system can be resolved only after AO is applied. This technique is widely used in other fields such as microscopy, optical fabrication and in retinal imaging systems to reduce optical aberrations. In fact, a Nobel Prize was given on AO based its application in microscopy in Chemistry in 2014, see Table 1.

There are three critical components for an AO system: (1) wavefront sensors, (2) wavefront reconstruction, and (3) deformable mirrors. Figure 32 shows a schematic view of a Natural Guide Start (NGS) AO system containing these three components. The NGS emits photons with flat wavefronts from effectively infinite distance. The distorted wavefronts after passing through turbulent atmosphere are recorded by wavefront sensors, and their signals serve as input for a wavefront reconstruction program which adjusts in real time a deformable mirror to remove wavefront distortions until corrected wavefronts become flat and recorded by the science camera.

A Shack-Hartmann sensor is a typical wavefront sensor shown in Fig. 33 measuring wavefront distortion by displacements of focal points of an array of miniature lenses from their equilibrium locations. The deformable mirrors can

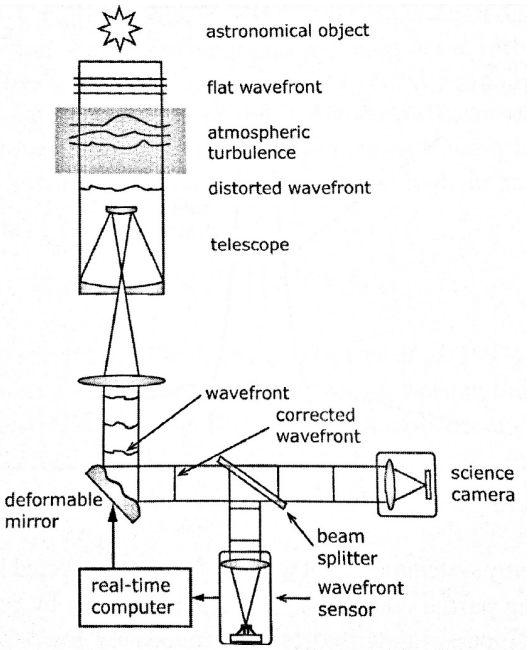

Fig. 32: A schematic of an AO system based on a natural guide star (NGS). From Rieke (2012).

be either segmented arrays of miniature mirrors, a continuous face sheet, or a bimorph containing two layers of piezoelectric materials with electrodes. The actuators to deform mirrors can be based on various means such as piezoelectric (crystals of aligned dipoles of molecules), electrostrictive (size change due to domain alignment), or by electromagnetic and electrostatic forces.

Modern AO systems are more advanced by using laser guide stars (LGS) either using Rayleigh scattering sensitive to low layer turbulence at a height

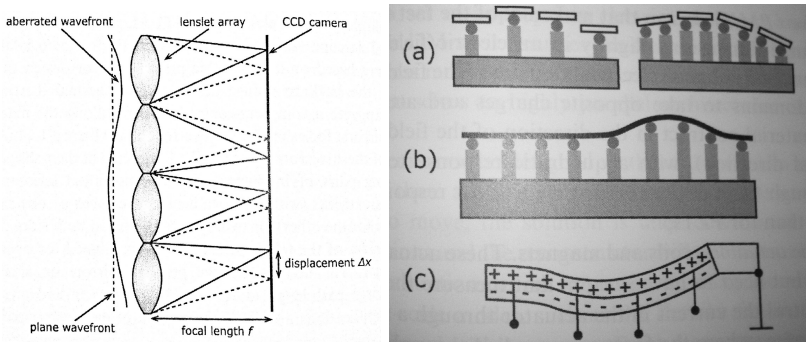

Fig. 33: (left panel) Shack-Hartmann sensor to measure wavefront distortion and (right panel) different deformable mirrors. From Rieke (2012).

of $\sim$ 10km or sodium atom resonance of pulsed laser light at $\sim$ 90 km to cover turbulence at all heights. Further sophistication has been introduced in Multiple Conjugate Adaptive Optics (MCAO) schemes which include using multiple guide stars and a combination of multiple turbulent layers via tomographic techniques, see Rieke (2012) for more details.

4.2.2 Aperture Synthesis

Aperture synthesis or synthesis imaging is another revolutionary technique based on interferometry that combines signals from a collection of telescopes to produce images having the same angular resolution as an instrument with a size of the entire collection. It also won the Novel Prize in physics in 1972, see Table 1.

To understand aperture synthesis, one can build up intuition from a simple dipole antenna, shown in the left panel of Fig. 34. The performance of an antenna can be evaluated by its radiation pattern based on the Reciprocity Theorem. When the wavelength is much longer that of the antenna, the radiation pattern generated by an oscillatory current in the dipole antenna forms a ring lobe with the antenna as its axis, see the right panel of Fig. 34. This axisymmetry breaks down when another dipole antenna is added beside the original one. If the oscillatory current is anti-phase between two antennas, the radiation patterns are shown in Fig. 35, where the ring lobe becomes two local lobes extending away from the two antennas. These two local lobes remain essentially same if two dipole antennas are bent into a loop antenna, restoring the axisymmetry of the two lobes along the loop antenna axis.

Adding many loop antennas in a paraboloid shape leads to a prime-focus parabolic antenna which enhances one lobe into the main lobe (called beam) while suppressing the lobe facing the opposite direction, as shown in Fig. 36. In the short wavelength limit, $\lambda \ll D$ where D is the aperture diameter, the

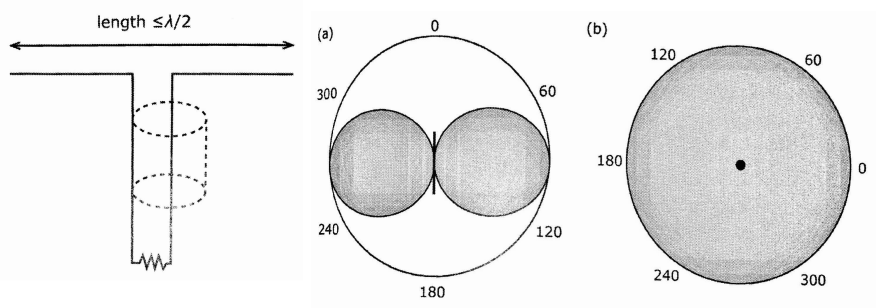

Fig. 34: (left panel) Dipole antenna and (right panel) (a) side cross-sectional view and (b) top cross-sectional view of the radiation pattern generated by an oscillatory current in the dipole antenna. From Rieke (2012).

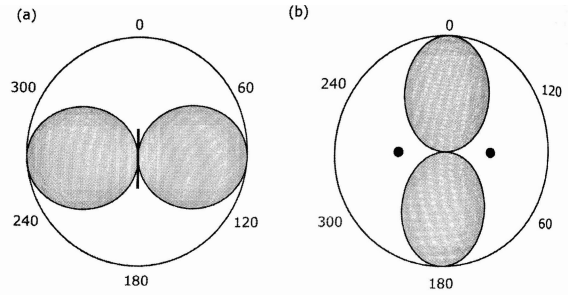

Fig. 35: (a) side cross-sectional view and (b) top cross-sectional view of the radiation pattern generated by an oscillatory current in two parallel dipole antennas. From Rieke (2012).

half-power beam width in radians, θ_0, is limited by diffraction and given by

$$\theta_0 \approx \frac{1.22\lambda}{D} (\text{in radians}), \tag{36}$$

which can be very small so that the observation has high angular resolutions with large sensitivities. Currently the 100 m Green Bank Radio Telescope at Green Bank, West Virginia is the world's largest fully steerable parabolic dish. The Five-hundred-meter Aperture Spherical Telescope (FAST) in China is currently the largest radio telescope, surpassing the 300 m Arecibo Observatory in Puerto Rico which collapsed in 2020.

To achieve significantly higher angular resolution, obviously a different approach is needed other than simply larger dish diameters. Radio interferometry attempts to increase higher angular resolutions by correlating measurements in radio frequencies from multiple telescopes within an array. In this case, the effective aperture diameter is increased to $B \sin\theta$ where B is

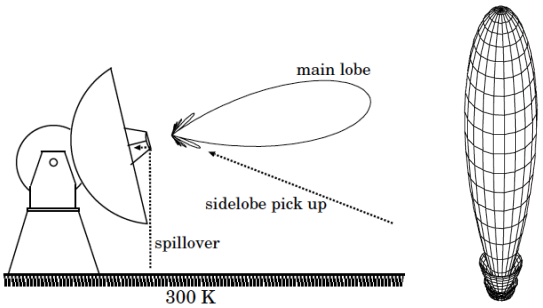

Fig. 36: (left panel) Paraboloid-shaped telescope has the main lobe towards the direction along which radio waves propagate. (right panel) The main lobe. From Rieke (2012).

the largest distance across the array, called "baseline" of the array in the left panel of Fig. 37.

Since each pair of correlated telescopes form a particular baseline corresponding to a specific Fourier component (see the top right panel of Fig. 37), the idea of aperture synthesis is to add a sufficiently large number of baselines in different orientations to achieve the desired angular resolution and noise level. As in paraboloid-shaped telescopes, the ultimate resolution of a telescope array is limited to $\sim \lambda/B$ but without filling the entire areas of two-dimensional space by telescopes. As an example, the bottom right panel of Fig. 37 shows that 4 telescopes can effectively achieve same performance of a fully filled array of 6 telescopes. Another advantage of aperture synthesis is to open up possibilities to form a much larger array by connecting telescopes across the world and even across satellites in space, significantly increasing resolutions. The accompanying challenge, however, is to find reliable ways to correlate signals over large distances especially for wavelengths which can be as short as mm or sub-mm.

Currently the largest radio telescope in the world is the Atacama Large Millimeter/submillimeter Array (ALMA) in Chile consisting of 66 12-meter dish telescopes with baselines ranging from 150 m to 16 km, see Fig. 38. Low-Frequency Array (LOFAR) uses 20,000 dipole antennae with a baseline longer than 1000 km. The next largest array is the Square Kilometer Array (SKA) with 131,000 tree-shaped antennae with a baseline longer than 3000 km and is scheduled to be completed by 2028.

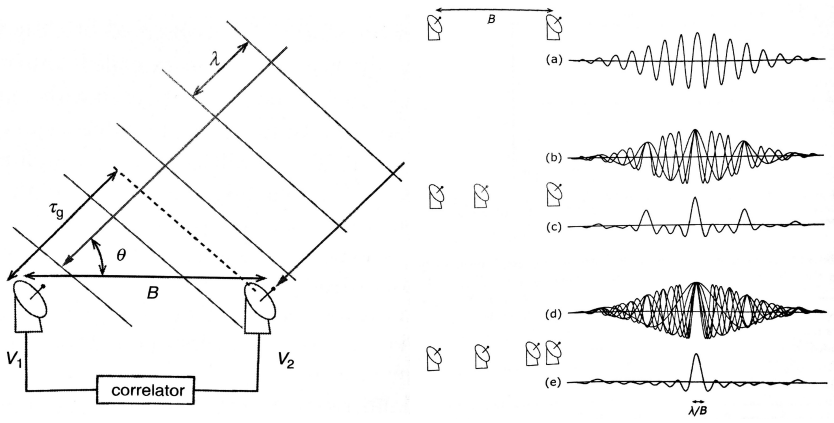

Fig. 37: (left panel) Radio interferometry by correlating signals from multiple telescopes. (right panel) Principle of aperture synthesis is to add a sufficiently large number of telescopes at proper locations to form different baselines in different orientations in order to achieve desired resolutions and noise levels. From Rieke (2012).

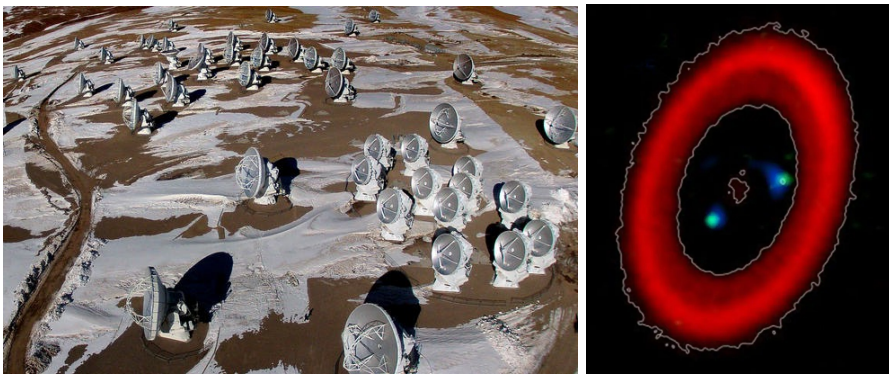

Fig. 38: (left panel) ALMA telescope array in Chile. (right panel) A recent image from ALMA showing a planet-forming system (PDS 70). From Doi et al (2024).

4.2.3 X-ray Astronomy and Gamma-ray Astronomy

Measuring high-energy photons in X-ray requires totally different diagnostics, *i.e.* X-ray telescopes on board of balloons, sounding rockets, or satellites in space since Earth's atmosphere absorbs most X-ray radiation. When the wavelength becomes comparable to crystal lattice spacing d, nothing works as a mirror to reflect photons other than at a small grazing angle from the crystal surface to satisfy Bragg's law (See Section 16 for more information).

$$m\lambda = 2d\sin\theta, \tag{37}$$

where m is diffraction order and θ is incident angle as shown in Fig. 39. As a result, one large paraboloid-shaped crystal can cover only a small light-collecting area. To reduce the required length, secondary reflection by a hyperboloid-shaped crystal can be used as shown in the left panel of Fig. 40. At the same time, to increase the light-collecting area, nested crystal shells can be used: 4 shells in Chandra (the right panel of Fig. 40), 58 shells in XMM-Newton satellites and 133 (!) shells in NuStar satellite. However, the number of shells is not the most challenging task; this is polishing the meter-sized crystals to the smoothness of a few atoms.

Gamma-ray astronomy requires yet another type of diagnostic, *i.e.* gamma-ray telescopes on board of satellites for gamma-ray energy between 5 MeV and ∼100 GeV, such as the Large Area Telescope (LAT) onboard the Fermi Gamma-Ray Space Telescope satellite. The working principle of LAT is shown in Fig. 41, whereby multiple layers of a pair-conversion and positron sensitive detector are stacked. When above a critical energy, 1.022 MeV of the gamma-ray energy is converted to an electron-positron pair when colliding with an atomic nucleus. Positron-sensitive detectors display the conversion timing and location, and with the information from multiple layers, the gamma-ray

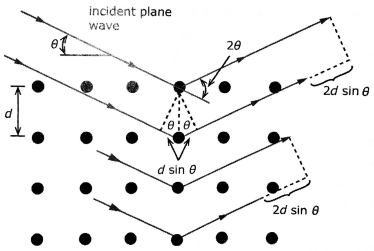

Fig. 39: Bragg condition for reflection of X-rays by a crystal. From Rieke (2012).

direction can be determined. The final deposition of energy is measured by calorimeters from which the gamma ray energy can be determined.

For gamma-ray energies above ∼100 GeV, arrays of ground-based telescopes can be used to detect air showers resulting from gamma-rays entering Earth's atmosphere, as shown in the left panels of Fig. 42. There are differences between gamma-ray showers and nuclear cosmic ray showers. Gamma-rays travel in the air at a speed of c/n, where $n(> 1)$ is the refractive index, and can generate pairs of electrons and positrons traveling at a speed v_p. The particle speed v_p is necessarily limited by c but can travel faster than the original gamma-ray speed of c/n. In such cases, these charged particles exert forces on electrons in air molecules along their paths and the influenced electrons can emit new photons, known as Cherenkov emission (1958 Novel Prize in physics). The Cherenkov emission itself can be gamma-rays, and the process can repeat until the original energy is exhausted. Additional gamma-rays can be emitted by pair annihilation or by Bremsstrahlung radiation when electrons or positions collide with the nuclei of air molecules.

The Cherenkov emissions from gamma-ray air showers typically have a very narrow angle on the order of 1° from the original gamma-ray direction, covering an area with about a 200 meter diameter over the ground. The emission angle can be calculated by referring to Fig. 43. In a given time t from Cherenkov

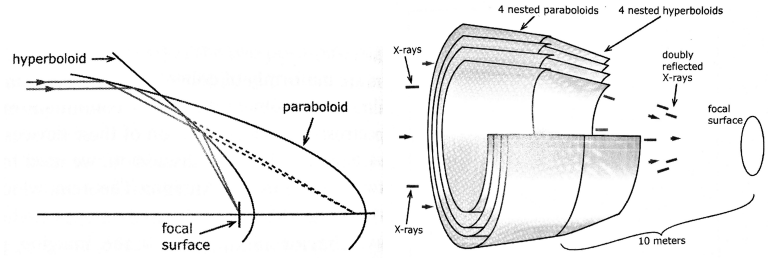

Fig. 40: (left panel) Secondary reflection by a hyperboloid-shaped crystal can shorten focal distance. (right panel) Nested crystal shells can increase light-collecting area in the case of Chandra satellite. From Rieke (2012).

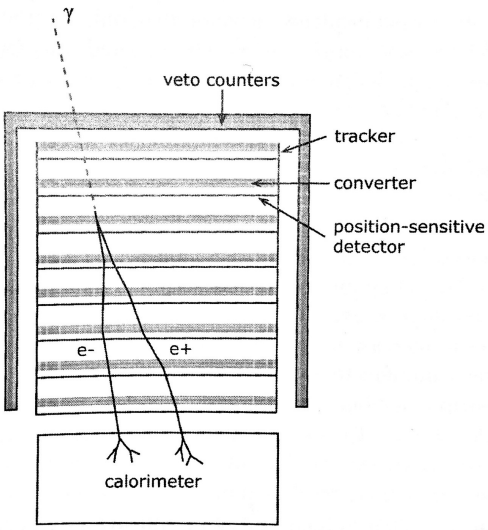

Fig. 41: The working principle of Large Area Telescope to detect gamma-ray on Fermi satellite. From Rieke (2012).

emission, the light wave travels over a distance of $(c/n)t$ while the particle travels over a distance of $v_p t = \beta ct$. Thus, we have

$$\cos\theta = \frac{(c/n)t}{\beta ct} = \frac{1}{n\beta}.$$

Since $n_{\rm air} \approx 1.0003$ and $\beta \approx 1$, $\theta = \cos^{-1}(1/1.0003) \approx 1.4°$.

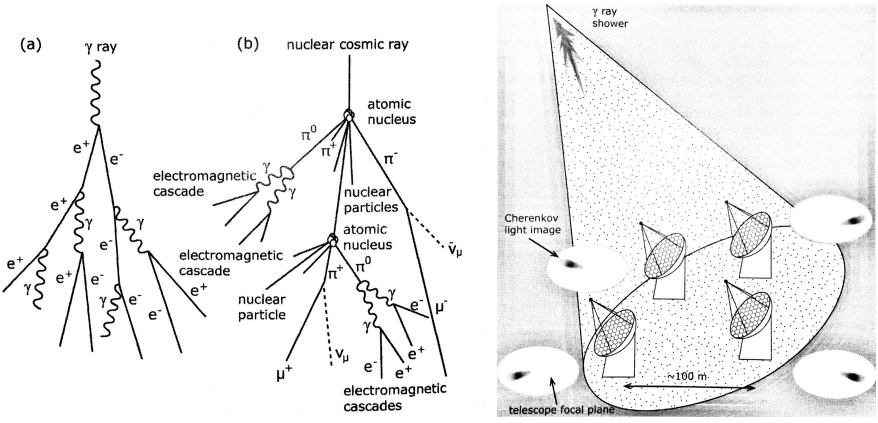

Fig. 42: (left panel) Air shower from gamma-ray photons or nuclear cosmic rays. (right panel) Gamma-ray air shower detected by an array of ground-based telescope. From Rieke (2012).

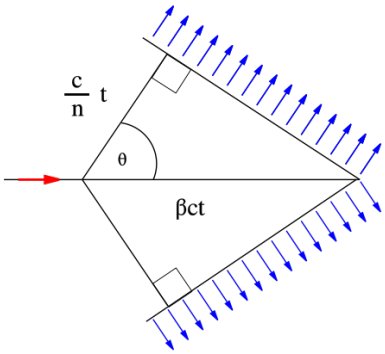

Fig. 43: Geometry of Cherenkov radiation.

4.3 Summary

- Space plasmas are measured by *in-situ* diagnostics onboard satellites flying through them. They include measurements of the electric field by double-probe techniques and of the magnetic field by vector fluxgate magnetometers. The particle measurements include Langmuir probes, retarding potential analyzers (RPA), and ion mass spectrometers. The latter typically uses both electric field and magnets to select mass-per-charge and ion velocity simultaneously.
- Solar and astrophysical plasmas are measured by *ex-situ* diagnostics onboard satellites or from the ground. Advanced techniques including adaptive optics and aperture synthesis have significantly expanded diagnostics capabilities by largely removing the effects from atmospheric turbulence and by achieving much higher angular resolutions. X-ray telescopes are based on specially designed grazing crystals; for low-energy gamma rays, gamma-ray telescopes are based on pair-conversion and positron sensitive detectors onboard satellites, while those for higher energies use detection of Cherenkov emissions from gamma-ray air showers by ground-based telescope arrays.

4.4 Further Reading

- Pfaff et al (1998a,b)
- Wüest et al (2007)
- Rieke (2012)
- Spann and Moore (2017); Moore and Spann (2017)

4.5 Homework Problem Set 2

Due February 13, 2026

1. Poloidal beta and internal inductance.
   Describe two different methods to measure

$$\beta_p + \frac{l_i}{2} \tag{38}$$

   in a tokamak with a circular cross-section. Are there ways to determine the breakdown between β_p and l_i?

2. Energy confinement time.
   Show that the energy confinement time of a tokamak may be expressed as

$$\tau_E = \frac{W}{P} = \frac{3}{8}\mu_0\beta_p\frac{R}{R_p}, \tag{39}$$

   where W is plasma kinetic energy, R_p is plasma resistance, $P = I_p^2 R_p$ is ohmic heating power, and R is plasma major radius. (Problem 2.5 of Hutchinson (2002))

3. *in-situ* measurements of ions in space.
   Ions are characterized by three quantities: mass m, speed V, and charge q. Please conceptually design an *in-situ* instrument to determine all these three quantities at once. Use methods that we have discussed in the class or lecture notes, but ideas beyond these materials are welcome.

4. Adaptive Optics (AO).
   AO techniques are highly successful in obtaining high-quality images in ground-based astronomy by removing influences from atmospheric turbulence.

   - What are three fundamental elements in AO systems?
   - AO is designed to remove effects from atmospheric turbulence, but is it possible to use AO to measure atmospheric turbulence in return?
   - If yes, what are possible limitations in such a measurement for atmospheric turbulence? If no, why not?
   - How about using AO to measure turbulence in plasma? If yes, what are possible limitations and if no, why not?

5 Introduction to Inertial Fusion Energy/High-Energy Density Laser Plasma Experiments

Whereas magnetic fusion devices aim to achieve ignition via the heating of a magnetically-confined plasma, inertial fusion relies on a rapid burst of intense laser power to compress a small target to enormous pressures. In addition to fusion energy applications, such high-energy density plasmas are relevant to astrophysics as well as nuclear weapons research. The world's most energetic laser facility is the National Ignition Facility, part of Lawrence Livermore National Laboratories. There, a ∼500 TW laser imparts some ∼2 MJ of energy to a two-millimeter fuel capsule. In 2022, NIF was the first facility of any kind to achieve controlled fusion ignition with ∼3 MJ of fusion energy produced, a scientific gain $Q > 1$ (Fig. 44). Since achieving this however required 300 MJ of energy from the grid, there is still a long way to net power generation.

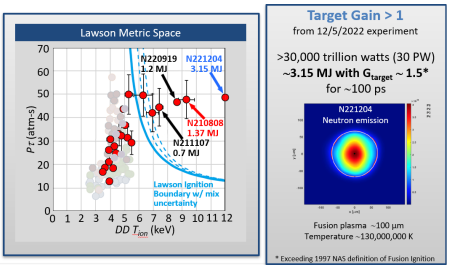

Fig. 44: Lawson Criterion for NIF Shots

5.1 Physical Principles

The details of laser high-energy density experiments can differ considerably from facility to facility. Here we focus on the indirect drive scheme used at NIF.

5.1.1 Indirect Drive

The method of so-called laser drive can be subdivided into two main categories: *direct drive* and *indirect drive*, contrasted in Fig. 45. In direct drive, lasers directly impinge on the target and compress it, as is the case at the University of Rochester's OMEGA laser facility. The disadvantage of direct drive lasers is that the intense laser-plsama effects caused by the first laser photons to strike the target decrease the efficiency of subsequent photons. By contrast, sites including NIF utilize indirect drive. There, lasers directly hit a cylindrical *hohlraum* surrounding the target. This hohlraum wall itself is made from a high-Z material such as gold or depleted uranium and releases x-rays when struck by the lasers. It is these x-rays which then compress the capsule. These

more energetic x-ray photons are less susceptible to laser plasma effects, the key advantage of indirect drive.

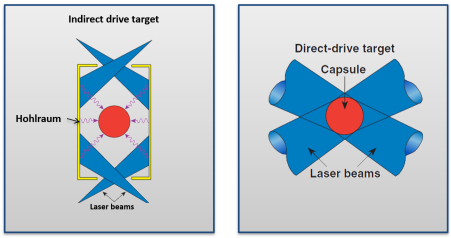

Fig. 45: Comparison of Indirect and Direct Drive Schemes

5.1.2 Implosion Shocks

In NIF, the fusion fuel within a target consists of a cryogenically-frozen spherical shell of deuterium-tritium (DT) ice enclosing DT gas within. Surrounding this is an ablator, often a plastic (CH) or high-density carbon (HDC). During the shot many lasers strike the hohlraum from different directions, ensuring that the target is uniformly bathed in x-ray flux. The ablator shell is blown off of the DT ice but, by Newton's third law, this sends the DT ice shell compressing inward. This can be thought of as a "spherical rocket" in that local momentum conservation propels the DT shell inward as the ablated material is sent outward. This generates a shockwave which heats the core of the DT gas to fusion conditions. As fusion is occurring, the DT shell is needed to ensure that alpha particles do not escape (Fig. 46).

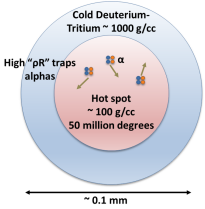

Fig. 46: NIF DT Target Fuel Structure

The conditions required for ignition in the hot spot can be expressed in the following relation:

$$E_{\text{ignition}} \sim \frac{\left[(\rho R)^3 T^3\right]_{\text{DT}}}{P_{\text{stag}}^2} \sim \frac{\text{const.}}{P_{\text{stag}}^2} \tag{40}$$

where ρR is the *areal density* and P_{stag} the stagnation pressure, the maximal pressure achieved at the core. The numerator reflects the Lawson

condition and is dependent upon the fuel used. Since the necessary conditions for DT fusions are independent of the implosion details, the numerator can be considered a constant. The stagnation pressure may be expressed as

$$P_{\text{stag}} \sim p_{\text{abl}}^{2/5} \frac{v_{\text{imp}}^2}{\alpha^{9/10}} \varepsilon \tag{41}$$

where p_{abl} is the ablation pressure, v_{imp} is the implosion speed, α is the entropy and ε is the "efficiency". The efficiency is less than one since the x-ray energy does not act as a perfect piston converting all energy to shock energy, but instead some energy is always lost to instabilities. This is why one should not simply naively aim to minimize the entropy α to increase the stagnation pressure: low entropy causes greater susceptibility to instabilities meaning lower ε. There is always a trade-off.

5.1.3 Symmetry

Ideally the target implosion would be perfectly spherically-symmetric, since this would suppress instabilities and result in the maximum conversion efficiency from laser power to fusion energy. Some imperfections are always present however. Furthermore even small perturbations are amplified by implosion and yield hydrodynamic instabilities (Fig. 47). The extent to which an implosion is symmetric is quantified by the Legendre moments: the so-called P2 parameter quantifies to what extent the shock is oblong rather than circular, P4 the degree to which it is square-like (Figs. 48, 49).

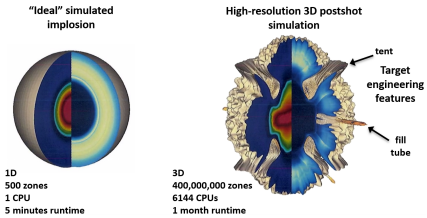

Fig. 47: Implosion Features

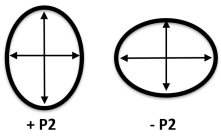

Fig. 48: P2 Illustration

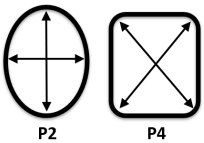

Fig. 49: P2 vs. P4 Illustration. A symmetric imposion has minimal P2 and minimal P4

P2 symmetry is determined by the cone fraction (CF), the proportion of beam power delivered by the inner as opposed to outer beams (Fig. 50).

$$\text{cone fraction} = \frac{\text{inner power}}{\text{inner power} + \text{outer power}} \tag{42}$$

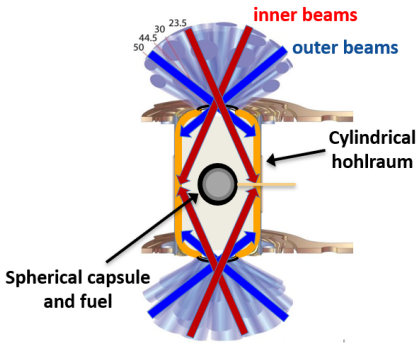

Fig. 50: NIF target chamber. On the right is the boom which places the target in place. To the left and upper right of the target are diagnostics.

Precise control is needed to ensure that this symmetry is not only established but maintained throughout the duration of the shot.

5.2 Design Considerations

There exist a multitude of design choices one can make when planning a NIF shot. Here we review some of the major considerations.

5.2.1 Hohlraum Fill Pressure

Hohlraums can either be filled with a gas (often Helium) of high-density ($\rho > 0.96\,\text{mg/cm}^3$) or one of lower density ($\rho = 0.03 - 0.3\,\text{mg/cm}^3$). High fill-density has the advantage of better restraining the hohlraum wall, allowing for

better control over long pulses. However it also exacerbates Raman backscattering losses and cross-beam energy transfer, resulting in the low-density configurations being more efficient.

5.2.2 Laser Pulse and Other Considerations

The material properties of the ablator guide the design of the laser pulse shape (Fig. 51). The initial shock strength must be sufficiently high to melt the capsule and not let it refreeze ($> 1\,\text{Mbar}$), since refreezing will roughen the surface. However we also do not want the shock to be too strong since that will make the entropy large.

To achieve more fine-tuning, the HDC ablator can be doped to improve hydrodynamic stability. Furthermore the hohlraum material and emission spectrum also play important roles in performance.

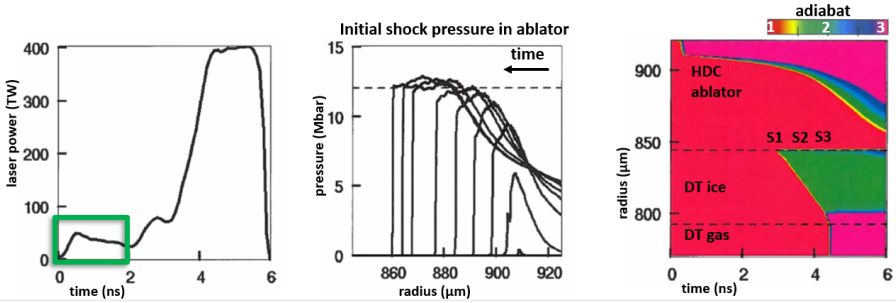

Fig. 51: Laser power over time, shock pressure in the ablator and the entropy over time.

5.3 Summary

- Laser energy in indirect drive schemes is transmitted to the target by way of x-rays emitted from a surrounding hohlraum.
- Targets in NIF consist of an ablator to generate the shock wave, a DT ice shell to trap alpha particles and a DT gas within to be compressed to fusion conditions.
- Target symmetry is key to reducing hydrodynamic instabilities and thereby improving fusion yield.
- There are a variety of design choices that one can optimize for a particular shot including laser pulse shape, fill pressure, hohlraum material, ablator choice, and target doping.

6 Inertial Fusion Energy and High-Energy Density Laser Plasma Diagnostics

6.1 Key Diagnostic Techniques

There are a variety of design choices involved in a target including ablator doping, hohlraum material, cone fraction among many others. To optimize performance researchers require specialized diagnostics which can evaluate the strengths and weaknesses of various performances. To this end not only is NIF equipped with a wide array of diagnostics but the targets themselves are often modified in order to facilitate certain kinds of measurements. We give a brief overview here.

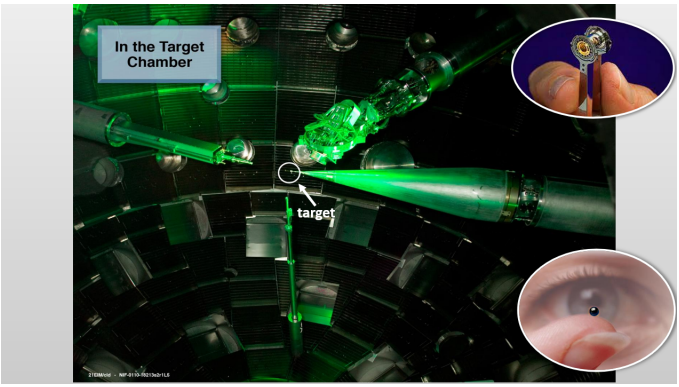

Fig. 52: NIF target chamber. On the right is the boom which places the target in place. To the left and upper right of the target are diagnostics.

6.1.1 Keyhole Targets

Inferring the details of the implosion process for a standard target is quite difficult. One approach to get preliminary measurements is to modify the target with a so-called "keyhole", shown in Fig. 53. This acts as a window into the the target through which a VISAR[1] laser can pass. This is part of an interferometer system: when the implosion occurs, the phase of the laser light reflected from the shock allows the shock speed to be inferred. Furthermore separate beams can measure the implosion in the equatorial and polar (up/down) directions so the symmetry of the implosion can be gauged (Fig. 54).

[1] Velocity interferometer system for any reflector

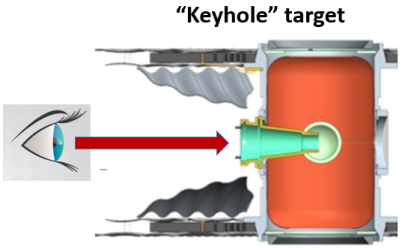

Fig. 53: Target keyhole diagram. The keyhole allows a laser to pass to the inside and reflect off of the incoming shock.

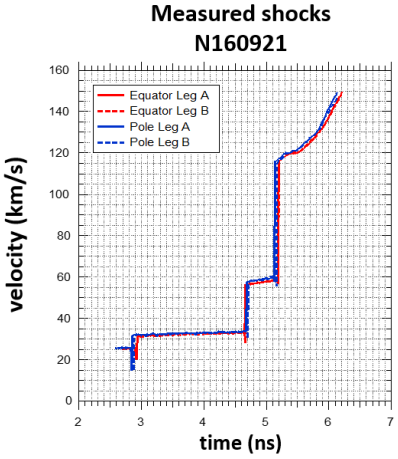

Fig. 54: Measured shock speeds using a keyhole. Note that the equatorial and polar implosion speeds closely track one another, evidence of good symmetry.

The chief disadvantage of the keyhole is that, of course, with the keyhole significantly perturbing the shape of the target, a full implosion is not possible. This technique is therefore best suited to describe the initial stages of the implosion before the effects of the keyhole become dominant.

6.1.2 Hydrogrowth Radiography

One common feature of implosions is the amplification of existing imperfections. This can be exploited for diagnostic purposes by observing how a shell with well-defined grooves implodes. Fig. 55 shows an example of such a target and the resultant radiography images.

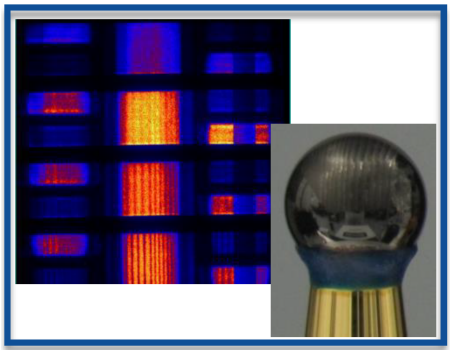

Fig. 55: Hydrogrowth radiography images and target. Notice the grooves become more pronounced as time goes on.

6.1.3 2D Convergent Ablator Target Radiography

A less invasive alternative to the keyhole target is to use X-rays to probe the structure of the imploding shell. The principle is much like medical X-ray imaging: emitted X-ray photons from a source pass through the shell and are collected on a detector at the opposite end. This results in an image like in Fig. 56 from which the symmetry values may be calculated.

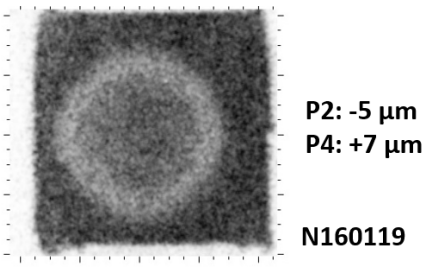

Fig. 56: Radiography measurement. Notice the denser outer shell surrounding the low-density interior.

Since radiography can be used with symmetric capsules they can reveal engineering features caused by the tent (e.g. Fig 57) and the fill tube. Since these features can ruin successful implosion, radiography is a key tool in determining how these may be mitigated.

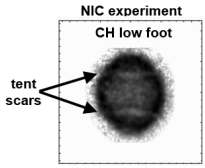

Fig. 57: Bands corresponding to the influence of the gossamer tent responsible for holding the target in place within the hohlraum.

Fig. 58: Target suspended by the "tent" within the hohlraum.

6.2 X-ray and Neutron Diagnostics

The final stages of the implosion can be probed via their X-ray and neutron fluxes. The X-ray emission reveals the shape of the ultimate hot spot (Fig. 59). Neutrons of course attest to the fusion gain.

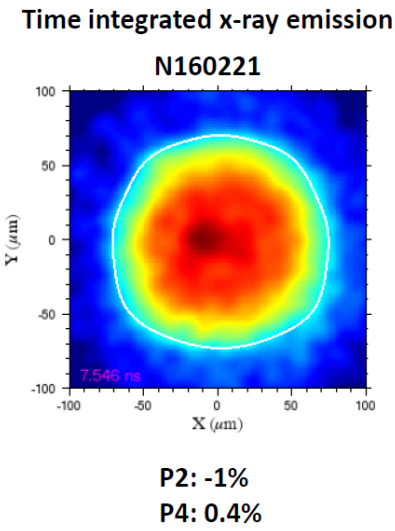

Fig. 59: Self-generated X-ray measurements.

To prepare a final shot aiming for an ignited DT plasma the testing phase progresses from diagnostics which probe the early behavior (e.g. keyhole) to those which probe the late-time behavior (e.g. X-ray and neutron diagnostics) as illustrated in Fig. 60.

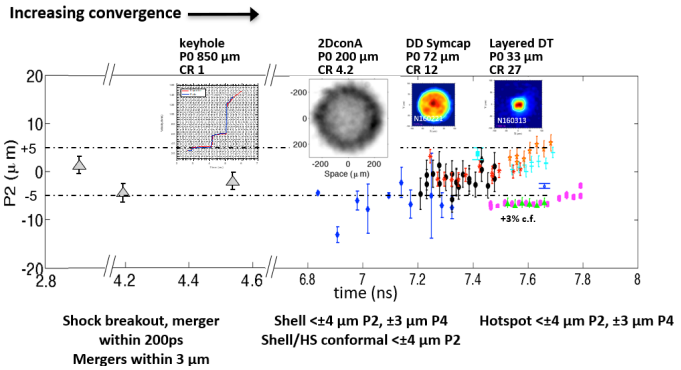

Fig. 60: Self-generated X-ray measurements.

6.3 Other Applications

In addition to investigating the plasma itself, NIF targets can also be used as radiation sources to study the interaction of X-rays, γ-rays and neutrons with

matter. Such experiments can study materials' equation of state, scattering cross section and resultant activation products.

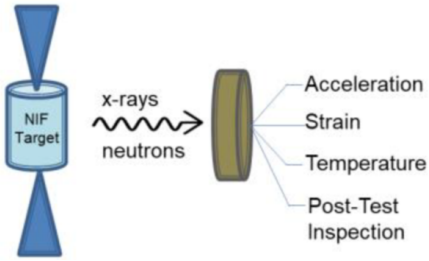

Fig. 61: Some material properties which can be probed using NIF target radiation.

6.4 Summary

- Targets are designed with diagnostic capabilities in mind. Different configurations probe different times of the implosion.
- Keyhole targets, radiography and radiation diagnostics characterize different aspects of the implosion and help researchers optimize performance.

6.5 Homework Problem Set 3

Due February 20, 2026

Inertial confinement fusion - target design and associated diagnostics

1. NIF's current yield record is nearly 9 MJ of fusion energy output from the target. How much energy in terms of average household electrical power does this record correspond to?
2. Considering an exemplar indirect-drive ICF target with parameters below, how much fusion yield would be produced (in joules) if the measured neutron energy was twice the implosion kinetic energy?
   - HDC initial shell density: 3.5 g/cm^3
   - HDC shell inner radius: 1000 microns
   - HDC shell thickness: 70 microns
   - DT fuel layer thickness: 50 microns
   - DT fuel initial density: 0.25 g/cm^3
   - HDC shell peak velocity: 350 km/s
   - HDC shell mass remaining: 5%
3. What combination of diagnostics could be implemented to infer dynamic properties in this exemplar target experiment?

7 Introduction to Low Temperature Plasmas

Low-temperature plasmas (LTPs) were the first plasmas studied and ever since have remained the most commercially-useful type of plasma. LTPs can be roughly defined as plasmas with electron temperatures lower than the ionization potential of the gas, typically $T_e \sim 1 - 10\,\text{eV}$. They are characterized by low ionization fractions $\alpha = N_i/(N_i + N_a)$ (i for ion and a for atom) and the dominance of electron-neutral collisions. LTPs can be non-equilibrium with electron temperatures exceeding those of the ions and neutrals, a property which is particularly useful in industrial applications.

7.1 Discharge Current Balance

The simplest kind of LTP system is the *gas discharge*, wherein current supplied by a circuit flows through a plasma from a positively charged anode to a negatively charged cathode.

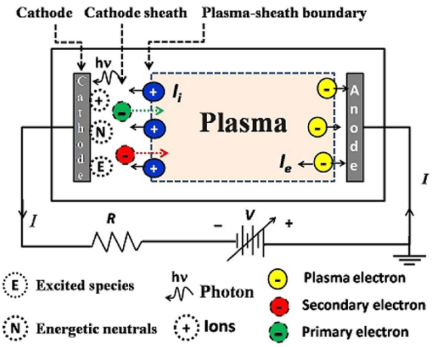

Fig. 62: Plasma discharge powered by an external power supply

7.1.1 Electron Sources

In order to make the gas conductive, electrons must be constantly supplied to act as current-carriers and ionize neutrals to sustain the discharge. There are several possible ways of doing this. The first is through some external source, such as an electron beam or light which triggers the emission of photoelectrons. The next is via *secondary-electron emission* (SEE): when an energetic particle, usually an ion, strikes the cathode and results in electrons being ejected from the surface. The rate of SEE increases with ion energy, and the total efficiency is quantified as the ratio of the electron current generated to the ion current $\gamma_{\text{ion}} = J_{eC}/J_{iC}$.

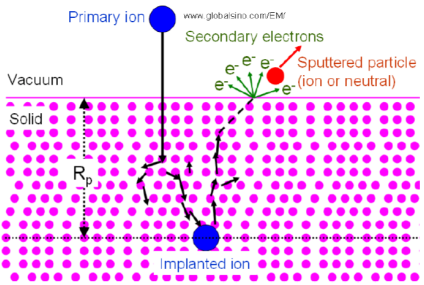

Fig. 63: Secondary Electron Emission

The last major way to generate electrons is via *thermionic emission*. When a metal is heated, some electrons become energetic enough to overcome the work function of the material and are emitted in large quantities. The Richardson-Dushman relation gives the electron current as

$$J = A_G T_{\text{wall}}^2 \exp\left(-\frac{-e(W-\Delta\phi)}{k_{\text{B}} T_{\text{wall}}}\right) \tag{43}$$

with $A_G = \lambda_R A_0$ where $A_0 = 4\pi m k_{\text{B}}^2 e/h^3$ and λ_R is a material factor of order unity. $\Delta\phi = \sqrt{eE/4\pi\epsilon_0}$ is needed to describe the Schottky effect whereby very large electric fields can facilitate electron escape. Thermionic emission is required to sustain the enormous currents for arc plasmas but not for lower-current discharges.

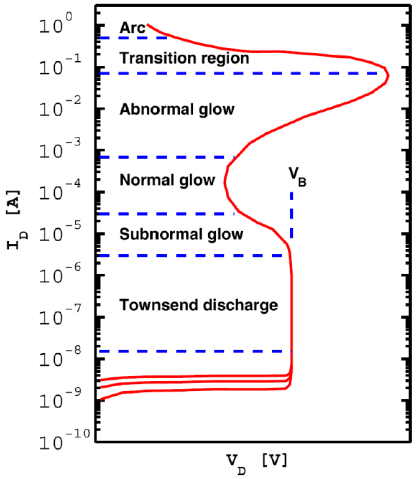

Fig. 64: Gas Discharge Types

7.1.2 Self-Sustaining Discharges

As in any steady-state circuit, the current flowing into the cathode must equal the current flowing out of the anode. By accounting for the ion and electron fluxes at each, along with the SEE at the cathode, we can formulate the following equalities:

$$J_{Ct} = J_i^C + J_{e,EE}^C - J_e^C \tag{44}$$

$$J_{At} = J_i^A - J_e^A \tag{45}$$

$$J_{Ct} A_C = J_{At} A_A \tag{46}$$

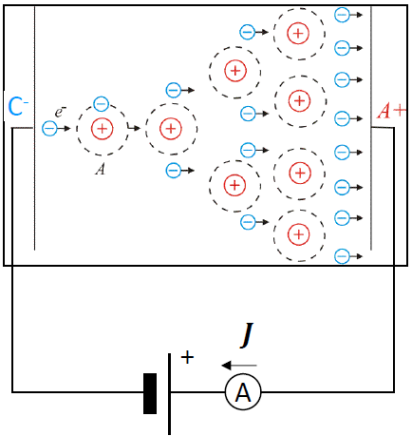

Fig. 65: Townsend discharge

We can apply this to consider a gas discharge supplied by an electron source, say photoelectrons. Suppose there is some initial cathode current of photoelectrons as in Fig. 65. The electron flux Γ_e will grow with distance from the cathode due to free electrons getting accelerated by the potential and ionizing more atoms, freeing more electrons, etc.:

$$\frac{d\Gamma_e}{dz} = n_e \nu_{iz} \tag{47}$$

where the ionizing collision frequency is the product of the neutral density with the reactivity $\nu_{iz} = n_a \langle \sigma_{iz} v_e \rangle$. This results in the electron current growing exponentially with distance from the cathode. The electron drift current can be expressed in terms of the electron mobility μ_e, the conductivity per number density:

$$J_{ed} = en_e v_d \approx \mu_e n_e E \tag{48}$$

Combining Eqns. 47, 48 together we find that the electron current at the anode is

$$J_{eA} = J_{eC}^0 \exp(\alpha L) \tag{49}$$

where the coefficient in the exponent α, the inverse of the ionization length scale, is

$$\alpha \equiv \frac{1}{\lambda_{iz}} = \frac{\nu_{iz}}{\mu_e E} \tag{50}$$

The increase in the electron current from the cathode to the anode must be offset by an equivalent ion current: hence

$$J_{iC} = J_{eC}^0 [\exp(\alpha L) - 1] \tag{51}$$

Suppose now there is some nonzero γ_{ion}. Then these ions impinging on the cathode can generate electrons of their own, potentially enough to result in a self-generated discharge which does not require further outside addition of electrons. The total electron current at the cathode in such a case is $J_{eC}^0 + \gamma_{\text{ion}} J_{iC}$, or

$$J_{eC} = J_{eC}^0 + \gamma_{\text{ion}} J_{eC} [\exp(\alpha L) - 1] \tag{52}$$

If our external electron current J_{eC}^0 were absent, the discharge could still be sustained provided that we still satisfy Eqn. 52, i.e.

$$\alpha L = \ln(1 + \gamma_{\text{ion}}^{-1}) \tag{53}$$

This is known as *Townsend's condition.*

7.2 Discharge Structure

The plasma parameters are generally not uniform throughout the length of the vacuum vessel, as shown in Fig. 66

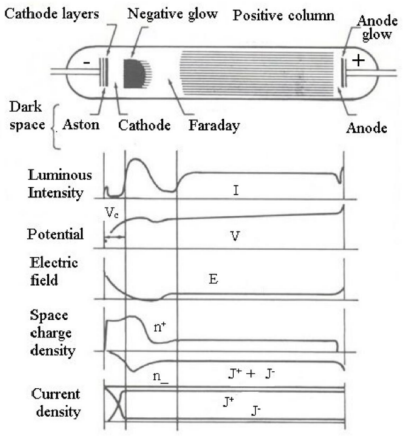

Fig. 66: Selected plasma parameters over space

The plasma will respond accordingly to ensure that the supplied voltage or current is maintained. One instance of this is how the anode sheath either attracts or repels electrons in order to maintain overall balance.

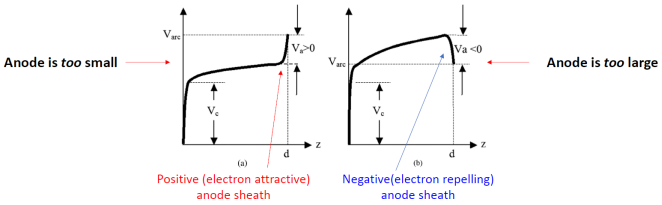

Fig. 67: Anode sheath for different anode sizes

7.3 Electron Kinetics

Due to the low ionization fraction, collisions between hot electrons and cold neutral atoms are very common. The extent of these collisions will determine how efficient a particular discharge is in converting the supplied power to the neutrals via the electrons.

7.3.1 Collision Types

While all collisions conserve momentum, kinetic energy may not be. Three types of collisions are possible.

1. *Elastic collisions.* Momentum is exchanged as the total kinetic energy remains constant, e.g.

$$\mathrm{e}_{\text{fast}} + \mathrm{A}_{\text{slow}} \rightarrow e_{\text{less fast}} + \mathrm{A}_{\text{less slow}} \tag{54}$$

2. *Inelastic collisions.* Some of the initial kinetic energy is lost to either exciting one of the particles or ionization, e.g.

$$\begin{aligned} \mathrm{e}_{\text{fast}} + \mathrm{A}_{\text{slow}} &\rightarrow \mathrm{e}_{\text{less fast}} + \mathrm{A}^{*} && (55)\\ &\rightarrow \mathrm{e}_{\text{less fast}} + \mathrm{A}^{+} + \mathrm{e} && (56)\\ & && (57) \end{aligned}$$

3. *Superelastic collisions.* Some internal energy is converted into final kinetic energy, e.g.

$$\mathrm{A}^{*}_{\text{slow}} + \mathrm{B}_{\text{slow}} \rightarrow \mathrm{A}_{\text{faster}} + \mathrm{B}_{\text{faster}} \tag{58}$$

Note that the star denotes an excited state.

7.3.2 Energy Relaxation Length

From mechanics we know that the change in energy due to a collision can be written as

$$\Delta\varepsilon_{\text{eff}} = -\frac{2m_1m_2}{(m_1+m_2)^2}\left(\varepsilon_1 - \varepsilon_2 + \frac{m_2-m_1}{2}v_1v_2\right) \tag{59}$$

For an electron striking a motionless atom, from $m_e \ll M$ we find

$$\frac{\Delta\varepsilon_{\text{eff}}}{\epsilon_1} \approx -\frac{2m_1}{M} \tag{60}$$

Hence we define $\delta \equiv 2m_e/M \ll 1$, δ denoting the rate of energy loss due to electron-neutral collisions. As an aside, note that the mass difference reduces the equilibration rate - electrons will thus Maxwellianize much faster among themselves than with the neutrals. This process is faster for slow electrons since they face a larger cross-section for Coulomb collisions than fast ones.

To calculate what effect these collisions will have, physically we may consider the competing forces of the electric field, which will accelerate electrons, and neutral collisions, which will retard them. Mathematically

$$\frac{d\varepsilon}{dt} \approx (\Delta\varepsilon_E - \varepsilon\delta)\nu_m \tag{61}$$

where the energy gained due to the electric field between collisions $\Delta\varepsilon_E$ can be expressed in terms of the mean free path λ_m or the drift velocity v_d:

$$\Delta\varepsilon_E \approx eE\lambda_m \approx \frac{eEv_d}{\nu_m} \tag{62}$$

The frequency scale for the electron losing all of its energy to neutrals is simply

$$\nu_R = \nu_m\delta \tag{63}$$

This is much slower than the collision frequency since each collision only slightly diminishes the electron's energy. This can be used to compute the energy relaxation length λ_ε, the length scale over which an electron would be expected to lose all of its energy to the neutrals:

$$\lambda_\varepsilon = \frac{v_d}{\nu_R} = \frac{\mu_e E}{\nu_m\delta} = \frac{eE}{m\nu_m^2\delta} \approx \frac{0.8\lambda_m}{\sqrt{2m/M}} \tag{64}$$

The 0.8 comes from the assumption of a Maxwellian electron distribution function. Note that thus far however we have not considered non-elastic collisions. This is justified since in most LTPs the electron energies are lower than ionization energies, rendering elastic collisions dominant, as one can see in the example for Argon (Fig. 68). However in molecular gases the main form is instead the excitation of molecules.

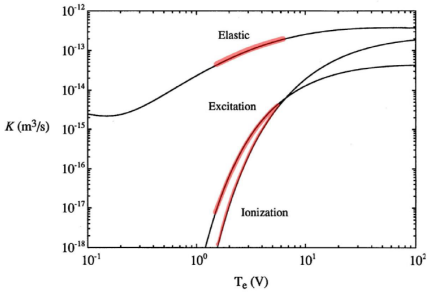

Fig. 68: Rate constants for electrons in Argon, $K = \langle\sigma v\rangle$

To properly account for not only elastic collisions but Coulomb collisions, excitation, ionization and boundary loss, further terms are needed. This of course results in a slightly lower value for the total energy relaxation length λ_ε^*, though still much greater than the mean free path.

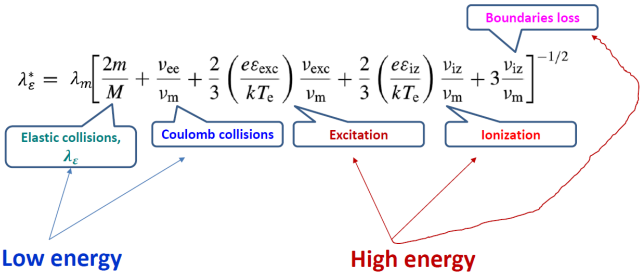

Thus if one's machine size is much larger than the energy relaxation length one would expect large energy transfer to the neutrals resulting in ionization, radical formation and glowing. If, conversely, one's machine size is much less than the energy relaxation length the electrons will retain nearly all their energy as they traverse from the cathode to the anode. The former situation occurs in moderate/high pressure plasmas which consequently exhibit local kinetics, whereas the latter would be described as nonlocal. In nonlocal systems an electron could, perhaps, gain energy in the cathode sheath and deposit it a great distance away.

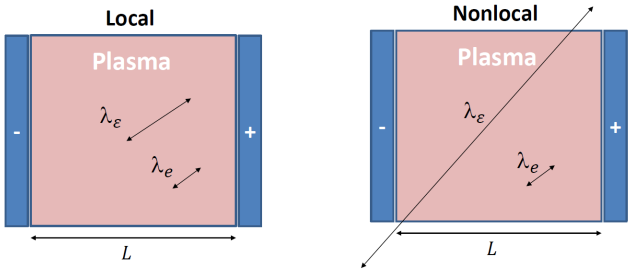

7.3.3 Reduced Electric Field

The fundamental scaling parameter for a discharge is not the electric field, but the so-called *reduced electric field* E/n_a defined in the units of Townsend (1 Td $= 10^{-17}$ V/cm^2). It can be shown that the following rough scalings hold:

$$v_d \propto \frac{E}{n_\alpha} \tag{65}$$

$$J_e \propto \frac{E}{n_\alpha} \tag{66}$$

$$\bar{\varepsilon}_e \propto \left(\frac{E}{n_\alpha}\right)^2 \tag{67}$$

7.4 Global Balance

7.4.1 Particle Balance

Overall in any partially ionized we must have particle balance: the ion-electron pairs generated within the volume V of the plasma must equal the plasma flux through the surface (area A). Mathematically

$$\nu_i n V = n c_S A \tag{68}$$

ν_i is the ionization rate: for inert gases it can be roughly expressed as

$$\nu_i = (5 \times 10^{-14}\,\mathrm{s}) \exp\left(-\frac{E_i}{T_e}\right)\left(\frac{N}{\mathrm{cm}^{-3}}\right) \tag{69}$$

where E_i is the ionization temperature. $c_s = \sqrt{T_e/M_{\mathrm{ion}}}$ is the *ion acoustic velocity* provided $T_e \gg T_i$. Since ions are more massive than electrons it is ion behavior which determines that of the overall plasma: since ions exit the boundaries at this rate, it determines the total loss. This will be discussed further in the lecture on Langmuir probes (Sec 9).

7.4.2 Energy Balance

We also must balance energy. The total power into the plasma $P_{\mathrm{in}} = IV$ must ultimately be absorbed $P_{\mathrm{abs}} = e(n c_s A)\varepsilon_T$ where ε_T is the average energy lost

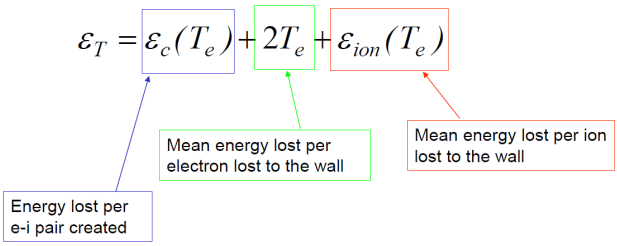

These relations have several counterintuitive results. For example, in any plasma with a sufficiently small λ_ε, increasing the supplied voltage will not make the plasma hotter since the extra electron energy will simply be lost to ionization. The net result will thus be to increase n, not T_e. To increase the temperature one could instead decrease the pressure since this will reduce neutral-electron collisions and allow electrons to retain more of the energy they gain from the electric potential.

7.5 Summary

- Low-temperature plasmas are characterized by low ionization fractions and the dominance of electron-neutral collisions over other types
- The energy relaxation length gives the length scale for electron energy loss
- Discharges can be analyzed by balancing both particle flux and energy

7.6 Homework Problem Set 4

Due February 27, 2026

Consider an argon plasma with electron temperature of 20 eV generated in 20 cm diameter and 20 cm length. The gas pressure in the chamber is 10 mtorr. The gas is at room temperature.

1. Estimate the (momentum transfer/elastic) collisional mean free path for electrons.
2. Estimate ionization mean free path for electrons.
3. Estimate the energy relaxation length for electrons in elastic range.
4. Estimate the energy relaxation length for electrons in inelastic range (suggested reference for cross sections is appended, but feel free to look for alternatives).
5. Make assessment about collisionality and non-locality for electrons in this setup. Can energetic electrons reach the boundaries of this setup or how far can they get before losing all their energy.
6. Vary the pressure (keep the rest parameters, constant) to show where the transition between local and nonlocal electron kinetics occur.
7. (Extra point) Explain why ionization losses and wall losses depend on the frequency of ionizing collisions.

8 Introduction to Vacuum Technology and Diagnostics

8.1 Vacuum Continuum

8.1.1 Types of Vacuum

A vacuum is often taken to be a space devoid of matter. In reality, of course, there is always some small gas density within any vacuum. Any space with a pressure below atmospheric pressure (1 atm = 760 Torr) can be considered a vacuum. The quality of the vacuum exists on a continuum from "low" vacuum with relatively high pressures to "high" vacua with extremely low pressures.

Classification	Vacuum Level [a], [b], [c], [d]	
	Pa	Torr
Low ("rough") Vacuum	133.3 to 1.33 x 10^{-1}	1 to 1 x 10^{-3}
Medium ("intermediate") Vacuum	<1.33 x 10^{-1} to 1.33 x 10^{-3}	< 1 x 10^{-3} to 10^{-5}
High ("HV") Vacuum	<1.33 x 10^{-3} to 1.33 x 10^{-6}	< 1 x 10^{-5} to 10^{-8}
Ultrahigh ("UHV") Vacuum	<1 x 10^{-7} to 1 x 10^{-8}	7.5 x 10^{-10} to 7.5 x 10^{-11}
Extreme Ultrahigh Vacuum	< 1 x 10^{-10}	< 7.5 x 10^{-13}
Interstellar Space	10^{-17}	7.5 x 10^{-20}

Fig. 69: Types of vacuum in both pascals and torrs

vacua of all kinds are characterized by their low particle density, reduced collisionality and longer particle mean free paths.

Pressure	Pressure	Density	MFP (N_2)
torr	*Pa*	*1/cub m*	*m*
760	1.01E+05	2.4E+25	1.0E-07
1	1.33E+02	3.2E+22	7.8E-05
10^{-3}	1.33E-01	3.2E+19	7.8E-02
10^{-6}	1.33E-04	3.2E+16	7.8E+01
10^{-10}	1.33E-08	3.2E+12	7.8E+05

Fig. 70: Typical parameters for nitrogen gas

8.1.2 Importance of Gas Pressure

Why are vacua need for plasma experiments? The fill pressure of the neutral gas has several key effects on plasma dynamics. Firstly, it affects the breakdown of the gas. If the pressure is too low there will not be enough particles to sustain a Townsend avalanche (Paschen's law). In this way the neutral pressure directly affects the ionization mean free path. Furthermore the pressure also affects transport properties: higher neutral pressure means more electron-neutral collisions. In magnetized plasmas high fill pressures can ruin confinement since these collisions will knock electrons off of field lines.

Another important effect is charge-exchange collisions which transfer energy from ions to neutrals (Fig. 71). If these are sufficiently frequent, nearly all of the total flux could be taken up by energetic neutrals instead of ions as shown in Fig. 72. As one can see in the plot, better vacua mitigate these effects.

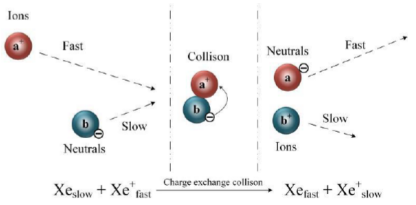

Fig. 71: Charge-exchange collision

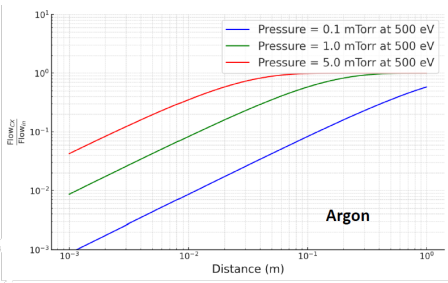

Fig. 72: Plot showing the fraction of the charge exchange neutral flux with distance in the plasma.

8.2 Pump Types

To actually generate a vacuum requires one or several pumps. Each has a unique method of operation and is suited to particular pressure ranges. A summary is shown in Fig. 73. Applications often require just two pumps: a low vacuum pump to go from atmospheric pressure to low pressure and then a high vacuum pump to reach high vacuum.

Fig. 73: Common pumps

Common pump types include the following:

1. Rotary oil-sealed *mechanical pumps* can bring pressures down from atmospheric pressure to 10^{-2} Torr

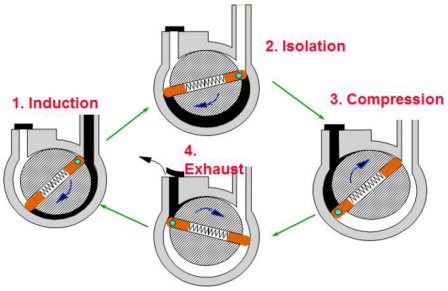

2. *Rotary blower pumps* can lower pressures to $10^{-2} - 10^{-3}$ Torr.

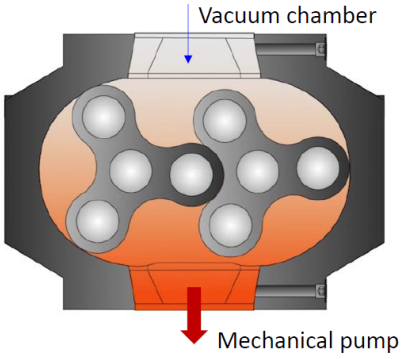

3. *Turbomolecular pumps* use rotors at up to $\sim 10^5$ RPM to impart momentum to gas molecules out of the vessel.

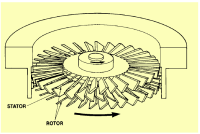

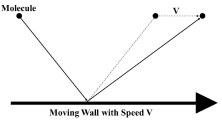

4. *Cryogenic pumps* use extremely low temperatures to cause the gas to undergo "cryo-condensation" and thereby become a solid. While this can yield extremely high vacua of $10^{-3} - 10^{-8}$ Torr it does not work for helium, an especially important consideration for tokamaks which must remove the helium generated from fusion. Helium can instead be removed by high surface area cryo-cold charcoal.

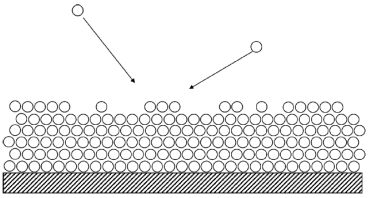

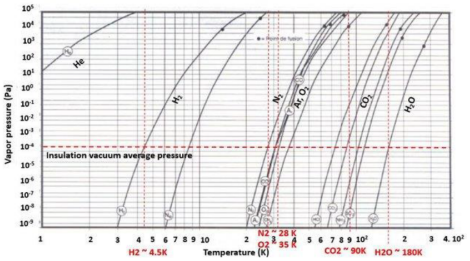

8.3 Pumping Systems

The pumps of course must be attached to each other and to the vacuum vessel via piping in order to function. In order to compute how quickly a pump will work to evacuate a particular vessel we need to consider the entire system, much like a circuit.

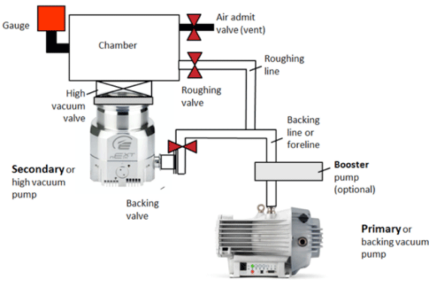

Fig. 74: Plot showing the fraction of the charge exchange flux with distance in the plasma.

8.3.1 Pump-Down Equation

Suppose we are trying to remove air from a given volume V at some constant pumping speed S. Note that the pumping speed S is not actually a speed but is instead a volumetric flow rate, often measured in liters per second. As volume is removed the remaining gas will expand to take its place. We would like to calculate how much time t it will take to reach a given final pressure P_f from an initial pressure of P_i.

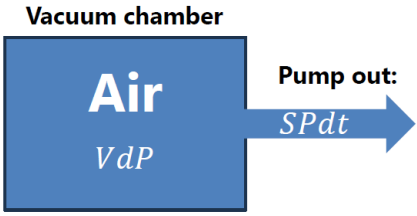

We can write an ODE for $P(t)$ if we assume constant temperature, in which case pressure is simply proportional to the number density N as $P = NT/V$. Particle conservation requires that decrease of particles within the chamber equal the flux out:

$$VdN = -SN\ dt \tag{70}$$

Rewriting in terms of pressure we get the *pump down equation* which can be solved for the pump-down time:

$$V\frac{dP}{dt} = -PS \tag{71}$$

$$t = \frac{V}{S} \ln\left(\frac{P_i}{P_f}\right) \tag{72}$$

In practice, however, the total time can be longer than Eqn. 72 suggests due to gas loads. Often as we are pumping gas out, gas is also making its way in. This can be intentional to supply fresh gas to an experiment, due to leaks, or due to *outgassing* whereby gases emerge from the inner walls of the vacuum vessel as the pressure is reduced.

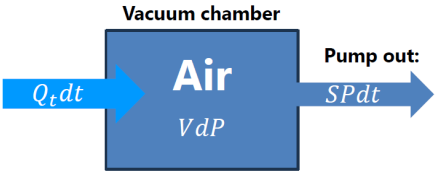

Fig. 75: Plot showing the fraction of the charge exchange flux with distance in the plasma.

The gas load is quantified as the pressure multiplied by the volumetric flow rate. If we suppose there is some gas load Q_t (Torr L/s) we can modify Eqn. 71 as

$$V\frac{dP}{dt} = -PS + Q_t \tag{73}$$

To maintain a steady-state, of course we need $Q_t = PS$. Let us consider a simple example relevant to mass flow controllers. These flows are measured for standard temperature and pressure (1 atm = 760 Torr) in units of SCCM (standard cubic meter per centimeter). So to maintain a pressure of 1 mTorr in our chamber with a mass flow rate of 10 SCCM, we need a pumping speed of

$$S = \frac{760\,\text{Torr} \times 100\,\text{SCCM}}{10^{-2}\,\text{Torr}} \approx 450\,\text{m}^3/\text{h} \tag{74}$$

8.3.2 Conductance

To model the tubing connecting the pumps and the vacuum vessel we can use a circuit analogy. Just as current flows from high voltage to lower voltage according to the electrical conductance, gas flows from high pressure to low pressure according to the pressure conductance C:

$$Q = C(P_U - P_D) \tag{75}$$

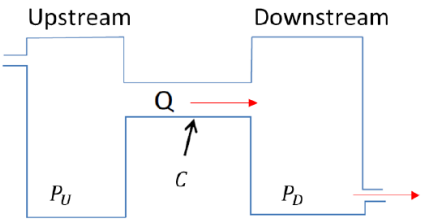

Note that the conductance has the same units as pumping speed S. Let's apply this to a simple case in which we have a turbopump pumping at speed S_D attached to a pipe with conductance C connecting it to the chamber. Since we have flow continuity, the flow coming out of the pump $S_D P_D$ must equal the flow into the chamber $S_U P_U$.

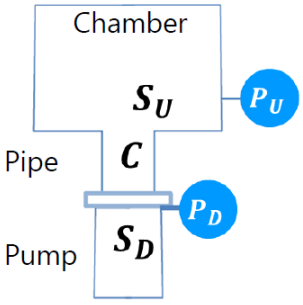

The total conductance from the outside to the chamber results from the net action of the pump with effective conductance S_D and the pipe with conductance C. Since resistances add normally in series, conductances combine as inverses:

$$\frac{1}{S_U} = \frac{1}{S_D} + \frac{1}{C} \tag{76}$$

so

$$S_U = \frac{S_D C}{S_D + C} \tag{77}$$

Thus even if the conductance and pumping speed are equal, only half of it will get to the vessel itself. The more tubing required to reach the chamber, the less able the pump will be able to reduce the pressure there.

The conductance within a particular bit of tubing depends on the particular flow regime. This is quantified by the *Knudsen number*, the ratio of the neutral mean free path to the scale length or pipe diameter.

$$\mathrm{Kn} = \frac{\lambda_a}{L} \tag{78}$$

If $\mathrm{Kn} \ll 1$ then we have our ordinary viscous flow, which in pipes is described by Poiseuille flow. Here there is a $C \propto R^4$ conductance scaling. However if $\mathrm{Kn} \gg 1$ then the mean free path is larger than the system size and we are in the *free molecular flow regime* with a $C \propto R^3$ scaling.

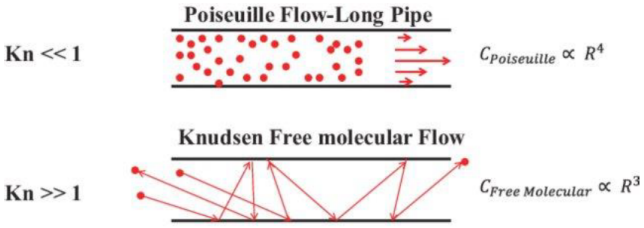

Fig. 76: Flow Regimes

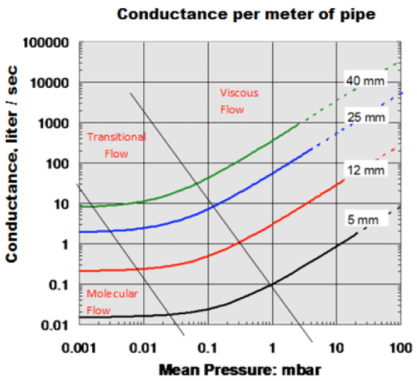

Fig. 77: Conductance dependence on pipe diameter and mean pressure

8.4 Vacuum Gauges

Lastly, we consider various gauges used to measure the pressure.

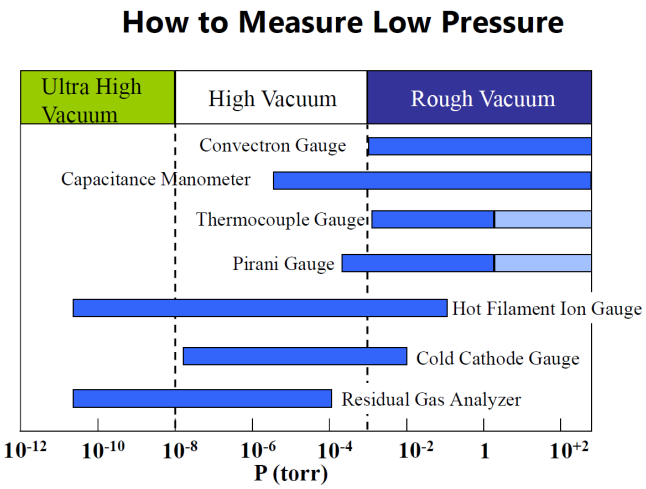

Fig. 78: Summary of pressure gauges

1. *Thermocouples* work for measuring pressures from 10 mTorr to atmospheric pressure. A filament is heated and the resultant temperature is measured using a thermocouple. Since the thermal conductivity of the gas is a function of the pressure, the pressure can be inferred from the thermocouple reading and knowing the type of gas.

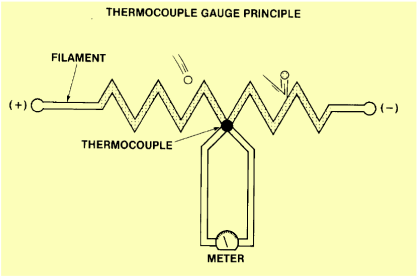

2. *Hot filament ion gauges* can measure very high vacuum, under 1 mTorr. These use the breakdown properties of the gas to infer the pressure.

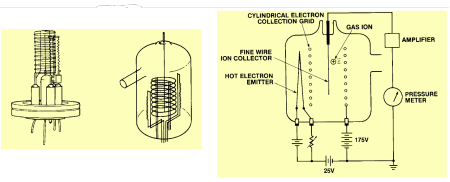

3. *Capacitive manometers* can be used with any gas type but have limited range and are difficult to calibrate. They can be configured to work from atmospheric pressure to 10^{-5} Torr.

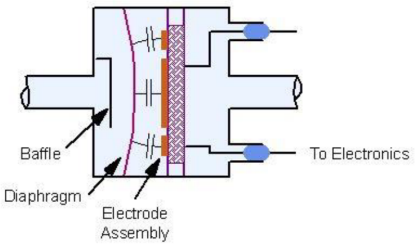

8.5 Summary

- Vacuum pumps are suited to particular pressure ranges, so typically a series of pumps are needed to achieve high vacuum
- The time to create a vacuum can be modeled by the pump-down equation combined with a circuit analysis
- Mechanical pumps work well to create a low vacuum while turbomolecular pumps can achieve high vacuum
- The Knudsen number Kn indicates the degree to which a gas is in the free molecular flow regime as opposed to acting as a fluid.

9 Langmuir Probes, Part I

Introduced by their namesake in the 1920s, Langmuir probes are as old as the study of low temperature plasmas. Their chief virtue is simplicity - a Langmuir probe consists essentially of just an electrode inserted into the plasma, making them some of the easiest and cheapest probes to implement.

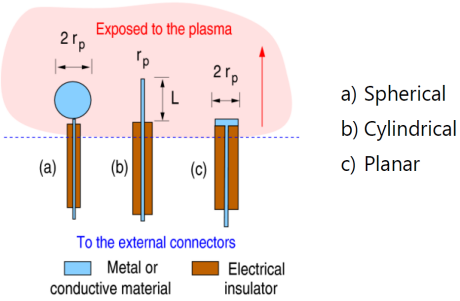

Fig. 79: Common Langmuir probe shapes.

By sweeping the bias of the electrode from low to high and measuring the resultant current drawn by the probe, a V-I characteristic curve can be obtained. Since this profile will depend on the plasma properties, analysis of the characteristic can tell us about the plasma.

The other key advantage is that Langmuir probes provide local measurements of plasma properties, unlike laser diagnostics or interferometry-based measurements. There are two major downsides however. Firstly, Langmuir probes, by directly absorbing electrons or ions from the plasma, are inherently invasive and care must be exercised to ensure that the act of measuring does not significantly alter the plasma under consideration. The second is that while obtaining the V-I characteristic is easy, interpreting it can be quite difficult. Even today there is still much we do not know about the plasma physics in the vicinity of Langmuir probes.

Probe physics is thus a complex and rich topic. For the sake of simplicity here we shall make the following assumptions:

1. $T_e \gg T_i$, i.e. ions are cold
2. Magnetic fields may be neglected
3. All ions are singly-ionized
4. Ionization may be ignored near the probe

9.1 Sheaths

The transition zone between the probe and the unperturbed plasma is known as the **sheath**. As the bridge from the external circuitry to the plasma, the

sheath physics will determine how the plasma properties relate to the V-I characteristic. For simplicity let us consider a planar probe ((c) in Fig. 79). This will allow us to consider a one-dimensional system wherien the sheath properties only depend on the distance from the wall x with uniformity assumed in y and z.

9.1.1 Matrix Sheath

Let us first consider the simplest case of an extremely fast perturbation, the biasing of the wall very negative $V_b \gg T_e$. Suppose that it is specifically faster than the ion plasma frequency timescale ω_{pi}^{-1}. In this case the electrons respond to the perturbation by rushing away from the wall while the ions remain motionless.

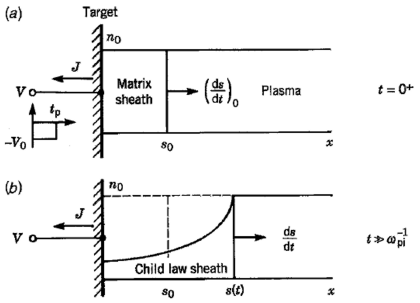

Fig. 80: (a) Matrix sheath as a result of a rapid perturbation, a (b) Child law sheath as a result of a slower perturbation.

In this case it is simple to show that the resultant potential is

$$\phi(x) = -\frac{en_0}{\epsilon_0}\frac{x^2}{2} \tag{79}$$

so the sheath size is

$$s = \lambda_D \left(\frac{2eV_b}{T_e} \right)^{1/2} \tag{80}$$

This is known as a *matrix sheath*.

9.1.2 Debye Shielding

Now let us consider a more interesting scenario wherein the wall is not biased at all and instead its potential is left to float and attain a steady-state with the plasma. Essentially we want to know what kind of sheath forms when we place a conducting solid within a plasma.

If we assume the usual case of electron temperatures similar to or greater than ion temperatures, the electrons will be far more mobile. Thus they will strike the wall much more rapidly than the ions and quickly charge it negative. It will continue charging negative until the wall potential is sufficiently low that it repels enough electrons to reach a steady-state. As we know from elementary plasma theory, the result will be that a positively-charged cloud will form around the negatively-charged wall to cancel the electric field and "shield" the electrode from the broader plasma. This is known as a *Debye sheath* and has an extent the order of the Debye length λ_D.[2]

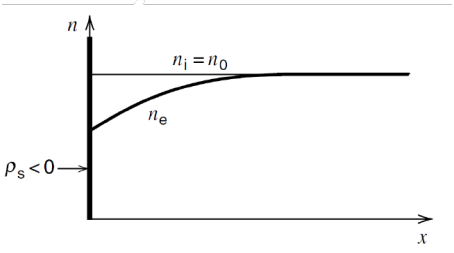

This can be shown through a quick calculation much like that in GPP I, where we similarly assume that

$$n_e(x) = n_0 e^{e\phi(x)/T_e} \approx n_0(1 + e\phi/T_e) \tag{81}$$

and $n_i = n_0$ (cold ions). From Poisson's equation we find

$$\frac{d^2\phi}{dx^2} = \frac{e}{\epsilon_0}(n_e - n_i) \tag{82}$$

[2] More detailed analysis will demonstrate that sheaths for biased probes can actually be as much as hundreds of Debye lengths - see more in the next section.

$$\frac{d^2\phi}{dx^2} = \frac{e^2 n_0}{\epsilon_0}\frac{\phi}{T_e} \tag{83}$$

$$\phi = \phi_0 e^{-|x|/\lambda_{De}} \tag{84}$$

with

$$\lambda_{De} = \sqrt{\frac{\epsilon_0 T_e}{e^2 n_e}} \tag{85}$$

So, as we expect, we find that there is a positively charged sheath between the negatively charged wall and the neutral unperturbed plasma far away.

9.1.3 Bohm Criterion

If the probe is floating, it has reached a state of sufficiently low voltage that the electron fluxes and ion fluxes are equal and hence there is no net flow of current. Let's analyze this steady-state mathematically. The ions are pushed towards the wall both by the pressure gradient and the electric field:

$$n_i M v_i \frac{dv_i}{dx} = -\frac{dp_i}{dx} + e n_i E \tag{86}$$

where M is the ion mass and this time x is the direction from the plasma to the wall. We can make some substitutions here. Firstly, we can replace the derivative of the ion flow velocity with a density derivative by invoking flux conservation $d(n_i v_i)/dx = 0$:

$$v_i \frac{dn_i}{dx} = -n_i \frac{dv_i}{dx} \tag{87}$$

Next, we can replace the pressure term using the adiabatic index γ_i to express

$$p_i = \gamma_i T_i n_i \tag{88}$$

Lastly, we can express the electric field in terms of the electron density from Eqn. 81:

$$\frac{dn_e}{dx} = \frac{e n_e}{T_e}\frac{d\phi}{dx} = -\frac{e n_e}{T_e} E \tag{89}$$

Substituting Eqns. 87, 88 and 89 into Eqn. 86 we find

$$-Mv_i^2\frac{dn_i}{dx} = -\gamma_i T_i\frac{dn_i}{dx} - \frac{n_i}{n_e}T_e\frac{dn_e}{dx} \tag{90}$$

This can be rewritten as

$$\left[v_i^2 - \frac{1}{M}\left(\gamma_i T_i + \frac{n_i}{n_e}T_e\frac{n_e'(x)}{n_i'(x)}\right)\right]\frac{dn_i}{dx} = 0 \tag{91}$$

Note that Eqn. 91 is trivially satisfied within the bulk plasma for there are no gradients. But what about the edge of the sheath? There from quasineutrality we have $n_i = n_e$, but what about the derivative ratio $n_e'(x)/n_i'(x)$? If this was less than one that would mean that for at least a small region in the sheath the electron density would be greater than that of the ions - a net negative charge, instead of a net positive one. But of course the sheath should be everywhere net positively charged, so instead we must have

$$\frac{n_e'(x)}{n_i'(x)} \geq 1 \tag{92}$$

Returning to Eqn. 91, since the ion slope is not zero and $n_i = n_e$ at the wall, we see

$$v_i^2 = \frac{1}{M}\left(\gamma_i T_i + T_e\frac{n_e'(x)}{n_i'(x)}\right) \tag{93}$$

Because $n_e'(x)/n_i'(x) \geq 1$, we find that

$$v_i^2 \geq \frac{\gamma_i T_i + T_e}{M} \tag{94}$$

This critical velocity is known as the **Bohm velocity** v_B (it is also just the ion sound speed c_S):

$$\boxed{v_B = \sqrt{\frac{\gamma_i T_i + T_e}{M}}} \tag{95}$$

In practice, we often assume cold ions and then it has the particularly simple form

$$v_B = \sqrt{\frac{T_e}{M}} \tag{96}$$

The *Bohm sheath criterion* states that ions must enter the sheath at a speed no less than the Bohm velocity. Put differently, ions must enter the sheath with kinetic energy of at least $T_e/2$.

9.1.4 Pre-Sheath

If ions are entering the sheath at the Bohm velocity then there must have been some potential which exists outside of the sheath accelerating them. This could not have been in the bulk plasma which is at a constant potential. This intermediate region between the unperturbed plasma and the sheath, across which a potential drop exists, is known as the **pre-sheath**. These can be much larger than the sheath itself.

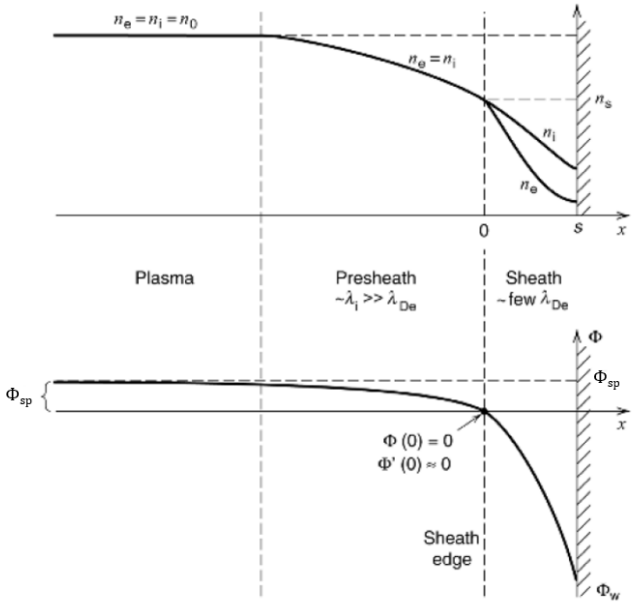

Fig. 81: V-I Characteristic

The potential of the plasma far away from the wall is known as the *plasma potential* V_{sp}, sometimes known as the space potential. This is constant in the plasma but drops across the pre-sheath to accelerate ions to the Bohm velocity. The magnitude of this potential drop must be $T_e/2$ to satisfy the Bohm criterion. It drops further in the sheath until we reach the potential

of the wall. If this is disconnected from any power source, we term the wall potential the *floating potential* V_F.

To summarize - if we place a disconnected electrode in the plasma, it will rapidly charge to a negative floating potential relative to the plasma far away. Near the electrode a positively-charged sheath will develop where quasineutrality is broken, extending for roughly a Debye length. Outside this sheath is a pre-sheath with charge balance but an electric field required to ensure that ions enter the sheath with the Bohm velocity.

9.2 V-I Characteristic

Now that we have a basic foundation in the simple case of an unbiased electrode, let us now consider what happens across the entire V-I characteristic. A typical one, annotated, is shown below. Note that I is the current from the probe to the plasma, not drawn from the plasma.

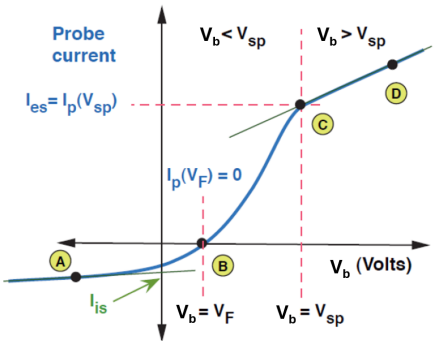

The first basic observation to make is that for very low voltages ions will be collected by the probe resulting in a negative current to the plasma. Electrons will be so repelled that even the highest-energy ones will not reach the probe, resulting in a current exclusively composed of ions. For very high voltage we will have the opposite situation: electrons of any energy will be attracted to the probe whereas all ions will be repelled. Between these two regions is an intermediate situation where both ion and electron fluxes contribute to some extent.

We can also identify the floating potential V_F and the plasma potential V_{sp} on the above plot. V_F will simply be where the probe draws no total current since this corresponds to the potential the probe would naturally attain without any power supply attached. The plasma potential V_{sp} can be noted as where I, here dominated by electrons, has an inflection point. Before this point only some electrons, the more energetic ones, contribute to the total current. As the voltage increases more and more electrons have enough energy to reach the probe, but after saturation there are no more electrons left (all are collected), so in principle there is no more current to be gained by increasing

the voltage. (As one can see, in practice, the current continues to increase, albeit more slowly. This will be discussed further in the next lecture.)

9.2.1 Ion Saturation Current

While before we considered the sheath in a disconnected electrode, all of our analysis still holds so long as the probe's potential is below the plasma potential. Hence the current due to the ions will simply be from the Bohm flux, provided we assume that ions are not streaming in super-sonically. This is called the *ion saturation current* I_{is} [3]. If n_s is the density of ions at the edge of the sheath, the total ion current is

$$I_{is} = en_s v_B A_p \tag{97}$$

where A_p is the probe area. The only unknown is n_s, which we would like to express in terms of n_0. Since we have quasienutrality in the pre-sheath, $n_s = n_{se}$. The drop in electron density over the potential drop of $T_e/2$ is determined by the Boltzmann distribution:

$$n_s = n_0 \exp\left(-\frac{eT_e/2}{T_e}\right) = n_0 e^{-1/2} \approx 0.61 n_0 \tag{98}$$

Thus

$$\boxed{I_{is} = 0.61 e n_0 \sqrt{\frac{T_e}{M}} A_p} \tag{99}$$

At point A in Fig. 81, the total probe current I_p will simply be this ion saturation current since the potential is sufficiently negative that no electrons have enough energy to reach the probe.

9.2.2 Electron Saturation Current

Now let us consider the other end of the V-I characteristic curve where the probe voltage equals the plasma potential. Now the current will be dominated by the more-mobile electrons who now face no potential barrier between the bulk plasma and the probe. This electron current is known as the *electron saturation current* I_{es} and at point C (Fig. 81) where the bias voltage $V_b = V_{sp}$, $I_p = I_{es}$. The electron current can be simply computed if we assume that the electrons have a Maxwellian energy distribution:

[3] Note that this is taken to be positive even though it results in a negative current on conventional V-I plots

$$\Gamma = \int_0^\infty v_x f(v_x) dv_x \tag{100}$$

$$\Gamma = \int_0^\infty n_0 v_x \left(\frac{m}{2\pi T_e}\right)^{1/2} \exp\left(-\frac{m v_x^2}{2T_e}\right) dv_x \tag{101}$$

$$\Gamma = n_0 \sqrt{\frac{T_e}{2\pi m}} \tag{102}$$

where m is the electron mass. Thus

$$\boxed{I_{es} = e n_0 \sqrt{\frac{T_e}{2\pi m}} A_p} \tag{103}$$

Note that we see that the electron saturation current is far higher than the ion saturation current:

$$\frac{I_{es}}{I_{is}} = \frac{1}{0.61}\sqrt{\frac{M}{2\pi m}} \tag{104}$$

For argon, for example, this ratio is over two orders of magnitude. Spanning this entire range of current is challenging, so tradeoffs need to be considered in circuit design.

9.2.3 Between Floating and Plasma Potentials

Now let us turn to the more interesting question of what happens between the electron and ion diffusion regions, i.e. between A and C. The ion current will still be coming in but because the potential is lower than the plasma potential, some electrons will not have sufficient energy to reach the probe. If, say, the probe voltage is 5 V below the plasma potential then only electrons with over 5 eV will be registered as current. If we assume a Maxwellian distribution of electron energies then the total electron current I_e will be just reduced by the Boltzmann factor:

$$I_e = I_{es} \exp\left(\frac{e(V_b - V_{sp})}{T_e}\right) \tag{105}$$

Thus the total current to the probe will be just $I_p = I_e - I_{is}$:

$$I_p \approx e n_e \left[\sqrt{\frac{T_e}{2\pi m}} \exp\left(\frac{e(V_b - V_{sp})}{T_e}\right) - 0.61\sqrt{\frac{T_e}{M}}\right] A_p \tag{106}$$

9.3 Calculating and Measuring Plasma Properties

The purpose of these models of the V-I characteristic is to enable us to infer plasma properties from them. We consider several here.

9.3.1 Plasma Potential

As discussed, the plasma potential can be directly read off of the V-I characteristic as the point where $I_p = 0$. From Eqn. 106 we see that this occurs when

$$\boxed{V_F - V_{sp} = -T_e \ln\left(\frac{1}{0.61}\sqrt{\frac{M}{2\pi m}}\right)} \tag{107}$$

For example, with an argon plasma at 10 eV we get a floating potential of $\sim$ 50 V. However for non-Maxwellian distributions this analysis can be complicated. Consider for instance if we have a bi-Maxwellian with large low-temperature population at $T_e = T_{el}$ and a high-temperature one at $T_e = T_{eh}$. In the pre-sheath the effective temperature will be approximately T_{el}, but in the sheath only the most energetic electrons will be present so the effective temperature there is T_{eh}. Thus one can show that the floating potential would be closer to

$$V_F - V_{sp} = -T_{eh} \ln\left(\sqrt{\frac{M}{2\pi m}}\right) - \frac{T_{el}}{2} \tag{108}$$

whereas the first term is the drop across the sheath dominated by high-energy electrons and the second term is the drop across the pre-sheath dominated by low-energy electrons.

9.3.2 Temperature

If we assume a Maxwellian distribution we can calculate the temperature via the V-I characteristic between B and C. There electrons will dominate the current so we can approximate from Eqn. 106

$$I_p \approx e n_e \sqrt{\frac{T_e}{2\pi m}} \exp\left(\frac{e(V_b - V_{sp})}{T_e}\right) \tag{109}$$

Thus if we plot I against V in a semilog plot, T_e can be found just from fitting the slope:

$$\boxed{T_e = e\left[\frac{d\ln I_p}{dV_b}\right]^{-1}} \tag{110}$$

In practice this graphical method is prone to error since these plots seldom yield a perfectly-straight line.

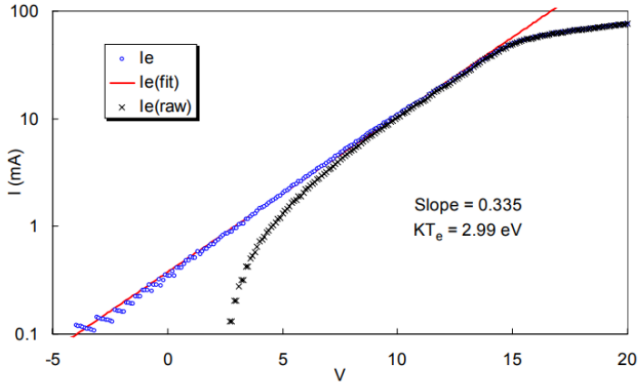

Fig. 82: Semilog plot of probe current from Francis Chen, "Langmuir Probe Diagnostics", IEEE-ICOPS meeting, Jeju, Korea, June 5, 2003

9.3.3 Plasma Density

Once the temperature is known, the density may be extracted from the ion saturation current (Eqn. 99):

$$\boxed{n_0 \approx \frac{I_{is}}{0.61e\sqrt{\frac{T_e}{M}}A_p}} \tag{111}$$

supposing that we have measured the size of the probe. In practice the error can be quite large since the saturation current must be extrapolated to the floating and plasma potential for it is not exactly constant.

9.4 Summary

- When an unbiased electrode is inserted into a plasma it attains a negative floating potential relative to the plasma
- Between the unperturbed plasma and a biased electrode are the pre-sheath and sheath. The pre-sheath is quasineutral but has a potential drop to accelerate ions to the Bohm velocity. In the sheath quasineutrality is broken.

- From Langmuir probe VI characteristics T_e, n_0, V_{sp}, V_F may be inferred

10 Langmuir Probes, Part II

10.1 Common Complications

In the previous section we considered the classical theory of an ideal planar Langmuir probe. However there are important effects which, in certain contexts, can completely alter this simple picture. We consider some of the common scenarios here.

10.1.1 Sheath Size Effects

As discussed previously, one would naively expect that once one reaches a sufficiently high (low) voltage, the electron (ion) current saturates since there are no more electrons (ions) available. In reality though the current magnitude continues to increase - why? Well let us consider the ion side. If we continue decreasing the voltage, while it is true that the ion density in the plasma does not change, the sheath grows and grows since more and more space is needed to overcome that potential difference. The 1D model breaks down. This increases the effective probe area A_p, so the current continues to grow without bound. The same is true with the electrons (though proceeding beyond the plasma potential triggers oscillations in this case).

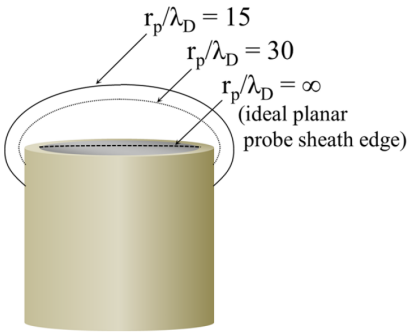

We can compute the size of the sheath s by equating the total Bohm current to the wall and the Child-Langmuir law:

$$en_s\sqrt{\frac{T_e}{M}} = \frac{4}{9}\epsilon_0\left(\frac{2e}{M}\right)^{1/2}\frac{V_0^{3/2}}{s^2} \tag{112}$$

$$s = \frac{\sqrt{2}}{3}\lambda_D\left(\frac{2eV_0}{T_e}\right)^{3/4} \tag{113}$$

Hence the sheath length scales with the three-quarters power of the voltage drop. The result is that the sheath thickness can range from just a few Debye

lengths to hundreds. As s grows larger, the effective collection area expands away from the probe, increases in size, and has its shape distorted.

10.1.2 Orbital Motion Limited Collection

As the sheath grows and grows, the prior analysis we have applied to determine $I_p(V_b)$ is no longer relevant. Suppose we have a situation as in the figure below wherein the sheath is significantly larger than the probe, here considered to be a long cylindrical probe (length $\ell \gg a$). Suppose we are in the electron saturation regime. We see that it is entirely possible that an electron with sufficient energy to reach the probe will not actually do so because it will swing around it and miss. Hence the chief requirement for reaching the probe is no longer energy but the poloidal velocity - if this is too large, the ion will miss the probe and return to the plasma. This is known as the *orbital-motion limited* or OML regime.

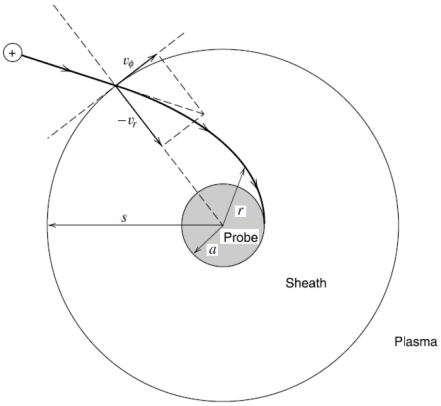

To characterize this motion, we begin with the conservation of energy and angular momentum respectively for a successfully-collected particle. We assume no collisions and that the particle is attracted to the probe.

$$\frac{1}{2}m(v_r^2 + v_\phi^2) + e|\phi_{sp} - V_b| = \frac{1}{2}m(v_r'^2 + v_\phi'^2) \tag{114}$$

$$sv_\phi = av_\phi' \tag{115}$$

Solving yields

$$v_\phi' = \frac{s}{a}v_\phi \tag{116}$$

$$v_r'^2 = v_r^2 + v_\phi^2 + \frac{2e|\phi_{sp} - V_b|}{m} - \frac{s^2}{a^2}v_\phi^2 \tag{117}$$

In order to reach the probe we assume that the velocity must be inward ($v_r < 0$) and have sufficient energy to reach the probe ($v_r'^2 \geq 0$). Taking the minimal condition where the energy is just enough ($v_r'^2 = 0$) we can find the largest allowable poloidal velocity:

$$v_{\phi 0} = \sqrt{\frac{v_r^2 + 2e/m|\phi_{sp} - V_b|}{s^2/a^2 - 1}} \tag{118}$$

To simplify this, let us assume the sheath is not only large but quite large, i.e. $a \ll s$ and furthermore that the probe is sufficiently biased that particles do not have enough energy to escape the sheath

$$v_r^2 \ll \frac{e|\phi_{sp} - V_b|}{m} \tag{119}$$

Hence we may simplify Eqn. 118 by dropping the v_r^2 in the numerator and -1 in the denominator to yield

$$v_{\phi 0} = \frac{a}{s}\sqrt{\frac{2e|\phi_{sp} - V_b|}{m}} \tag{120}$$

Now let us convert this into a current. For this we can integrate the Maxwellian

$$f = \frac{m}{2\pi e}\exp\left[-\frac{m(v_r^2 + v_\phi^2)}{2eT_s}\right] \tag{121}$$

to find

$$I_p = -2\pi s\ell n_s e\int_{-\infty}^{0} dv_r v_r \int_{-v_{\phi 0}}^{v_{\phi 0}} dv_\phi f(v_r, v_\phi) \tag{122}$$

$$I_p = 2en_s a\ell\sqrt{\frac{2e|\phi_{sp} - V_b|}{m}} \tag{123}$$

If we further are in a regime where the magnitude of V_b is much greater than the plasma potential we get the following especially simple form:

$$\boxed{I_p = 2en_s a\ell\sqrt{\frac{2|V_b|}{m}}} \tag{124}$$

Note that this equation is equally valid for both electrons and ions, one would simply need to replace m with M in the above formula. As one can see, one key advantage of the OML regime is that we can measure the density n_s easily since all other quantities in the equation or known. While n_s is the density at the edge of the sheath, since the Bohm current arguments no longer apply this is essentially just the density of the bulk plasma n_0. Thus this is a simple way to determine the density of a plasma without needing temperature information.

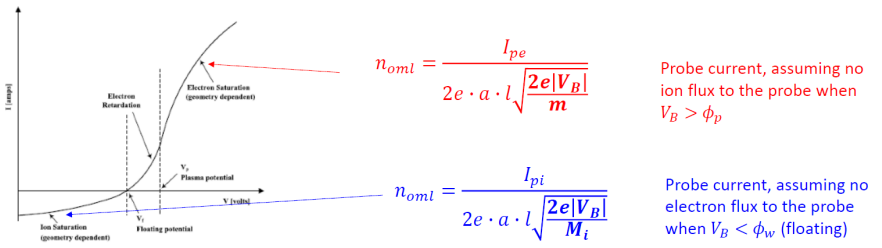

More broadly, this formula is relevant in the far extremes of the Langmuir probe V-I characteristic when OML applies. As one final note, systems with non-negligible collisions disrupt orbits and can either enhance or reduce total probe current I_p.

10.1.3 Ion Beams

One other feature that can be noticed past the plasma potential is ion beams. Suppose there is an intense ion beam. This will register as negative current on the typical V-I characteristic until the voltage is sufficiently high to repel the beam. This manifests as a sudden increase in net current in the electron collection regime past a certain critical voltage - this voltage gives the energy of the beam, the change in current the size

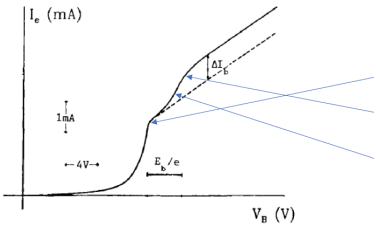

FIGURE 10. Laboratory I-V characteristic showing the presence of an ion beam.

Fig. 83: Note the transition region corresponding to the spread in energy of the ion beam. Adapted from F. F. Chen, Langmuir Probe Diagnostics, UCLA, 2003, N. Hershkowitz, How Langmuir Probe Works, 1989

10.1.4 Probe Measurements in a Magnetic Field

So far we have assumed that there is no significant magnetic field within a plasma. Of course in many plasma applications non-negligible fields do exist: how do they affect our analysis? The key length scale to consider is the electron gyroradius ρ_e: if this is much larger than the probe size then we can effectively ignore magnetic fields as particles travel through the sheath. Hence if

$$r_p < \rho_e \equiv \frac{m v_{et}}{eB} \tag{125}$$

we can apply the classical probe theory hitherto used. This is not a particularly onerous requirement and occurs in many systems with weaker magnetic fields. If however fields are especially strong, and the gyroradius is less than the probe radius, gyromotion cannot be ignored. In this case electrons will stream towards the probe along streamlines. The most common situation is partially-ionized plasmas in which the electrons are magnetized, but the ions are not.

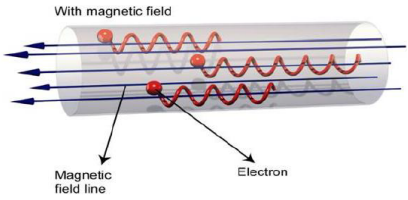

Fig. 84: B.-W. Koo, N. Hershkowitz, and M. Sarfaty, J. Appl. Phys. 86, 1213 (1999)

If the electrons are moving sufficiently quickly the probe can effectively deplete the flux tube of field lines which terminate on the probe. This field-line depletion is counterbalanced by cross-field diffusion, described by coefficient $D_\perp = \nu_e (v_{et}/\omega_{ce})^2$. Thus if

$$\frac{16 D_\perp}{d^2} \ll \frac{v_{et}}{L_{\rm col}} \tag{126}$$

where $L_{\rm col}$ is the collection length of the flux tube, electron escape will dominate over replenishment from other field lines resulting in a strong plasma perturbation. To test whether a strong perturbation exists, one can check the floating potential nearby: ideally, it should be unaffected by the Langmuir probe.

The field geometry also informs the probe geometry. The recommended best practices for Langmuir probe orientation are shown below

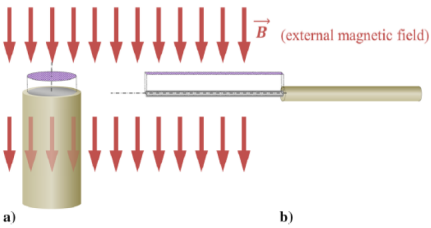

The flux *along* the field line in such a case will simply be

$$\Gamma_{pe} \approx n_e \sqrt{\frac{T_e}{2\pi m_e}} \exp\left(\frac{e\phi_w}{T_e}\right) \tag{127}$$

whereas the flux *across* the field line will be reduced as

$$\Gamma_{\perp} \approx \frac{\Gamma_{pe}}{1 + \left(\frac{\omega_{ce}}{\nu_e}\right)^2} \tag{128}$$

where ν_e is the electron momentum transfer collision frequency. If ω_{ce}/ν_e is large then we will see a substantial decrease in perpendicular flux.

Broadly when magnetic fields significantly affect the V-I characteristic the standard theory breaks down and can no longer be used in the same way to infer n_e, T_e, etc. A typical evolution of the characteristic as B is increased is shown below - note also that a 10 eV ion beam is present.

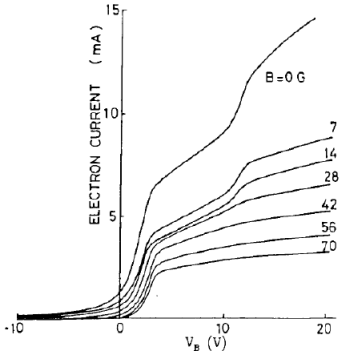

As one can see, since the electrons are magnetized the total electron current is sharply diminished as the magnetic field is increased.

10.2 Advanced Probe Designs

While a single Langmuir probe is a powerful diagnostic, it also has key limitations. The requirements of broad voltage sweeping and a large magnitude difference in ion and electron collection currents makes circuitry quite complex, especially if one wishes to get time-resolved data. Thus there are several variations of the Langmuir probe which use of clever circuitry and/or physics to enable simpler data collection. We consider several here.

10.2.1 Double Probe

As the name would suggest, a double probe has two electrodes facing into the plasma. The probe itself is floating but uses a floating power supply to generate a swept potential difference between the two probes.

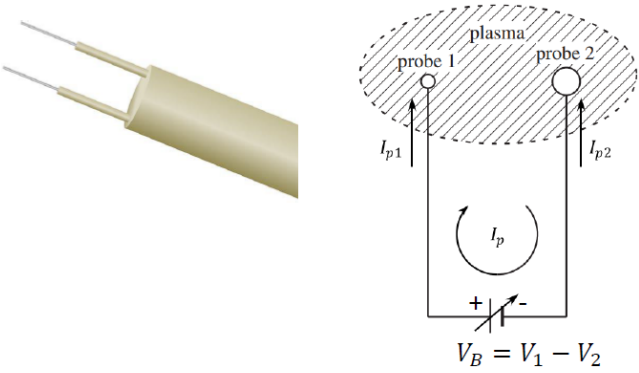

The probe current through the first probe (taken as I_p) is negative that of the second, $I_p \equiv I_{p1} = -I_{p2}$. Breaking into electron and ion components as usual we have

$$I_{p1} = I_{e1} + I_{i1} \approx n_e \sqrt{\frac{T_e}{2\pi m}} \exp\left(\frac{eV_1}{T_e}\right) A_{p1} - I_{i1} \tag{129}$$

$$I_{p2} = I_{e2} + I_{i2} \approx I_{2i} - n_e \sqrt{\frac{T_e}{2\pi m}} \exp\left(\frac{eV_2}{T_e}\right) A_{p1} \tag{130}$$

where the voltages are relative to the plasma potential (as we shall see, only their difference ends up mattering). We can express the ratio of the electron currents in terms of I_p and the Bohm currents to find

$$\frac{I_{e1}}{I_{e2}} = \exp\left(\frac{eV_b}{T_e}\right) = \frac{I_{p1} + I_{i1}}{I_{i2} - I_{p1}} \tag{131}$$

If we assume a symmetrical probe ($A_{p1} = A_{p2}$), the Bohm currents to both should be the same, so we can rewrite to find

$$I_p \left[\exp\left(\frac{eV_b}{T_e}\right) + 1\right] = I_i \left[\exp\left(\frac{eV_b}{T_e}\right) - 1\right] \tag{132}$$

$$I_p = I_i \tanh\left(\frac{eV_b}{2T}\right) \tag{133}$$

so our final form is

$$I_p = 0.61 e n_0 \sqrt{\frac{T_e}{M_i}} A_p \tanh\left(\frac{eV_b}{2T}\right) \tag{134}$$

By sweeping V_b around zero we can fit the resulting curve to infer n_0 and T_e. Double probes feature far simpler circuitry since sweeping is minimal and there are no high currents. The downside is that it works only for Maxwellian electron distributions and so cannot discern other kinds of energy distributions. The V-I characteristic for a typical double probe is shown below.

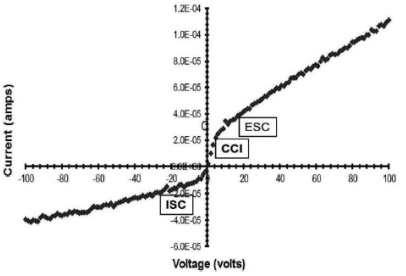

A variation known as the *triple probe* avoids the need to sweep voltage by adding a third floating electrode. This extra datum allows for, in essence, three points on the characteristic from which n_0 and T_e may be inferred.

10.2.2 Emissive Probe

Another way to improve upon the standard Langmuir probe is to take advantage of thermionic emission. An *emissive probe* utilizes a filament which can be either left cold or heated to high temperatures. In the latter case it emits an electron flux of its own. By measuring at which voltage this emissive current ceases to flow, the plasma potential may be easily inferred. First let us consider the basic physics of a floating wall from which electrons are emitted.

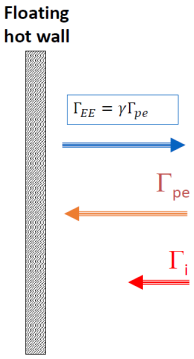

Our flux balance reads

$$\Gamma_{pi} + \Gamma_{EE} - \Gamma_{pe} = 0 \tag{135}$$

where the sum of the ion flux, secondary electron flux and electron flux is zero. The ratio between the incoming electron flux and the one emitted by the wall is the critical parameter which we call γ, defined as $\gamma \equiv \Gamma_{EE}/\Gamma_{pe}$. This allows us to write

$$\Gamma_{pe} = \frac{1}{1-\gamma}\Gamma_{pi} \tag{136}$$

Mathematically this does not change much: for instance the wall potential in such a case is no longer Eqn. 107 but simply

$$V_F - V_{sp} = -T_e \ln\left(\frac{1-\gamma}{0.61}\sqrt{\frac{M}{2\pi m}}\right) \tag{137}$$

since the electron current (in the numerator) is reduced by a factor $1-\gamma$. This implies that if γ gets sufficiently close to 1 we will run into issues, namely that the floating potential might rise *above* the space charge. In actuality this is prevented from occurring due to space-charge effects (as quantified by the Child-Langmuir relation).

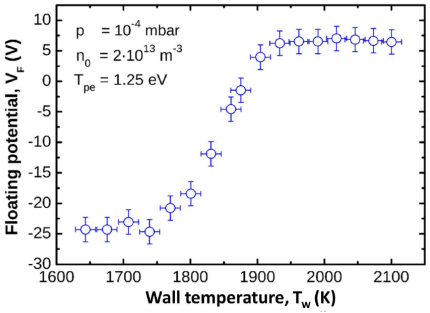

If the wall temperature is relatively low, then of course $\gamma \to 0$ and we recover the old solution wherein the floating potential sits well below the space potential. As it increases however this difference decreases as shown below.

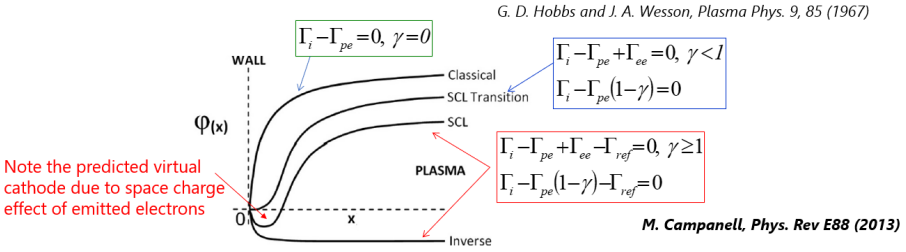

FIG. 1. Qualitative drawings of the potential relative to the wall in the classical (monotonic, Φ_f negative), SCL (nonmonotonic, Φ_f negative), and inverse (monotonic, Φ_f positive) sheath regimes.

As the temperature and associated electron emission rises the probe characteristic goes from the classical regime to the space-charge limited regime. Eventually the electron emission becomes so large that, in order to preserve quasineutrality in the plasma, a "virtual cathode" forms which turns emitted electrons back towards the wall.

The actual utility of a thermionic probe comes from comparing the cold probe (when the temperature is sufficiently low that $\gamma = 0$ and we have essentially just a Langmuir probe) V-I characteristic and hot probe (with significant Γ_{EE}). This lets us tease out the current collected by the probe (i.e. not counting the emitted current, which is negative) and the emitted current.

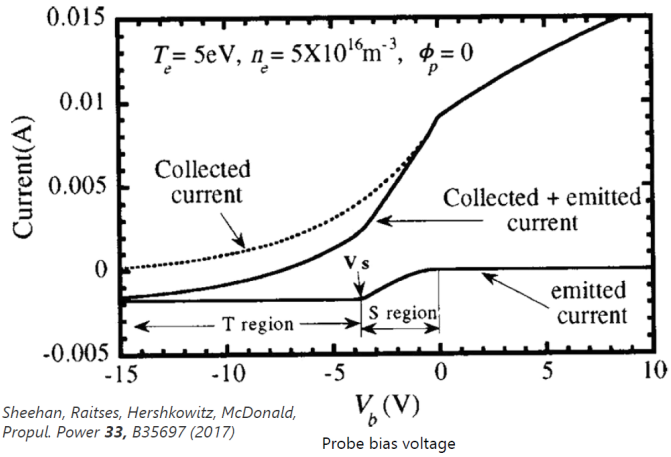

The plasma potential (defined as 0 in the above figure) can be clearly seen by the location where the collected current and total current meet. For once $V_b > V_{sp}$ the emitted current will stop flowing and, even with a hot filament, we are returned to the same plot as for the cold filament. This results in a much clearer measurement than is possible with a Langmuir probe.

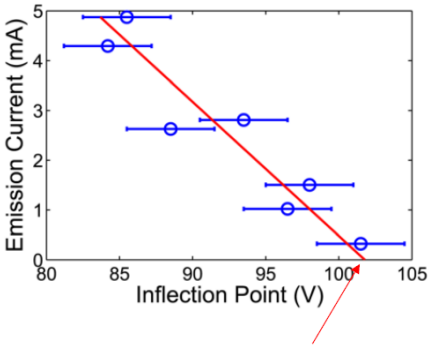

The basic structure of a floating probe is shown below. Note that the filament on the right itself has a potential drop across of around 4 V, so often an error of 2 V relative to the value at the middle is assumed.

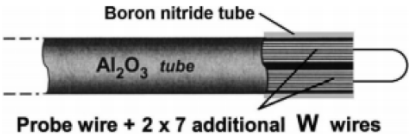

10.3 Summary

- When the sheath size grows much larger than the probe, classical Langmuir probe theory fails and the orbital motion limited regime (OML) is entered. In this regime it is possible to infer the density of the plasma.
- When there is a non-negligible magnetic field in a plasma, gyromotion and field line electron depletion need to be considered.
- Double probes are a variant of the standard Langmuir probe which are easier to build and use but assume Maxwellian temperatures
- Emissive probes use a heated filament to allow for easy measurement of the plasma potential and other properties.

10.4 Homework Problem Set 5

Due March 6, 2026

1. Consider a plasma with two populations of electrons: bulk plasma electrons with Maxwellian EEDF and beam electrons. Also consider a planar probe (or wall) immersed in this plasma. Plasma electrons, beam electrons and ions generate fluxes, Γ_{pe}, Γ_{eb}, and Γ_i, respectively, toward the probe wall.
2. Applying assumptions about plasma (e.g. $T_e \gg T_i$, collisionless sheath) and plasma-probe interactions which we used in derivation of this equation:

$$\phi_{wp} \approx -T_e \ln\left(\frac{1}{0.61}\sqrt{\frac{M}{2\pi m_e}}\right),$$

   find a floating potential of a planar wall immersed in this plasma with two populations of electrons.
3. Plot the dependence of the floating potential on Γ_i/Γ_{eb}.

11 Energy Distribution Function Measurements

While assuming a Maxwellian distribution for ions and electrons is greatly simplifying, low collisionality in many low-temperature plasmas means that such assumptions are not always warranted. In order to study non-Maxwellian distributions we need to either consider how to use probes without assuming Maxwellian distributions or consider new designs. The objective is to determine the electron energy distribution function (EEDF) or ion energy distribution function (IEDF). The former can be done with the same Langmuir probe as previously discussed while the latter needs a new kind of probe, the retarding potential analyzer.

11.1 1D EVDF and 1D EEDF

While we assumed a Maxwellian distribution to develop classical probe theory in previous sections, this is by no means necessary. In principle, the shape of the EEDF can be extracted from the V-I characteristic of a standard Langmuir probe. If our probe has a voltage V relative to the plasma potential ϕ_p, the total electron current registered at the probe in the planar 1D case is

$$I_e = eA_p \int_{v_{\min}}^{\infty} f_z(v_z) dv_z \tag{138}$$

where $f_z(v_z)$ is the velocity distribution function along the z-direction and $v_{\min}$ is the minimum required velocity to overcome the sheath $\phi_p - V_B > 0$ and reach the probe:

$$v_{\min} = \sqrt{\frac{2e}{m_e}(\phi_p - V_B)} \tag{139}$$

By taking the derivative with respect to voltage (not velocity) we can find the relationship between the 1D EEDF and the voltage derivative

$$\frac{dI_e}{dV_b} = eA_p \frac{d}{dV_B} \int_{v_{\min}}^{\infty} v_z f(v_z) \frac{dv_z}{dV_b} dV_b = -eA \left[v_z f(v_z) \frac{dv_z}{dV_b} \right]_{v_z = v_{\min}} \tag{140}$$

$$\frac{dI_e}{dV_b} = A \frac{e^2}{m_e} f_z(v_{\min}) \tag{141}$$

Thus in terms of particle energy $\varepsilon = \phi_p - V_B$ we may write

$$f_{1\mathrm{D}}(\varepsilon) = \frac{1}{eA_p} \left(\frac{2m_e}{e\varepsilon} \right)^{1/2} \frac{dI_e}{d\epsilon} \tag{142}$$

Thus we can find the 1D EEDF from the derivative of the V-I characteristic. From here we can calculate the electron density and temperature:

$$n_e = \int_0^\infty f_{1\mathrm{D}}(\varepsilon)d\varepsilon \tag{143}$$

$$T_{e,\mathrm{eff}} = \frac{2}{n_e}\int_0^\infty \varepsilon f_{1\mathrm{D}}(\varepsilon)d\varepsilon \tag{144}$$

11.2 Druyvesteyn Method

While working with the 1D distribution function simplified our calculations, often we wish to consider the ordinary 3D energy distribution functions $f(\mathbf{v})$ and $f(\varepsilon)$. The collected current in this case is simply

$$I_e = eA_p\int_{-\infty}^\infty dv_x\int_{-\infty}^\infty dv_y\int_{v_{\min}}^\infty v_z f(\mathbf{v})dv_z \tag{145}$$

While the math is more involved, it can be shown[4] that the energy distribution function $f(V_B)$ in this case can be expressed as

$$f(V_b) = \frac{2}{e^2A_p}\sqrt{2em_eV_b}\frac{d^2I_e}{dV_b^2} \tag{146}$$

Thus the 3D energy distribution function can be found with the *second* derivative instead of the first derivative. The density and temperature equations thus become

$$n_e = \int_0^\infty f(\varepsilon)d\varepsilon \tag{147}$$

$$T_{e,\mathrm{eff}} = \frac{2}{3n_e}\int_0^\infty \varepsilon f(\varepsilon)d\varepsilon \tag{148}$$

Sometimes in analysis the *electron energy probability function* (EEPF) is reported, defined as

$$P(\varepsilon) = \frac{f(\varepsilon)}{\sqrt{\varepsilon}} \tag{149}$$

The advantage of the EEPF is that a Maxwellian distribution appears as a straight line on a semilog plot.

[4]See M. J. Druyvesteyn's 1930 paper in Zeitschrift für Physik or Lieberman and Lichtenberg p.175

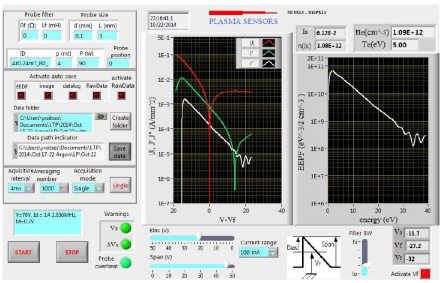

The primary difficulty with this method is that taking derivatives, especially second-derivatives, of noisy data is quite challenging numerically. Often the original data need to be smoothed first, but this can introduce its own sources of error.

11.3 Retarding Potential Analyzer

Since the ion current is dwarfed by the electron current in Langmuir probes, we will need a different type of diagnostic if we wish to measure the IEDF. The solution is a *retarding potential analyzer* or retarding field analyzer. This uses a series of biased grids to filter the incoming ions by energy: by sweeping the bias grid we will be able to infer how many ions at each energy level are present in the plasma.

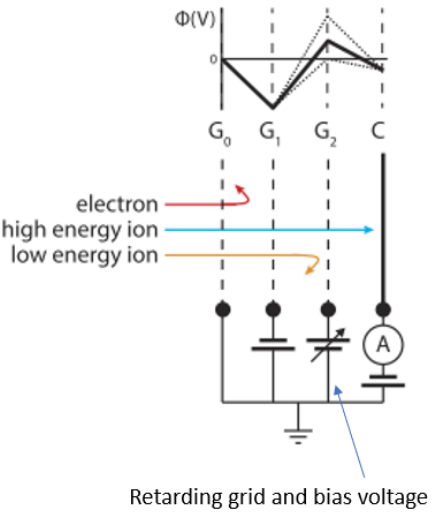

Three or sometimes four grids are used in total. Moving from the plasma to the collector the four grids are:

1. The first is either grounded or floating and serves to shield the plasma from the potential of the subsequent grids.
2. The next grid is biased negative to ensure that electrons are rejected and do not reach the collector.
3. The selector grid has its voltage swept to get measurements of the ion current as a function of energy.
4. The optional fourth grid is also biased negative in order to force electrons emitted by ion-induced secondary electron emission at the collector to return whence they came, lest they contribute to the total current reading.

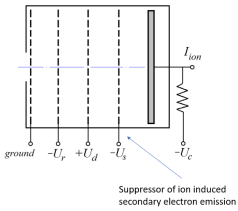

If V is the bias voltage and I is the current, one can straightforwardly show that

$$f(V) = \frac{1}{eA}\left(\frac{2M}{Ve}\right)^{1/2}\frac{dI_i}{dV} \tag{150}$$

The derivation is left as an exercise to the reader (see HW #5). Its interpretation is simple: if the current jumps sharply as V is increased at a specific value of V, then there must be many ions around that energy level. If there is little change then, conversely, there must be few. Note that only the mass-charge ratio factors in here, not either the mass or charge independently. While the working principle is rather simple, implementations need to consider the following parameters and complications

1. **Inter-grid distance**. To mitigate space-charge effects, the inter-grid distance should be no larger than the Langmuir sheath size.
2. **Grid transparency**. Since there are several grids, slight misalignment or opacity can greatly reduce the total ion flux measured by the collector.
3. **Grid mesh size**. If the grid mesh spacing is too large (i.e. there is too much space between the wires making up the grid) the potential will sag between the wires.
4. **Pressure buildup**. For continuously-running experiments, the buildup of neutrals inside the RPA can reduce the accuracy of measurements due to charge-exchange collisions. One can estimate via particle-balance roughly how much time one has before λ_{ia} falls to a value comparable to the length of the probe.

11.4 Summary

- The Druyvesteyn method may be used to infer the electron energy distribution function from an ordinary Langmuir probe
- A retarding potential analyzer uses a series of biased grids to filter incoming ions by energy and thereby infer the ion electron energy distribution function

11.5 Homework Problem Set 6

Bonus homework - not listed in the lecture notes.

12 Laser-Induced Fluorescence

Laser-induced fluorescence (LIF) works by using a laser to excite fluorescence in plasma atoms. By measuring the properties of the emitted photons, the plasma temperature and density may be inferred.

12.1 Physical Principles

Fluorescence is simply the process by which an atom absorbs a photon of a given energy and then spontaneously emits another lower-energy photon (or sometimes a photon of the same energy). In LIF the initial photon is supplied by an external laser which promotes electrons in the atoms to higher energy levels from either the ground state or a metastable state. The emission is caused by the photon moving to a lower energy level.

12.1.1 Atomic Transition Mechanisms

To get some basic physical intuition, let us consider a simple two-level model of possible electron states, 1 and 2, the latter at higher energy. There are several processes that can cause an electron to gain energy and be promoted from state 1 with energy E_1 to level 2 with energy E_2:

- *Photoabsorption* (induced excitation).
- *Collisional excitation*. This is negligible in such a two-level system.

There are even more processes whereby the electron loses energy and goes from 2 to 1:

- *Stimulated emission*
- *Fluorescence* (spontaneous emission)
- *Collisional de-excitation*

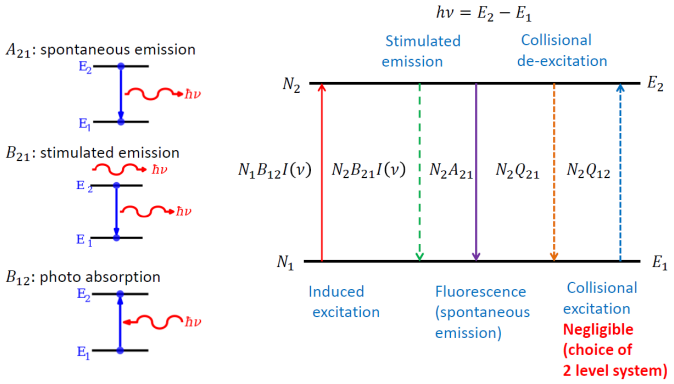

Fig. 85: Note that it should read $h\nu$ and not $\hbar\nu$ on the left.

12.1.2 Einstein Coefficient Relations

The interplay between all these effects can be analyzed by solving for steady-state conditions wherein there is no net change in particle number in either state. This principle is known as *detailed balance*. In the simplest case of a two-level system, the balance between spontaneous emission, stimulated emission and photoabsorption yields

$$A_{21}n_2 + B_{21}n_2\rho(\nu) - B_{12}n_1\rho(\nu) = 0 \tag{151}$$

Since the Einstein coefficients only depend on the internal quantum configuration of the atom, we are free to assume a blackbody form for $\rho(\nu)$ and use this to solve for A_{21}, B_{21} and B_{12}:

$$\rho(\nu) = F(\nu)\frac{1}{e^{h\nu/T} - 1}, \qquad F(\nu) = \frac{8\pi h\nu^3}{c^3} \tag{152}$$

From this one can show that the coefficients relate to one another as

$$\frac{A_{21}}{B_{21}} = F(\nu), \qquad \frac{B_{21}}{B_{12}} = \frac{g_1}{g_2} \tag{153}$$

where g_1 and g_2 are the level degeneracies.

12.1.3 Florescence Signal Regimes

Since fluorescence here represents the spontaneous 2 to 1 to transition, the total signal can be written as

$$S = \frac{\Omega}{4\pi}A_{12}N_2 \tag{154}$$

where Ω is the solid angle of the detector. In steady-state, the upward and downward transitions are equal in magnitude so

$$N_1B_{12}\rho_L = N_2(A_2 + Q_{21} + B_{21}\rho_L) \tag{155}$$

where ρ_L is the spectral energy density provided by the laser and Q represents collisional de-excitation.

Thus we find that

$$S = \frac{\Omega N_{\text{tot}}B_{12}\rho_L}{4\pi} \times \frac{A_{21}}{A_{21} + Q_{21} + (B_{21} + B_{12})\rho_L} \tag{156}$$

From this we can see that there are two regimes of laser intensity. If ρ_L is sufficiently low that spontaneous emission and collisional excitation dominate over stimulated emission/absorption, i.e. $(B_{21} + B_{12})\rho_L(\nu) \ll A_{21} + Q_{21}$,

$$S \approx \frac{\Omega N_{\text{tot}} B_{12} \rho_L}{4\pi} \times \frac{A_{21}}{A_{21} + Q_{21}} \tag{157}$$

Thus S varies linearly with laser intensity, the so-called *linear regime*. If, conversely, ρ_L is sufficiently high that stimulated emission/absorption dominate, i.e. $(B_{21} + B_{12})\rho_L(\nu) \gg A_{21} + Q_{21}$, then the signal becomes a constant independent of ρ_L:

$$S \approx \frac{\Omega N_{\text{tot}} A_{12}}{4\pi} \times \frac{B_{12}}{B_{21} + B_{12}} \tag{158}$$

This is known as the *saturation regime* and is best avoided. Working in the linear regime avoids possible photoionization and and allows for the critical Q_{21} frequency to be determined.

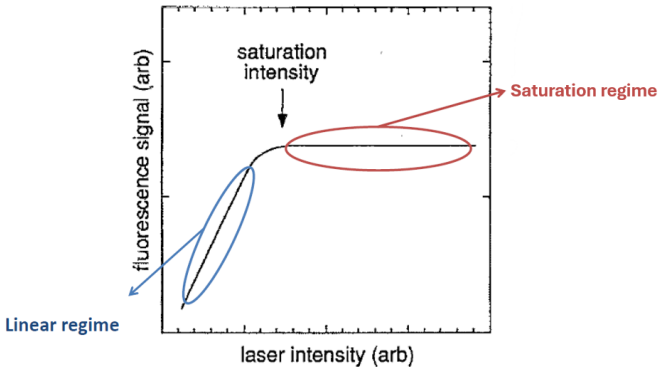

12.2 Temperature Measurements

The temperature can be measured by leveraging the Doppler effect, much like in Thomson scattering. Here the laser wavelength is swept. At zero temperature there would only be any fluorescence signal for the wavelength corresponding to the precise energy difference of the transition. At finite temperature, however, this broadens into a Gaussian shape.

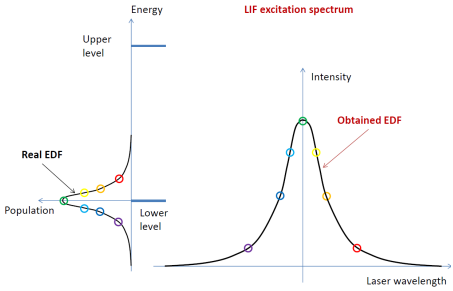

The broadness of this response is directly related to temperature as

$$\Delta\lambda_{\text{Doppler}} = \lambda_0 \sqrt{\frac{8T \ln 2}{mc^2}} \tag{159}$$

Thus the temperature can be inferred from the width of the resulting Gaussian.

12.3 Absolute Density Measurements

LIF can also be used to measure the absolute density, though this is more complex. Of course, the signal will only reflect the number density of the species at the excited level – relating this to the density of the species overall is non-trivial. Let us consider an example with Argon metastable states with fluorescence from level 2 to level 3. The LIF signal may be expressed as

$$S_{\text{LIF}} = \frac{1}{4\pi} \int \eta \frac{hc}{\lambda_{23}} n_{\text{exc}}(x, y, t) A_{23} \, dx \, dy \, dz \, dt \tag{160}$$

where $\eta = \Omega \varepsilon_{\text{fl}}$ where ε_{fl} is the detector efficiency at the fluorescence wavelength and n_{exc} is the density of the species at the excited level, λ_{23}. The red parameters are those which are unknown and must be determined. The instrumental factor η can be determined via comparison to Rayleigh scattering measurements and the excited state population can be determined from quantum models of the possible atomic transitions.

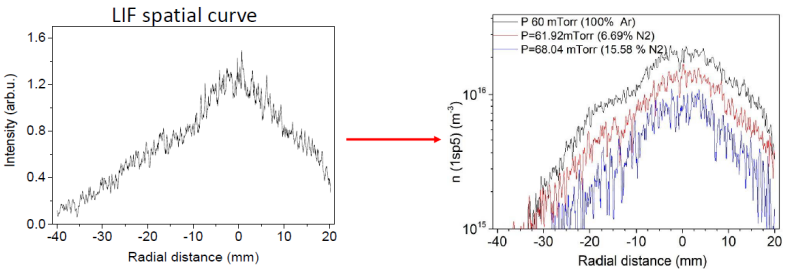

12.4 Variants

Planar LIF uses a sheet-like laser to get a 2D profile instead of a 1D one.

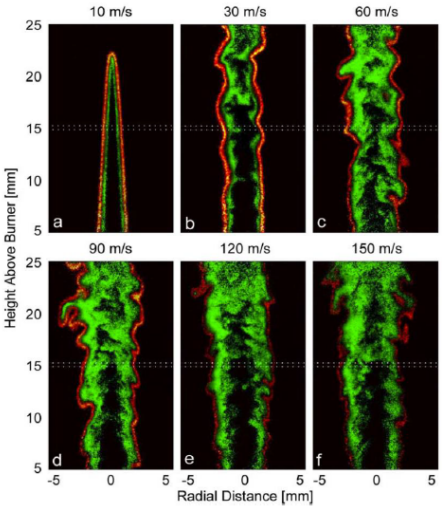

Fig. 86: From Li et al., ECM 2009, poster 259

Two-photon absorption laser induced fluorescence (TALIF) uses two photons to enable excitation to higher levels. This results in a squared dependence of S on laser intensity and some simpler absolute calibration at the price of more complex selection rule physics and greater sensitivity to the spatial and temporal properties of the laser.

12.5 Summary

- TALIF utilizes laser-induced fluorescence signals to infer spatially-resolved neutral temperature and density

13 Diagnostics Based on Refractive Index

By measuring the plasma refractive index, many other properties can be determined without physically inserting probes into the plasma. As long as the light waves do not have excessive power, perturbations to the plasma can be ignored. The light waves can be active sources such as lasers or passive sources such as background radiation.

Following the standard plasma wave theories (Stix, 1992; Hutchinson, 2002), we define

$$N \equiv \frac{kc}{\omega}; \quad X \equiv \frac{\omega_{pe}^2}{\omega^2}; \quad Y \equiv \frac{\omega_{ce}}{\omega},$$

where N is the refractive index. Light wave propagation parallel to the magnetic field in a uniform plasma can be described by

$$N^2 = 1 - \frac{X}{1 \pm Y} \tag{161}$$

whereas perpendicular propagation is described by

$$N^2 = 1 - X; \qquad \text{ordinary waves or O-waves} \tag{162}$$

$$N^2 = 1 - \frac{X(1-X)}{1 - X - Y^2}; \quad \text{extraordinary waves or X-waves.} \tag{163}$$

Therefore, N depends on the electron density (n_e) and magnetic field (B), and thus, measuring N can help us infer n_e and B. In this lecture, we introduce the following three diagnostics:

- Interferometer
- Reflectrometer
- Faraday rotation measurements.

As is standard, in this lecture we shall use the local WKB (Wentzel, Kramers, Brillouin) approximation appropriate for media which slowly vary in space and time. The WKB approximation is sometimes called the geometric optics approximation, enabling *ray tracing techniques* which provide the direction of wave propagation by solving $\boldsymbol{k}$ from the homogeneous dispersion relation using local plasma parameters for a given ω with wave fields expressed in the form of

$$e^{i\left(\int \boldsymbol{k}\cdot d\mathrm{l} - \omega \mathrm{t}\right)},$$

where $d\boldsymbol{l}$ is along the ray path. The homogeneity approximation assumes that the length scales of inhomogeneities are much longer than the wavelength. When such approximations do not apply, *full wave treatments* are required to solve partial differential equations under proper boundary and initial conditions. When the inhomogeneity is in only one direction and the wave energy is small enough to justify the linear approximation, the full wave treatments reduce to 1D eigenvalue problems, see Chap.4 of Hutchinson (2002) for more details.

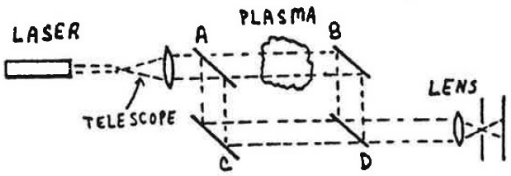

Fig. 87: Principle of Mach-Zehnder interferometer.

13.1 Interferometer

When plasma is unmagnetized ($Y = 0$) or $\omega \gg \omega_{ce}$ ($Y \ll 1$), we have $N^2 = 1 - X$ so N depends only on electron density, n_e. Even if the plasma is strongly magnetized, the O-waves in the perpendicular direction of magnetic field have the same dependence on electron density, $N^2 = 1 - X$. In these cases, therefore, electron density can be determined by measuring the refractive index, N. For a given ω, k is smaller than that in vacuum so that $N \equiv kc/\omega < 1$, or equivalently the phase is shifted for the same path length. Therefore, measuring N is equivalent to measuring the phase shift, ϕ, due to the presence of a plasma on the laser path, i.e.,

$$\phi = \int k\, dl = \int N \frac{\omega}{c} dl.$$

Interferometers are intended to measure the phase difference between two laser paths, one passing through the plasma and the other not. Figure 87 illustrates the principle of a representative type of interferometer, the Mach-Zehnder interferometer. The phase shift due to the plasma where $N < 1$ can be determined by comparing phases between the laser passing beamsplitter A and reflector B, and the laser passing reflector C and beamsplitter D,

$$\begin{aligned}\Delta\phi &= \int (k_{\text{plasam}} - k_{\text{ref}})\, dl = \int (N-1)\, \frac{\omega}{c} dl \\ &= \frac{\omega}{c} \int \left(\sqrt{1 - \frac{n_e}{n_c}} - 1 \right) dl \approx -\frac{\omega}{2cn_c} \int n_e dl = -r_e \lambda \int n_e dl, \quad (164)\end{aligned}$$

if $X \equiv n_e/n_c \ll 1$ or $n_e \ll n_c$. The critical density n_c for O-wave cutoff and the classical electron radius r_e are given respectively by

$$\begin{aligned} n_c &= \frac{\omega^2 m_e \epsilon_0}{e^2} \approx 1.1 \times 10^{27} \lambda_{\mu\text{m}}^{-2} \text{m}^{-3}, \\ r_e &= \frac{1}{4\pi\epsilon_0} \frac{e^2}{m_e c^2} \approx 2.8 \times 10^{-15} \text{m}. \end{aligned}$$

Note that $c = f\lambda = \omega\lambda/2\pi$. For a good approximation, $n_e < 0.1 n_c$ or $\omega > 10 \max(\omega_{\text{pe}})$ is sufficient. As a rough guide, Table 5 lists typical coherent

Table 5: Laser selection for plasmas with different density ranges.

n_e	λ	λ range
$< 2 \times 10^{19}\mathrm{m}^{-3}$	3 mm	mm waves
$< 2 \times 10^{21}\mathrm{m}^{-3}$	300 μm	far infrared
$< 1 \times 10^{26}\mathrm{m}^{-3}$	0.7μm	visible, HeNe laser

source selection options for plasmas with different electron densities. The basic tradeoff is as follows: while high-frequency, short-wavelength sources minimize beam diffraction and refraction, they are also more sensitive to mechanical vibrations than low-frequency, long-wavelength sources. See Chapter 4 of Hutchinson (2002) for more discussion.

Phase differences can be measured by interfering two images as shown in Fig. 87 where the light intensity forms constructive and destructive patterns or fringes on the detector plate. Because of its periodicity, however, special care is needed to determine phases beyond π. One technique is to introduce background interference fringes via a deliberate, small mis-alignment of the reference laser path. Any additional fringe shift due to plasma is superposed on the background which aids interpretation of the data by providing reference fringes outside of the plasma. An example is shown in Fig. 88. The phase shift can be roughly estimated by number of fringes inside the plasma minus number of fringes outside of the plasma.

This technique however does not apply to cases where simultaneous access to the outside of the plasma is difficult, such as tokamaks. In addition, the fringes are essentially based on Amplitude Modulation (AM) or homodyne reception which is sensitive to other effects such as absorption. Furthermore, for short-wavelength lasers such as CO_2 lasers whose wavelength is 10.6 μm, mechanical vibration on the order of 1 μm can cause significant phase shifts. In such cases, a temporal reference interference signal can be added by using

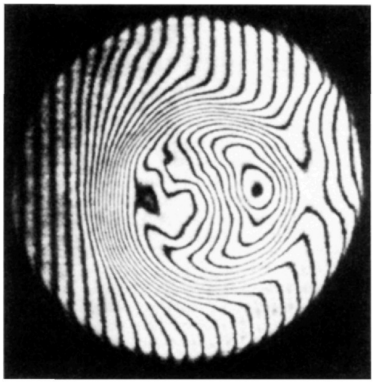

Fig. 88: Interferometric image of a theta-pinch plasma. From Hutchinson (2002).

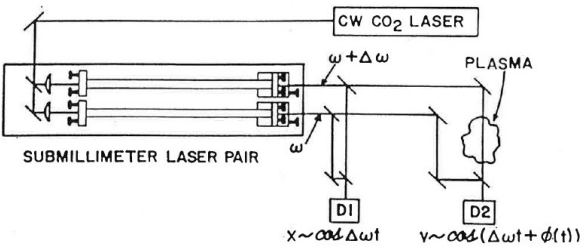

Fig. 89: Frequency-modulated heterodyne interferometer by Wolfe et al., from Hutchinson (2002)).

Frequency Modulation (FM) or heterodyne reception to the laser frequency. An example is shown in Fig. 89.

Another technique to reduce sensitivity due to mechanical vibrations is based on two-color interferometers, sometime also called dispersion interferometers or second-harmonic interferometer (Hopf et al, 1980). The idea is shown in Fig. 90 where frequency doubling crystals are used twice; one before passing the plasma and one after passing the plasma. The phase shifts are given by

$$\Delta\phi_1 = 2\left(\omega t + \frac{\omega\Delta d}{c} + r_e\lambda\int n_e dl\right)$$
$$\Delta\phi_2 = 2\omega t + \frac{2\omega\Delta d}{c} + r_e\frac{\lambda}{2}\int n_e dl,$$

respectively. Here Δd is the change in laser path distance due to vibrations. Therefore, the difference between these two phase shifts,

$$\Delta\phi_1 - \Delta\phi_2 = \frac{3}{2}r_e\lambda\int n_e dl, \tag{165}$$

depends only on the line-integrated density, immune to Δd. A simple implementation by Bretz et al (1997) as a homodyne system is shown in Fig. 90. The dispersion interferometers can be also implemented as a heterodyne system to be more robust against various imperfections (e.g. Akiyama et al, 2025).

Lastly, an inversion process, called *Abel Inversion*, is needed to determine the 1D profile $f(r)$ from multiple line-averaged measurements at different

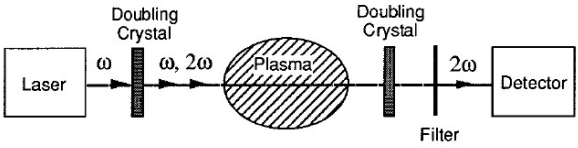

Fig. 90: Two-color interferometer using second harmonic dispersion interferometer by Bretz et al (1997).

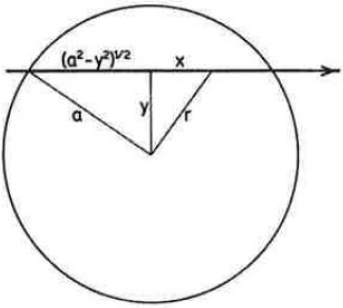

Fig. 91: Geometry for Abel Inversion. From Hutchinson (2002).

impact parameters y from $r = 0$, $F(y)$,

$$F(y) = \int_{-\sqrt{a^2-y^2}}^{+\sqrt{a^2-y^2}} f(r)dx = 2\int_y^a \frac{f(r)rdr}{\sqrt{r^2-y^2}}. \tag{166}$$

The latter equal sign is obtained by converting integration in x to r, see Fig. 91:

$$x^2 + y^2 = r^2; \quad 2x\,dx = 2r\,dr; \quad dx = \frac{r}{x}dr = \frac{r}{\sqrt{r^2-y^2}}dr.$$

Equation (166) can be inverted via the Abel transformation to yield

$$f(r) = -\frac{1}{\pi}\int_r^a \frac{dF}{dy}\frac{dy}{\sqrt{y^2-r^2}}, \tag{167}$$

assuming $f(a) = 0$. The inversion process can be also performed to determine 2D profiles but this requires additional constraints, see Chapter 5.3.8 of Hutchinson (2002).

13.2 Reflectometer

In the opposite limit to the prior case where $X \ll 1$, if conversely $X > 1$ or $n_e > n_c$, the incoming O-waves experience a cutoff and get reflected, traveling back along the same path. Detecting reflected waves as part of a *reflectometer* setup can provide valuable information about the electron density profile. The reflection occurs at $X = 1$ for O-waves when the plasma is unmagnetized or the propagation direction is perpendicular to the magnetic field. For X-waves, according to Eq. (163), reflection occurs at

$$X = 1 \pm Y,$$

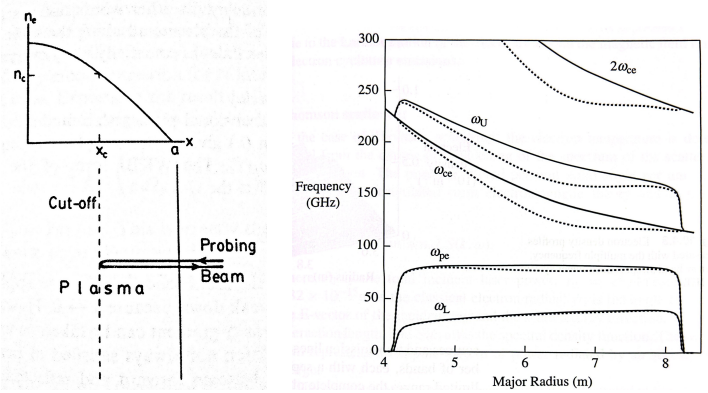

Fig. 92: (left) Geometry of a reflectometer, from Hutchinson (2002). Calculated positions of cutoff and absorption layers for an ITER plasma, from Wesson (2011). Dotted lines include relativistic corrections.

corresponding to the L-cutoff and R-cutoff, respectively. Figure 92 shows a typical reflectometer geometry and various cutoff ($\omega_{\rm pe}$, $\omega_{\rm L}$, $\omega_{\rm U}$, and absorption ($\omega_{\rm ce}$ and $2\omega_{\rm ce}$)) locations for an ITER plasma.

The phase difference between incoming waves and reflected waves at position a, often defined as the plasma edge location, contains information about refractive index N along the way as well as the reflection location x_c,

$$\phi = \frac{\omega}{c}\int_{x_c}^{a} N dl - \frac{\pi}{2},$$

where $\pi/2$ is due to reflection. At many frequencies, the reflection location can be determined as a function of frequency via Abel Inversion (Hutchinson, 2002; Wesson, 2011),

$$x_c(\omega) = a - \frac{c}{\pi}\int_0^{\omega} \frac{d\phi}{d\omega'}\frac{d\omega'}{\sqrt{\omega^2 - \omega'^2}}, \tag{168}$$

which is equivalent to obtaining the electron density profile. If the measurement is continuous in time, even temporal fluctuations of density profile can be deduced. Before this technique was applied to laboratory plasmas, the electron density profile was measured in Earth's ionosphere by radar reflection.

Recently a powerful Millimeter-wave Imaging Reflectometry (MIR) (Mazzucato, 2001) has been developed to measure the time evolution of 2D density fluctuations. MIR is an active, radar-like technique combining imaging principles with a probing beam of millimeter-wave radiation. The principles are shown in Fig. 93. First, the probing beam illuminates an extended region of the cutoff layer, where the curvature of the illuminating beam is matched to that of the cutoff surface (both toroidal and poloidal). Then, the cutoff layer is imaged onto a detector array at the image plane (3 example points shown),

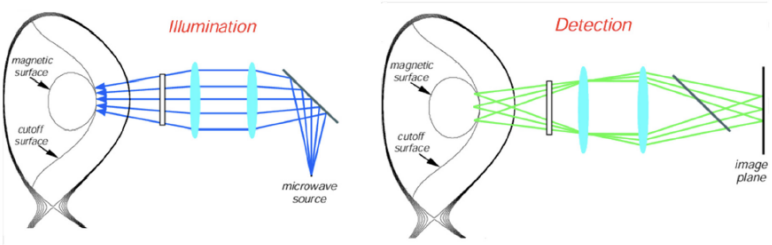

Fig. 93: Principles of Millimeter-wave Imaging Reflectometry (MIR) (Wang et al, 2017)

thereby eliminating the interference effects of multiple reflections. The illumination and detection systems share the common plasma-facing optics. Both O-waves and X-waves are used, and the latter sometimes is advantageous to avoid ω_{ce} absorption and to work around flat or slightly non-monotonic density profiles.

There is a more sensitive technique called Phase Contrast Interferometry (PCI) to measure small phase changes but will not be covered here. See Hutchinson (2002) and Wesson (2011) for more detailed discussion.

13.3 Magnetic Field Measurement via Faraday Rotation

So far we have been avoiding the magnetic field's involvement in the refractive index measurements in order to determine the electron density, but magnetic field information can also be obtained in properly arranged measurements, as N depends on both X for ω_{pe} and Y for ω_{ce},

$$N_{\pm}^2 \approx 1 - X \pm XY\cos\theta, \tag{169}$$

where the $\pm$ sign corresponds O-waves and X-waves, respectively.

Now consider two circularly polarized waves propagating in the z direction,

$$\frac{E_x}{E_y} = \pm i,$$

and having different refraction indices, $N_{\pm}$. Then any waves with an arbitrary polarization, including linearly polarized waves, can be regarded as a superposition of these two circularly polarized waves. For example, a linearly polarized wave at $z = 0$ having only E_x can be decomposed to

$$\boldsymbol{E}(z=0) = E(1,0) = \frac{E}{2}\left[(1,i) + (1,-i)\right].$$

At $z > 0$ then this decomposition becomes,

$$\begin{aligned}\boldsymbol{E} &= \frac{E}{2}\left[(1,i)\exp\left(iN_+\frac{\omega}{c}z\right)+(1,-i)\exp\left(iN_-\frac{\omega}{c}z\right)\right]\\ &= E\exp\left(i\frac{N_+ + N_-}{2}\frac{\omega}{c}z\right)\left(\cos\frac{\Delta\phi}{2}, i\sin\frac{\Delta\phi}{2}\right),\end{aligned} \tag{170}$$

where the wave is still linearly polarized but the polarization is rotated by an angle,

$$\alpha = \frac{\Delta\phi}{2} \equiv \frac{N_+ - N_-}{2}\frac{\omega}{c}z, \tag{171}$$

which is called *Faraday rotation*. Using Eq. (169) and assuming $1 - X \gg XY\cos\theta$, α can be calculated as

$$\begin{aligned}\alpha &= \frac{1}{2}\sqrt{1-X}\left(\sqrt{1+\frac{XY\cos\theta}{1-X}}-\sqrt{1-\frac{XY\cos\theta}{1-X}}\right)\frac{\omega}{c}z\\ &= \frac{1}{2}\sqrt{1-X}\left[\left(1+\frac{1}{2}\frac{XY\cos\theta}{1-X}\right)-\left(1-\frac{1}{2}\frac{XY\cos\theta}{1-X}\right)\right]\frac{\omega}{c}z\\ &= \frac{1}{2}\frac{XY\cos\theta}{\sqrt{1-X}}\frac{\omega}{c}z\\ &\approx \frac{\omega_{\rm pe}^2\omega_{\rm ce}\cos\theta}{2\omega^2 c}z\end{aligned}$$

where we take $X \ll 1$ in the the last line. Here $\omega_{\rm ce}\cos\theta$ can be expressed as $\boldsymbol{\omega}_{\rm ce}\cdot\boldsymbol{dl}/dl = (e/m_e)\boldsymbol{B}\cdot\boldsymbol{k}/k$, which is proportional to the magnetic field component in the $\boldsymbol{k}$ direction. If the plasma or magnetic field is nonuniform, the line-integrated Faraday rotation is given by

$$\alpha \approx \int \frac{\omega_{\rm pe}^2}{2\omega^2 c}\boldsymbol{\omega}_{\rm ce}\cdot\boldsymbol{dl} = r_e\lambda\int n_e\frac{\boldsymbol{\omega}_{\rm ce}}{\omega}\cdot\boldsymbol{dl} = \frac{e}{2m_e c}\int\frac{n_e}{n_c}\boldsymbol{B}\cdot\boldsymbol{dl}. \tag{172}$$

Note that the line-integrated Faraday rotation is density-weighted, and thus, the density profile is needed to deconvolve the magnetic field profile. Therefore, the challenge is to perform the inversion twice: first to use the phase shift to obtain the density profile and then to use the polarization rotation to obtain the magnetic field profile. As a result, Faraday rotation is always measured together with interferometry to simultaneously obtain electron density. Figure 94 shows a heterodyne scheme based on polarization modulation: two beams at slightly different frequencies, both going through plasma. The density is simultaneously measured by adding a reference beam not going through the plasma. Due to the small rotation angle, Faraday rotation measurement is generally difficult in the laboratory but some success has been reported.

Faraday rotation measurements have been more successful in astronomy. When radio waves from a distant source pass through a galaxy before being measured by a radio telescope (or an array of them via aperture synthesis (see

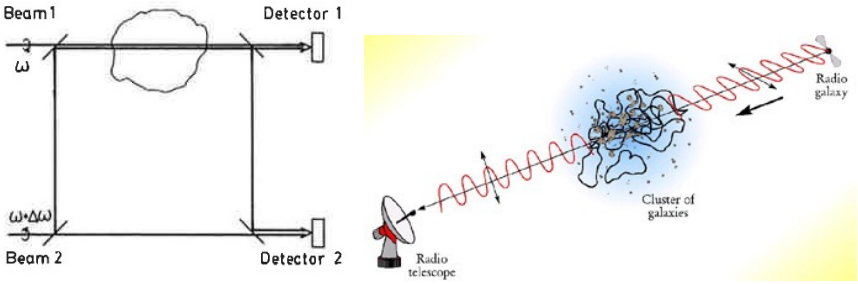

Fig. 94: (left) A heterodyne scheme for simultaneous Faraday rotation and interferometry. From Hutchinson (2002). (right) Faraday rotation measurements in radio astronomy.

Lecture 4)), the polarization angle can be determined since it is proportional to the wavelength squared,

$$\mathrm{RM} = 0.81 \left(\frac{L}{1\mathrm{pc}}\right) \left(\frac{n_e}{1\mathrm{cm}^{-3}}\right) \left(\frac{B_\parallel}{1\mu\mathrm{G}}\right) \left(\frac{\lambda}{1\mathrm{m}}\right)^2 \mathrm{rad}, \tag{173}$$

where RM stands for Rotation Measure. Here 1 parsec (pc) = 3.26156 light year = 0.20626×10^6 Astronomical Unit (AU; Sun-Earth distance)=3.0867×10^{16} m. Since the group velocity of light waves is reduced due to the presence of the plasma,

$$V_g \equiv \frac{\partial\omega}{\partial k} = c\sqrt{1-\frac{\omega_{\mathrm{pe}}^2}{\omega^2}} \approx c\left(1-\frac{\omega_{\mathrm{pe}}^2}{2\omega^2}\right), \tag{174}$$

waves with different frequencies arrive with a delay which is also proportional to the wavelength squared,

$$\mathrm{DM} \equiv \int n_e\, ds = 0.05 \left(\frac{L}{1\mathrm{pc}}\right) \left(\frac{n_e}{1\mathrm{cm}^{-3}}\right) \left(\frac{B_\parallel}{1\mu\mathrm{G}}\right) \left(\frac{\lambda}{1\mathrm{m}}\right)^2 \mathrm{sec}, \tag{175}$$

where DM stands for Dispersion Measure. From measurements of DM and RM, the electron density and parallel magnetic field can be determined with some accuracy.

In reality, the RM measurements are much more complicated than simple formula shown above due to many factors including multiple sources along the line of sight and diffusive nature of magnetic field in astrophysical objects. Analyzing the RM data sometime is called "Faraday-complex" as it requires careful considerations of these factors while the DM data are often quite straightforward. One nice example is shown in Fig. 95 for the first Fast Radio Burst reported in 2007.

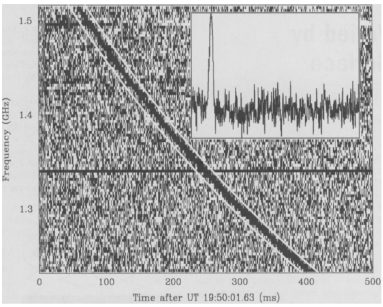

Fig. 95: Measurement of Dispersion Measure for the first Fast Radio Burst (FRB) (Lorimer et al, 2007).

13.4 Summary

- The refractive index of O-waves and X-waves contains valuable information about the electron density through the phase shift and about the magnetic field through the polarization angle.
- Interferometers measure phase shift due to reduction of refractive index in the plasma by using coherent sources at sufficiently high frequencies to avoid cutoff.
- Interferometric fringe patterns provide a snapshot measurement of 2D line-averaged density profile with reference fringes from the vacuum region. The heterodyne scheme based on frequency modulation provides temporal measurement of line-averaged density. Abel inversion of the line-averaged data is needed to determine the 1D density profile.
- Reflectometers measure the phase difference between incoming and reflected waves at frequencies below cutoff. Density profiles can be determined via Abel inversion of frequency-dependent measurement of phase differences. Millimeter-wave Imaging Reflectometry (MIR) is a powerful diagnostic to measure local density fluctuations.
- The Faraday rotation of polarization angle can be measured by a frequency-modulated heterodyne scheme but requires the simultaneous determination of electron density.
- Both the electron density and the magnetic field can be determined in radio astronomy by measuring the Dispersion Measure (DM) and the Rotation Measure (RM).

13.5 Further Reading

- Chapter 4 of Hutchinson (2002)

13.6 Homework Problem Set 7

Due March 27, 2026

1. Consider an interferometer at wavelength, $\lambda = 10.6\ \mu$m (CO_2 laser) which operates in the presence of spurious vibrations of the optical components. To compensate for these vibrations, interferometry is performed simultaneously using the same optical components at a wavelength of $\lambda = 0.633\mu$m (HeNe laser). The HeNe interferometer is affected much less than the CO_2 interferometer by the plasma phase shift, but still somewhat. If $\omega \gg \omega_{\rm pe}$ for both wavelengths:

   - Derive an expression for the plasma line integrated density, $\int n_e dl$, in terms of the phase shifts, ϕ_c and ϕ_h, of the two interferometers.
   - If ϕ_H can be measured with an accuracy of $\pm\pi$, what uncertainty does this introduce into the plasma density measurement?
   - Evaluate the fractional error in measuring a 1 m thick plasma of density 10^{20} m^{-3}, assuming ϕ_c is measured exactly.

2. In some plasmas, one cannot guarantee doing interferometry with the ordinary mode. It is of interest to calculate the error occurring in the deduced density if we use the expression for the ordinary mode index of refraction when really the mode is the extraordinary mode. Consider perpendicular propagation and calculate an approximation for the difference in refractive index between the ordinary and extraordinary wave for $\omega \gg \omega_{\rm pe}$. Hence, calculate the fractional error in using the above expression to determine the density if the extraordinary mode is used in a plasma with density $n_e = 10^{20}$ m^{-3}, $B = 6$ T, and $f = 10^{12}$ Hz.

3. Conceptually design an interferometer using frequency doubling crystals (Bretz et al, 1997) between two satellites flying together in Earth's magnetosphere. Assume electron density is $1 - 100$ cm^{-3}. Provide information on possible laser frequency and the distance between satellites.

14 Cyclotron, Synchrotron, and Bremsstrahlung Radiation

Photons are effective messengers carrying important information about the plasma and are often a primary target for plasma diagnostics. In the previous lecture, we have discussed cases where photons from an external source travel through the plasma and can carry valuable information such as electron density and magnetic field. Other times, however, photons can be emitted from charged or neutral particles within the plasma, transport through the plasma, and perhaps get re-absorbed. Some of them escape from the plasma and can reach detectors, also carrying valuable information. This lecture begins with a discussion on plasma emissivity, absorption and an introduction to optical depth.

14.1 Photon Transport in Plasma and Blackbody Radiation

First consider a simple case where radiation intensity decreases along a ray path from $I_\omega(0)$ at $s = 0$ to $I_\omega(s)$ at $s = s_{\rm det}$ due to absorption (Fig. 96), following the transport equation,

$$\frac{dI_\omega(s)}{ds} = -\alpha_\omega(s) I_\omega(s). \tag{176}$$

Here $I_\omega(s)$ is the radiation intensity at s in units of radiative power per unit area per unit solid angle per unit frequency while $\alpha_\omega(s)$ is the absorption coefficient at s in units of inverse length. Integrating this equation along the ray path from $s = 0$ to $s = s_{\rm det}$ yields

$$[\ln I_\omega(s)]_0^{s_{\rm det}} = -\int_0^{s_{\rm det}} \alpha_\omega ds \equiv -\tau, \quad \text{or} \quad I_\omega(s_{\rm det}) = e^{-\tau} I_\omega(0) \tag{177}$$

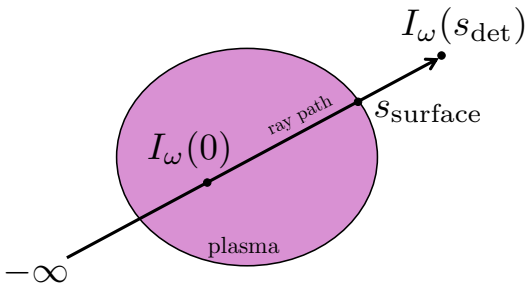

Fig. 96: Photon transport along the ray path in a plasma.

where τ is a dimensionless parameter called *optical depth*. When $\tau \ll 1$, the plasma is said to be *optically thin* so that radiation intensity at the detector $I_\omega(s_{\rm det}) \approx I_\omega(0)$ with negligible attenuation. When $\tau \gg 1$, the plasma is said to be *optically thick* so that $I_\omega(s_{\rm det}) \approx 0$ with negligible radiation power reaching the detector.

Next consider another simple case where the emissivity $j_\omega(s)$ is finite along the ray path, having units of radiation power per unit area per solid angle per unit frequency per length. There is no radiation absorption. The transport equation is given in this case by

$$\frac{dI_\omega(s)}{ds} = j_\omega(s), \tag{178}$$

which is integrated from $s = -\infty$ to the detector to yield the radiation intensity at the detector,

$$I_\omega(s_{\rm det}) = \int_{-\infty}^{s_{\rm det}} j_\omega(s) ds. \tag{179}$$

Now consider a combined case where both j_ω and α_ω are non-negligible but their ratio, j_ω/α_ω, is constant in space. The corresponding transport equation is given by

$$\frac{dI_\omega}{ds} = j_\omega - \alpha_\omega I_\omega, \tag{180}$$

which can be integrated from $s = 0$ to $s_{\rm det}$ as in the following. First rewriting this equation to

$$\frac{dI_\omega}{I_\omega - \frac{j_\omega}{\alpha_\omega}} = -\alpha_\omega ds \tag{181}$$

and then integrating it as

$$\left[\ln\left|I_\omega(s) - \frac{j_\omega}{\alpha_\omega}\right|\right]_0^{s_{\rm det}} = -\int_0^{s_{\rm det}} \alpha_\omega ds = -\tau \tag{182}$$

yields the solution

$$I_\omega(s_{\rm det}) = e^{-\tau} I_\omega(0) + \frac{j_\omega}{\alpha_\omega}\left(1 - e^{-\tau}\right). \tag{183}$$

In the optically thin limit of $\tau \to 0$, the solution of Eq. (179) is recovered with the integration starting point of $s = 0$ replaced by $s = -\infty$. In other words, the radiation originated between $s = -\infty$ and $s = s_{\rm det}$ along the ray path all arrive at the detector without loss, as expected.

In the opposite optically thick limit of $\tau \to \infty$ or practically $\tau \geq 2$,

$$I_\omega(s_{\rm det}) = I_\omega(s_{\rm surface}) = \frac{j_\omega}{\alpha_\omega}, \tag{184}$$

where $s_{\rm surface}$ is the point on the ray path intercepting the plasma surface, see Fig. 96. For plasmas in thermodynamic equilibrium, the surface radiation

can be treated as "blackbody" per Kirchoff's law of thermal radiation (1868), $B(\omega)$,

$$\frac{j_\omega}{\alpha_\omega} = B(\omega) = \frac{\omega^2}{4\pi c^2}\frac{\hbar\omega}{e^{\hbar\omega/kT}-1} \approx \frac{\omega^2 kT}{4\pi c^2} \tag{185}$$

where the second equal sign is Planck's radiation formula for photons obeying Bose-Einstein statistics (1904), and the following approximation is due to Rayleigh-Jeans approximation in the classical limit of $\hbar\omega \ll kT$. Therefore, by measuring radiation power's frequency dependence, the plasma surface temperature can be determined, independent of density. This is the basic principle behind of the determination of electron temperature using cyclotron emission measurements.

The dielectric nature of the plasma can be taken into account by using plasma dispersion relations based on the WKB approximation when inhomogeneity scales are much longer than the wavelength. For a given frequency, the complex wavenumber, k, is calculated for each mode (O- and X-mode) based on the dispersion relation, with contributions from each harmonic. The radiation power in dielectric plasmas is given by

$$I_\omega(s_{\rm det}) \approx \frac{\omega^2 kT}{4\pi c^2}\left(1-e^{-\tau}\right); \quad \tau = -\int_{-\infty}^{s_{\rm det}} 2\Im(k)\, ds. \tag{186}$$

Five specific cases for cyclotron emission (see below) are discussed in detail in Chapter 5.2.5 of Hutchinson (2002).

14.2 Radiation by Accelerated Charges

Electromagnetic fields can be generated by electric charges and their movement, *i.e.* current, both of which are abundant in plasmas. A typical way to calculate such fields is to use the vector potential, $\boldsymbol{A}$, and the scalar potential, ϕ, under the Lorentz gauge $\boldsymbol{\nabla}\cdot\boldsymbol{A} + (1/c)\partial\phi/\partial t = 0$ where

$$\boldsymbol{E} = -\frac{\partial \boldsymbol{A}}{\partial t} - \boldsymbol{\nabla}\phi; \quad \boldsymbol{B} = \boldsymbol{\nabla}\times\boldsymbol{A}.$$

For a point charge of q at position $\boldsymbol{r}(t)$ with velocity $\boldsymbol{v}(t)$ in free space, *i.e.* with no plasma dielectric effects, the resultant *Lienard-Wiechert potentials* (1898-1901) are given by

$$\phi = \frac{q}{4\pi\epsilon_0}\left[\frac{1}{\kappa R}\right]; \quad \boldsymbol{A} = \frac{\mu_0 q}{4\pi}\left[\frac{\boldsymbol{v}}{\kappa R}\right], \tag{187}$$

where $\boldsymbol{R} \equiv \boldsymbol{r} - \boldsymbol{r}'$ is the vector from the charge to the field point. The square brackets indicate that a quantity is to be evaluated at the retarded time, $t' = t - |\boldsymbol{R}|/c$. Defining $\hat{\boldsymbol{R}} \equiv \boldsymbol{R}/R$, $\boldsymbol{\beta} \equiv \boldsymbol{v}/c$, and $\kappa \equiv 1 - \hat{\boldsymbol{R}}\cdot\boldsymbol{\beta}$, the far-field electric field, which decays only $\propto 1/R$ (as opposed $1/R^2$ in near field)

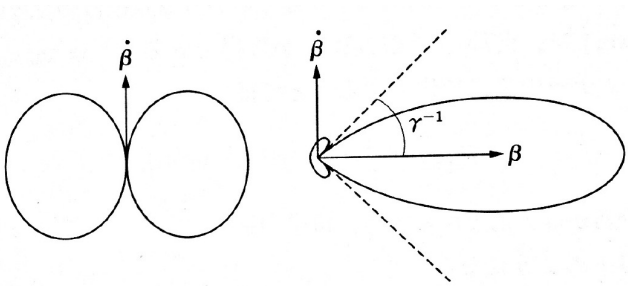

Fig. 97: (left) Dipole radiation pattern from an accelerated charge in the non-relativistic limit; (right) Strongly enhanced radiation from a relativistic electron towards its moving direction. In this case $\beta = 0.7$ and enhancement is within an angle $\sim 1/\gamma(\text{rad}) \sim 45°$. From Miyama et al (2008).

contributing to radiation, is given by

$$\boldsymbol{E}_{\rm far} = \frac{q}{4\pi\epsilon_0}\frac{1}{c\kappa^3 R}\left[\hat{\boldsymbol{R}} \times \left(\hat{\boldsymbol{R}} - \boldsymbol{\beta}\right) \times \dot{\boldsymbol{\beta}}\right]. \tag{188}$$

Since $\boldsymbol{B}_{\rm far} = \left[\hat{\boldsymbol{R}}\right] \times \boldsymbol{E}_{\rm far}/\mu_0 c$, the radiation power per unit area is given by Poynting vector,

$$\boldsymbol{S} \equiv \boldsymbol{E}_{\rm far} \times \boldsymbol{B}_{\rm far} = \frac{1}{\mu_0 c}\left|\boldsymbol{E}_{\rm far}\right|^2 \hat{\boldsymbol{R}} \propto \frac{1}{R^2}, \tag{189}$$

which is constant after integrated over the spherical surface with a radius of R from the radiating charge. This constant is the total radiation power, $P_{\rm total}$. In the non-relativistic limit, the radiation exhibits a dipole pattern shown in Fig. 97 (left),

$$\boldsymbol{S} = \frac{q^2}{16\pi^2\epsilon_0 c}\frac{\sin^2\theta}{R^2}\dot{\beta}^2, \tag{190}$$

which can be integrated over the spherical surface to yield the *Larmor formula* (1897) for the total radiation power,

$$P_{\rm total} = \frac{q^2}{6\pi\epsilon_0 c}\dot{\beta}^2. \tag{191}$$

With this fundamental knowledge on radiation from accelerated charged particles in hand, we can discuss three kinds of radiation emitted from plasma:

- Cyclotron or gyro-radiation: radiation from magnetized charged thermal particles. Synchrotron radiation is a version of it but from relativistic electrons and is also covered in this Lecture.
- Bremsstrahlung radiation: radiation from electrons due to the Coulomb electric field of an ion. This kind of radiation is covered in the next Lecture.

- Cherenkov radiation: radiation from background electrons accelerated by passing-through energetic electrons. The concept has been discussed in Lecture 3 and more discussion can be found in Chap. 5.2.9 of Hutchinson (2002) on possible uses for the measurement of relativistic electrons.

14.3 Cyclotron Radiation

Here we just need to calculate radiation power using Eq. (188) and Eq. (189) from electrons' cyclotron motion in the $(\boldsymbol{x}, \boldsymbol{y})$ plane in a given magnetic field, B in the $\boldsymbol{z}$ direction. The frequency spectrum can be obtained by a Fourier transformation. A summary is given here while the details are provided in Chapter 5.2 of Hutchinson (2002).

Using the cyclotron frequency, ω_c, defined by

$$\omega_c = \frac{eB}{m_e\gamma} = \frac{\Omega}{\gamma}; \quad \gamma \equiv \frac{1}{\sqrt{1-\beta^2}}, \tag{192}$$

an electron's position and velocity can be written as

$$\begin{aligned} \frac{\mathrm{r}}{c} &= \frac{\beta_\perp}{\omega_c}\left(\boldsymbol{x}\sin\omega_c t - \boldsymbol{y}\cos\omega_c t\right) + \beta_\parallel t\boldsymbol{z} \\ \boldsymbol{\beta} &= \beta_\perp\left(\boldsymbol{x}\cos\omega_c t + \boldsymbol{y}\sin\omega_c t\right) + \beta_\parallel \boldsymbol{z}. \end{aligned}$$

The resultant radiation power spectrum per angular frequency (ω) and per solid angle (Ω_s) from an observer is given by the *Schott-Trubnikov formula*

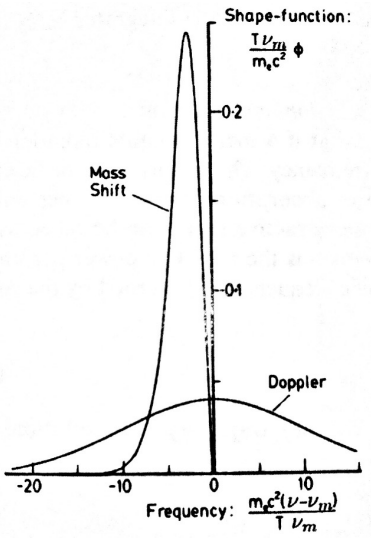

Fig. 98: Spectral shape of cyclotron emission for oblique and perpendicular propagation, giving Doppler- and mass-shift-broadened shapes, respectively. From Hutchinson (2002).

(1912, 1958), see Chapter 5.2.1 of Hutchinson (2002),

$$\frac{d^2P}{d\omega d\Omega_s} = \frac{e^2\omega^2}{8\pi^2\epsilon_0 c}\sum_{m=1}^{\infty}\left[\left(\frac{\cos\theta+\beta_\parallel}{\sin\theta}\right)^2 J_m^2(\xi)+\beta_\perp^2 J_m'^2(\xi)\right] \frac{\delta\left[\left(1-\beta_\parallel\cos\theta\right)\omega - m\omega_c\right]}{1-\beta_\parallel\cos\theta} \tag{193}$$

where $\xi \equiv (\omega/\omega_c)\beta_\perp \sin\theta = k_\perp \rho_e$ since $k_\perp = k\sin\theta = (\omega/c)\sin\theta$. θ is the angle between the radiation ray path and magnetic field. Here are a few important features to notice from Eq. (193):

- The cyclotron radiation spectrum consists of discrete peaks at harmonics, m,

$$\omega_m = \frac{m\omega_c}{1-\beta_\parallel\cos\theta} = \frac{m\Omega}{1-\beta_\parallel\cos\theta}\sqrt{1-\beta^2} \tag{194}$$

  as expected from the periodicity of the electron motion. When this is applied to a distribution of electrons with different velocities, however, each peak is broadened by two effects:

  1. Broadening due to relativistic mass increase by $\sqrt{1-\beta^2}$.
  2. Broadening due to Doppler effects by $(1-\beta_\parallel\cos\theta)^{-1}$.

  The relative importance of these two broadening effects is decided by the observing angle from the magnetic field. For small angle θ (closer to the parallel direction) such that $\beta_\parallel\cos\theta > \beta^2$, Doppler broadening dominates. Otherwise, the relativistic mass increase dominates for larger angles θ (closer to perpendicular). There are two additional broadening effects which are not captured by Eq. (193) but are sometimes important to include:

  3. Natural or radiation broadening due to electron energy loss by radiation itself, and
  4. Collisional broadening due to broken cyclotron orbits interrupted by collisions.

- The spectrum is Doppler shifted by $(1-\beta_\parallel\cos\theta)^{-1}$ due to parallel motion along the magnetic field relative to the observer.

Now we are ready to calculate the plasma emissivity due to cyclotron radiation. Note that the Doppler effect due to the observer should be removed by multiplying $1-\beta_\parallel\cos\theta$ to Eq. (193) before integrating over electron distribution functions, see the discussion in Chapter 5.2.1 of Hutchinson (2002). The results are shown in Fig. 98 where the two cases are plotted.

When the observing angle is sufficiently oblique, or $\cos\theta \gg \beta$, Doppler broadening dominates, leading to a Gaussian line shape for the Maxwellian

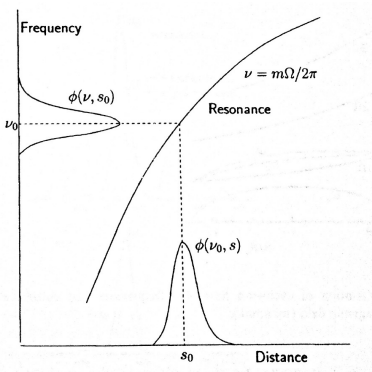

Fig. 99: Frequency maps to location in a spatially varying magnetic field, giving localized measurements of T_e by frequency-resolved spectra. From Hutchinson (2002).

electron distribution of a temperature of T_e with this Gaussian functional form:

$$\exp\left[-\frac{m_e c^2}{2T_e}\left(\frac{\omega-\omega_m}{\omega_m\cos\theta}\right)^2\right].$$

When the observing angle is sufficiently perpendicular, or $\cos\theta \leq \beta$, the relativistic mass shift (or mass increase) broadening dominates, leading to frequency downshift for the Maxwellian electron distribution of a temperature of T_e with this functional form:

$$\exp\left[-\frac{m_e c^2}{2T_e}\left(1-\left(\frac{\omega}{\omega\Omega}\right)^2\right)\right].$$

In either case, T_e can be uniquely determined from the spectral shape.

14.4 Electron Temperature Measurement in Tokamaks

The above calculations in free space show the promise of measuring electron temperature by measuring cyclotron emission spectra. However, applying to thermal plasmas requires taking into account the dielectric nature of the plasma as discussed in Chap. 14.1, via Eq. (186). In the case of gradually varying magnetic field in space as in tokamaks, resonant frequency maps to space if the magnetic strength profile is known for a given harmonic, see Fig. 99. The radiation strength at each frequency maps to local electron temperature if the optical depth is known and there is no incident reflection from outside,

$$I(\omega_0) = \frac{\omega_0^2 kT(s_0)}{4\pi c^2}\left(1-e^{-\tau_m}\right), \tag{195}$$

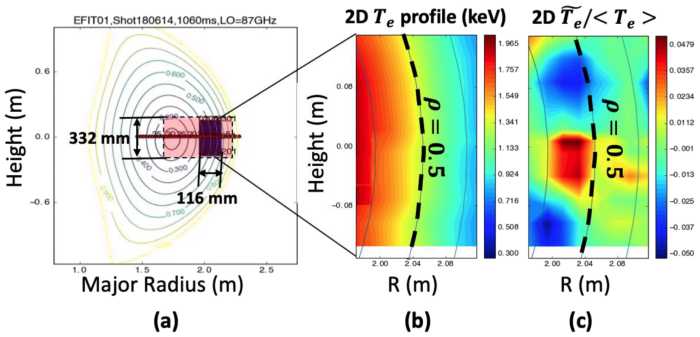

Fig. 100: ECEI results of T_e profiles in 2D including its fluctuations. From Zhu et al (2020).

where ω_0 is the angular cyclotron frequency at s_0. For each harmonic of cyclotron emission and absorption, the optical depth is also different at each resonance, and is given by (Hutchinson, 2002)

$$\tau_m = \frac{L\alpha_m(s_0)}{m\Omega}; \qquad L \equiv \frac{\Omega}{|d\Omega/ds|}. \tag{196}$$

This forms the basis of the successful Electron Cyclotron Emission (ECE) diagnostic for T_e and its fluctuations, currently widely used in tokamaks. Full theoretical and experimental details are reviewed by Bornatici et al (1983) and Park et al (2003), respectively. Due to interference with other plasma waves, second harmonic X-mode waves, which are optically thick, are typically used (Park et al, 2003). Figure 100 shows modern ECE Imaging results with T_e fluctuations successfully measured. One caveat of ECE diagnostics is that signals can be significantly modified by the presence of non-thermal electrons which are often in the relativistic regime. This is our topic in the next section.

14.5 Synchrotron Radiation

Cyclotron radiation in astrophysical plasmas occurs in very low frequencies due to their weak magnetic fields. At a typical field of 1μG, f_{ce}=2.4 Hz which is difficult to detect. However, relativistic effects of high-energy electrons boost its radiation power drastically as shall be seen below, and in such cases, the radiation is called synchrotron radiation.

Lets take Eq. (188) for $\boldsymbol{E}_{\rm far}$ to the relativistic limit: $\gamma \equiv (1-\beta^2)^{-1/2} \to \infty$ so that $\beta = (1-\gamma^{-2})^{1/2} \approx 1-(1/2)\gamma^{-2}$. When the angle between $\boldsymbol{R}$ and $\boldsymbol{\beta}$, θ, is small, $\cos\theta \approx 1-(1/2)\theta^2$. Thus,

$$\kappa \equiv 1 - \hat{\boldsymbol{R}}\cdot\boldsymbol{\beta} = 1-\beta\cos\theta \approx \frac{1}{2}\left(\theta^2 + \frac{1}{\gamma^2}\right). \tag{197}$$

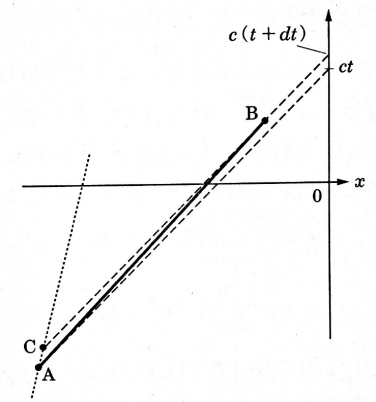

Fig. 101: Relativistic beaming effect for radiation. From Miyama et al (2008).

We can see that when $\theta < 1/\gamma$, κ has minimum values $\sim 1/\gamma^2$ but increases quickly when $\theta > 1/\gamma$. Since Lienard-Wiechert potentials are both proportional to κ^{-1}, the total radiation power is proportional to κ^{-2}, and highly concentrated within the angle of $1/\gamma$, called the radiation cone. Figure 97 (right) shows an example of radiation power enhancement due to the *relativistic beaming effect* for $\beta = 0.7$ with the beaming angle of $\sim 1/\gamma(\text{rad}) \sim 45°$. The radiation asymmetry between the beaming and anti-beaming directions at $\theta = 0$ can be estimated by

$$\frac{\kappa^{-2}_{\text{beaming}}}{\kappa^{-2}_{\text{anti-beaming}}} = \frac{(1+\beta)^2}{(1-\beta)^2} \approx 16\gamma^4, \tag{198}$$

which diverges quickly when $\gamma \to \infty$.

The physical explanation for relativistic beaming effect is given in Fig. 101. The observer at $x = 0$ observes two radiating particles during the time interval between t and $t + dt$. The first particle moves from A to B with a speed near c, following the solid line. The second particle moves from A to C with a speed of $(1/4)c$ following the dotted line. The observer receives all radiation from both particles between two dashed line during the same interval. Obviously, the observer receives much more radiation (or information) from the first particle than the second one. This is due to the relativistic beaming effect.

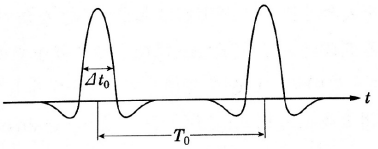

Fig. 102: Relativistically modified form of radiation power from an electron spiraling around a magnetic field. From Miyama et al (2008).

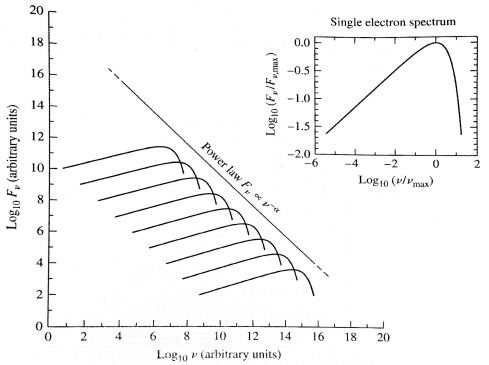

Fig. 103: Even though a single electron spectrum is not a power-law, a power-law energy distribution of electrons can lead to a power-law spectrum of the total synchrotron radiation. From Miyama et al (2008).

The radiation cone concept from a single relativistic electron can be applied to the case when the electron exhibits helical motions along magnetic field. Instead of sinusoidal modulations of radiation power at a single cyclotron frequency in the non-relativistic case, highly pulsed radiation power shown in Fig. 102 is seen by an observer when entering the radiation cone in the relativistic case. The peak frequency, $\nu_{\max}$, is determined by the pulse width and is proportional to γ^2, since the cone angle is proportional to $1/\gamma$ and the angle change rate is also proportional to $1/\gamma$ (Miyama et al, 2008). Therefore, we have

$$\nu \sim \nu_{\max} \propto \gamma^2,$$

which leads to

$$\gamma \propto \nu^{\frac{1}{2}} \quad \text{and} \quad d\gamma \propto \nu^{-\frac{1}{2}} d\nu.$$

Since synchrotron radiation power is proportional to γ^2, we have

$$\frac{d\gamma}{dt} \propto -\gamma^2, \tag{199}$$

and thus, a power-law energy spectrum of energetic electrons, $\gamma^{-p}d\gamma$, will result in a power-law spectrum of synchrotron radiation,

$$\frac{d\gamma}{dt}\gamma^{-p}d\gamma \propto \gamma^{2-p}d\gamma \propto \nu^{\frac{2-p}{2}}\nu^{-\frac{1}{2}}d\nu = \nu^{-\frac{p-1}{2}}d\nu \equiv \nu^{-\alpha}d\nu. \tag{200}$$

The situation is illustrated in Fig. 103. More specifically, for example, the power law index of cosmic ray electron in local interstellar medium is $p = 2.4$, the resultant synchrotron radiation power law index is $\alpha = (p-1)/2 = 0.7$. Since electrons lose their energy efficiently through synchrotron radiation, the observed steady-state spectra can tell us about the supply of energetic electrons, which depends critically on the acceleration mechanism.

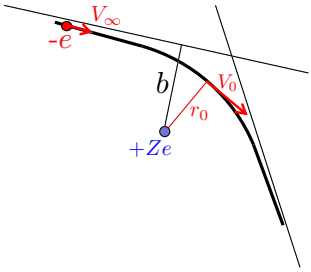

Fig. 104: Trajectory of an electron during its collision with an ion with $+Z$ charge. The impact parameter is b, and electron velocity in the ion rest frame is V_∞ at ∞ distance and is V_0 at the closest distance of r_0.

14.6 Bremsstrahlung Radiation

In contrast to cyclotron radiation, emitted by electrons accelerated by a magnetic field, Bremsstrahlung radiation ("breaking" radiation in German) is emitted by electrons accelerated by the electric field from other charged particles during collisions. The other charged particles are ions in most cases since electron-electron collisions generate negligible radiation because in those collisions there is no net acceleration of the center of charge. The electron-ion collisions can be free-free collisions, meaning that electrons are not bounded to ions before or after the collision when the total energy is positive. The electron-ion collisions can be also free-bound collisions when electrons are captured by ions when the total energy is negative. Sometimes, the radiation from this type of collisions is called recombination radiation and is also included in Bremsstrahlung radiation. The strategy taken here is to calculate the free-free radiation in the non-relativistic or classical limit, and all other effects are treated as order-of-unity corrections encapsulated within the *Gaunt factor*. Measuring Bremsstrahlung radiation spectra can determine the electron temperature and "$Z_{\rm eff}$" or the Z-effective of the plasma.

Consider an electron with V_∞ at infinity approaching at an impact parameter of b to the stationary ion with $+Ze$ charge, shown in Fig. 104. The electron has a speed of V_0 at the closest approach distance of r_0 from the ion. The conservation of angular momentum demands

$$V_\infty b = V_0 r_0, \tag{201}$$

so that the duration of this close interaction is given by $\tau_{\rm close} \approx 2r_0/V_0$. The attracting force acting on the electron from the ion during this duration is given by

$$F = m_e \left|\dot{\boldsymbol{V}}\right| \approx \frac{Ze^2}{4\pi\epsilon_0 r_0^2}. \tag{202}$$

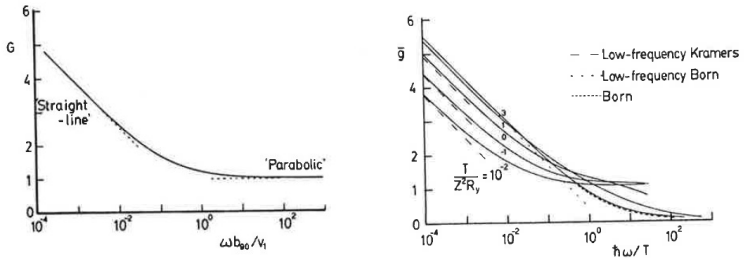

Fig. 105: Gaunt factor as a function of frequency for a single electron (left) and Maxwellian-averaged (right). From Hutchinson (2002).

The total radiation power by the electron in the classical limit as a function of time is given by the Larmor formula, Eq. (191),

$$P_{\text{total}}(t) = \frac{e^2}{6\pi\epsilon_0 c^3}\dot{V}^2(t). \tag{203}$$

Then the total radiation energy, W, is obtained by time integration and can also be expressed as an integration over a radiation power spectra in frequency, ν, *i.e.*,

$$W = \int_{-\infty}^{\infty} P_{\text{total}}(t)\, dt = \int_0^{\infty} P_{\text{total}}(\nu)\, d\nu, \tag{204}$$

where

$$P_{\text{total}}(\nu) = \frac{dW}{d\nu} = \frac{e^2}{3\pi\epsilon_0 c^3}\left|\int_{-\infty}^{\infty}\left|\dot{\boldsymbol{V}}\right| e^{i\omega t} dt\right|^2; \quad \omega = 2\pi\nu. \tag{205}$$

The peak frequency spectral power can be estimated as the following. First, we estimate:

$$\int_{-\infty}^{\infty}\left|\dot{\boldsymbol{V}}\right| e^{i\omega t} dt \approx \left|\dot{\boldsymbol{V}}\right|\int_{-\tau_{\text{close}}/2}^{\tau_{\text{close}}/2} e^{i\omega t} dt = \left|\dot{\boldsymbol{V}}\right|\tau_{\text{close}}\frac{\sin\left(\omega\tau_{\text{close}}/2\right)}{\omega\tau_{\text{close}}/2} \approx \left|\dot{\boldsymbol{V}}\right|\tau_{\text{close}}$$

for frequencies satisfying $\omega\tau_{\text{close}} \ll 1$. Next, using Eq. (202) and Eq. (201), we have

$$\left|\dot{\boldsymbol{V}}\right|\tau_{\text{close}} \approx \frac{Ze^2}{4\pi\epsilon_0 m_e r_0^2}\frac{2r_0}{V_0} = \frac{Ze^2}{4\pi\epsilon_0 m_e}\frac{2}{r_0 V_0} = \frac{Ze^2}{2\pi\epsilon_0 m_e V_\infty b}.$$

Therefore, the peak radiation spectral power is given by

$$\left.\frac{dw}{d\nu}\right|_{\omega\tau_{\text{close}}\ll 1} = \frac{e^2}{3\pi\epsilon_0 c^3}\left(\frac{Ze^2}{2\pi\epsilon_0 m_e V_\infty b}\right)^2 = \frac{Z^2 e^6}{(4\pi\epsilon_0)^3}\frac{16}{3m_e^2 c^3}\frac{1}{(V_\infty b)^2}. \tag{206}$$

Please note that the above equation is different by a factor of π from Eq. (5.3.16) of Hutchinson (2002).

Next we integrate over all impact parameters b. The electron flux through a ring between b and $b + db$ from a single ion is $n_e V_\infty \cdot 2\pi b \cdot db$. Thus, the integration over b for ion density of n_i yields

$$\begin{aligned}\frac{dP}{d\nu} &= n_e n_i V_\infty \int_0^\infty \frac{dW(\nu, b)}{d\nu} 2\pi b \cdot db \\ &\approx n_e n_i \frac{Z^2 e^6}{(4\pi\epsilon_0)^3} \frac{32\pi}{3m_e^2 c^3} \frac{1}{V_\infty} \int_{b_{\min}}^{b_{\max}} \frac{db}{b} \\ &= n_e n_i \frac{Z^2 e^6}{(4\pi\epsilon_0)^3} \frac{32\pi^2}{3\sqrt{3} m_e^2 c^3} \frac{1}{V_\infty} G, \end{aligned} \tag{207}$$

where the Gaunt factor (Gaunt, 1930), G, is defined as

$$G \equiv \frac{\sqrt{3}}{\pi} \ln \frac{b_{\max}}{b_{\min}}. \tag{208}$$

For the Coulomb Logarithm, $b_{\max}$ is chosen to be the Debye length λ_D and $b_{\min}$ is chosen to be b_{90} which is the impact parameter at which electron is scattered by 90°. G is a function of frequency: $G = 1$ for large-frequency emissions which occur for large-angle scattering during which electrons abruptly change their trajectories due brief but intense acceleration. G increases linearly for low-frequency emissions which occur due to the gradual change of electron trajectories during small-angle scatterings, see Fig. 105 (left).

Finally, thermal Bremsstrahlung radiation can be obtained by integrating over the electron distribution, $f(\boldsymbol{V})$, $\int (dP/d\nu) f(\boldsymbol{V}) d\boldsymbol{V}$. For an isotropic Maxwellian distribution, the Bremsstrahlung emissivity $j(\nu)$ in units of of power per solid angle per unit frequency per unit volume can be calculated

$$4\pi j(\nu) = n_e n_i \frac{Z^2 e^6}{(4\pi\epsilon_0)^3} \frac{32\pi^2}{3\sqrt{3} m_e^2 c^3} \int_0^\infty \frac{G(\nu, V)}{V} 4\pi V^2 f(V) dV. \tag{209}$$

Here we run into a problem - the classical Gaunt factor $G(\nu, V)$ is of order unity across all frequencies. Naively, this would suggest that a 100 eV plasma is nearly equally Bremsstrahlung emissive in the 10 eV photon range as in the 1 MeV photon range. We thus run into the same problem of diverging total power loss as in the ultraviolet catastrophe with blackbodies. We can address this by, in essence, cutting off the integral not at 0 but at the velocity corresponding to an energy of $h\nu$. This ensures that the photon energy is no greater than the electron energy ($h\nu \leq mV^2/2$). This yields

$$4\pi j(\nu) = n_e n_i Z^2 \left(\frac{e^2}{4\pi\epsilon_0}\right)^3 \frac{32\pi^2}{3\sqrt{3} m_e^2 c^3} \left(\frac{2m_e}{\pi T}\right)^{1/2} e^{-h\nu/T} \bar{g}, \tag{210}$$

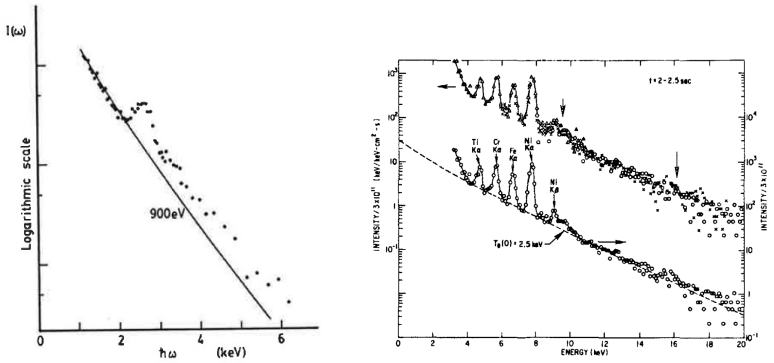

Fig. 106: Example Bremsstrahlung radiation measurements. Left panel is from Hutchinson (2002) and right panel is from Hill et al (1985) using x-ray pulse height analyzer based on a solid state detector.

where the Maxwellian-averaged Gaunt factor $\bar{g}$ is given by (Hutchinson, 2002)

$$\bar{g}(\nu, T) = \int_0^\infty G(\nu, E' + h\nu) e^{-E'/T} \frac{dE'}{T},$$

which is shown in Fig. 105 (right). Classically $\bar{g}$ is around unity over a wide range of frequency, but the $e^{-h\nu/T}$ term prevents divergence. See Hutchinson (2002) for more details on corrections due to quantum effects and contributions from recombination.

14.7 Measurements Using Bremsstrahlung Radiation

Equation (210) is our main result regarding the Bremsstrahlung radiation spectrum and can be used to measure important quantities in hot plasmas. The spectral exponential slope determines electron temperature; some examples are shown in Fig. (106). These spectra are obtained by counting received photons which generate a charge pulse proportional to the photon energy. Measurements from the spectral slope are convenient since they obviate the need for absolute calibration. However, spectral contamination by impurity lines are a serious concern as evident from the examples. Calculating the slope from continuum radiation is essential for this method.

With absolute calibration, however, additional information about the ion charge Z can be obtained. Integrating Eq. (210) over frequency yields the total radiation power,

$$P_{\rm Brem} = 1.69 \times 10^{-32} \left(\frac{n_e}{\rm cm^{-3}}\right) \left[\sum Z_i^2 \left(\frac{n_i}{\rm cm^{-3}}\right)\right] \left(\frac{T_e}{\rm eV}\right)^{1/2} \ {\rm watt/cm^3}, \quad (211)$$

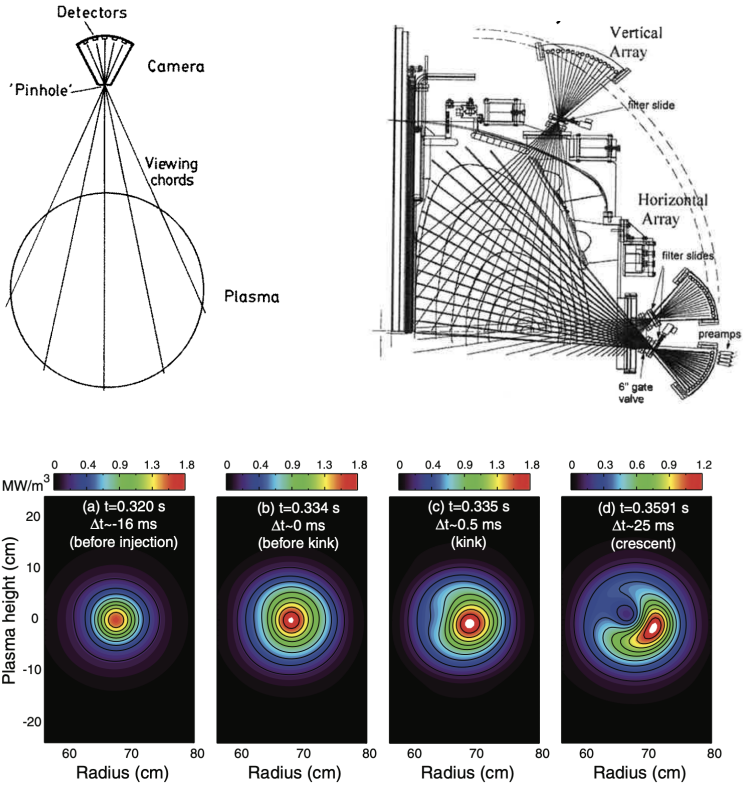

Fig. 107: Experimental setup for multiple chords measurements through a pinhole, from Hutchinson (2002). Multiple views allow tomographic reconstruction of emissivity revealing internal structures of hot plasmas, from Delgado-Aparicio et al (2012).

showing that Bremsstrahlung radiation power is proportional to

$$\sum_i n_e n_i Z_i^2 \equiv n_e^2 Z_{\text{eff}}.$$

This can be rewritten by using quasineutrality $n_e = \sum n_i Z_i$ as

$$Z_{\text{eff}} = \frac{\sum n_i Z_i^2}{\sum n_i Z_i}. \tag{212}$$

Z_{eff} is a kind of mean ion charge of the plasma in terms of the total Bremsstrahlung emission, an important energy loss mechanism in fusion plasmas. Achieving Z_{eff} close to unity is always a desirable but challenging goal for fusion experiments.

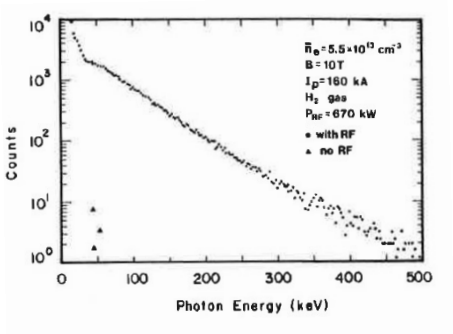

Fig. 108: An example of x-ray spectrum with a high-energy tail generated during RF current drive, from Hutchinson (2002).

Other than Z_{eff}, Eq. (211) shows P_{Brem} is proportional to a particular combination, $n^2\sqrt{T_e}$, which can be used to study structures in the hot plasma. At the optimum frequency of $h\nu \sim kT_e$, emission is strong and often falls into soft X-ray range in hot fusion plasmas. Tomographic measurements in this frequency range are often used to detect the time evolution of internal structures, and some recent examples are shown in Fig. 107.

Lastly, Bremsstrahlung radiation at high frequencies provides information on non-thermal electrons. An example is shown in Fig. 108. In principle, Eq. (209) can be inverted to obtain the electron tail distribution function but in realty this is difficult due to effects like relativistic beaming as we discussed before in Fig. 97. Nonetheless, such information is still valuable especially during unusual events like disruptions to generate runaway electrons or during RF current drive in Tokamaks as shown in Fig. 108. Non-thermal electron acceleration during magnetic reconnection is another example.

14.8 Summary

- Concept of optical depth and blackbody radiation to determine electron temperature.
- Lienard-Wiechert potentials to calculate radiation by accelerated charges. Total radiation power by Larmor formula in the non-relativistic limit.
- Doppler broadening and mass-shift broadening of cyclotron radiation spectrum.
- Electron cyclotron emission measurement of localized electron temperature in tokamaks.
- Synchrotron radiation of relativistic electrons: relativistic beaming effect and synchrotron radiation spectrum.
- Bremsstrahlung radiation arises when electrons collide with ions and is a major energy loss channel for hot fusion plasmas.
- Bremsstrahlung radiation spectra are well approximated by classical treatment with a correction factor (Gaunt factor) around unity.

- Bremsstrahlung spectral shape in continuum gives measurement of electron temperature while absolute radiation power provides an estimate of Z_{eff} important for impurity radiation loss in hot plasmas. Soft X-ray tomography at electron thermal energy provides internal structure measurements.

14.9 Further Reading

- Chapter 5 of Hutchinson (2002)
- Bornatici et al (1983)
- Park et al (2003)
- Miyama et al (2008)

14.10 Homework Problem Set 8

Due April 6, 2026

1. Dependence of radiation.
   (a) Why does cyclotron radiation typically not depend on electron density but does depend on electron temperature in tokamaks?
   (b) Why does Bremsstrahlung radiation typically depend on electron density and electron temperature?
   (c) Why is synchrotron radiation so enhanced compared with cyclotron radiation? By how much is it enhanced?
   (d) Assuming a Gaunt factor of unity, calculate the predicted power-law frequency spectral slope due to Bremsstrahlung radiation from energetic electrons that form a power-law spectrum with a slope of p.
2. The cyclotron radiation spectrum consists of discrete peaks at harmonics, m,
$$\omega_m = \frac{m\omega_c}{1-\beta_\parallel \cos\theta} = \frac{m\Omega}{1-\beta_\parallel \cos\theta}\sqrt{1-\beta^2},$$
which is broadened by the Doppler effects and relativistic mass increases. Conceptually design an electron cyclotron emission diagnostic to measure both the parallel and perpendicular electron temperature.
3. Calculate Z_{eff} for the following two cases:
   (a) A magnetically confined fusion plasma with primary D+ ion species, with 0.1% by ion number density Molybdenum, at average ionization state $\langle Z_{\text{Mo}} \rangle = 32$.
   (b) A laser-heated plasma from ionized plastic: 50% H^+ and 50% fully stripped C^{6+} ions.

15 Line Radiation

One simple way to classify radiation emitted by plasmas is according to whether the electrons start or end free or bound to a nucleus. The four-combinations, written as before-after, are

1. Free-free: cyclotron/synchrotron, Bremsstrahlung, and Cherenkov radiation
2. Free-bound: recombination
3. Bound-free: photo-ionization
4. Bound-bound: line radiation or absorption, which is the subject of this Lecture.

Once bound electrons are involved, the spectra will be necessarily discrete, called "line radiation", and only the free-free radiation is continuous, as discussed in the previous Lecture. Radiation or absorption involving molecules are due to transitions between vibrational or rotational states, so they are also discrete in nature but they can appear as a "radiation band" if multiple lines are packed in a narrow frequency range or even appear as a continuous spectrum if not resolved properly.

Spectroscopy is the science of measuring and interpreting the photons emitted and absorbed by molecules, atoms, and ions. The frequency range extends from infrared with wavelength $\lambda > 700$ nm and energy less than 2 eV mainly from molecules, to optical with $\lambda = 300 - 700$ nm and energy $= 2 - 4$ eV from transitions between nearby levels, and to x-ray with $\lambda < 10$ nm and energy more than 100 eV from transitions deep into lower energy levels, as shown in Fig. 109.

The history of spectroscopy is intricately linked to the history of modern physics. Detailed study of atomic physics led to quantum mechanics and most of what we know of matter was learned through spectroscopy. Spectroscopy connected astronomy and cosmology to the laboratory where physics can be reproduced and quantified, and it is not an overstatement to say that spectroscopy puts the "physics" in astrophysics. Specifically for plasma physics, spectroscopic diagnostics reveal details about temperature, density and electromagnetic fields. In a sense, spectroscopy links the very small with the very large as in laboratory plasma astrophysics, the fundamental with the practical as in diagnosing and controlling fusion plasmas.

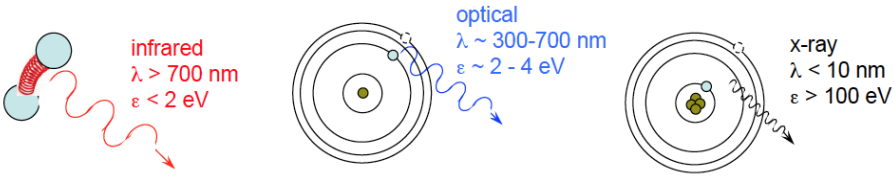

Fig. 109: Wavelength ranges and their corresponding photon energies for each category of radiation. From National Undergraduate Fellowship Lecture by S. Hansen (2012).

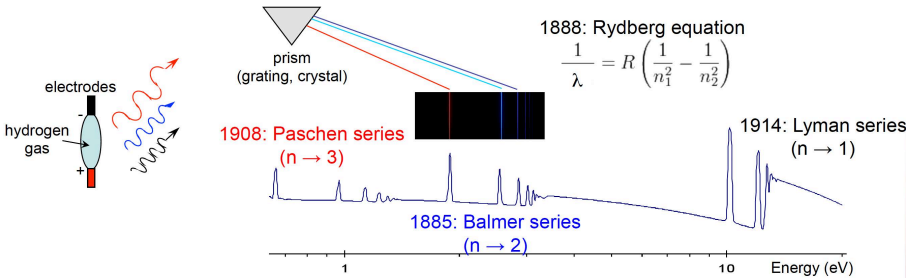

Fig. 110: Discoveries of the Balmer series, Paschen series, and Lyman series, as well as Rydberg equation. Here the Rydberg constant is $R = 1.097 \times 10^7 \mathrm{m}^{-1}$. From the National Undergraduate Fellowship Lecture by S. Hansen (2012).

Figure 110 summaries the early history of spectroscopy on emission from Hydrogen atoms. Various spectral lines were observed from plasma discharges between electrodes in hydrogen gas, and their wavelengths were well-quantified by the elegant Rydberg equation. Based on this, Neils Bohr in 1913 proposed an empirical model of the atom that would account for the measured spectrum of hydrogen: electrons occupy discrete, stable orbitals with energies given by the simple expression, $E_n = -13.6Z^2/n^2(\mathrm{eV})$, where n is the primary quantum number. This was a significant step towards a full quantum model of atoms. Nowadays, spectroscopy is both easy and sophisticated enough to become a fundamental diagnostic to determine many important plasma parameters both in fusion and astrophysical plasmas.

15.1 Einstein Coefficients and Line Strength

The radiation photon energy $h\nu_{ij}$ is related to the electron level energy before and after the transition by

$$h\nu_{ij} = E_i - E_j \tag{213}$$

where E_i and E_j are upper and lower level energies, respectively. The transition here is bidirectional: electron can transit from an upper level with energy of E_i to a lower level of E_j, called "decay", by releasing a photon with energy $h\nu_{ij}$, or a photon with energy of $h\nu_{ij}$ can be absorbed so that electron can transition from a lower level with energy of E_j to an upper level with E_j, called "excitation".

As introduced in Section 12, there are two types of decay: spontaneous decay with a probability per unit time of A_{ij} and induced decay with a probability per unit time of $B_{ij}\rho(\nu_{ij})$, where $\rho(\nu)$ is radiation energy per unit frequency at the subject atom. In contrast, there is only one type of excitation: induced excitation with a probability per unit time of $B_{ji}\rho(\nu_{ij})$. Note the difference between B_{ij} and B_{ji}.

The meanings of "spontaneous" and "induced" are self-evident. Spontaneous means the transition occurs in vacuum while induced means the

Table 6.1. *Spectral line data for hydrogen.*

Line	Wavelength (nm)	A_{ij} (10^8 s^{-1})	f_{ji}	g_i
L_α	121.57	4.699	0.4162	8
L_β	102.57	0.558	0.0791	18
L_γ	97.25	0.128	0.0290	32
H_α	656.28	0.441	0.641	18
H_β	486.13	0.0842	0.119	32
H_γ	434.05	0.0253	0.044	50

Fig. 111: Spectral line data for hydrogen. From Hutchinson (2002).

transition occurs in the presence of radiation or electromagnetic field at the frequency satisfying Eq. (213). The coefficients, A_{ij}, B_{ij}, and B_{ji} are called Einstein coefficients for this atomic transition, and are related to each other by the nature of thermodynamic equilibrium for both atoms and radiation ρ. As discussed in Lecture 14, the thermodynamic equilibrium blackbody radiation is given by

$$\rho(\nu) = \frac{8\pi h\nu^3}{c^3}\frac{1}{e^{h\nu/kT}-1} \tag{214}$$

which is characterized by its temperature, T.

At the same temperature T, the number of atoms, N_i, in a quantum state, i, is given by the Boltzmann distribution,

$$N_i \propto g_i e^{-E_i/kT}$$

where g_i is the degree of degeneracy for this energy level. Therefore, we have

$$\frac{N_i}{N_j} = \frac{g_i}{g_j}e^{-(E_i-E_j)/kT} = \frac{g_i}{g_j}e^{-h\nu_{ij}/kT}. \tag{215}$$

The plasma is in thermal equilibrium only if the total rate of transitions from i to j is equal to the rate at which they transition from j to i, i.e.,

$$(A_{ij} + B_{ij}\rho)\, N_i = B_{ji}\rho N_j$$

which leads to an expression for ρ using Eq. (215),

$$\rho = \frac{A_{ij}}{(N_j/N_i)B_{ji} - B_{ij}} = \frac{A_{ij}}{(g_j/g_i)e^{h\nu_{ij}/kT}B_{ji} - B_{ij}}. \tag{216}$$

Comparing Eqs. (214) and (216) immediately leads to the relation between Einstein coefficients,

$$A_{ij} = \frac{8\pi h\nu_{ij}^3}{c^3}B_{ij} \tag{217}$$

$$g_j B_{ji} = g_i B_{ij}, \tag{218}$$

where all these are proportional to the *line strength* in spectroscopy. Example line strengths are shown in Fig. 111 where Einstein coefficients are on the order of $(\text{ns})^{-1}$. This means these line transitions occur on the nanosecond timescale, which is short for most plasmas in space and astrophysics and laboratory experiments other than laser-generated plasmas.

15.2 Thermal Equilibria and Collisional Transitions

The above discussions are based on *complete thermal equilibrium* for atoms following a Boltzmann distribution and photons following the blackbody radiation formula. Such equilibria are difficult to find in nature or in the lab; perhaps the only such example is stellar interiors, which are optically thick with small spatial gradients. In complete thermal equilibrium cases, the relative populations of the ionization states can be explicitly calculated (Hutchinson, 2002) to obtain the *Saha Equation* by treating the ionization states as special cases with free electrons,

$$\frac{n_{i+1}}{n_i} = \frac{g_{i+1}}{g_i}\frac{1}{n_e}\left[\frac{2m^3}{h^3}\left(\frac{2\pi T_e}{m}\right)^{3/2}\right] e^{-\chi_i/T_e}, \tag{219}$$

where χ_i is the ionization energy. Equation (219) predicts rather surprising results: for hydrogen atom density n_i and hydrogen ion density n_{i+1} supposing a T_e only 1 eV compared with ionization energy $\chi_i = 13.6$ eV, we have

$$\frac{n_{i+1}}{n_i} = \frac{4 \times 10^{21}\text{m}^{-3}}{n_e}.$$

This means the plasma is almost fully ionized if n_e is low enough ($< 10^{21}\text{m}^{-3}$). This is not what we have normally in the laboratory nor in space nor astrophysics. This is because these plasmas are not truly in the complete thermal equilibrium.

In reality, *local thermal equilibrium* or LTE models are often used. In these models, atoms adopt state populations following Boltzmann distributions while the radiation is not necessarily thermal following blackbody distributions. The insufficient radiative transitions are made up by sufficient electron collisional transitions when the electron density is high enough in typical LTE models (Hutchinson, 2002),

$$n_e \gg 10^{19}\left(\frac{T_e}{e}\right)^{1/2}\left(\frac{\Delta E}{e}\right)^3 \text{m}^{-3}$$

where ΔE is the energy level difference. This is a condition that is difficult to satisfy in magnetized laboratory experiments as well as in many space

and astrophysical plasmas. In contrast, this can be easily satisfied in high-energy-density plasmas, which are typically however too short for spontaneous transitions.

There are numerous electron collisional transitions (Hutchinson, 2002) and here we mention only three primary ones:

1. Electron impact excitation and de-excitation. These processes are in contrast to photon-induced excitation (including absorption) and decay that we discussed before.
2. Electron impact ionization and three-body recombination ($e^- + e^- + A^+ \rightarrow e^- + A^*$) which is important for low-temperature plasmas. This is in contrast to photo-ionization and recombination.
3. Dielectronic recombination and autoioninzation for multiple-electron species other than hydrogen or hydrogen-like atoms: capturing a free electron and using its energy to excite a second electron to an upper energy level, followed by a radiation. Its inverse is autoionization, in which radiation can excite a bounded electron to an upper energy level, and when the electron transitions back to a lower energy level the released energy frees up a second electron to ionize the atom.

Instead of Einstein coefficients, the probabilities of collisional transitions are quantified by cross sections, $\sigma_{ij}(v)$, for the transition from i level to j level for an electron traveling at a speed v in a density n_i of atoms. The unit of $\sigma_{ij}(v)$ is area (m^2) so that the number of collisions per unit length of an electron traveling at v is calculated by $\sigma_{ij}(v)n_i$. Converting this to per unit time, the number of collisions is $\sigma_{ij}(v)vn_i$ or simply $\sigma_{ij}vn_i$. Writing this per atom (or ion) is $\sigma_{ij}v$ which can be averaged over electrons with a distribution $f(v)$,

$$\int \sigma_{ij} v f(v) d^3v = n_e \langle \sigma_{ij} v \rangle \quad \text{or} \quad \langle \sigma_{ij} v \rangle \equiv \frac{\int \sigma_{ij} v f d^3v}{\int f d^3v}. \tag{220}$$

Here $\langle \sigma_{ij} v \rangle$ is called the rate coefficient of this particular collision process per atom (or ion) per electron.

Combining both Einstein coefficients for spontaneous and radiation-induced transitions and rate coefficients for collision transitions by electrons, we can write down a set of differential equations for density $n_i(t)$ of each state i,

$$\frac{dn_i}{dt} = -\sum_{j \neq i} \left[n_i A_{ij} - n_j A_{ji} + (n_i B_{ij} - n_j B_{ji}) \rho(\nu_{ij}) \right. \\ \left. + n_e n_i \langle \sigma_{ij} v \rangle - n_e n_j \langle \sigma_{ji} v \rangle \right]. \tag{221}$$

When the time dependence is set to zero, Eq. (221) describes equilibrium solutions for each n_i.

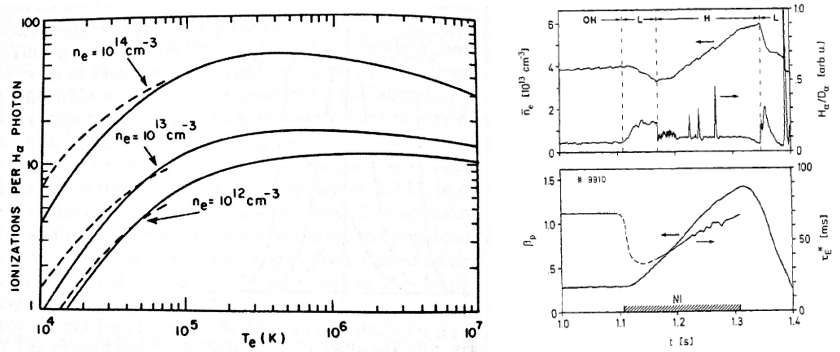

Fig. 112: (left) Number of ionizations per H_α photons emitted as functions of electron temperature. From Hutchinson (2002). (right) Transition from L to H-mode of confinement indicated by H_α/D_α line intensity reduction. From Keilhacker et al (1984).

15.3 Line Intensity Measurements

Two well-known LTE models based on electron collisional transitions are discussed below. One is called the *coronal equilibrium model* due to its successful application in solar corona. The model is a steady state model as the time derivative terms are negligible in Eq. (221). The solar corona is optically thin such that all spontaneous radiation escapes before absorbed to induce upward transition, compared to collisional upward transitions. On the other hand, the solar corona has sufficiently low electron density such that downward transitions are dominated by spontaneous transitions. Therefore, upward collisional transitions balance downward spontaneous transitions in coronal equilibrium models. As a special case, if electrons are sufficiently energetic, an excited state density n_i can be populated by collisions from the ground state of 1, the density ratio is simply given by

$$\frac{n_i}{n_1} = \frac{n_e \langle \sigma_{1i} v \rangle}{\sum_j A_{1j}}. \tag{222}$$

Since the time scale to achieve steady state between ground states and excited states is typically much shorter (∼ns) than between ground states and ionized states (∼ms), there exists an intermediate time scale for which the time dependence needs to be kept for ionized states for some coronal equilibrium models. An example of time scale estimate is given in Chap 6.2 of Hutchinson (2002) for magnetically confined fusion plasmas. This subcategory is called the *collisional radiative model* in which the left-hand side of Eq. (221) needs to be kept only for ground states with different ionization stages.

Coronal equilibrium models have been applied in fusion plasmas to provide a convenient measure of particle confinement. In steady state, charged particles

lost from confinement need to be replaced by ionization which can be calculated from the intensity of certain lines, when the excited state density and ionization rate are both proportional to electron density. When the electron temperature is sufficiently larger than the ionization energy, its dependence on temperature is weak as shown in Fig. 112 (left). For this reason, H_α line intensity measurement serves a convenient measure of particle confinement in fusion plasmas; a reduction in H_α is often regarded as an improvement of particle confinement such as H-mode. An example is shown in Fig. 112 (right) from ASDEX tokamak where the H-mode was first discovered by Wagner et al (1982). However, in general, line intensities depend on election temperature and their dependence differs between lines such that the line intensity ratios can be used to determine electron temperature.

Often, however, collisional radiative models can provide more accurate predictions due to their flexibility to adapt to the specific conditions of a plasma. Figure 113 shows examples of the application of both the coronal equilibrium model and the collisional radiative model to a Helium glow discharge on Large Helical Device (LHD) (Goto et al, 2003, 2004b,a). Time dependence and finite optical opacity sometimes need to be taken into account in order to accurately model line radiation spectra. In many practical situations in the lab, solar and astrophysics, however, non-Local Thermal Equilibrium or NLTE models are required with highly detailed atomic structures.

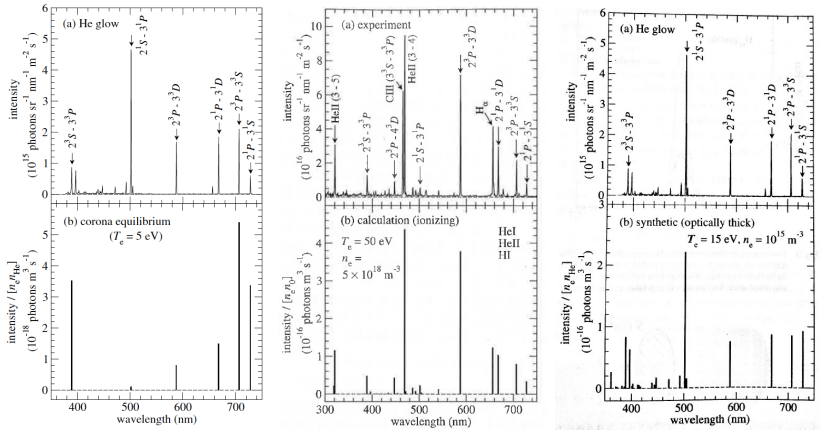

Fig. 113: Examples of application of radiation models: (left panel) The steady state coronal equilibrium model does not predict measured spectra (Goto et al, 2003); (middle panel) The time-dependent collisional radiative model explain the measurement better (Goto et al, 2004b); (right panel) The time dependent collisional radiative model with finite optical thickness performs best (Goto et al, 2004a).

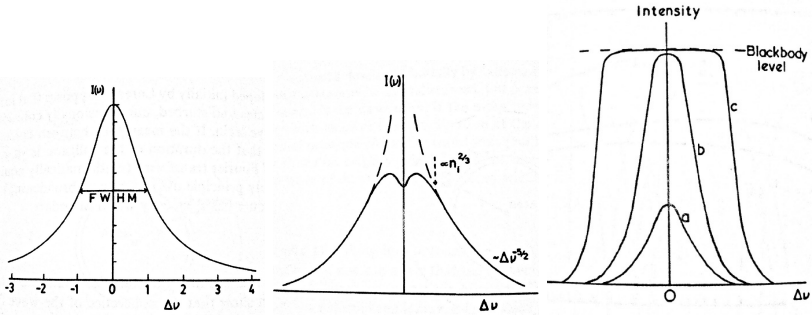

Fig. 114: (left panel) Definition of FWHM (full-width-half-maximum) of a line; (middle panel) line broadening due to the Stark effect from plasma pressure; (right panel) "broadening" due to high optical opacity. From Hutchinson (2002).

15.4 Line Shape Measurements

In addition to line intensity, the detailed shape of each line can be informative about the plasma conditions when measured with sufficient spectral resolution. We discuss four kinds of line broadening below.

Natural broadening of a line is due to uncertainty principle of a quantum state between energy and time,

$$\Delta E \Delta t \approx \frac{h}{4\pi}$$

which can be translated to broadening in spectrum,

$$\Delta\nu = \frac{\Delta E}{h} \approx \frac{1}{4\pi\Delta t} = \frac{\sum_j A_{ij}}{4\pi}. \tag{223}$$

Since Einstein coefficients represent the time scale of exponentially decaying probability functions, upon Fourier transformation, the resultant natural broadening leads to a Lorentzian shape of spectral lines,

$$I(\nu) = \frac{I(\nu_0)}{1 + \left(\frac{\nu-\nu_0}{\Delta\nu}\right)^2}. \tag{224}$$

Typically, line broadening is quantified by its FWHM or full-width-half-maximum, which is given by $\Delta\nu_{1/2} = 2\Delta\nu$, see the left panel of Fig. 114.

Doppler broadening is due to the Doppler shift in the spectrum from light-emitting thermal ions or atoms towards the observer, $\Delta\nu = \nu V_{\rm th}/c$ where the thermal speed $V_{\rm th} \equiv \sqrt{2T/M}$. The resultant line shape takes the form of

$$I(\nu) = I(\nu_0) e^{-\left(\frac{\nu-\nu_0}{\Delta\nu}\right)^2} \tag{225}$$

with its FWHM given by $\Delta\nu_{1/2} = 2\sqrt{\ln 2}\Delta\nu$.

The FWHM of broadened spectral lines reflects random ion motion or temperature along the line of sight, after removing other broadening such as natural broadening. This technique is widely used in the laboratory to measure ion temperature, but also in natural plasmas such as in the solar chromosphere where various neutral and ion lines are identified. However, the line broadening along a particular line of sight has an ambiguity about whether the broadening is due to thermal motion of atoms without flows along the line of sight or "random" or "turbulent" flows at different locations along the line of sight but without large thermal spread. Resolving this ambiguity requires measurements along multiple lines of sight from different angles of the same plasma and the employment of advanced techniques similar to tomographic reconstruction not only in physical space but also in spectral space.

Instead of measuring broadening for ion temperature, measuring ion flow is generally harder due to the need for absolute wavelength calibration, which can be done by a combination of forward and backward directions. Heavier ions or impurities are more difficult due to their smaller speeds for the same temperature.

Stark broadening is also called pressure broadening or collisional broadening. It arises due to the electric field from the presence of nearby charged particles. Since electrons move fast, the perturbation time on the light-emitting ions or atoms is short and their effects on line broadening is small. In contrast, ions moving slowly more strongly affect the line shape, termed Stark effects. The quasi-static assumption is valid due to slowly moving ions and the Stark broadening can be estimated as follows.

The effect on the light-emitting atoms is dominated by the closest ion as its electric field E decreases as $1/r^2$ with distance. The probability of the light-emitting atoms to experience such an electric field is proportional to its volume, $4\pi r^2 dr$. Thus, the emitting spectral change due the closest ion is given by

$$I(\nu)d\nu \propto r^2 dr \propto E^{-5/2}dE \propto (\Delta\nu)^{-5/2}\, d\nu \tag{226}$$

where we used $E \propto r^{-2}$. (Note that $r \propto E^{-1/2}$ and $dr \propto E^{-3/2}dE$ lead to $r^2 dr \propto E^{-5/2}dE$. Also $E \propto \Delta\nu$) Equation (226) simply leads to

$$I(\nu) \propto (\Delta\nu)^{-5/2} \tag{227}$$

implying that Stark effects from nearby ions are large at the line shape tails, as expected. This is illustrated in the middle panel of Fig. 114. The dependence of Eq. (227), however, does not extend to the line center as the electric field of the ion will cease to affect the light-emitting atoms at a distance r with other ions starting to be present on average, $(4/3)\pi r^3 \sim n_i^{-1}$ or $r \propto n_i^{-1/3}$. This leads to $\Delta\nu \propto E \propto r^{-2} \propto n_i^{2/3}$. Thus, Stark effects stop at $\sim n_i^{2/3}$ as illustrated in Fig. 114.

The full-scale calculations yield Stark broadening FWHM,

$$\Delta\nu_{1/2} = 0.54\alpha_{1/2}\left(\frac{n_i}{10^{20}\mathrm{m}^{-3}}\right)\ \mathrm{nm}, \tag{228}$$

where $\alpha_{1/2}$ is given in Hutchinson (2002). Stark broadening is used to measure density in high-density plasmas, such as divertor plasmas in tokamaks, atmospheric plasmas during lightning and laser-produced plasmas.

Line "broadening" in optically thick plasmas can occur due to the re-absorption of photons when the line radiation approaches blackbody level. An illustration is given in the right panel of Fig. 114. In this case, the atomic kinetics rate equations and radiation transport equation have to be solved self-consistently: the radiation field intensity is needed to compute photo-excitation and photo-ionization rates while the level populations are needed to compute the emissivity and opacity that determine the radiation field intensity.

Lastly, when multiple broadening effects exist, some convenient facts are

- Convolution of a Gaussian with a Gaussian is still a Gaussian: $\Delta^2 = \Delta_1^2 + \Delta_2^2$;
- Convolution of a Lorentzian with a Lorentzian is still a Lorentzian: $\Delta = \Delta_1 + \Delta_2$;
- Convolution of a Lorentzian and Gaussian yields the Voigt function.

Otherwise, the solutions are only available numerically.

15.5 Summary

- Line radiation occurs when bound electrons in atoms or discrete motions (oscillations or rotations) in molecules are involved and its understanding led to the beginning of modern physics via quantum mechanics.
- Einstein coefficients characterize spontaneous and radiation-induced transitions in atoms on the ns timescale while collisional transitions are due to electron impact and can be much faster or slower.
- Complete thermal equilibria are for both excited states and radiation while local thermal equilibria (LTE) are only for excited states.
- Line intensities are modeled by coronal equilibrium models or collisional radiative models, some of which are quite involved, to explain the measurements.
  - For hot plasmas such as at the edge of fusion plasmas during their H-mode confinement, H_α line intensity can be used for particle confinement measurements since its dependence on electron temperature is weak.
  - For colder plasmas such as low-temperature plasmas, when line intensity depends on electron temperature differently for different lines, the ratio of line intensities can be used to determine electron temperature.
- Line broadening includes natural broadening due to spontaneous delays, Doppler broadening to measure ion temperature, and Stark broadening to measure ion density.

15.6 Further Reading

- Chapter 6 of Hutchinson (2002)

15.7 Homework Problem Set 9

Due April 13, 2026

1. Show that two levels i, j of an atom will be in local thermodynamic equilibrium in a plasma of negligible optical depth if

$$n_e \gg \frac{A_{ij}}{\langle \sigma_{ij} v \rangle}.$$

2. Answer the following questions:

   (a) Why can the electron temperature sometimes be determined by the ratio of two lines? What are the assumptions or requirements behind this technique?

   (b) Why are H_α line measurements frequently used in fusion experiments? What are the assumptions or requirements behind this technique?

   (c) What are complete thermal equilibrium and local thermal equilibrium (LTE)? What are two well-known LTE models? Give at least one example plasma for complete thermal equilibrium, and also one for each of LTE models.

3. Spectral form.

   (a) Show that the convolution of Gaussians and Lorentzians are still Gaussians and Lorentzians, respectively.

   (b) Stark broadening is proportional to $(\Delta\nu)^{-5/2}$ at the wing of a spectral line. Which functional shape among Gaussians and Lorentzians should we use to quantify this broadening?

16 X-Ray Diagnostics

Whether from bremsstrahlung, cyclotron radiation or line radiation, x-ray emission is a key feature of many plasmas. X-ray diagnostics are thus crucial for understanding such plasmas and their evolution in time. Via careful measurements of the x-rays emitted by a plasma, we may infer the properties thereof.

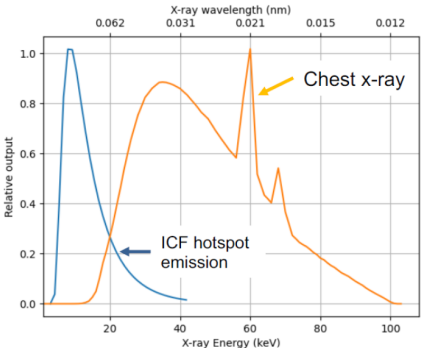

Fig. 115: Typical x-ray energies

16.1 Imaging Techniques

X-ray diagnostics are seldom as simple as placing an x-ray detector at the end of the chamber. There are several main schemes for optimally arranging the x-ray source, detector and intervening walls to optimize the data.

16.1.1 Object Placement

For best results, one must carefully consider the relative placement and sizes of the x-ray source, detector and barriers in between. If the object is too far from the detector the image will blur as shown below

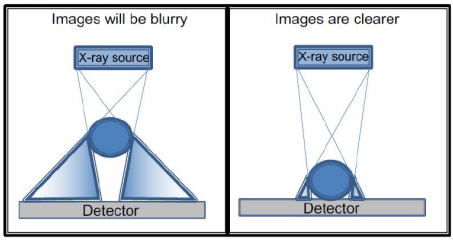

The so-called "penumbral blur" can also occur if the source is too large. A smaller source improves resolution at the cost of having to wait longer for enough x-rays acquire an image.

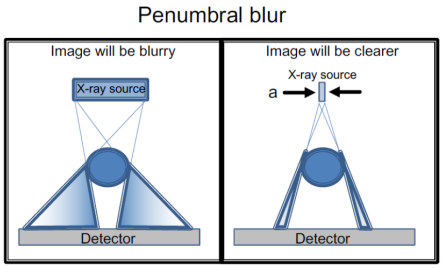

16.1.2 X-Ray Mirrors

X-rays behave much like visible light and thus many optical techniques can be applied here also.

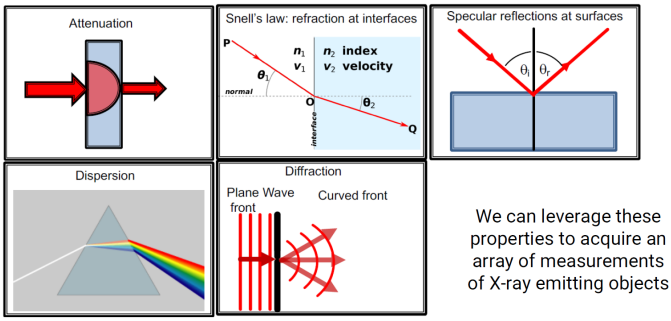

One particularly useful example is the x-ray mirror. At sufficiently low incoming angles x-rays can be totally internally reflected according to Snell's law, with critical angle α_c

$$\alpha_c \sim \sqrt{2\delta} \tag{229}$$

where the index of refraction in the mirror is $n = 1 - \delta$.[5] Since δ is usually quite small this critical angle is of the order of a degree. This grazing incidence requires an extremely smooth surface ($\lessapprox 0.5\,\text{nm}$ RMS) to work properly. Some other details to note: α_c decreases as the x-ray energy increases and materials with high electron densities function best as mirrors.

[5] Note that this is indeed less than 1, a peculiarity of x-rays.

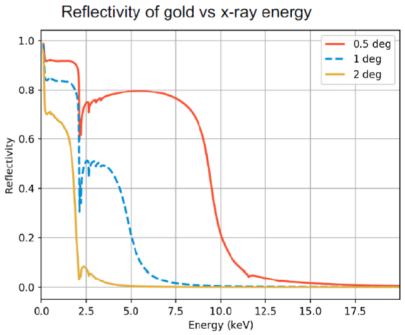

Fig. 116: Reflectivity of gold versus x-ray energy for a variety of angles. As one would expect, lower angles result in the best reflection.

16.1.3 Pinhole Imaging

Another method with origins in visible light is the pinhole camera, which uses a physical obstruction to produce an inverted image. These easy-to-manufacture options have an infinite depth of focus and work with all wavelengths.

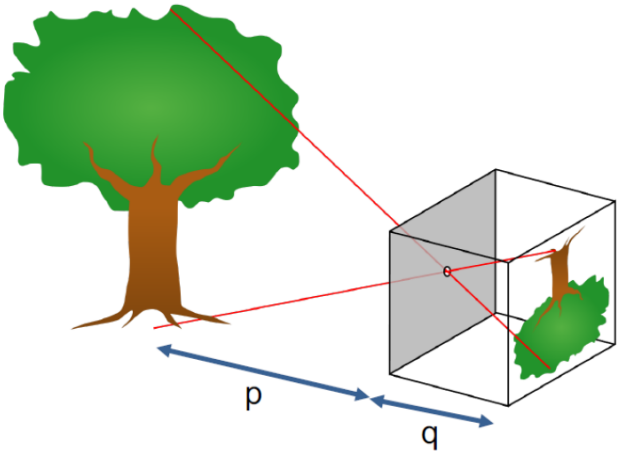

By en:User:DrBob (original); en:User:Pbroks13 (redraw) - http://commons.wikimedia.org/wiki/Image:Pinhole-camera.png, Public Domain, https://commons.wikimedia.org/w/index.php?curid=4099853

As one can see there will be some inherent *geometric blur* expressed as

$$a' = a(1 + q/p) \tag{230}$$

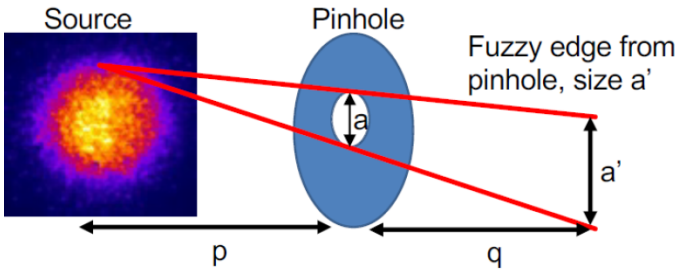

Furthermore since these pinholes are so small ($\sim 1 \times 10^{-9}$ steradians) there is also a blur due to diffraction $\sim \lambda q/a$. Where these two blurs are equivalent is the optimal resolution.

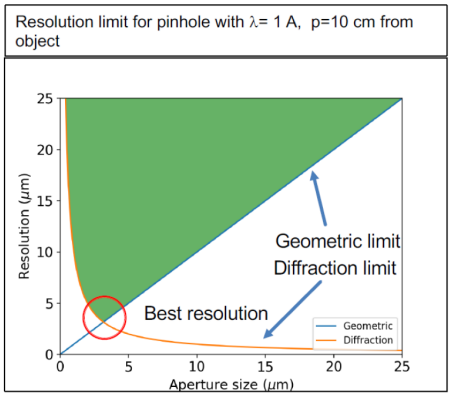

A variation of pinhole imaging is called *penumbral imaging*. Here a large aperture is used. While this results in the center of the image containing little useful information, from the edges known as the *penumbra* the original signal may be reconstructed.

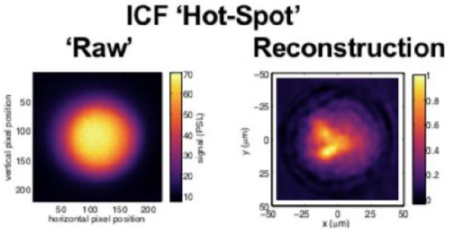

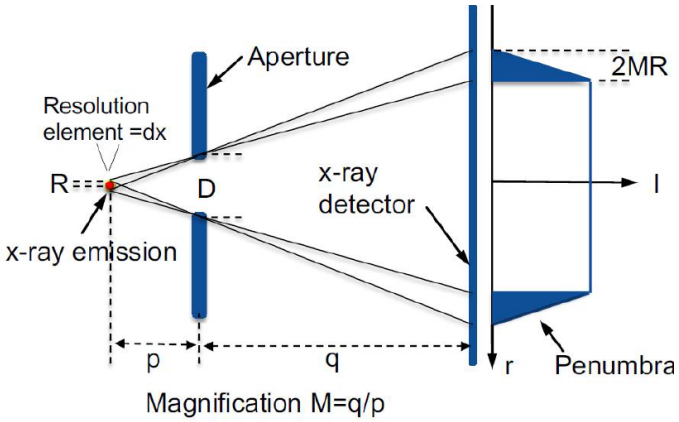

The full circular area of the aperture gives a signal-to-noise ratio improvement over the pinhole of $\sqrt{D\ dx}/R$, a 10-100x improvement over the standard pinhole.

A final variation is the *pinhole array* wherein data are aggregated from many pinholes.

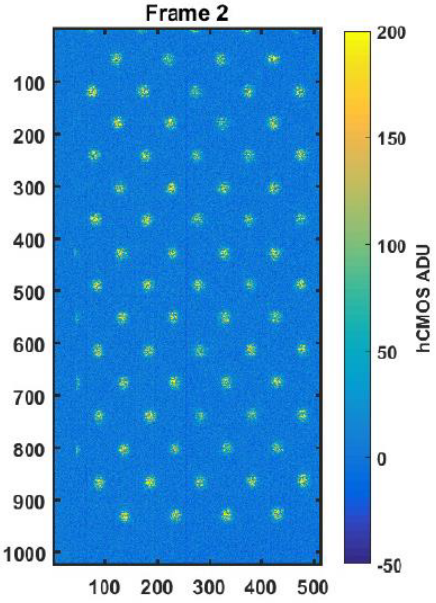

The signal to noise ratio increases as the square root of the total number of pinholes used. As more pinholes are used, the image gets clearer.

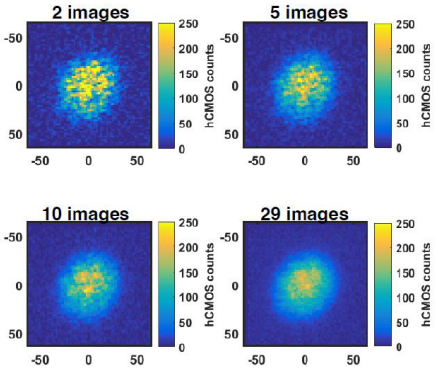

16.2 Instrumentation

Of course, none of the aforementioned techniques are of any use unless the final x-ray photons can be converted to a recorded form, whether that be a voltage signal, photographic plate, etc. Here we discuss the key instrumentation needed to detect x-rays after whatever desired configuration has been established.

16.2.1 Photomultiplier Tube

X-ray photons can be converted into a voltage signal via the photoelectric effect. Even though the cross section for bound electrons is much higher than that of free ones, the photoelectric effect does not result in a sufficiently high current on its own for practical purposes. Thus a *photomultiplier tube* is used. It consists of a photocathode coupled to a series of dynodes which multiply the original electron flux via secondary electron emission. This is quantified by the quantum efficiency QE which relates the ratio of the electron flux to photon flux.

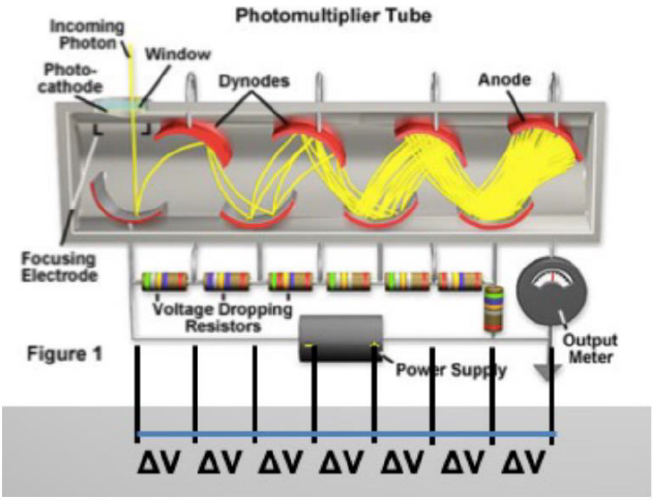

Figure 1

16.2.2 Microchannel Plate

An alternative to the photomultiplier tube is the *microchannel plate*. One can consider the microchannel plate to be, in principle, an array of small photomultiplier tubes. When electrons hit one of the many channels within the larger array the electron flux is multiplied several times over before exiting:

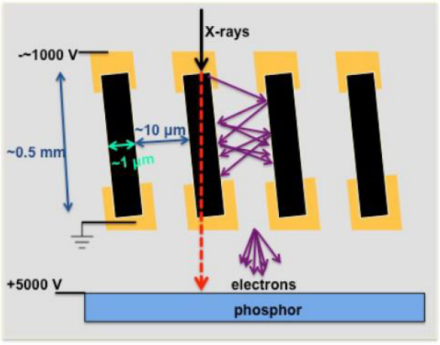

These microchannels are arrayed in a plate, offering spatial resolution.

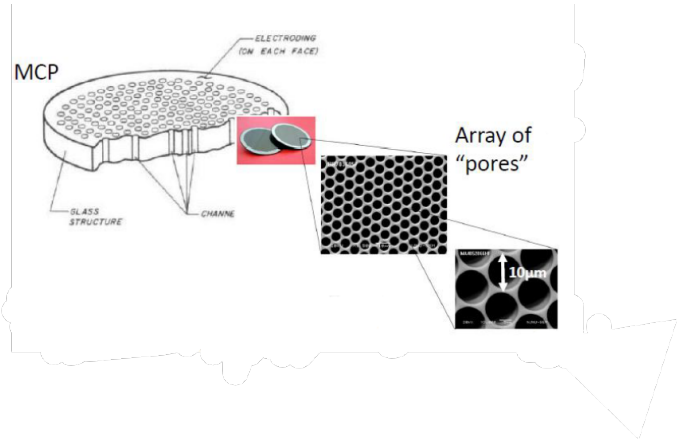

Some common pitfalls with these types of diagnostics include:

1. Depletion of voltage due to an excess of charge
2. Space charge effects
3. Magnetic fields
4. Burning out the photocathode
5. Fragility of the equipment
6. Ground loops

16.2.3 Streak Cameras

In certain contexts like ICF, researchers are interested in the temporal evolution of plasmas on very small timescales. For x-ray measurements this can be accomplished via streak cameras, which distribute a 1D-resolved spatial signal over time, producing a 2D image. The basic working principle is as follows: incoming x-ray photons are converted to electrons via the photoelectric effect. These electrons are focused by optics and then deflected by an electric field. By sweeping this electric field with time, electrons from different times will be deflected by different amounts, resulting in dispersion in time.

These systems typically work with x-ray energies between $0.1 - 20\,\text{keV}$ and can achieve a spatial resolution of $\sim 100\,\mu\text{m}$. Similar techniques can be used for optical wavelengths from $200 - 1000\,\text{nm}$, where $< 1\,\text{ps}$ temporal resolutions are possible. This is how the VISAR system operates.

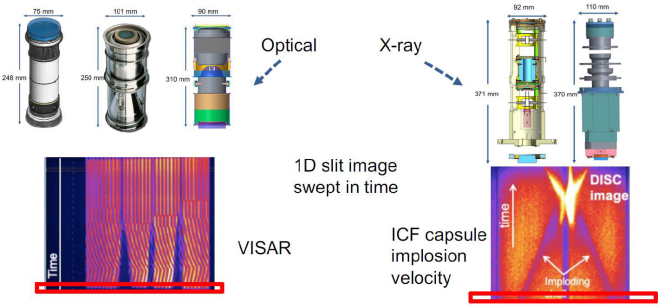

A schematic of the physical steps required to convert the incoming photons into a streak image is shown below. In Step 1 the photons are converted into photoelectrons. Next, in Step 2 they are accelerated by an electric field. Since all electrons go through this field, the energy spread $\Delta E/E$ is reduced, thereby reducing the transit-time spreading.

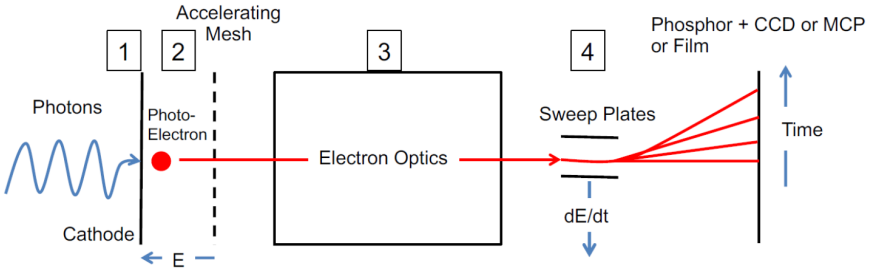

In Step 3 the electrons are focused by electron "optics" in a manner much analogous to how optical lenses can be used with visible light. In the final step, Step 4, the electrons are subjected to another electric field perpendicular to their direction of motion which deflects them. This field is varied in time, spreading out the resultant location at which the electrons strike the final surface. This surface can be a phosphor with charge coupled device (CCD), a microchannel plate, or just film.

Common issues include the following:

1. Too many photons can damage the photocathode and result in space-charge effects
2. No signal can be measured if there are conversely too few photons or if there are misalignments or mistimings in the system

16.2.4 Crystal Imagers

Of course, the diffraction properties of x-rays can be directly exploited to reflect a narrow band of x-ray energies according to Bragg's law.

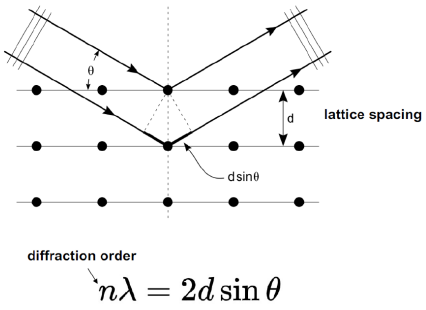

Since the reflection is based on the crystal properties the material will be tailored to the particular application. A curved mirror can act as a spherical mirror for x-rays with a focal length $f = R/2$ as in classical optics. These can achieve far larger collection areas of $1 \times 10^{-3} - 1 \times 10^{-4}$, 4-5 orders of magnitude larger than for pinholes. Such results can also be resolved in space. Below see a schematic of the XICS crystal spectrometer system from C-MOD which uses a spherically-bent crystal and a 2D pixel detector.

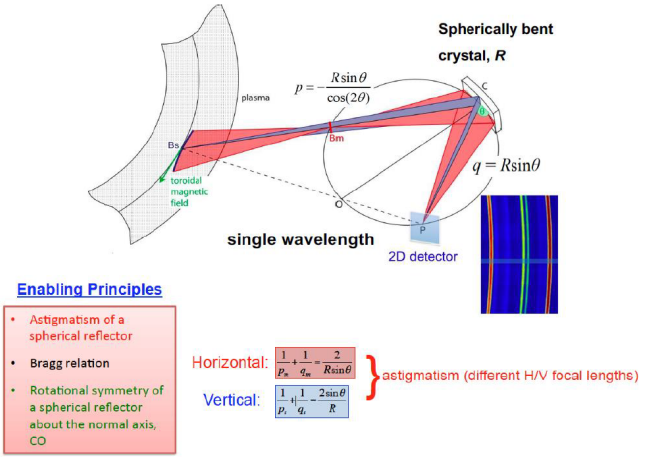

16.3 Summary

- Optical techniques such as mirrors, pinholes and apertures can be used x-ray images
- Photomultiplier tubes and microchannel plates convert x-ray photons into voltage signals
- Streak cameras enable x-ray measurements with excellent time resolution

17 Neutron and Proton Imaging

17.1 Neutron Imaging

As the lowest-temperature nuclear fusion reactions all produce neutrons, neutron diagnostics have been critical for all experiment seeking to create a burning plasma. Neutrons not only provide the most direct measurements of fusion reactions but can also tell us about the plasma through which they propagate. Gamma rays play a similar role.

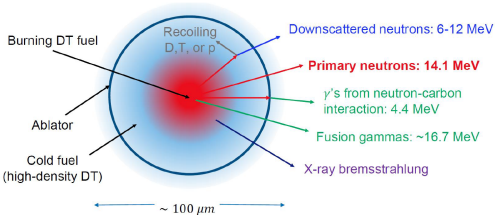

Fig. 117: Neutrons emitted from the implosion of a DT capsule as in a NIF shot. Primary neutrons escape the target unaffected and give data about the hotspot. Since downscattered neutrons lose energy due to collisions with the cold imploding shell, these give data about the surrounding cold fuel and the implosion symmetry.

Time-integrated slices from several angles enable the reconstruction of the 3D shape of the implosion. These can be especially powerful when combined with x-ray observations.

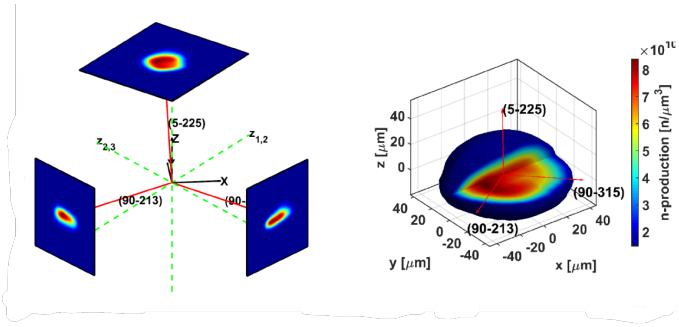

Unlike for x-rays, there are no standard optics for neutrons and gamma rays since they are hard to shield and measure, both having mean free paths in metals on the order of one centimeter.

Neutron imaging does however, in general, use apertures like for x-rays. When this aperture is much smaller than the system this is essentially a camera obscura pinhole technique yielding an image resembling the source. When the

aperture size is larger than the source we can use penumbral imaging like before.

Since neutrons have a large mean free path the walls surrounding the aperture must be sufficiently thick in order for them to work. For thickness t, the transmitted flux T is the incoming flux N_0 multiplied by $e^{-t/\lambda}$ where t is the wall thickness and λ the mean free path.

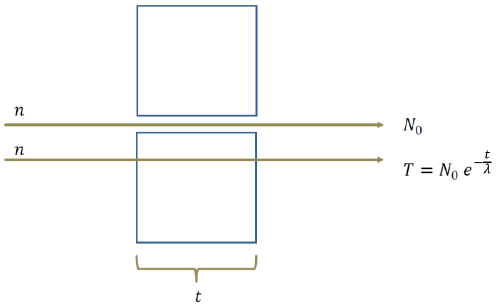

The ratio between N and T, gives the *contrast ratio*

$$\mathrm{CR} = e^{t/\lambda} \tag{231}$$

For example, the 20 cm apertures for 14.1 MeV neutrons at NIF with $\lambda = 3.1$ cm yield CR ≈ 634. The higher this is, the clearer the image.

Since apertures are thick there is additional freedom to shape them - different configurations can be optimized for different ends. Care must be exercised to separate the features of the image from artifacts caused by the aperture.

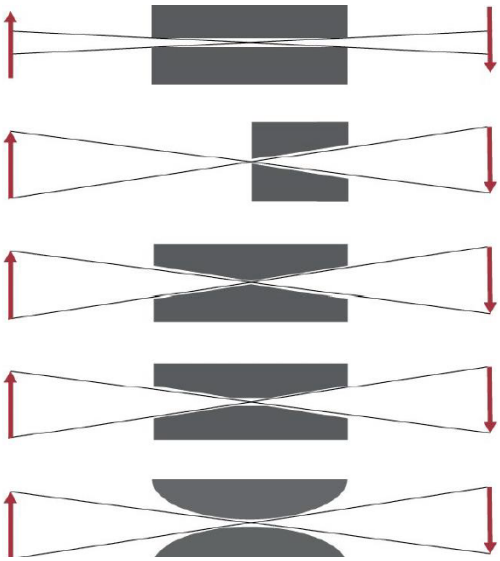

Ultimately many systems need to work together in order to generate a neutron image.

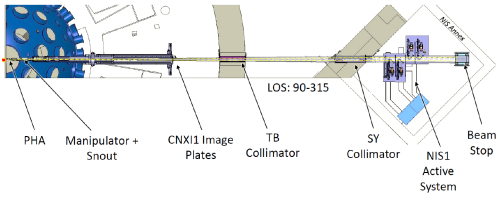

The final signal is generated by neutron scattering off of hydrogen in plastic.

Spatial Resolution $< 300\ \mu m$

17.2 Proton Radiography

Since neutrons are chargeless they cannot tell us about the electromagnetic fields within a target. This is where protons come in. By sending protons through the target and observing their deflection by the fields therein, we can infer information about the electric and magnetic fields.

Individual protons leave damage tracks in CR-39 plastic. Through chemical etching, these tracks expand into pits visible by microscope.

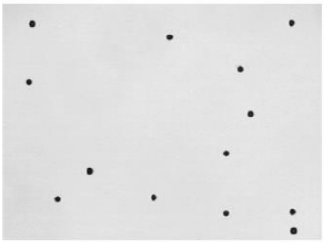

Etched CR-39 from 2.01 MeV protons

The proton energy can be inferred from the size of the pits.

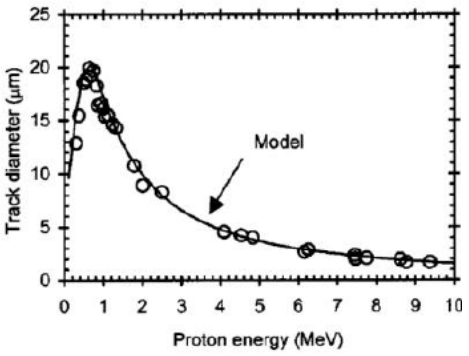

from Seguin RSI 2003

Filters can also be used as part of broader stacks to measure different proton populations.

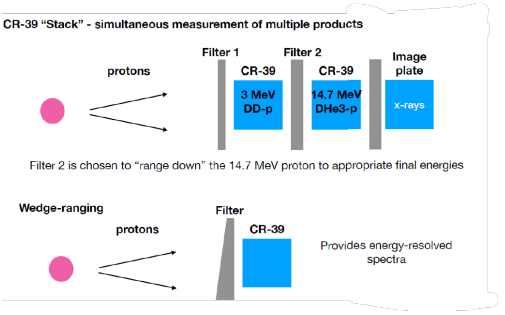

The angular deflection of a proton due to some field configuration is denoted by α.

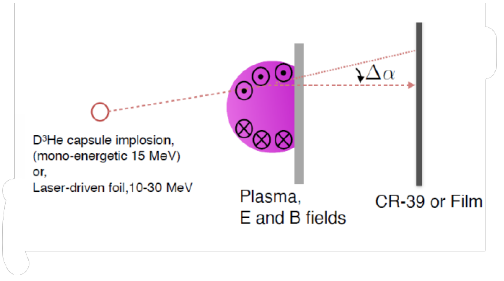

To infer the electromagnetic fields we can use the formulae for anticipated deflections:

$$\Delta\alpha_B = \frac{e}{m_p V_p} \int \mathbf{B} \times d\boldsymbol{\ell} \tag{232}$$

$$\Delta\alpha_E = \frac{e}{m_p V_p^2} \int \mathbf{E}_\perp \, \mathrm{d}\ell \tag{233}$$

There are two main methods to back out the fields from these. For the first, the protons are divided into discrete beamlets which reveals the structure of the distortions caused by the field (e.g. Petrasso et al, 2009).

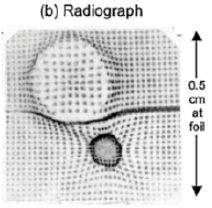

For the second, the equation

$$\nabla \cdot \alpha = \frac{\delta I}{I} \tag{234}$$

is inverted (e.g. Bott et al, 2017).

17.3 Summary

- Neutrons and gamma rays offer information both about the fusion hotspot and the colder surrounding plasma
- Neutrons are characterized by long mean free paths in metals, complicating the design of apertures
- Proton trajectories can be used to infer the electric and magnetic fields within a target plasma

17.4 Homework Problem Set 10

Due April 17, 2026

X-ray and Neutron imaging diagnostics - Pinhole camera foundation

The pinhole imager shown below has a small round pinhole aperture located at $(0, 0, 0)$ in a perfectly absorbing barrier in the (x, y) plane. The source plane and image plane are also oriented in the (x, y) plane at $z = -L_s$ and $z = L_i$, respectively. Since neutrons travel in straight lines, a neutron from a source at point (x, y) in the source plane that passes through the pinhole will

strike a point $(x', y') = (-Mx, -My)$ at the image plane where the source magnification M is defined to be positive.

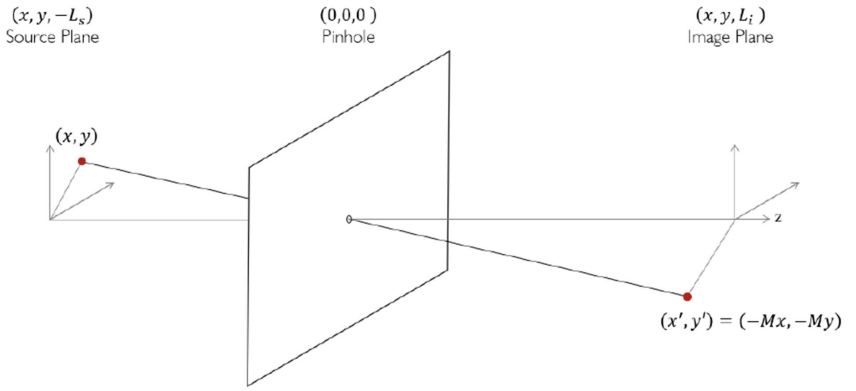

1. Determine M in terms of other variables in the diagram.
2. If the pinhole has a finite diameter, d, determine the diameter, D, of the image projected by the point source in terms of d and M.
3. Consider point sources A and B in the source plane that are casting round images A' and B' at the image plane. Define the resolution, R_p, as the separation between A and B that is required for A' and B' to just touch. Determine R_p.

18 Scattering of Electromagnetic Waves

Scattered light from plasma contains invaluable information that is difficult to obtain otherwise. This is why measuring scattered light remains a powerful plasma diagnostic despite its difficulty and expense.

The scattering process of incoming electromagnetic waves by plasma can be described using either classical or quantum physics but with the same outcome in the non-relativistic limit:

1. Classical picture: the incoming electromagnetic waves apply forces on electrons, which get accelerated and emit electromagnetic waves as scattered light;
2. Quantum picture: the incoming photons "collide" with electrons and get "bounced off" as scattered light.

In this Lecture, we will use both treatments as convenient.

There are several different regimes depending on the incoming photon energy. When incoming light is in the visible frequencies, the typical photon energy is on the order of 1 eV which is much less than the electron rest mass energy of about 511 keV. In this classical limit, the scattering process is called Thomson scattering (see Fig. 118 for a well-known example); the incoming photons have little effect on the electrons. When the photon energy is comparable or larger than the electron rest mass energy, the photon momentum cannot be ignored and the scattering process is called Compton scattering; full relativistic effects need to be taken into account. On the other hand, when electrons are sufficiently energetic in the lab frame, the scattered photons are energized and the scattering process is called inverse Compton scattering. Each of these will be discussed in turn.

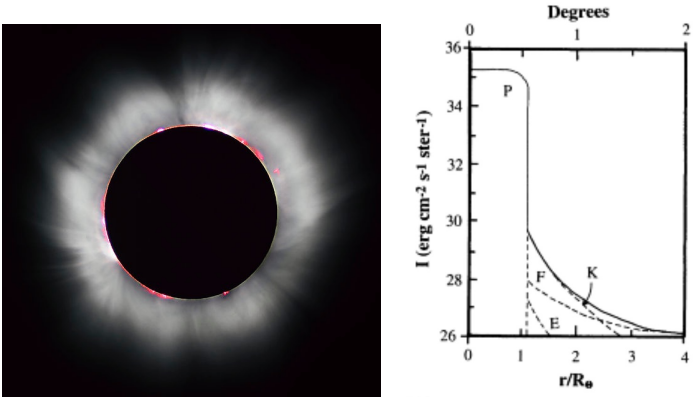

Fig. 118: (left panel) The solar corona is visible due to Thomson scattering of solar radiation; (right panel) various radiation intensities as a function of distance from solar surface. P=photo, K=kontinuierlich or continuous, F=Fraunhofer or dark referring absorption lines, E=Emission line.

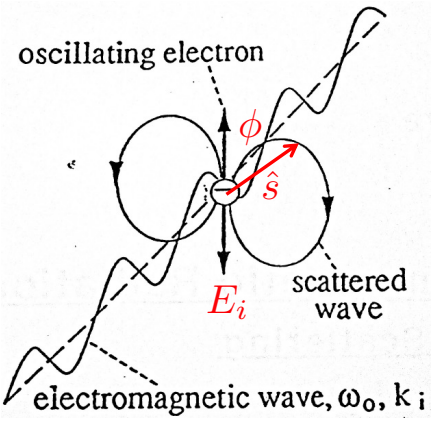

Fig. 119: Scattered electromagnetic wave as emitted from oscillating electrons driven by the incoming electromagnetic wave or light wave.

In most cases, ions do not participate the scattering process except for the case of Thomson scattering in the coherent or collective mode (see below).

18.1 Thomson Scattering

18.1.1 Incoherent or Non-collective Thomson Scattering

We will base our discussion on that of Section 14, where we learned that electromagnetic wave radiation was due to accelerated charges as illustrated in Fig 119. The electric field $\boldsymbol{E}_i$ of the incoming electromagnetic wave drives plasma electrons to oscillate and emit electromagnetic waves as scatted light. In the non-relativistic limit, the electron acceleration is given by the equation of motion,

$$\dot{\boldsymbol{v}} = -\frac{e}{m_e}\boldsymbol{E}_i \tag{235}$$

which can be used in the non-relativistic form of the far-field of electric field due to oscillating electrons, Eq. (188), to yield,

$$\boldsymbol{E}_s = -\frac{e}{4\pi\epsilon_0}\left[\frac{1}{c^2 R}\hat{\boldsymbol{s}}\times\hat{\boldsymbol{s}}\times\dot{\boldsymbol{v}}\right] = \left[\frac{r_e}{R}\hat{\boldsymbol{s}}\times\hat{\boldsymbol{s}}\times\dot{\boldsymbol{E}}_i\right] \tag{236}$$

where the electron classical radius is $r_e \equiv e^2/4\pi\epsilon_0 m_e c^2$. Here $\hat{\boldsymbol{s}}$ is $\hat{\boldsymbol{R}}$ in Eq. (188).

From the Poynting vector of the scattered wave, Eq. (189) with $R = 1$, the radiation power per solid angle is given by

$$\frac{dP}{d\Omega_s} = r_e^2 \sin^2\phi \; c\epsilon_0 \left|E_i\right|^2 . \tag{237}$$

The angular dependence with respect to $\boldsymbol{E}_i$ is also shown in Fig. (119). Since $c\epsilon_0 |E_i|^2$ is the total incident power, the Thomson scattering cross-section, σ, is given by

$$\frac{d\sigma}{d\Omega_s} = r_e^2 \sin^2\phi. \tag{238}$$

Since $d\Omega_s = 2\pi \sin\phi \; d\phi = -2\pi \; d(\cos\phi)$, the total Thomson scatting cross-section is

$$\begin{aligned} \sigma &= 2\pi r_e^2 \int_0^\pi \sin^3\phi \; d\phi = -2\pi r_e^2 \int_1^{-1} \sin^2\phi \; d(\cos\phi) \\ &= 2\pi r_e^2 \int_{-1}^{1} (1-\cos^2\phi) d(\cos\phi) = \frac{8\pi}{3} r_e^2. \end{aligned} \tag{239}$$

Here we observe several characteristics of Thomson scattering:

- σ is a constant; the scattered power is simply proportional to electron density, n_e, and the total scattered light power gives a measurement of n_e.
- The scattered wave frequency is equal to the incident wave frequency, which means that the scattered wave energy is equal to incident wave energy, i.e., Thomson scattering is elastic scattering.
- If the incident wave is linearly polarized, as shown in Fig. 119, the scattered light is also linearly polarized.
- The backward-forward symmetry is kept during scattering process, implying that the total scattered wave momentum is zero. This is consistent with the non-relativistic assumption which will become inadequate when the incident wave momentum is non-negligible.

More than just the electron density n_e can be learned from Thomson scattering. Similar to the discussion in Lecture 14, the line broadening of scattered light contains information on electron temperature, T_e, due to the Doppler effect as explained below in two steps by using the quantum picture of Thomson scattering:

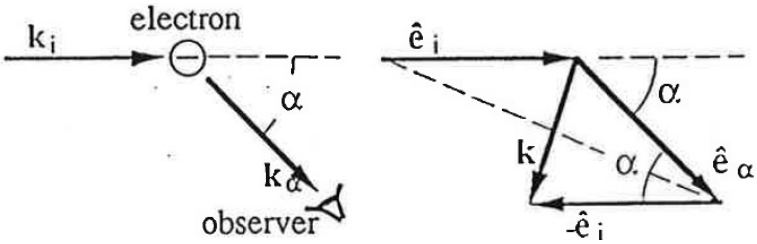

Fig. 120: (left panel) Geometry of Thomson scattering measurement for incident laser wavenumber vector $\boldsymbol{k}_i$ and observed scattered light wavenumber vector $\boldsymbol{k}_\alpha$; (right panel) scattering vector, $\boldsymbol{k}$, due to electron velocity in the same direction.

1. Consider the rest frame of an electron moving at velocity $\boldsymbol{V}$. The incident laser wavenumber vector is $\boldsymbol{k}_i$ and the observed scattered light wavenumber vector is $\boldsymbol{k}_\alpha$, as shown in the left panel of Fig. 120. The laser frequency seen by the electron is Doppler-shifted from the laser frequency ω_i in the lab frame to be
$$\omega' = \omega_i \left(1 - \frac{\hat{\boldsymbol{e}}_i \cdot \boldsymbol{V}}{c}\right) \tag{240}$$
where $\hat{\boldsymbol{e}}_{\boldsymbol{i}}$ is the unit vector of $\boldsymbol{k}_{\boldsymbol{i}}$. The scattered light remains at the same frequency at ω' in the electron rest frame in the non-relativistic limit as discussed above.
2. Now return to the lab frame. The scattered laser frequency is Doppler-shifted again from ω' in the electron rest frame to
$$\omega_\alpha = \omega' \left(1 + \frac{\hat{\boldsymbol{e}}_\alpha \cdot \boldsymbol{V}}{c}\right) \tag{241}$$
where $\hat{\boldsymbol{e}}_{\boldsymbol{\alpha}}$ is the unit vector of $\boldsymbol{k}_{\boldsymbol{\alpha}}$.

By combining Eqs. (240) and (241), the total Doppler shift is
$$\omega = \omega_\alpha - \omega_i \approx \omega_i \frac{(\hat{\boldsymbol{e}}_\alpha - \hat{\boldsymbol{e}}_i) \cdot \boldsymbol{V}}{c} = \omega_i \frac{\boldsymbol{k} \cdot \boldsymbol{V}}{k_i c}, \tag{242}$$
where the direction of scattering vector $\boldsymbol{k}$ is shown in Fig. 120 and its size is given by
$$|\boldsymbol{k}| = |\boldsymbol{k}_\alpha - \boldsymbol{k}_i| = 2 \sin \frac{\alpha}{2} k_i. \tag{243}$$
Therefore, the frequency or wavelength spread of scattered light reflects the electron velocity distribution in the $\boldsymbol{k}$ direction. The simplest quantity that can be determined by such measurements is the electron temperature, T_e, and

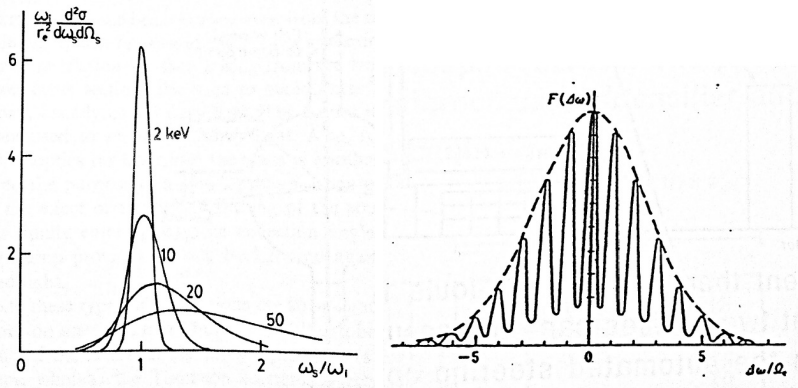

Fig. 121: (left panel) Relativistic effects and (right panel) magnetic field effects on Thomson scattering spectra.

additional information such as non-thermal components could also be measured if there are an adequate number of photons available. Such measurements are difficult in general due to the small Thomson scattering cross section but have been getting easier recently due to technological advances.

Two additional effects are worth mentioning here: relativistic effects and magnetic field effects. As discussed in Lecture 14, when electrons are relativistic, the scattered light can exhibit beaming effects which increases the total scattering power and also shifts towards higher energies or higher frequencies. An example is shown in the left panel of Fig. 121 where spectra for electron temperature increases from 2 keV to 50 keV with visible differences from 10 keV. Note that even 50 keV temperature is still small compared to electron rest mass energy, the (inverse) Compton effects become non-negligible (see below).

Another effect is due to the magnetic field. Instead of traveling in straight lines, the electron's trajectory becomes helical when the magnetic field is sufficiently strong. The resultant orbital integration becomes a summation of Bessel functions, leading to harmonics in the broadened line shape as shown in the right panel of Fig. 121. Note that this is observable only when $\boldsymbol{k}$ and $\boldsymbol{B}$ are almost perpendicular to each other. Due to various difficulties, it is still impractical to use this feature to measure $\boldsymbol{B}$ in hot plasmas; see Hutchinson (2002) for more discussion.

Most practical challenges of Thomson scattering stem from the small cross section: it requires intense lasers, little stray light, and low electronic noise detectors. It also has to work against other radiation such as Bremsstrahlung. Nonetheless, modern Thomson scattering diagnostics have become increasingly sophisticated: one example is Laggner et al (2019) for hot plasmas in NSTX-U and another example is Shi et al (2022) for relatively cold plasmas.

18.1.2 Coherent or Collective Thomson Scattering

The above discussion assumed that the measured scattering light by a detector is a simple summation of the scattered light from all electrons. This is true only when collective effects of plasma are absent, *i.e.*, when the incident laser wavelength is short compared to Debye length, $k_i\lambda_D \gg 1$. When $k_i\lambda_D \ll 1$, the contribution to the scattering process from both the subject electron with a charge of $-e$ *and* its shielding cloud of electrons with a net charge of $+e$ need to be taken into account. As a result, the scattered wave power is greatly reduced by the canceling effects due to shielding electrons.

When the subject particle is an ion with a charge of $+e$, then its shielding cloud is made of electrons with a net charge of $-e$. Even though the scattering power from the subject ion is small due to its slow acceleration, the scattering power from the shield cloud of electrons remains large. In such a case, the scattering light contains indirect but valuable information about ions! When $k_i\lambda_D \ll 1$, Thomson scattering is said to be coherent or collective. In contrast, when $k_i\lambda_D \gg 1$, Thomson scattering is said incoherent or non-collective.

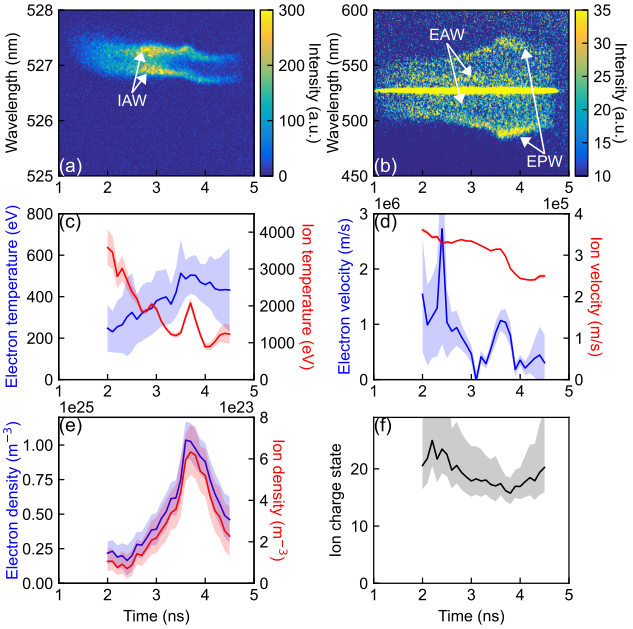

Fig. 122: Experimentally measured (a) IAW and (b) EPW spectra and inferred plasma parameters (c) temperatures, (d) velocities, (e) densities, and (f) ion charge state. From Ji et al (2024).

The coherent Thomson scattering power per frequency per solid angle is given by Hutchinson (2002),

$$\frac{d^2P_s}{d\nu_s d\Omega_s} = \frac{r_e^2 P_i}{A} \left|\hat{\boldsymbol{e}}_\alpha \times (\hat{\boldsymbol{e}}_\alpha \times \hat{\boldsymbol{e}}_i)\right|^2 n_e V S(\boldsymbol{k}, \omega) \tag{244}$$

where $\boldsymbol{k} = \boldsymbol{k}_\alpha - \boldsymbol{k}_i$ and $\omega = \omega_\alpha - \omega_i$. Here V is the scattering volume and A is incident beam area. $S(\boldsymbol{k}, \omega)$ is called *scattering form factor*, representing plasma collective effects and is given by

$$S(\boldsymbol{k}, \omega) \approx \frac{1}{n_e T_e V} \left|N_e(\boldsymbol{k}, \omega)\right|^2 \tag{245}$$

Here $N_e(\boldsymbol{k}, \omega)$ is Fourier transformation of the Klimontovitch density which includes all (incoherent and coherent) information about the discrete particles in a finite volume and time period.

In a special case for uniform unmagnetized plasmas in the measurement volume, $S(\boldsymbol{k}, \omega)$ can be explicitly calculated. In such a case, the plasma dielectric constant is expressed as $\epsilon = 1 + \chi$ where χ is the susceptibility, representing the effects of electric polarization due to electrons and ions, respectively, $\chi = \chi_e + \chi_i$. Each susceptibility can be calculated via the Vlasov equation, which is an approximation of the Klimontovitch equation, see Chap. 1 of Ji

(2024). With χ_e and χ_i known, the scattering form factor is given in Chap. 7.3 of Hutchinson (2002)

$$S(\boldsymbol{k},\omega) = \frac{2\pi}{kn_e}\left[\left|1-\frac{\chi_e}{1+\chi_e+\chi_i}\right|^2 f_{ek}\left(\frac{w}{k}\right) + \left|\frac{\chi_e}{1+\chi_e+\chi_i}\right|^2 \sum_i Z_i^2 f_{ik}\left(\frac{w}{k}\right)\right], \tag{246}$$

where the first term represents contributions from incoherent electrons, the "1" inside $|\ldots|^2$, and from coherent electron response the $\chi_e/(1+\chi_e+\chi_i)$ term. The second term represents contributions only from the shielding electron response to the subject ion. f_{ek} and f_{ik} are the electron and ion velocity distribution functions, respectively, projected in the $\boldsymbol{k}$ direction. When $k_i\lambda_D \gg 1$, no coherent or collective effects exist, $\chi_e = 0$; and $S(\boldsymbol{k},\omega)$ simply becomes $\frac{2\pi}{kn_e} f_{ek}\left(\frac{w}{k}\right)$, representing only incoherent effects from electrons as discussed in the previous subsection. When $k_i\lambda_D \ll 1$, the shielding electron responses are large, and thus χ_e is large and the first term approaches zero, representing cancellation effects by the shielding electrons, while the second term remains large.

Additional understanding can be gained by noticing where in Eq. (246) $\epsilon = 1+\chi_e+\chi_i$ appears in the denominator. For longitudinal waves in unmagnetized plasmas, the dispersion relation is given by $\epsilon = 0$ which yields electron plasma waves (EPW) for electrons, $\omega^2 = \omega_{pe}^2 + 3(kv_{th,e})^2$, and ion accoustic waves (IAW) for ions, $\omega/k = \sqrt{Z_iT_e/m_i}$. In other words, during coherent Thomson scattering when incident electromagnetic waves with wavelengths longer than Debye length, among all coherent plasma responses, the responses with EPW and IAW characteristics stand out like "resonance". That is, for a given k, the scattered light peaks at frequencies satisfying dispersion relation of $\epsilon = 0$. Thus, measuring these peaks and their widths provides a nearly complete set of local plasma parameters of interest. An example is shown in Fig. 122.

The coherent Thomson scattering process discussed above is due to the thermal fluctuations that exist intrinsically in plasmas such as discreteness of particles represented in the Klimontovich equations. However, plasmas often contain other fluctuations due to instabilities, and they can also scatter incident electromagnetic waves in principle. In such cases, $N_e(\boldsymbol{k},\omega)$ in Eq. (245) can be simply replaced by the non-thermal density fluctuations $n_e(\boldsymbol{k},\omega)$ due to instabilities. An alternative way to explain this type of scattering is by invoking the refractive index, N, discussed in Lecture 13. Electron density fluctuations result in a fluctuating N which distorts the wavefront and thereby causes incident waves to deviate from their original propagation path.

A typical setup is to measure frequency spectra for a given $\boldsymbol{k}$. An example is shown in Fig. 123 for a microwave scattering system (wavelength = 1.1 mm) to measure the density fluctuations on electron scales in NSTX.

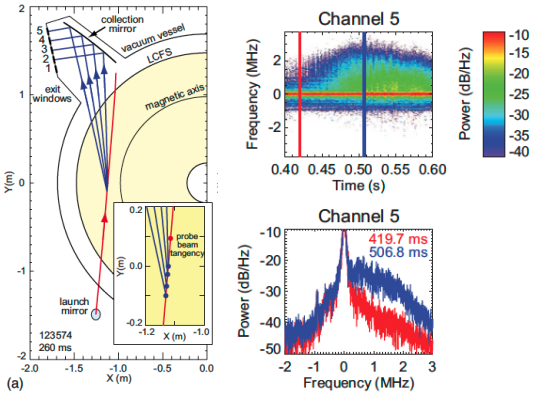

Fig. 123: (left panel) Diagnostics setup for microwave scattering on NSTX and (right panel) Measured spectrogram and frequency spectra at two different times for $k_\perp \rho_e = 0.42$. From Smith et al (2008).

18.2 Compton Scattering

The picture presented above on Thomson scattering is not fully self-consistent based on classical physics. For example, the backward-forward symmetry is kept during scattering process, as illustrated in Fig. 119, by ignoring the incident photon momentum. However, when the photon (or electron) energy is comparable or larger than the electron rest mass energy, the momentum conservation needs to be enforced and the scattering process is called *Compton scattering*; full relativistic effects need to be taken into account.

Consider a case shown in Fig. 124 where an incident photon gets scattered by an electron at rest. The four-momentum vectors of the photon and electron before the collision are given by

$$P_\gamma^\mu = \left(\frac{E}{c}, \frac{E}{c}, 0, 0\right)$$
$$P_e^\mu = (m_e c, 0, 0, 0)$$

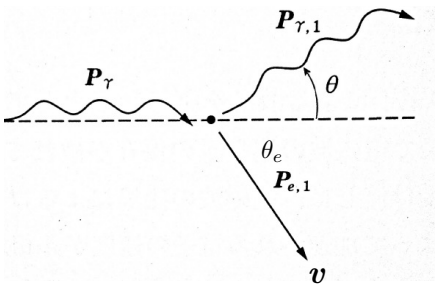

Fig. 124: Compton scattering of a photon by an electron at rest. Modified from Miyama et al (2008).

and their counterparts after collision are

$$P^{\mu}_{\gamma,1} = \left(\frac{E_1}{c}, \frac{E_1}{c}\cos\theta, \frac{E_1}{c}\sin\theta, 0\right)$$
$$P^{\mu}_{e,1} = \left(\sqrt{p^2+m_e^2c^2}, p\cos\theta_e, -p\sin\theta_e, 0\right).$$

Here the electron energy is given by $\sqrt{p^2c^2+m_e^2c^4}$ where p is electron momentum. The three unknowns are E_1, p, and θ_e, and can be solved by three equations from the four-momentum conservation, $P^{\mu}_{\gamma} + P^{\mu}_{e} = P^{\mu}_{\gamma,1} + P^{\mu}_{e,1}$,

$$\frac{E}{c} + m_e c = \frac{E_1}{c} + \sqrt{p^2+m_e^2c^2} \tag{247}$$
$$\frac{E}{c} = \frac{E_1}{c}\cos\theta + p\cos\theta_e \tag{248}$$
$$0 = \frac{E_1}{c}\sin\theta - p\sin\theta_e. \tag{249}$$

To eliminate θ_e, move the E_1 term to the left-hand side in Eq. (248) and Eq. (249), square and add them, leading to

$$E^2 - 2EE_1\cos\theta + E_1^2 = c^2p^2. \tag{250}$$

Similarly, by moving the E_1 term to the left-hand side in Eq. (247), and squaring, we obtain

$$\begin{aligned}(E-E_1)^2 + 2(E-E_1)m_ec^2 + m_e^2c^4 &= c^2p^2 + m_e^2c^4\\ (E-E_1)^2 + 2(E-E_1)m_ec^2 &= c^2p^2.\end{aligned} \tag{251}$$

Equating Eq. (250) and Eq. (251) eliminates p, yielding the solution for E_1,

$$E_1 = \frac{E}{1+\frac{E}{m_ec^2}(1-\cos\theta)} \tag{252}$$

which can be rewritten as

$$\lambda_1 = \lambda + \lambda_c(1-\cos\theta). \tag{253}$$

Here $\lambda_c \equiv h/m_ec = 0.0243\mathring{A}$ is the Compton wavelength for the photons with electron rest mass energy. Therefore, the photons' wavelengths increase because they lose energy to the electrons. The fractional change in wavelength is on the order of λ_c/λ, which is significant only when λ is sufficiently short or the photons are relativistic. The scattering cross section gets smaller with photon energy according to the well-known Klein-Nishina formula as an early

achievement of quantum-electrodynamics (QED),

$$\frac{d\sigma}{d\Omega_s} = \frac{r_e^2}{2}\frac{E_1^2}{E^2}\left(\frac{E}{E_1} + \frac{E_1}{E} - \sin^2\theta\right), \tag{254}$$

which reduces to Thomson scattering cross section, Eq. (238), in the limit of $E_1 = E$.

18.3 Inverse Compton Scattering

In contrast to the case when electrons are at rest in the lab frame while the photon energy is relativistic, consider the opposite case when electrons move at a finite speed of v_e before colliding with photons, whose energy is non-relativistic. Figure 125 (left panel) shows a case where photons can receive energy from electrons, as opposed to losing energy by Compton scattering, thus it is termed as *inverse Compton scattering*.

First, lets examine the frequency shift (or energy change) due to the relativistic Doppler shift from the lab frame (K) to electron rest frame (K'):

$$E' = E\gamma(1 - \beta\cos\theta) \tag{255}$$

$$E_1' = E_1\gamma(1 - \beta\cos\theta_1), \tag{256}$$

where $\beta = v_e/c$. Next, consider the electron rest frame as shown in Fig. 125 (right panel). According to Eq. (252), $E_1' \approx E'$ since $E' \ll m_e c^2$. Thus, equating Eq. (255) with Eq. (256) yields

$$E_1 \approx E\frac{1 - \beta\cos\theta}{1 - \beta\cos\theta_1} > E \tag{257}$$

since $\theta > \theta_1$. This photon energy increase is called *Sunyaev-Zel'dovich Effect or SZE*, and when averaged over a thermal electron distribution with temperature of T_e, the averaged fractional photon energy increase is given by

$$\left\langle\frac{\Delta E}{E}\right\rangle = \frac{4T_e}{m_e c^2} = 0.04\left(\frac{T_e}{5\text{keV}}\right). \tag{258}$$

SZE has been observed in Cosmic Microwave Background (CMB) radiation when passing through hot plasmas in intra-cluster medium (ICM) of galaxy clusters. Figure 126 shows an example of SZE distortion of CMB spectra for a fictional cluster that is over 1000 times more massive than a typical cluster to illustrate the small effect. Nonetheless, SZE has been used to detect and study hot plasmas in the ICM as galaxy cluster structures (Carlstrom et al, 2002).

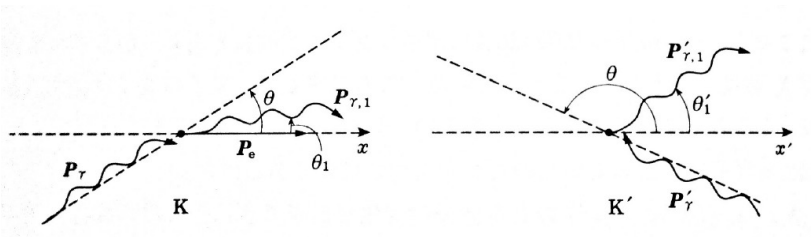

Fig. 125: Inverse Compton scattering in the lab frame, K (left panel) in the electron rest frame, K' (right panel). From Miyama et al (2008).

18.4 Summary

- Incoherent Thomson scattering is a powerful diagnostic to measure the electron velocity distribution function in hot plasmas of magnetically confined fusion plasmas, despite its small cross section.
- Coherent or collective Thomson scattering, when $k_i\lambda_D \ll 1$, is also a powerful diagnostic to measure various important plasma parameters, even including ion information, through electron plasma wave (EPW) and ion acoustic wave (IAW) resonances in high-energy-density (HED) plasmas.
- Coherent or collective Thomson scattering can be also used to measure short-wavelength density fluctuations in magnetic confined fusion plasmas.
- When the photon energy is relativistic, they can lose energy through Compton scattering.
- When electrons are hot, photons can receive energy via inverse Compton scattering, called the Sunyaev-Zel'dovich effect important in cosmology and astrophysics.

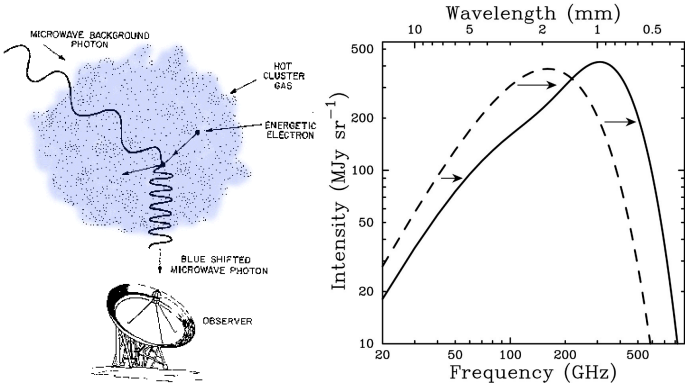

Fig. 126: Cosmic Microwave Background (CMB) radiation gets boosted in energy due to Sunyaev-Zel'dovich Effect (SZE): schematic illustration (left panel) and spectral distortion by a fictional cluster that is over 1000 times more massive than a typical cluster from Carlstrom et al (2002) (right panel).

18.5 Further Reading

- Chapter 7 of Hutchinson (2002)
- Froula et al (2011)
- Miyama et al (2008)

18.6 Homework Problem Set 11

Due April 17, 2026

1. Conceptually design a simple incoherent Thomson scattering system for FLARE to measure $n_e = 5 \times 10^{19}\text{m}^{-3}$ and $T_e = 10\text{eV}$. It is unknown if a coherent Thomson scattering system is possible but please list possible challenges for such a system. FLARE technical information can be found at flare.pppl.gov.

19 Neutral Particles

Electrically-neutral particles are an important component of plasmas. These particles often critically influence other components, including both electrons and ion species, as discussed in Section 15 on line radiation. At some other times, active injection of neutral particles into plasmas creates numerous opportunities to diagnose the plasma, not only for ions but also for the magnetic field.

19.1 Collisional Processes and Neutral Particle Transport

There are three important types of collisions for neutral particles in plasmas:

1. Electron-impact ionization. For this process, the neutral particle speed is unimportant as electrons typically move much faster. There is a sharp ionization threshold (Fig. 127) at the Rydberg energy, R_y, with a cross-section on the order of πa_0^2 where a_0 is Bohr radius.
2. Ion-impact ionization. The situation is similar to electron-impact ionization, except ions need to be higher energy by a factor of m_i/m_e.
3. Charge-exchange collisions. An electron jumps from neutral particles to ions (instead of being set free), so that neutral particles are ionized while ions recombine to neutrals or become one electron charge less ionized. If incident and target atoms are of the same species, the charge exchange is said to be symmetric and the bound electron does not change its energy other than the energy differences between two atoms but reduced by m_e/m_i. The "jump" by the electron is of resonant nature with much larger efficiency than impact ionization: the charge-exchange cross section $\sim 50\pi r_0^2$. However, when the energy difference between two atoms is larger than $R_y m_i/m_e$, $\sim$ 20 keV for hydrogen, the charge exchange cross section drops because the electrons associated with incident atoms are too energetic to be captured by ions. This is shown in Fig. 127.

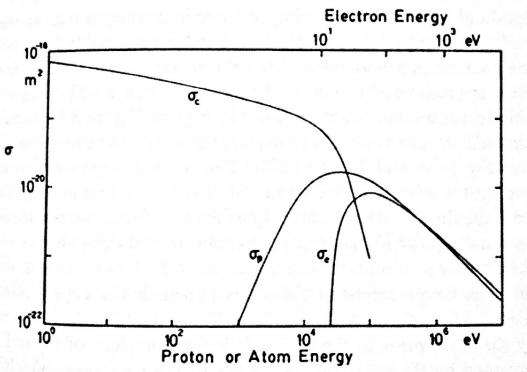

Fig. 127: Cross-sections of charge-exchange, ion-impact and electron-impact collisions for neutral particles. From (Hutchinson, 2002).

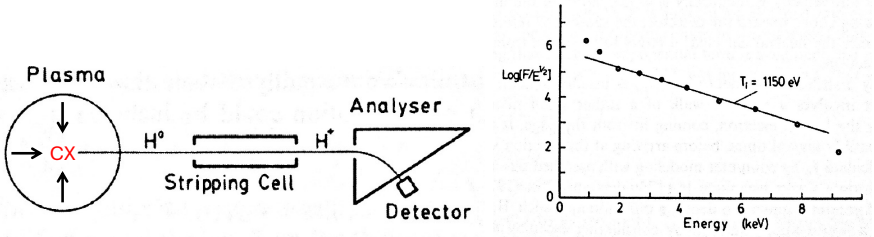

Fig. 128: (left panel) A typical experimental a setup of a Neutral Particle Analyzer (NPA). Cold neutrals penetrate into the hot plasma core where charge-exchange collisions occur to release fast neutral particles, which become ions in a stripping cell before being detected. (right panel) An example measurement showing neutral energy spectra, indicative of hot ion temperature in the core. From (Hutchinson, 2002).

The neutral particle transport, or neutral penetration into plasma, can be discussed in a similar way to optical depth for photon transport in Lecture 6. The probability for a neutral to survive along its travel path l from location A to location B, using the mean number of collisions per unit length, α, is

$$P_{AB} = \exp\left[-\int_A^B \alpha(l)dl\right], \tag{259}$$

where

$$\alpha = \frac{1}{V_a}\left[\langle\sigma_e v_e\rangle\, n_e + \left(\langle\sigma_i v_i\rangle + \langle\sigma_c v_i\rangle\right) n_i\right]. \tag{260}$$

and V_a is neutral particle speed. In hot fusion experiments, for the cold neutrals at the plasma's edge from gas puffing or surface outgassing, the first term on the right-hand side of Eq. (260) dominates. These cold neutrals do not penetrate too deep into the plasma due to electron-impact ionization. For a small number of neutrals which have managed to penetrate into the plasma core, they charge exchange with hot ions which subsequently become fast neutral particles. Measuring such fast neutral particles can provide valuable information on ions and neutrals in the core. Figure 128 shows an experimental setup of Neutral Particle Analyzer (NPA) and an example measurement. Such measurements reveal the hot ion temperature in the core but require rather complicated analysis, see Chap. 8.1 of Hutchinson (2002).

19.2 Neutral Beam Injection

Neutral Beam Injection (NBI) has been a major technique to heat fusion plasmas beyond about 1 keV, the maximum electron temperature achievable by Ohmic heating. Figure 129 (left panel) shows a typical setup to generate NBI. The ion source generates D^+, D_2^+, and D_3^+ deuterium molecules and get accelerated to equal energy, E, and dissociated in neutralizer. So in addition to the

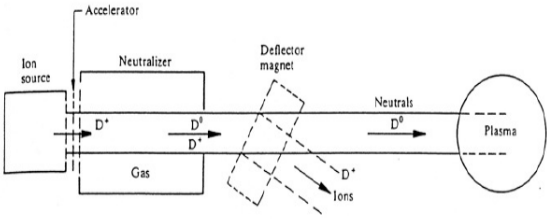

Fig. 129: Layout of a Neutral Beam Injection (NBI) system.

primary component of neutrals with energy of E, there are secondary components with energies of $E/2$ and $E/3$. For such fast neutral particles, V_a is much larger than ion thermal speed. Therefore, the averaged cross section is simply

$$\langle \sigma v_i \rangle \equiv \frac{1}{n_i} \int \sigma \left(|\boldsymbol{v}_i - \boldsymbol{V}_a| \right) |\boldsymbol{v}_i - \boldsymbol{V}_a| f_i(\boldsymbol{v}_i) d\boldsymbol{v}_i \approx \sigma(V_a) V_a. \tag{261}$$

Thus, Eq. (260) becomes

$$\alpha \approx (\sigma_i + \sigma_c) n_i, \tag{262}$$

since the electron impact ionization term is small due to large V_a. Therefore, Eq. (259) becomes

$$P_{AB} = \exp \left[-(\sigma_i + \sigma_c) \int_A^B n_i dl \right] \tag{263}$$

for fast neutral particle injection. For example, 10 keV neutrals can penetrate by about 0.1 m into a plasma with density of $10^{20}\mathrm{m}^{-3}$. Neutrals with higher energy can penetrate deeper but for typical positively charged ions, the neutralization efficiency drops when approaching 100 keV (see above due to dropping charge exchange cross section). Such difficulty does not exist for negatively charged ions, and thus, Negative NBI or N-NBI has been used. Figure 129 (right panel) shows its neutralization efficiency and penetration length as functions of energy. Modern tokamaks, such as the new JT-60SA, use extensively both P-NBI and N-NBI systems, see Fig. 131. ITER uses two N-NBI systems at 1 MeV to heat and fuel plasma due to its large size.

Active NBI systems for hot fusion plasmas also create unique opportunities to diagnose plasmas. Below we discuss the following four specific techniques:

1. Charge-exchange with impurity ions – Charge Exchange Recombination Spectroscopy (CHERS) to measure impurity temperature and flow;
2. Emission from beam atoms – Beam Emission Spectroscopy (BES) to measure n_e fluctuations;
3. Charge-exchange with majority ions - Main Ion Charge Exchange Spectroscopy (MICER) to measure majority ion temperature and flow;
4. Motional Stark Effect (MSE) to measure magnetic field pitch angle.

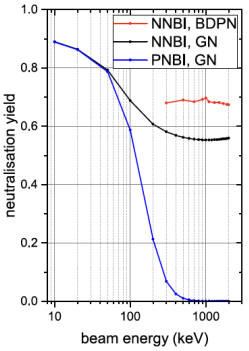

Fig. 130: Neutralization efficiency for positive NBI and negative NBI as a function of beam energy. From Hopf et al (2021).

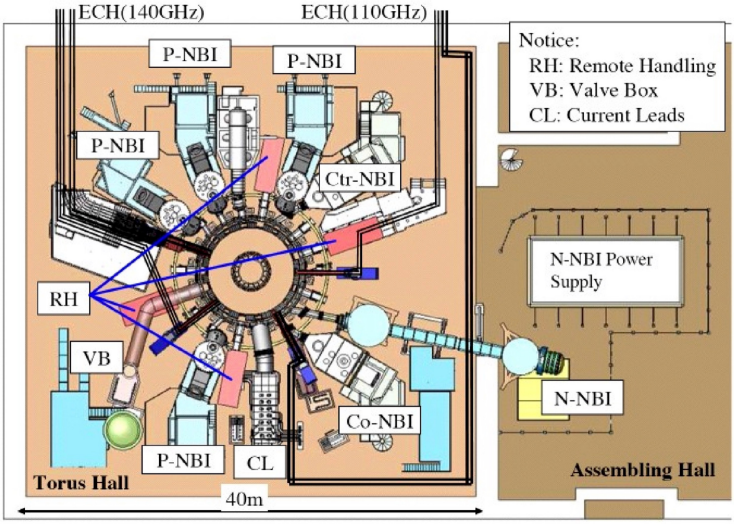

Fig. 131: Layout of NBI systems for JT-60SA.

19.2.1 Charge Exchange Recombination Spectroscopy (CHERS)

The underlying charge exchange process is

$$\mathrm{H}^0 + \mathrm{A}^{Z+} \longrightarrow \mathrm{H}^+ + \mathrm{A}^{*(Z-1)+} \longrightarrow \mathrm{H}^+ + \mathrm{A}^{(Z-1)+} + h\nu \qquad (264)$$

where the fully stripped impurity ions (A^{Z+}) gain an electron (called hydrogen-like) at an excited state ($\mathrm{A}^{*(Z-1)+}$) and then decay to their ground state ($\mathrm{A}^{(Z-1)+}$) by emitting a photon with energy of $h\nu$. The emitted photons contain information about the impurity ions, which can be spectroscopically

measured. From the intensity, the impurity density can be determined with absolute calibration. From the Doppler shift and the broadening of the line, impurity flow and temperature can be determined as in Lecture 7. This technique enables fully stripped impurity ions (typically in hot fusion plasmas) to radiate and has a large number of possible lines to choose from. Figure 132 shows a schematic layout of CHERS where good spatial resolutions are achieved by crossing the measurement line-of-sights with NBI. Multiple views allow measurements of different components of the impurity flow vector as well as temperature anisotropy.

There are also some difficulties to overcome for this technique to be useful:

- Contributions from edge. Impurities get ionized at the plasma edge and also radiate there. Removing edge contributions often is difficult and NBI intensity modulation can help discriminate against background radiation;
- Contributions from the radiation "plume" along the field line due to electron-impact ionization after charge exchange but before decay radiation. See "plume" in Fig. 132;
- Fine structure in lines when temperature is low;
- Zeeman effect due to the magnetic field.

Figure 133 shows an example measurement after overcoming some of these difficulties.

19.2.2 Beam Emission Spectroscopy (BES)

Line emissions from beam atoms after being excited by collisions with plasma electrons are Doppler shifted, so they are easy to identify in the spectra. An example is shown in Fig. 134 where different peaks are readily identifiable for each beam component: E, $E/2$, and $E/3$, generated at the ion source as mentioned above. (Three groups at each energy due to Stark splitting will be discussed in the next subsection.) Although its line profile does not contain information from the plasma, its intensity does. It is directly proportional to electron density and only weakly depends on other parameters such as electron temperature and ion temperature. The situation is ideal to use a bright and visible line like H_α line at 656.3 nm to measure electron density fluctuations in both space and time. The detection geometry is similar to what is shown for CHERS, Fig. 132, but tangential views along flux surface are preferred due to

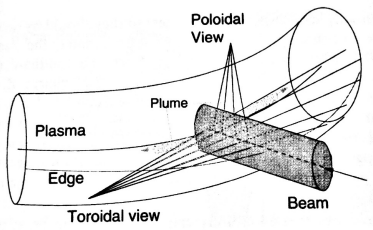

Fig. 132: Experimental setup for a CHERS system.

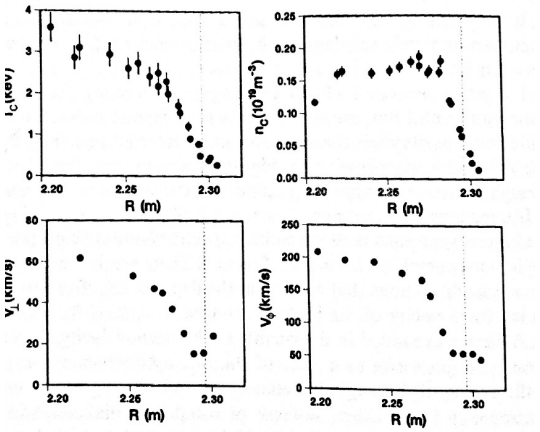

Fig. 133: Example measurements of C^6 ions by CHERS in DIII-D tokamak: temperature, density, perpendicular and toroidal velocities. From Hutchinson (2002).

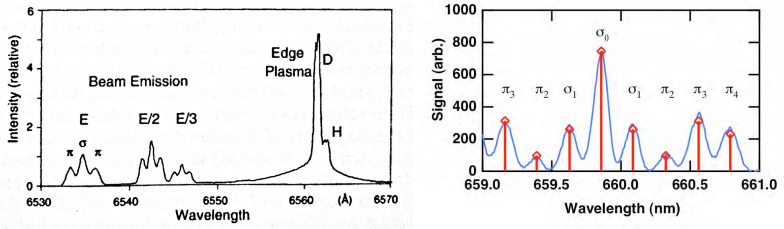

Fig. 134: Example spectra during neutral beam injection into a tokamak and fine spectral structures. From Hutchinson (2002).

small expected density variations along the field line. Since the beam Doppler shift is also important, tangential NBI is required.

The line intensities can be modeled using time-dependent collisional radiative models as discussed in Lecture 7 (Section 15). Since the initial condition of injected neutral particles is known, the governing equations are greatly simplified and can be integrated from $t = 0$ (Hutchinson, 2002),

$$\frac{dN_1}{dt} = -D_1 N_1 \tag{265}$$

$$\frac{dN_2}{dt} = P_{12} N_1 - D_2 N_2 \tag{266}$$

$$\frac{dN_3}{dt} = P_{13} N_1 + P_{23} N_2 - D_3 N_3, \tag{267}$$

where D_i is the total loss rate and P_{ij} is the rate at which the excited state j is populated from state i. This idea has led to a comprehensive spectral model called FIDASIM (Fast Ion D Alpha Sim) code which provides predictions of line spectra for Deuterium NBI-heated tokamaks (Heidbrink et al, 2011).

Figure 135 shows an example measurement of electron density fluctuation by BES across a patch in DIII-D. Such measurements are used extensively in turbulence analysis.

19.2.3 Motional Stark Effect (MSE) Diagnostics

As shown in Fig. 134, the line emission for each beam energy spits into 3 components: one α component and two π components. This is due to the Stark shift (see Lecture 7) of line emission from the local motional electric field, $\boldsymbol{V} \times \boldsymbol{B}$ where $\boldsymbol{V}$ is the beam velocity. The α component is polarized perpendicular to and the π components are polarized parallel to the local electric field. By measuring the polarization angle of these lines using refractive index modulators (Levinton, 1999), the precise angle of local electric field and thus magnetic field can be determined. This is called Motional Stark Effect (MSE) diagnostics. Furthermore, each component of these lines further splits into 3 lines due to the magnetic field strength, as shown in the right panel of Fig. 134.

The geometry for the diagnostics is shown in Fig. 136. The local toroidal coordinate $(\hat{\phi}, \hat{\theta}, \hat{r})$ is defined at the intercept point between neutral beam and sightline of the detector. The magnetic field vector at that location is given by $\boldsymbol{B} = (B_\phi, B_\theta, 0)$ and the injected neutral beam velocity vector is given by $\boldsymbol{V} = (V\cos\alpha, 0, -V\sin\alpha)$, where V is neutral particle speed and α is the angle between $\boldsymbol{V}$ and $\hat{\phi}$. Therefore, the motional electric field is given by

$$\boldsymbol{E}_M \equiv \boldsymbol{V} \times \boldsymbol{B} = (-VB_\theta \sin\alpha, VB_\phi \sin\alpha, VB_\theta \cos\alpha). \tag{268}$$

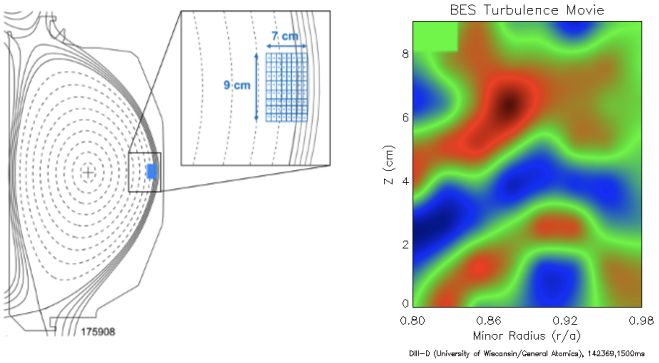

Fig. 135: (left panel) A patch of DIII-D tokamak cross section measured by BES diagnostics and (right panel) measured electron density fluctuations. From G. McKee (2012).

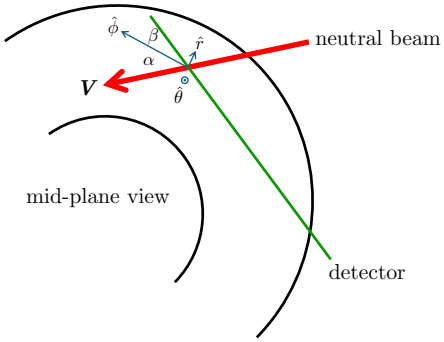

Fig. 136: Geometry for Motional Stark Effect diagnostics.

Now, assume the unit vector of the sightline is given by $\hat{s} = (\cos\beta, 0, \sin\beta)$ as shown in Fig. 136. The tangent of the detected polarization angle, γ, within the perpendicular plane of $\hat{s}$ is then given by

$$\tan\gamma = \frac{VB_\theta \cos(\alpha+\beta) + E_r \cos\beta}{VB_\phi \sin\alpha}. \tag{269}$$

Here E_r is radial electric field in the lab frame where ions are assumed to be at rest and is given by

$$E_r = \frac{1}{Z_i e n_o}\frac{\partial P_i}{\partial r}, \tag{270}$$

where Z_i, n_i, and P_i are ion charge, density and pressure, respectively. When ions are not at rest in the lab frame, the additional motional electric field should properly be added. Typically E_r is much smaller than E_M: $E_r \sim 10\text{kV/m}$ while $E_M \sim 100\text{kV/m}$. In such cases, the field line pitch angle, B_θ/B_ϕ, can be determined as

$$\frac{B_\theta}{B_\phi} = \tan\gamma \frac{\sin\alpha}{\cos(\alpha+\beta)}, \tag{271}$$

which in turn can determinethe safety factor, q. One such example from TFTR is shown in Fig. 137 from Levinton (1999).

The dependence of polarization angle on E_r as shown in Eq. (269) provides an opportunity to measure it, as E_r is important in confinement physics. There are three different ways in general:

1. Two different beams; this is equivalent to two different values of α.
2. Two different view angles; this is equivalent to two different values of β.
3. Two different energies of the same beam (E, $E/2$, $E/3$); this is equivalent to two different values of V.

There are successful examples for each of the above.

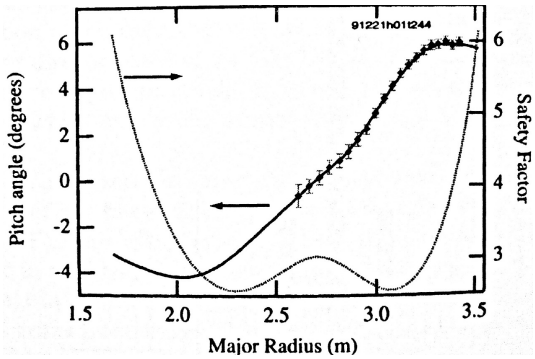

Fig. 137: Example measurements of field line pitch angle and safety factor using MSE diagnostics from TFTR (Levinton, 1999).

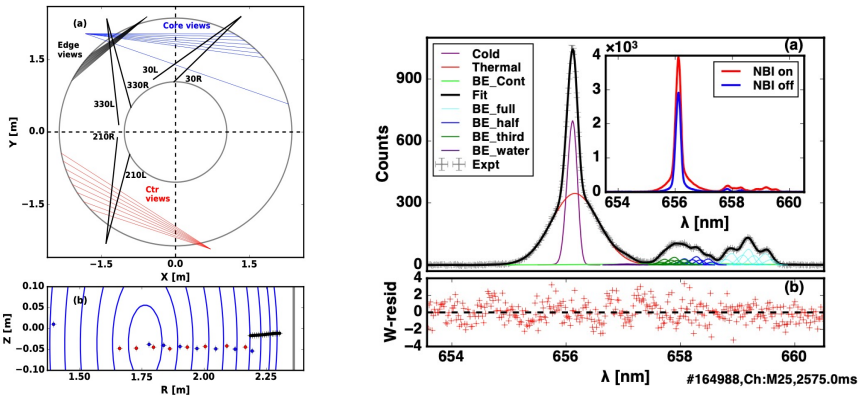

Fig. 138: (left panel) Midplane view of MICER setup on DIII-D and example of measured spectrum and background subtraction. From Haskey et al (2018).

19.2.4 Main Ion Charge Exchange Spectroscopy (MICER)

The original difficulties in measuring majority or main ions using charge exchange spectroscopy have been due to strong background emissions from various effects. However, significant progress over the years on the CHERS, BES and MSE diagnostics, matched by comprehensive modeling efforts including FIDASIM and a specially designed MICEFIT spectral fitter, it becomes possible to cleanly separate out the background emissions from those from main ions. The underlying process is similar to Eq. (264) with impurity ions replaced by main ions, typically Deuterium ions,

$$D^0 + D^+ \longrightarrow D^+ + D^{*0} \longrightarrow D^+ + D^0 + h\nu. \tag{272}$$

Figure 138 shows a MICER experimental setup on DIII-D for both core and edge views (left panel) and an example spectrum for both measurement and

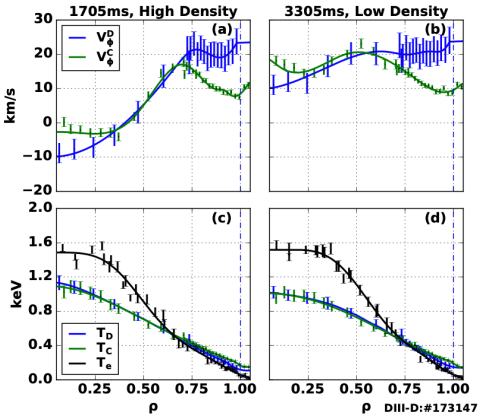

Fig. 139: Various quantities of main ions (D) measured by MICER and impurity ions (C) measured by CHERS. From Haskey et al (2018).

modeling. These measurements have sufficient precision to determine main ion quantities which are compared well with impurity measurements by CHERS, shown in Fig. 139.

It should be noted here that there exist other diagnostic techniques based on neutral beam injection such as Zeeman effects to measure magnetic field. While generally hard to apply, Zeeman diagnostics have been successfully used to the measure solar magnetic field (see a recent review by Pevtsov et al (2021)). It is described in Chap. 8.2 of Hutchinson (2002). Pellet injection to fuel fusion reactions also provide similar opportunities to NBI.

19.3 Heavy Ion Beam Probe (HIBP)

Lastly, we briefly discuss a useful diagnostic based on injecting a beam of ions at high energies which are sufficiently massive so that their ion gyroradius large

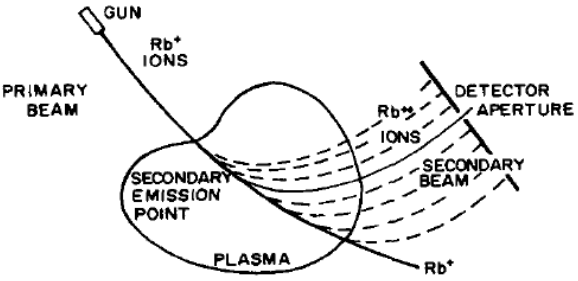

Fig. 140: Experimental setup for a heavy ion beam probe (HIBP). From Crowley (1994).

enough to directly travel out of the plasma. A typical Heavy Ion Beam Probe (HIBP) setup is shown in Fig. 140, where Rb ions are injected into plasma. In principle, the primary beam landing location contains integrated electric and magnetic field information along their path, similar to the electron beam technique used in spacecraft described in Fig. 28 in Lecture 3. However, since the fields are highly nonuniform, multi-chord deconvolution is necessary as in Abel inversion discussed in Lecture 13 and it is typically difficult to perform, as both the electric field and magnetic fields are vectors.

The real usefulness of HIBP lies in its secondary beams, which form after ions in the primary beam get further ionized by adding one more electron charge. Due to their larger charge, they receive a larger force from electric and magnetic fields, and thus follow a different path than the primary beam, see Fig. 140. The landing location and its energy change from the primary beam contains information on the location of ionization and *electric potential* at that location, respectively. Determining the electric field requires information on the spatial gradient of electric potential, which can pose a challenge. Since the ionization is mainly by impact electrons, the secondary beam intensity is proportional to electron density at the ionization location. With location, electron density fluctuation, and electric potential measured simultaneously with sufficient time resolution, detailed physics studies become possible on topics such as turbulent transport due to electrostatic drift waves in tokamaks and stellarators (Fujisawa, 2009).

19.4 Summary

- Three important collisional processes exist for neutral particles in plasmas and charge exchange collision is a particularly process important at low energies.
- Neutral particle transport properties are important to interpret passive neutral particle measurements from hot fusion plasmas.
- Neutral beam injection (NBI), including Native NBI, is essential to heat and fuel fusion plasmas but also provides unique opportunities to diagnose plasmas.
- Charge Exchange Recombination Spectroscopy (CHERS) measures density, velocity and temperature of impurity ions, Beam Emission Spectroscopy (BES) measures electron density fluctuations, while Motional Stark Effect (MSE) Diagnostics measure magnetic field pitch angle.
- By fully taking into account all emission lines, important properties of majority ions can be determined by Main Ion Charge Exchange Spectroscopy (MICER).
- Heavy Ion Beam Probe (HIBP) is a useful diagnostic to measure local electron density and electric potential internal to hot fusion plasmas.

19.5 Further Reading

- Chapter 8 of Hutchinson (2002)

19.6 Homework Problem Set 12

Due April 22, 2026

1. Calculate the minimum neutral hydrogen energy in order to reach the center of ITER plasma assuming reasonable magnitudes and profiles for electron density, electron temperature and ion temperature.
2. Consider a plasma with two ion species: protons and a single type of impurity with charge Z. Suppose Z_{eff} is measured by Bremsstrahlung radiation and electron density n_e is measured by an interferometer. What is the proton density?
3. Discuss potential benefits and difficulties when adding beam energy modulation to HIBP.

References

Akiyama T, Hisakado T, Vollmer D, et al (2025) Development of a wide bandwidth heterodyne dispersion interferometer for electron density measurement of atmospheric pressure plasmas. Plasma Physics and Controlled Fusion 67(11):115019. https://doi.org/10.1088/1361-6587/ae1412

Boozer AH (1983) Transport and isomorphic equilibria. Physics of Fluids 26(2):496–499. https://doi.org/10.1063/1.864166

Bornatici M, Cano R, De Barbieri O, et al (1983) Electron Cyclotron Emission and Absorption in Fusion Plasmas. Nuclear Fusion 23:1153. https://doi.org/10.1088/0029-5515/23/9/005

Bott AFA, Graziani C, Tzeferacos P, et al (2017) Proton imaging of stochastic magnetic fields. Journal of Plasma Physics 83(6):905830614. https://doi.org/10.1017/S0022377817000939

Bretz N, Jobes F, Irby J (1997) The design of a second harmonic tangential array interferometer for C-Mod. Review of Scientific Instruments 68(1):713–716. https://doi.org/10.1063/1.1147683

Carlstrom JE, Holder GP, Reese ED (2002) Cosmology with the Sunyaev-Zel'dovich Effect. Annual Review of Astronomy and Astrophysics 40:643–680. https://doi.org/10.1146/annurev.astro.40.060401.093803

Cooper CM, Wallace J, Brookhart M, et al (2014) The Madison plasma dynamo experiment: A facility for studying laboratory plasma astrophysics. Physics of Plasmas 21(1):013505. https://doi.org/10.1063/1.4861609

Crowley TP (1994) Rensselaer heavy ion beam probe diagnostic methods and techniques. IEEE Transactions on Plasma Science 22(4):291–309. https://doi.org/10.1109/27.310636

Delgado-Aparicio L, Bitter M, Granetz R, et al (2012) Molybdenum emission from impurity-induced m = 1 snake-modes on the Alcator C-Mod tokamaka). Review of Scientific Instruments 83(10):10E517. https://doi.org/10.1063/1.4733731

Doi K, Kataoka A, Liu HB, et al (2024) Asymmetric dust accumulation of the pds 70 disk revealed by alma band 3 observations. The Astrophysical Journal Letters 974(2):L25. https://doi.org/10.3847/2041-8213/ad7f51, URL https://dx.doi.org/10.3847/2041-8213/ad7f51

Freidberg JP (2014) Ideal MHD. Cambridge University Press, Cambridge, UK

Froula DH, Glenzer SH, Luhmann NC, et al (2011) Plasma Scattering of Electromagnetic Radiation: Theory and Measurement Techniques, 2nd edn. Academic Press, Amsterdam, https://doi.org/10.1016/C2009-0-20048-1

Fujisawa A (2009) A review of zonal flow experiments. Nuclear Fusion 49(1):013001. https://doi.org/10.1088/0029-5515/49/1/013001

Gekelman W, Pribyl P, Lucky Z, et al (2016) The upgraded large plasma device, a machine for studying frontier basic plasma physics. Review of Scientific Instruments 87(2):025,105. https://doi.org/10.1063/1.4941079

Goto M, Murakami I, Fujimoto T (2003) Light, Plasma, and Microscopic Processes. J Plasma Fusion Research (in Japanese) 79:1287

Goto M, Murakami I, Fujimoto T (2004a) Towards Deeper Understanding of a Plasma. J Plasma Fusion Research (in Japanese) 80:139

Goto M, Murakami I, Fujimoto T (2004b) What Do Spectra Tell Us? J Plasma Fusion Research (in Japanese) 80:45

Haskey SR, Grierson BA, Stagner L, et al (2018) Active spectroscopy measurements of the deuterium temperature, rotation, and density from the core to scrape off layer on the diii-d tokamak (invited). Review of Scientific Instruments 89(10):10D110. https://doi.org/10.1063/1.5038349

Heidbrink WW, Liu D, Luo Y, et al (2011) A code that simulates fast-ion d_α and neutral particle measurements. Communications in Computational Physics 10(3):716–741. https://doi.org/10.4208/cicp.190810.080211a

Hill KW, Bitter M, Diesso M, et al (1985) Tokamak Fusion Test Reactor prototype x-ray pulse-height analyzer diagnostic. Review of Scientific Instruments 56(5):840–842. https://doi.org/10.1063/1.1138517

Hopf C, Starnella G, den Harder N, et al (2021) Neutral beam injection for fusion reactors: technological constraints versus functional requirements.

Nuclear Fusion 61(10):106032. https://doi.org/10.1088/1741-4326/ac227a

Hopf FA, Tomita A, Al-Jumaily G (1980) Second-harmonic interferometers. Opt Lett 5(9):386–388. https://doi.org/10.1364/OL.5.000386, URL https://opg.optica.org/ol/abstract.cfm?URI=ol-5-9-386

Hutchinson IH (2002) Principles of Plasma Diagnostics. Cambridge University Press, Cambridge, UK

Jarboe TR (1994) Review of spheromak research. Plasma Physics and Controlled Fusion 36(6):945–990. https://doi.org/10.1088/0741-3335/36/6/002

Ji H (2024) General Plasmaa Physics II: Magnetohydrodynamics. URL https://w3.pppl.gov/~hji/GPPII_Lecture_Notes_10-07-24.pdf

Ji H, Toyama H, Shinohara S, et al (1990) A simple method of equilibrium determination and its application to a RFP plasma with thin shell. Plasma Physics and Controlled Fusion 32(1):79–89. https://doi.org/10.1088/0741-3335/32/1/007

Ji H, Yamada M, Hsu S, et al (1999) Magnetic reconnection with sweet-parker characteristics in two-dimensional laboratory plasmas. Phys Plasmas 6:1743

Ji H, Terry S, Yamada M, et al (2004) Electromagnetic fluctuation during fast reconnection in a laboratory plasma. Phys Rev Lett 92:115,001. https://doi.org/10.1103/PhysRevLett.92.115001

Ji H, Gao L, Pomraning G, et al (2024) Study of magnetic reconnection at low-β using laser-powered capacitor coils. Physics of Plasmas 31(10):102,112. https://doi.org/10.1063/5.0223922, URL https://doi.org/10.1063/5.0223922

Keilhacker M, Becker G, Bernhardi K, et al (1984) Confinement studies in L and H-type Asdex discharges. Plasma Physics and Controlled Fusion 26(1A):49–63. https://doi.org/10.1088/0741-3335/26/1A/305

Krall NA, Trivelpiece AW (1973) Principles of plasma physics. McGraw-Hill, New York

Laggner FM, Diallo A, LeBlanc BP, et al (2019) A scalable real-time framework for thomson scattering analysis: Application to nstx-u. Review of Scientific Instruments 90(4):043,501. https://doi.org/10.1063/1.5088248, URL https://doi.org/10.1063/1.5088248

Levinton F (1999) The motional Stark effect: Overview and future development. Rev Sci Instrum 70:810

Lorimer DR, Bailes M, McLaughlin MA, et al (2007) A Bright Millisecond Radio Burst of Extragalactic Origin. Science 318(5851):777. https://doi.org/10.1126/science.1147532

Luce TC (2011) Realizing steady-state tokamak operation for fusion energy. Physics of Plasmas 18(3):030,501. https://doi.org/10.1063/1.3551571

Marrelli L, Martin P, Puiatti ME, et al (2021) The reversed field pinch. Nuclear Fusion 61(2):023001. https://doi.org/10.1088/1741-4326/abc06c

Mazzucato E (2001) Microwave imaging reflectometry for the visualization of turbulence in tokamaks. Nuclear Fusion 41(2):203. https://doi.org/10.1088/0029-5515/41/2/307, URL https://doi.org/10.1088/0029-5515/41/2/307

Miyama S, Nomoto K, Futamase T (2008) Fundamentals of Astrophysics II, Modern Astronomy Series Vol. 12 (In Japanese). NIPPON HYORON SHA CO.,LTD, Tokyo, Japan

Moore T, Spann J (2017) Introduction: Particles and fields. Journal of Geophysical Research (Space Physics) 122(2):1435–1436. https://doi.org/10.1002/2017JA023887

Nier AO, Schlutter DJ (1985) High-performance double-focusing mass spectrometer. Review of Scientific Instruments 56(2):214–219. https://doi.org/10.1063/1.1138333

Olson J, Egedal J, Clark M, et al (2021) Regulation of the normalized rate of driven magnetic reconnection through shocked flux pileup. Journal of Plasma Physics 87(3):175870301. https://doi.org/10.1017/S0022377821000659

Park H, Chang CC, Deng BH, et al (2003) Recent advancements in microwave imaging plasma diagnostics. Review of Scientific Instruments 74(10):4239–4262. https://doi.org/10.1063/1.1610781

Petrasso RD, Li CK, Seguin FH, et al (2009) Lorentz Mapping of Magnetic Fields in Hot Dense Plasmas. Phys Rev Lett 103(8):085001. https://doi.org/10.1103/PhysRevLett.103.085001

Pevtsov AA, Bertello L, Nagovitsyn YA, et al (2021) Long-term studies of photospheric magnetic fields on the Sun. Journal of Space Weather and Space Climate 11:4. https://doi.org/10.1051/swsc/2020069

Pfaff RF, Borovsky JE, Young DT (1998a) Measurement Techniques in Space Plasmas – Fields. Geophysical Monograph Series 103. https://doi.org/10.1029/GM103

Pfaff RF, Borovsky JE, Young DT (1998b) Measurement Techniques in Space Plasmas – Particles. Geophysical Monograph Series 102. https://doi.org/10.1029/GM102

Rieke GH (2012) Measuring the Universe. Cambridge University Press, Cambridge, UK

Shi P, Srivastav P, Barbhuiya MH, et al (2022) Laboratory observations of electron heating and non-maxwellian distributions at the kinetic scale during electron-only magnetic reconnection. Phys Rev Lett 128

Smith DR, Mazzucato E, Lee W, et al (2008) A collective scattering system for measuring electron gyroscale fluctuations on the national spherical torus experiment. Review of Scientific Instruments 79(12):123,501. https://doi.org/10.1063/1.3039415

Spann J, Moore T (2017) Introduction: Photons and ground-based. Journal of Geophysical Research: Space Physics 122(2):1437–1438. https://doi.org/https://doi.org/10.1002/2017JA023888

Spitzer L (1958) The Stellarator Concept. Physics of Fluids 1(4):253–264. https://doi.org/10.1063/1.1705883

Steinhauer LC (2011) Review of field-reversed configurations. Physics of Plasmas 18(7):070501. https://doi.org/10.1063/1.3613680

Stix TH (1992) Waves in plasmas. Springer-Verlag, New York

Taylor JB (1974) Relaxation of Toroidal Plasma and Generation of Reverse Magnetic Fields. Phys Rev Lett 33:1139–1141

Wagner F, Becker G, Behringer K, et al (1982) Regime of Improved Confinement and High Beta in Neutral-Beam-Heated Divertor Discharges of the ASDEX Tokamak. Phys Rev Lett 49(19):1408–1412. https://doi.org/10.1103/PhysRevLett.49.1408

Wang Y, Tobias B, Chang YT, et al (2017) Millimeter-wave imaging of magnetic fusion plasmas: technology innovations advancing physics understanding. Nuclear Fusion 57(7):072007. https://doi.org/10.1088/1741-4326/aa5e30

Wang Y, Gilson E, Ebrahimi F, et al (2022) Observation of axisymmetric standard magnetorotational instability in the laboratory. Phys Rev Lett 129:115,001

Wesson J (2011) Tokamaks, 4th Ed. Oxford University Press, Oxford, UK

Wüest M, Evans DS, von Steiger R (2007) Calibration of Particle Instruments in Space Physics. ESA Communications, Noordwijk, The Netherlands

Yamada M, Ji H, Hsu S, et al (1997) Study of driven magnetic reconnection in a laboratory plasma. Physics of Plasmas 4(5):1936–1944. https://doi.org/10.1063/1.872336

Zhu Y, Yu JH, Yu G, et al (2020) W-band system-on-chip electron cyclotron emission imaging system on DIII-D. Review of Scientific Instruments 91(9):093504. https://doi.org/10.1063/5.0018082